Infrared Spectra of Cool Stars and Sunspots

A Thesis submitted for the Degree

of

Doctor of Philosophy of the University of London

by

Serena Viti

Department of Physics & Astronomy

University College London

University of London

September 1997

Ai miei genitori

Abstract

This thesis covers both the theoretical and the experimental aspects of cool and low mass stars' studies. In particular, it concentrates on M dwarfs which constitute about 88% of our Solar neighbourhood.

Although so numerous, the physics of M dwarfs is still poorly understood. Most of their energy (about 80%) is emitted between 1 and 5 microns, where strong absorption bands, caused mainly by the water molecule, are present. The interpretation of their colours and of their bolometric luminosities requires sophisticated modelling. The thesis is divided into two parts. The first part consists of the computation of molecular data of water. The applications of these data are various. For example some of these data are used for spectroscopic assignments of water lines in the sunspots. Some will be incorporated in the latest atmospheric models for cool stars.

The codes employed calculate quantum mechanically the rotation-vibration energy levels, wavefunctions and associated dipole transition strengths of triatomic molecules. Two water linelists have been calculated and are widely described in this thesis; the first completed linelist, VTP1, has been computed with an accurate empirically determined potential energy surface. It contains all the energy levels and dipole transitions up to J = 38 belonging to the ground vibrational state and some of the ones belonging to the following vibrational bands: 100, 001, 010, 021, 101. The second linelist, ZVPT, has been computed with an *ab initio* potential energy surface. It includes all the rotational levels up to $J = 33$ and all the energy levels up to 20000 cm^{-1}. A third, more comprehensive linelist, VT2, is partially complete.

The second part of the thesis consists of the description of the observations, reductions and analysis of infrared data obtained with CGS4 (UKIRT) on several cool stars. Among these stars, I have also performed a detailed spectral analysis of the eclipsing binary system CM Draconis: I derived a direct measurement of its metallicity and effective temperature by direct comparison of the observed and synthetic spectra. I produced the synthetic spectra by using one of the latest model atmosphere codes.

Contents

List of Tables

List of Figures

Acknowledgement

First of all, I would like to thank Jonathan Tennyson for being a great supervisor, for making this Ph.D. thesis happen and for being there anytime I needed his help.

During the last three years I have been involved in several projects which would not have been possible without :

(1) Hugh Jones, who I particularly thank for a great collaboration during the work described in Chapters 2, 8 and 9. I am especially grateful to him for infecting me with his enthusiasm and for introducing me to the more 'astronomical' aspect of this work, in particular the observing and the spectral analysis of stellar atmospheres, which I enjoyed very much.

(2) Oleg Polyansky with whom I collaborated during the course of the work described in Chapters 5 and 6. His use of my linelists made the solar assignments possible!

(3) Steve Miller for collaborating with me in the work described in Chapter 9 but especially for his help, useful discussions and encouragement throughout the course of my work.

(4) Nikolai Zobov for providing the 'Z' to ZVPT and for contributing to the solar assignments presented in Chapter 6.

(5) Peter Bernath and Lloyd Wallace for a fruitful collaboration which lead to many results discussed in Chapter 6.

(6) France Allard and Peter Hauschildt for giving me access to their model atmospheres codes and for computing the grids of models which I used in Chapters 2 and 9.

(7) Andreas Schweitzer for taking the optical spectrum of CM Draconis which lead to a much more comprehensive analysis described in Chapter 9.

(8) Andy Longmore without whom I would not have had the pleasure of going observing for the first time, which lead to useful work described in Chapters 8 and 9.

I would also like to thank Tony Lynas-Gray, for many useful discussions and many pleasant drinks in the Housman room.

I am grateful to Nic Fulton and James Henderson for 'chatting' with me about my work. Many thanks to the TAMPA group and especially to Darian who bravely proof-read this thesis, Jeremy, who had to share an office with me for longer than others, and Rita and Paul for nice chats and meals!

There are many people, too numerous to mention who have helped me through the last three years to whom I offer my deepest thanks. First of all, I would like to thank my parents for their moral and economic support. Without them this thesis would not be here today! I would like particularly to thank Orsola De Marco for being my best friend during the last three years and for sharing with me the joys and pains of a Ph.D. Also I would like to thank the 'chaps' for contributing to my social life, in (first name) alphabetical order: Chris, Daniel, Kaj, Matthew and Matt. Because of them, my (very long!) days at work became fun! A special thankyou to my "babies" (i) Kaj who, besides being a good friend, has been very patient with me and helped me out while fighting with the many figures in this thesis that didn't want to stay in their place and also for solving most of the various computer-related problems I have had throughout these three years. (ii) Matthew for being one of my best friends and suffering this flatmate in the last few weeks of her writing up!

Chapter 1

Astronomical introduction: low mass stars

1.1 Introduction to low mass stars

Low mass ($M \leq 0.6 M_{\odot}$) stars (LMS) are the most numerous stars in our Galaxy (Gould *et al*, 1996; Mera *et al*, 1996). Referring to the HR diagram, LMS mainly lie at the bottom of the Main Sequence (MS). They are low mass (dwarfs) and cool ($T_{eff} \leq 5000K$). Their luminosity is sub-solar (bottom right of the HR diagram).

In this chapter I will introduce LMS by briefly describing their characteristics, their location, the way they are studied and finally a historical background, together with the observational and theoretical current state of the art.

Studies of LMS are relevant for the understanding of many important issues such as star formation theory and dark matter candidates (Allard & Hauschildt, 1995). An advantage in studying LMS is their number and proximity. They are so numerous that statistically they form a very close and large sample for which distances and therefore other parameters can be measured. LMS space density is high. They constitute ~ 80 % of the stars of our solar neighbourhood (Dahn *et al*, 1986).

The spectral type of LMS ranges from mid-K to late-M. This means that their tem-

perature ranges from 5000 to 1500K .

By definition, LMS masses are between $\sim$ 0.6 $M_{\odot}$ to the hydrogen burning minimum mass of 0.075 – 0.0085 $M_{\odot}$ depending on their metallicity. There is no restriction on their age. They are long-lived. Their lifetime can be longer than the Hubble time (Reid *et al*, 1995) so the local sample includes stars of all ages since the formation of the Galactic disk.

Their atmospheres are complex (Allard *et al*, 1997). Unlike hotter stars, their near-infrared spectrum, where the bulk of their radiation is, does not resemble a blackbody curve. This is due to the presence of many molecular species that cause strong absorption throughout the spectrum, from the visible to the ultraviolet. For temperatures less than 5000K, many molecular species do not dissociate and they contribute to the opacities. More specifically, the optical spectrum of LMS is dominated by titanium monoxide, TiO, first identified by Fowler (1904). TiO is particularly strong in the regions centered at 0.6 and 0.9 μm. The infrared part of the spectrum is instead dominated by water vapour, H_2O (Alexander *et al*, 1989). In particular, strong water vapour bands are measured in the regions centered at $\sim$1.4, $\sim$1.9, $\sim$2.5 and $\sim$3.2 μm (Tinney *et al*, 1993; Jones *et al*, 1995 and also Chapter 2, Chapter 8 and Chapter 9 of this thesis). Figure 1.1 shows a sequence of LMS which differ mainly in temperature. The strength of the water bands centered at the above wavelengths decreases with the increase of temperature (Jones *et al*, 1995).

The presence of molecular species throughout the spectrum is a major complication for LMS studies. For example, while the atmospheres of hotter G-K stars can be compared with that of our Sun, there are no terms of comparisons for the cooler objects.

Deriving LMS stellar parameters, such as effective temperatures, surface gravities and metallicities, is still a challenging problem (Allard *et al*, 1997). To tackle this challenge one relies entirely on a good and extended sample of observations of LMS together with accurate *a priori* atmospheric models.

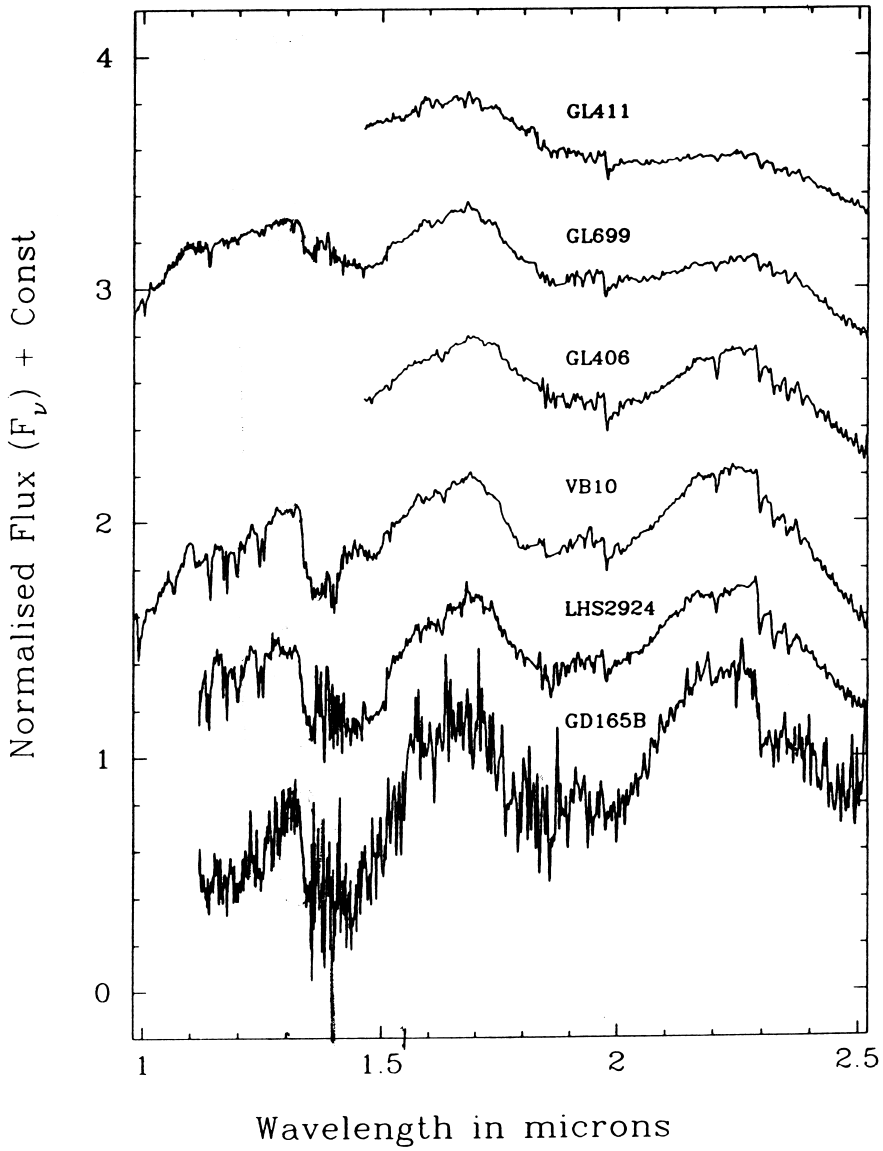

Figure 1.1: A sequence of M dwarfs from Jones *et al* (1994). The spectra have been normalized for the purpose of display. The increases of the humped appearance in the regions centered at ~ 1.4 and ~ 1.9 μm are due to the increasing of the water absorption as the effective temperature decreases.

1.2 Some basic definitions

In this section, I briefly define terms and concepts of common use in astronomy. For a much more detailed explanation or derivation of equations which will only be stated here, refer to Zelik & Smith (1987) or Bowers & Deeming (1984).

- **Spectral Classification** To classify stars, astronomers divide them into spectral classes based on their temperature and luminosity. The spectral sequence is:
  O, B, A, F, G, K, M according to their temperature (O are the hottest). A numeric sub-classification within each of the above spectral classes is added and it goes from 0 (early) to 9 (late). For example, the Sun is a G2 star. This thesis is concerned with M stars and, in particular, M dwarfs (as opposite to M giants).

- **Distances** Because of the numerosity of M dwarfs, many of them are close by (see below for details). For close–by stars, the best method to measure their distance is by making use of the perspective effect of our line of sight, the *trigonometric parallax*. This effect is due to the Earth motion around the Sun so that the nearest stars appear to move relative to the more distant stars. The trigonometric parallax of a star is defined as the angle π subtended as seen from the star by the Earth's orbit of radius 1 AU (1AU = 1.496×10^{11} m). The trigonometric parallaxes are measured by photographing a given star from different points in the Earth's orbit. Usually parallaxes are measured in arcseconds while distances are measured in *parsecs* (pc) where 1 pc = 206,265 AU.

- **Reddening Effect** The 'reddening effect' is caused by absorption by dust in the Interstellar Medium between us and a star. The star looks redder because the interstellar dust does not dim the light equally at every wavelength: more light is scattered in the blue than in the red. In this work, the stars studied are nearby and therefore show little reddening.

- **Proper motion** Another useful property of a star is its *proper motion* which is the motion of a star in the plane of the celestial sphere. The proper motion will be greater the closer the star is to us.

- **Magnitudes** The brightness of a star is measured by its *magnitude*. The magnitude scale is an arbitrary logarithmic scale where the brightest stars have lower numerical magnitude than the faintest ones. It is useful to define four types of magnitude: (i) apparent magnitude; (ii) absolute magnitude; (iii) apparent bolometric magnitude; (iv) absolute bolometric magnitude. The *apparent magnitude* of a star is defined as:

$$m - n = 2.5 \log(l_n / l_m) \tag{1.1}$$

where m and n are the apparent magnitudes of two stars and l_n and l_m are their apparent brightnesses. Magnitudes are measurable at most of the wavelengths. However, usually what is needed is the absolute luminosity of a star and not the flux received from them. The luminosity of a star relates to its *absolute magnitude* defined as the magnitude that would be observed if the star were placed at a distance of 10 pc from the Sun. By convention, absolute quantities are capitalized and apparent ones are written lower-case. The absolute magnitude is defined by:

$$M = m + 5 + 5 \log \pi^{''} \tag{1.2}$$

where $\pi^{''}$ is the parallax.

From outside the Earth's atmosphere, the radiative flux from the stars per unit wavelength l_λ can define the total *bolometric flux*:

$$l_{bol} = \int_0^\infty l_\lambda d\lambda \tag{1.3}$$

The *apparent bolometric magnitude* of a given star is:

$$m_{bol} = -2.5 \log l_{bol} + constant \tag{1.4}$$

where the constant is an arbitrary zero point. The *absolute bolometric magnitude* of the star, M_{bol}, is the bolometric magnitude if the star were at the standard distance of 10 pc.

- **Colours**

  The most common magnitude system used as reference for classifying a star is the Johnson UBV colour system (U for ultraviolet, B for blue, V for visible). Currently though, extensions to this system have been made to include the R and I in the red and the J, H, K and M in the infrared.

  A quantitative measure of the colour of a star is given by its colour index (CI) which is defined as the difference between magnitudes at two different wavelengths. Hence, for example, $B - V$ is the colour index corresponding to the difference in magnitude between the B band of the spectrum and the V band. A magnitude difference corresponds to a flux ratio.

- **The H-R Diagram** One of the best tools for grouping spectral classes is the Hertsprung-Russell diagram (HR). This is a two dimensional diagram, usually plotting absolute magnitude M versus spectral type Sp. This is equivalent to luminosity versus effective temperature, defined, for a given star, by the continuum, which is usually approximated by the Planck blackbody spectral-energy distribution.

1.3 Observations and Models of LMS

Infrared observations have improved significantly during the last few years. This has led to a huge increase in the identification of M dwarfs and candidate brown dwarfs (BD), together with a few identified ones (Nakajima *et al*, 1995; Rebolo *et al*, 1995). Modelling their atmosphere is complicated by the need to account for the molecular and atomic opacities. Improvements in atmospheric modelling depend therefore on more accurate molecular data (Allard *et al*, 1995). The need for accurate model atmospheres comes from the realization that atmospheres are a rich source of information. Atmospheric studies can reveal the structure and evolution of LMS (Tsuji & Ohnaka, 1994).

1.3.1 LMS distances

For close–by stars, the best method to determine their distance is by measuring their *parallax*.

Measuring accurately the distance is important. Luminosity is essentially the only parameter that can be determined unambiguously (Tinney, 1993) and because of the strict relationship between luminosity and distance, the measurement of the latter in an unbiased way becomes essential. Until recently, parallaxes were obtainable only for very close objects (d $\sim$ 30pc) (Tinney, 1993). As a consequence, the colour–magnitude diagram was sparsely populated, creating uncertainty both in the interpretation of large scale surveys, which aim to measure the luminosity function at the bottom of the Main Sequence (e.g Hawkins & Bessell, 1988; Tinney *et al*, 1992), and in the study and interpretation of the individual very faint objects. In 1993 a trigonometric parallax program was carried out with a CCD detector on the 60" telescope at Palomar Mountain. The final results from this program brought 34 new parallax measurements. See Tinney (1993) for full details of the program. With the increased number of measured parallaxes, colour-magnitude relations have been constructed and proper fits to the Main Sequence can be achieved (Tinney, 1993).

1.3.2 Do LMS rotate?

The rotation of low mass stars is often neglected (Martin *et al*, 1996). However, rotation is a key parameter in star formation and evolution. For solar-type stars, for example, it provides a clock as the stars efficiently lose angular momentum in the latest stages of the pre-main sequence evolution and during the main sequence. In cool stars, rotation is measured in two ways: (i) photometrically, through the changes in the stellar light due to spots which transit the line of sight as the star rotates; and (ii) spectroscopically, through the rotational broadening of absorption features. The first method directly provides the rotational period while the second method gives the so–called projected equatorial velocity, $v \sin i$, where v is the rotational velocity and i is the inclination angle. Both methods can

be combined to give the inclination of the rotation axis to the line of sight.

In the last few years, a significant number of very late type M dwarfs have been discovered (see for example Kirkpatrick *et al*, 1995) and objects below the hydrogen burning limit have been observed (see for example, Oppenheimer *et al*, 1995; Rebolo *et al*, 1995). Knowledge of the rotation of these objects will help studies (i) of the evolution of their angular momentum, (ii) of their activity and (iii) of their internal structure (Martin *et al*, 1996).

1.3.3 Luminosity and mass

A precise knowledge of LMS masses is important. Their density and distribution are still poorly known. This is mainly due to the lack of information on mass. Also, the most direct way of distinguishing between substellar objects and very low mass objects is by defining the initial mass limit. The initial mass function (IMF) of star forming clouds, its dependence on the environmental conditions, and its evolution as stellar interactions modify the distribution of masses, are still poorly understood (Ray & Beckwith, 1994). A reliable IMF and mass function (MF) are needed. However, the stellar mass function cannot be observed directly but must be derived from the stellar luminosity function (LF) (Bessell & Stringfellow, 1993). A correct determination of the MF relies on an accurate transformation from luminosity to mass. An accurate LF and a good relationship between mass and luminosity is, therefore, essential. LF and indirectly MF have been both measured (eg. Hawkins & Bessel, 1988) and synthetically computed (eg. D'Antona & Mazzitelli, 1996).

From an observational point of view, until a few years ago most of the luminosity determinations were on a measured optical colours such as R-I and V-I (Leggett & Hawkins, 1988; Hawkins & Bessell, 1988 and references therein). However, it is thought that for LMS, optical colours contain almost no information on the effective temperature since most of the flux is in the near infrared (Leggett, 1992). For example, R-I colours of entire samples of LMS "saturate" and do not increase above 2.5 (Leggett & Hawkins, 1988). To

obtain a luminosity function, J,H,K colours are needed.

One of the most astonishing results from Hubble Space Telescope (HST) studies on LMS has been the relative deficiency of very low luminosity objects (Paresce *et al*, 1995). The LFs derived from observations of globular clusters and of the Galactic halo are in excellent agreement (De Marchi & Paresce, 1997). However, once the LFs are converted into MFs, the agreement breaks down. In fact, according to the adopted M-L relation, the MF either drops drastically or increases at the lower end of the main sequence. This disagreement is due to (i) the uncertainties in the physical models of LMS and (ii) the lack of full understanding of their dynamical evolution (D'Antona & Mazzitelli, 1996). Both constitute a handicap in understanding galaxy formation, the chemical evolution of the galaxies and the structure of the interstellar medium, for which a detailed knowledge of the IMF is required (Adams & Fatuzzo, 1996). Despite these uncertainties, several detailed studies of clusters and single objects suggest that the IMF flattens out below ~ 0.2 $M_{\odot}$.

At present, one of the best way of obtaining *direct* information on the IMF is from Doppler searches for low mass companions (Basri & Marcy, 1997). By determining the velocity accurately, one can imply a lower limit on the mass of the companions that can be detected at a given separation. It is however clear that, to aid observations and surveys, modelling of the IMF is needed.

Concluding, empirically it looks like the IMF turns over at very low masses. In theory there is no reason why stars should not continue to form below the hydrogen burning limit mass since the gravitational forces that control the formation of stars are independent of the nuclear processes that are responsible for the star luminosity. However, HST observed relatively few faint objects near the hydrogen burning limit, strongly suggesting that the number of brown dwarfs is too small to be interesting on a galactic scale. Blitz (1996) gives an extensive review on why this could be so.

1.4 Binaries

Statistically, most low mass stars come in binaries (Allen, 1973). Usually they are secondary companions to white dwarfs or G stars. More rarely, it is possible to have binary systems containing two M dwarfs of the same size. For binary stars close to Earth, parallax observations are possible and distances can be deduced. If eclipsing, masses can be determined by studying the orbital motion. Elemental abundances can be partly deduced by the spectroscopic analysis of the brightest companion. These types of systems are therefore extremely useful because they allow one to determine parameters such as the masses and radii with a precision not possible for single stars. The only two eclipsing M-dwarf binary systems known so far are YY Geminorum and CM Draconis (Popper, 1980). Their fundamental parameters have been accurately measured and they therefore provide an essential test for the latest evolutionary and atmospheric models (Chabrier & Baraffe, 1995). Due to their faintness, such binaries are less likely to be found in photometric surveys searching for variability and this explains their deficiency. CM Draconis is considered in detail in Chapter 9.

1.5 Low mass stars' atmospheres

In order to investigate comprehensively low mass stellar evolution, one needs to consider the following elements:

- A good equation of state of hydrogen/helium mixtures in both the molecular and metallic regime.
- A complete set of opacities for the relevant molecular and atomic species.
- An accurate atmospheric algorithm which is able to solve the radiative transfer equation, the non-LTE rate equations and the radiative equilibrium equation.
- Screened nuclear rates for all the important fusion processes.

For LMS, atmospheric modelling is of particular importance. The photosphere needs to be carefully modelled. Comparison of synthetic and observed spectra of LMS photospheres can directly yield the properties of effective temperature, surface gravity and metallicity which can then be used to infer mass and age. The characteristics of the photosphere of a star depends on the opacity of the gases forming it. Most of the hydrogen is locked in H_2 and most of the carbon in CO, with excess of oxygen bound in molecules such as TiO, VO and H_2O (Allard *et al*, 1997). This causes the optical spectrum to be mainly dominated by TiO and VO absorption and the infrared spectrum by H_2O, leaving no window for the actual continuum (Allard *et al*, 1997). Molecular absorption is not the only reason why atmospheric modelling of LMS is a difficult and challenging task. LMS have a large convective zone. This limits the approximation of the Local Thermal Equilibrium (LTE). Moreover, new insights on the photospheres of M dwarfs have recently brought forward the ideas that dust grains might form there since the chemical conditions are favourable (Tsuji *et al*, 1996a). This idea has led to many groups searching for evidence of dust (see, for example, Jones *et al*, 1997).

Molecular absorption bands have been used as a diagnostic of spectral type since the 1860s. TiO was first identified as the dominant feature in the optical spectra of cool giants (Fowler, 1904). Over the last 30 years, diatomic molecules have been included in detailed calculations of stellar opacity. In fact, since TiO is dominant in cool stars optical spectra, it can be used as a spectral classification tool: TiO increases in strength from being barely discernible at type K7 to dominate the spectrum among the latest type (M6-M7) dwarfs. This broad classification embraces essentially all non–degenerate stars which are less luminous than $\sim 0.1L_\odot$ (where the luminosity, as the mass, is measured with respect to the luminosity of the Sun) with temperatures cooler than 4000K and masses less than $0.65M_\odot$. The success of recent studies and a desire to understand cooler objects mean that attention is starting to focus on incorporating accurate data for triatomic molecules (Jones *et al*, 1995).

Although the presence of molecular absorption makes the task of modelling LMS atmospheres a very challenging and difficult one, molecular absorption can play a very important role in determining the effective temperature and metallicity scale. For example, H_2O opacity decreases with increasing temperature. This implies that high resolution data combined with accurate modelling could consistently provide a tool to determine stellar parameters.

1.5.1 The effective Temperature

The effective temperature of LMS is a key parameter in understanding their properties. The effective temperature is defined in the equation:

$$L = 4\pi R^2 \sigma T_{eff}^4 \tag{1.5}$$

where L is the luminosity of the star, R is the radius of the photosphere and σ is the Stefan-Boltzmann constant. There is a strict connection between effective temperature, mass and age.

Usually, stellar radius data are absent and therefore effective temperatures are estimated by fitting the observed spectrum with some synthetic model where the flux is predicted by varying the input parameters such as the effective temperature and metallicity.

Until a few years ago, techniques to derive an effective temperature scale for LMS were all based on fitting a blackbody to the observed infrared colours of each star (e.g. Veeder, 1974). A major problem with this technique is the dominance of strong H_2O absorption bands in the infrared which results in blackbody fits that overestimate luminosities and temperatures because they measure the flux at its peak. Berriman and Reid (1987) tried to solve this problem by taking as a reference wavelength the one centred at 2.2 μm. It was assumed that there was no significant backwarming at this wavelength and therefore it measures the continuum emission from a blackbody with a temperature the same as the star's effective temperature. Others tried the same method by taking different central

wavelengths as references, see for example Tinney *et al* (1993). Although an improvement, this technique still causes problems for stars with effective temperature $\leq$ 3000K where H_2O absorption is strongest. For these objects, no reference wavelength would be useful to measure the real continuum. Recently, improvements in models atmospheres (Allard *et al*, 1995) have led to a new method of deriving effective temperatures, to within 100K–200K. This technique uses the dominance of H_2O vapour absorption itself across the near-infrared in M dwarfs to fit blackbody curves to points in the spectra which are affected by the same amount of H_2O absorption. This technique is based on the direct relationship between the strength of the H_2O bands and the effective temperature. As the temperature increases, H_2O dissociates more. By studying H_2O from a spectroscopic point of view, one can potentially determine the strength of the water bands at any specific temperature. By comparing directly observed and synthetic spectra, an effective temperature scale can be derived. This technique is widely discussed in Kirkpatrick *et al* (1993) and Jones *et al* (1994 and refs therein).

However, there is still insufficient reliable water data to reduce the error in effective temperature measurements. This problem will be explored in Chapter 2.

1.5.2 The metallicity

The metallicity is an indicator of the chemical composition of the stellar photosphere. Usually the metallicity is in fact [M/H] where [M] $\equiv$ log M_{star} - log $M_{\odot}$ for any abundance M and [M/H] is the ratio of metal abundance to hydrogen content in the star so far. In all cool stars' models atmospheres, solar abundances and solar abundances ratios are assumed.

The metallicity of LMS plays an important role in determining the composition and the chemical history of the Galaxy. LMS have a long lifetime and therefore they can be indicators of what happened in the early times of the Galaxy formation.

The IMF also depends on the metallicity. The IMF is founded on an accurate mass-luminosity relationship which is very sensitive to the stellar chemical composition (D'Antona

& Mazzitelli, 1996). Of course, the metallicity affects the Spectral Energy Distribution (SED) of the object. However, the dependence of its photometric properties on the metallicity is not yet well determined.

Usually, colour-colour or colour-magnitude diagrams are used as indicators of metallicity. However, often, these two types of diagram, constructed with evolutionary and atmospheric models, do not reproduce the JHK fluxes within a reasonable error and therefore cannot be uniquely used to determine metallicities (Leggett *et al*, 1996). For early type M dwarfs, since the local space distribution is in broad agreement with that of well-studied classes of hotter stars (Mihalas & Binney, 1981), one can use kinematic population tables (see for example Leggett, 1992) to assign approximate metallicities. Finally, spectroscopy is also used to determine a metallicity scale; for example, in the optical, TiO bands (7670-7860 $\AA$) and VO bands ($\sim$7400 and $\sim$7900 $\AA$) are good indicators of metallicity since they both contain two metals and double-metal lines of these bands are weak in metal-poor stars (Leggett 1992). Note that models always assume solar abundances and solar abundances patterns. However, it is not excluded that some stars might be chemically peculiar. One of these cases could be the binary system CM Draconis. In Chapter 9 its metallicity will be considered in length.

1.5.3 The age

As mentioned above, LMS vary widely in age. This is because they have a main sequence lifetime much longer than the Hubble time and therefore a local sample can consist of stars of all ages since the formation of the galactic disk. Given an age indicator, such as chromospheric activity, LMS could be a probe for important galactic parameters. Beside the cosmological importance, age is vital for allocating any LMS in the H-R diagram since all low mass objects take at least 0.5 Gyrs to contract into a stable position in the MS. The age severely affects the spectral type determination of substellar objects since by definition these objects never reach thermal equilibrium and their luminosity and effective temperature decrease monotonically with time. Age is strictly correlated with metallicity

and, to a lesser extent, surface gravity (e.g Sandage, 1986)

Stars are generally divided into two classes, Population I, young and metal rich, and Population II, old and metal-poor. However, this classification is rather vague. Being metal-poor does not necessarily imply being old .

Strictly from an age point of view LMS can span $\sim$ 10Gyrs of age and can be divided as follows:
(i) young LMS ($\tau \leq 10^9$ yrs) (ii) old LMS ($\tau \geq 1$ Gyr). For masses ≥ 0.09 $M_\odot$, the evolutionary tracks for stars between 0.6 and 10 Gyr are almost indistinguishable but below 0.09 $M_\odot$ the mass of the star, with a known temperature and luminosity, cannot be well determined without first assigning the age (Jones *et al*, 1994).

1.5.4 The surface gravity

The atmosphere of a star is generally much thinner than the radius of the star. Therefore, the gravitational acceleration, g, is essentially constant throughout the atmosphere and it is usually referred to as *surface gravity*.

The surface gravity of a star is often replaced by its logarithmic value log g for simplicity. Unlike effective temperatures and metallicities, surface gravities for LMS are often assumed to vary very little since the thickness of the atmosphere is assumed to be constant. However, Burrows *et al* (1994) pointed out that LMS can indeed have a reasonably wide range of surface gravity spanning 4.0 to 5.5 for ages 0.1-10 Gyr.

Theoretically, to find the best value for log g one can replace the Stefan-Boltzmann relationship $L=4\pi r^2\sigma T_{eff}^4$ with $r^2 = GM/g$ to give:

$$\log T_{eff} = 0.25(\log g + \log L - \log M - \log 4\pi\sigma) \tag{1.6}$$

However the luminosity is not directly observable and it is often substituted by the absolute bolometric magnitude (Jones *et al*, 1996). Therefore Equation 1.6 is more usefully written if we substitute in standard solar values, $M_{bol\odot} = 4.75$, $L_\odot = 3.826\times10^{26}$ W and $M_\odot = 1.99\times10^{30}$ kg. There are a limited number of objects for which the bolometric magnitude is well determined. Hence, often the bolometric magnitude is replaced by the absolute

K-band luminosity based on the Henry & McCarthy (1993) work who derived binary $M/\mathrm{M}_{\odot}$ versus M_K relationships valid over the range 0.080–1.000 $M/\mathrm{M}_{\odot}$. However, these relationships are based on a sample of M-dwarfs with intermediate disk characteristics i.e. neither young or old. Consequently, they cannot be expected to be valid unless metallicity and age are taken into account (Jones *et al*, 1996).

Empirically it can be shown that surface gravities increase with decreasing temperature (Jones *et al*, 1996). Therefore, surface gravity is another parameter, together with the metallicity and the effective temperature that could be constrained by an accurate modelling able to match the observations.

1.6 Brown dwarfs

The definition of a *brown dwarf* (BD) is not yet well established. Here we use the definition adopted by Basri and Marcy (1997). A brown dwarf is an object which produces a non-negligible luminosity by nuclear fusion during its youth but never stabilizes its luminosity by hydrogen burning. All brown dwarfs burn deuterium. This occurs early in their evolution. The highest mass BD also engage in some hydrogen burning for a period of time. Fusion might even dominate over gravitational contraction as a source of luminosity early on but the crucial point is that the luminosity derivative will never be zero or positive after deuterium burning is finished. The object will not reach a stable temperature or luminosity and therefore will continuously grow cooler and dimmer. At later stages, gravitational contraction is the only power source. The lowest mass stars, although they eventually stabilize their luminosity with hydrogen burning, do not do so for a billion years, and therefore they cool for a long time very much like the hottest BDs (Burrows *et al*, 1993a).

For lower mass BDs, the temperature and luminosity are low at all ages. Below about 60 $\mathrm{M}_{jupiter}$ there is never sufficient core temperature to completely burn even lithium which is the next most fragile element after deuterium. At this stage one can distinguish between BDs and planets: the former are still primarily supported by free electron degeneracy while

Jupiter itself has a substantial support from electrostatic pressure. The search for such self-gravitating objects is primarily motivated by the need to construct an initial mass function. BDs are concentrated at the bottom of the main sequence and can give insight into what actually happens there. They can help build up a luminosity and mass function scale. BDs are very faint but when observed, one can actually calculate their parameters with more precision than other stars.

Searching for BDs had been unsuccessful until two years ago when the first brown dwarf, GL 229B, was discovered (Nakajima *et al*, 1995). Many groups have searched for BDs (i) by looking for companions of nearby stars; (ii) by looking into very red field stars in search of an isolated BD. Both approaches are limited by our poor knowledge of their expected ages. A way around this is to look for BDs in close clusters where the age is constant. The younger the cluster is, the more luminous the BDs would be. As an example, the Pleiades is one of the best young clusters to look for BDs (see for example Jameson & Skillen, 1989; Hambly & Jameson, 1991).

Until a good sample of positive BDs has been collected, there will still be doubts on what really distinguishes an M dwarf, a brown dwarf and a giant planet, despite the definition given above.

An insight into the detailed structure of the atmosphere of low mass stars in general can reveal patterns strictly related to M dwarfs or BD only and therefore make them easier to recognize and identify. In particular, a new test for identifying brown dwarfs has recently been found: the Lithium test (Rebolo *et al*, 1992). In stellar interiors lithium nuclei are destroyed via proton collisions at relatively low temperatures. This element has long been used as a tracer of internal structure in stars of different types (eg. Michaud & Charbonneau, 1991). The strong convection of very low mass stars causes an extremely efficient mixing of lithium and indeed significant lithium depletion has been observed in these stars, even in the very young ones. Objects with masses ≤ 0.065 $M_{\odot}$ are well below the hydrogen burning mass limit and they cannot reach the Li burning temperature (2.5×10^6 K). Unlike LMS, they must preserve a significant amount of their initial lithium

content during their lifetime. This can be detected spectroscopically and can provide a diagnostic of substellar nature for BD candidates (Rebolo *et al*, 1992; Magazzu' *et al*, 1993). In an old BD, therefore, the retention of lithium is the only test that can provide an absolute confirmation of the lack of hydrogen burning. Moreover, by looking, for example, in young clusters in which the lower main sequence is known to have depleted lithium, one can look for the boundary of faint luminosities below which lithium has not yet been depleted.

1.7 Observational history of LMS

Because of their large number density, an observable sample of low mass stars can be formed by looking at our solar neighborhood. This allows distance to be easily calculated with parallax techniques. Moreover it avoids the 'reddening effect' that one has with more distant stars.

Despite being so close, even observed LMS are extremely faint and, until few years ago, instrumental developments were not advanced enough to obtain a large sample of data. One of the main problems is the telluric absorption both in the optical and infrared window: the detection of faint M dwarfs can be very much affected by atmospheric absorption and many of the molecular bands and atomic features can be highly affected. A good choice of standard stars can eliminate, at least partly, these effects (Jones *et al*, 1994).

For infrared observations there are now good ground-based telescopes, for example UKIRT (UK Infrared Telescope) in Hawaii. Its new improved CGS4 (Cooling Grating Spectrograph) can take near-infrared spectra of very faint stars at sufficient resolution to resolve many water bands and at the same time to obtain a fairly good flux calibrated SED (Jones *et al*, 1995 and Chapter 8 in this work).

With the launch of ISO (Infrared Space Observatory), spectra can be obtained avoiding the problems of telluric absorption.

Optically, high resolution observations can be obtained with the WHT (William Herschel Telescope), INT (Isaac Newton Telescope), AAT (Anglo Australian Telescope) and

others. Although most of the flux comes from the infrared (IR), one should not underestimate the amount of information that can be obtained from the optical. For example, many metal lines and TiO bands that are in the optical can be good indicators of metallicity, surface gravity and effective temperature (see Chapter 9). Also, recent observations of TiO in the region 0.65–0.76 μm indirectly prove the existence of dust (Jones *et al*, 1997).

Finally, HST has provided a new insight on the space density of very LMS and BDs, revealing a real deficiency of the latter and therefore almost certainly excluding the hypothesis that BD could account for the missing matter in the Universe (see for example Paresce *et al*, 1995).

1.8 Modelling history of LMS: atmospheric models

Atmospheric modelling of cool stars is characterized by the inclusion of accurate molecular and atomic opacities and a rigorous theory of convection. Only recently could models even partly handle these two problems.

Briefly, the history of modern modelling starts with Mould (1975, 1976) who first produced an extensive grid of convective M dwarf model atmospheres with a temperature range of 4750 down to 3000K. This was the first generation of models to include molecular opacities such as TiO opacities (Tsuji 1966), H_2O opacities (Auman, 1967) and a mixing-length treatment of convection (Bohm-Vitense, 1958; Kippenhan, 1962). It was not until 15 years later that other models by Allard (1990), Kui (1991), Brett & Plez (1993), Allard & Hauschildt (1995), Brett (1995a,b) and Tsuji *et al* (1996a,b) were developed. The 1990s generation models managed to overcome the '3000K' barrier. They handled molecular opacity using band models and Straight Mean (SM) techniques. They included a series of molecules: not only TiO and H_2O but also some important hydrides, VO and CO.

Currently, several atmospheric codes are in regular use. The main ones are those of Tsuji *et al* (1996a,b), Brett (1995), Allard & Hauschildt (1995). Although these latest models have greatly improved over the years, near-infrared studies have shown that they still fail to reproduce the desired match with the observed SED (Jones *et al*, 1995; Allard

et al, 1995). The main problem with current models is still the lack of basic atomic and molecular input data, of accurate oscillator strengths and a good treatment of Non Local Thermal Equilibrium (NLTE).

In the absence of detailed lists of transitions, atmospheric models often resort to techniques that give average opacities such as the Just Overlapping Line Approximation (JOLA) (Zeidler & Koester, 1982). This technique approximates the absorption within a band with help of only a limited number of molecular constants: the rotational line structure in the bands is then reproduced by a continuum distribution. These molecular constants are generally taken from compilations such as Huber & Herzberg (1979) or Rosen (1970). An extensive review of model atmospheres of LMS and BD can be found in Allard *et al* (1997).

I choose here to briefly describe one of them, the atmospheric code PHOENIX (see for example Allard & Hauschildt, 1995) since it will be used in Chapter 2, Chapter 7 and Chapter 9 to analyze some observations.

1.8.1 The atmospheric code PHOENIX

Originally PHOENIX was aimed to compute the radiation emergent from a rapidly expanding supernova or nova envelope during the first weeks and months after the explosion (Hauschildt, 1991). In the last few years, PHOENIX has also been adapted to construct model atmospheres for M dwarfs and giants, brown dwarfs, hot winds from CV's (Cataclysmic Variables) in outburst and AGN disks.

Among the physical assumptions of the code, we have:

(i) spherical symmetry;

(ii) steady state;

(iii) energy conservation, especially radiative equilibrium in the Lagrangian frame;

(iv) Non Local Thermodynamic Equilibrium (NLTE) for H,He, Li, C, N, O, S, Si, Mg, Ca, TI, Co, Fe.;

(v) Local Thermodynamic Equilibrium (LTE) for the remaining elements.

The application of PHOENIX to M and brown dwarf atmospheres is described by Allard *et al* (1994), Allard & Hauschildt (1995) and Allard *et al* (1997). Some specific assumptions for cool stars' applications are listed below:

(i) the atmospheres are approximated as plane parallel since the gravities are high ($\log g \sim 5.0$).

(ii) The effects of convective motion on line formation are neglected since the velocities of the convection cells are too small to be detected in low-resolution spectra.

(iii) A treatment for molecular line broadening due to collisional processes is not included.

(iv) These models include linelists for molecules if possible or otherwise the JOLA approximation is used.

PHOENIX has been successfully applied in many works such as Allard *et al* (1994, 1996), Jones *et al* (1994, 1995, 1996), Leggett *et al* (1996) and in Chapter 2, 7 and 9 of this work.

Chapter 2

Why do we need more data on water?

The opacity problem in the atmospheres of cool stars has been addressed by many groups. Usually they have used statistical methods where high temperatures data were extrapolated from low temperature experiments (Ferriso *et al*, 1966; Ludwig, 1971; Ludwig *et al*, 1973; Phillips, 1990; Riviere *et al*, 1995 and so on). Statistical data have been widely used until recently (Lunine *et al*, 1986; Bessell *et al*, 1989; Leinert *et al*, 1990).

In the early 90s computational data became available and they mostly replaced the experimental data apart from Ludwig's. Three years ago, up to date model atmospheres used water opacity data from: (i) Ludwig (1971); (ii) Jørgensen and Jensen linelist (JJ93) (Jørgensen and Jensen, 1993); (iii) Miller and Tennyson linelist (MT) (Miller *et al*, 1994). We have computed model atmospheres with three sets of available data and compared them with the latest observations of an M dwarf, TVLM 513–46546 (TVLM). The observations were made during the commissioning of the upgraded Cooled Grating Spectrometer (CGS4, Puxley *et al*, 1992) on the UK Infrared Telescope (UKIRT) on Mauna Kea, Hawaii. The procedure of the observations and the data reduction are described in Chapter 8. The models were taken from a large grid computed with the model atmosphere code PHOENIX. The models are described in detail by Allard & Hauschildt (1995). More

details can be also found in Chapter 9. The models used here come from a number of different generations of the code. We find that the improvements in the code are overwhelmed by the large differences in the molecular datasets considered. Figures 2.1 to 2.5 compare the three linelists. The models have been computed at a T_{eff} of 2500K, log g = 5.0 and at solar metallicity. From all the figures it is obvious that the Ludwig data opacity set is inadequate to reproduce detailed spectroscopic structure while it matches the overall SED quite well.

Figure 2.1 indicated the poor overall match between observations and models. The model including water vapour from JJ93 looks the most promising although the match would be reasonable only at much lower resolution.

Figure 2.2 covers a spectral region where there is little H_2O and TiO present and shows a good match between models and observations.

Figure 2.3 shows a region dominated by water vapour. The model including water vapour form JJ93 again looks the most promising but only at much lower resolution.

Figure 2.4 shows a region dominated by water vapour. The model including water vapour from the MT linelist gives a promising match to the observed data. The model including water vapour from the MT linelist gives a promising match to the observed data.

Figure 2.5 shows a region containing water vapour and strong CO absorption bands. The model including water vapour from the MT linelist gives a good match to the observed data.

Concluding, we find serious problems with the water vapour used in the modelling of cool objects. Shortward of 1.7 μm the JJ93 gives a reasonable match to the observed water bands at very low resolution. However, JJ93 should not be used for detailed spectral analysis. Certainly it is not good enough if we need to use molecular bands as a 'tool' to construct an effective temperature scale for M dwarfs. Beyond around 1.7 μm it appears that the preliminary MT linelist is sufficiently complete to give a very good representation of stellar features (although the lack of hot water vapour transitions considered means that it does not match so well at shorter wavelengths). The MT linelist suggests that an

excellent match to the water vapour transitions will be possible and that is the goal of the thesis.

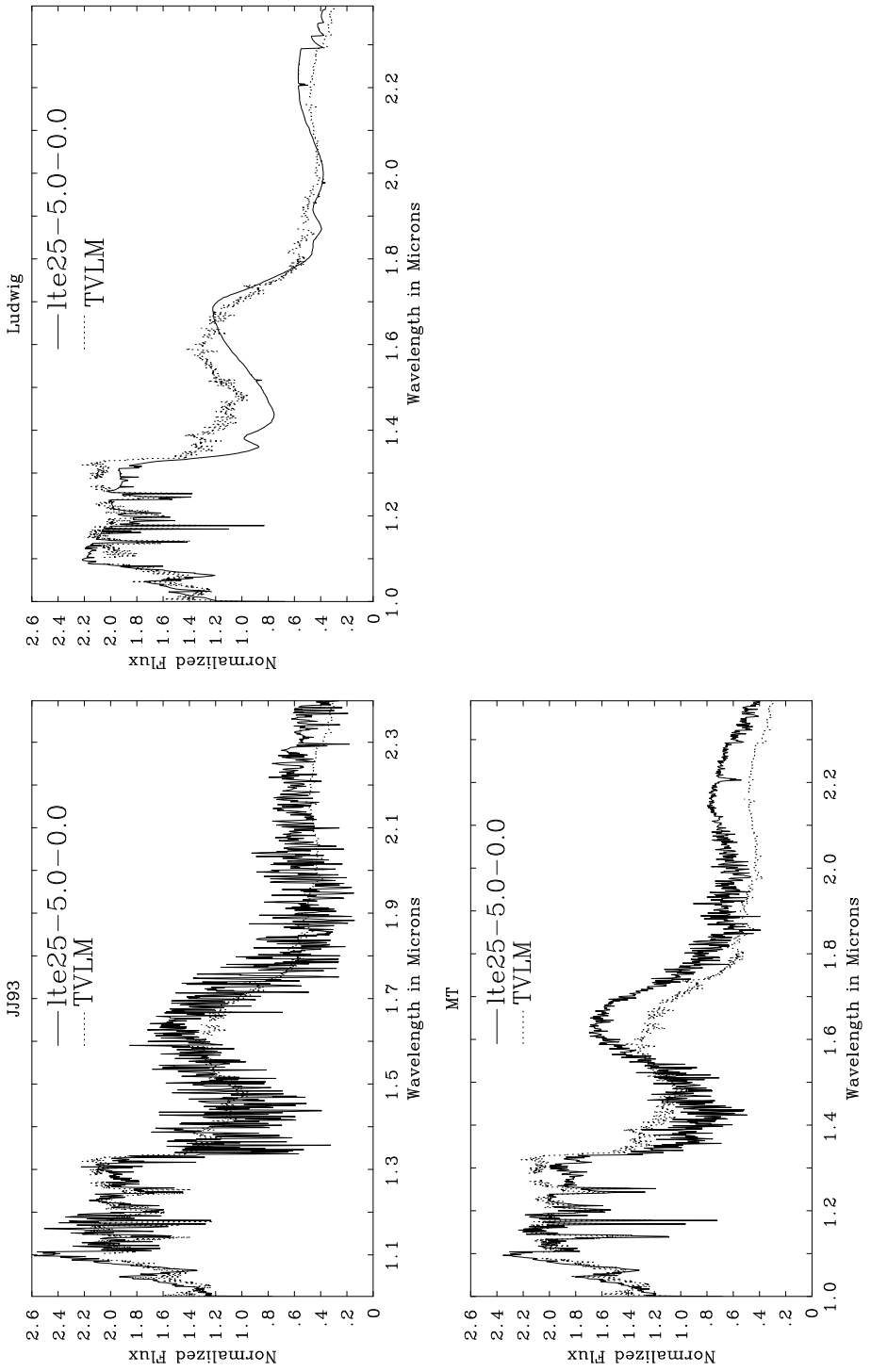

Figure 2.1: Comparison of the observed spectrum of TVLM 513–46546 from 1.0 to 2.4 μm with the model atmosphere code PHOENIX using different input data for the water vapour opacity. Top Left: JJ93; Top Right: Ludwig; Bottom Left: MT. The notation used for the model is: lteTT-G.G-Z.Z, where lte = local thermodynamic equilibrium, TT = $T_{eff}/100$, G.G = log g (surface gravity), Z.Z = [M/H] (metallicity)

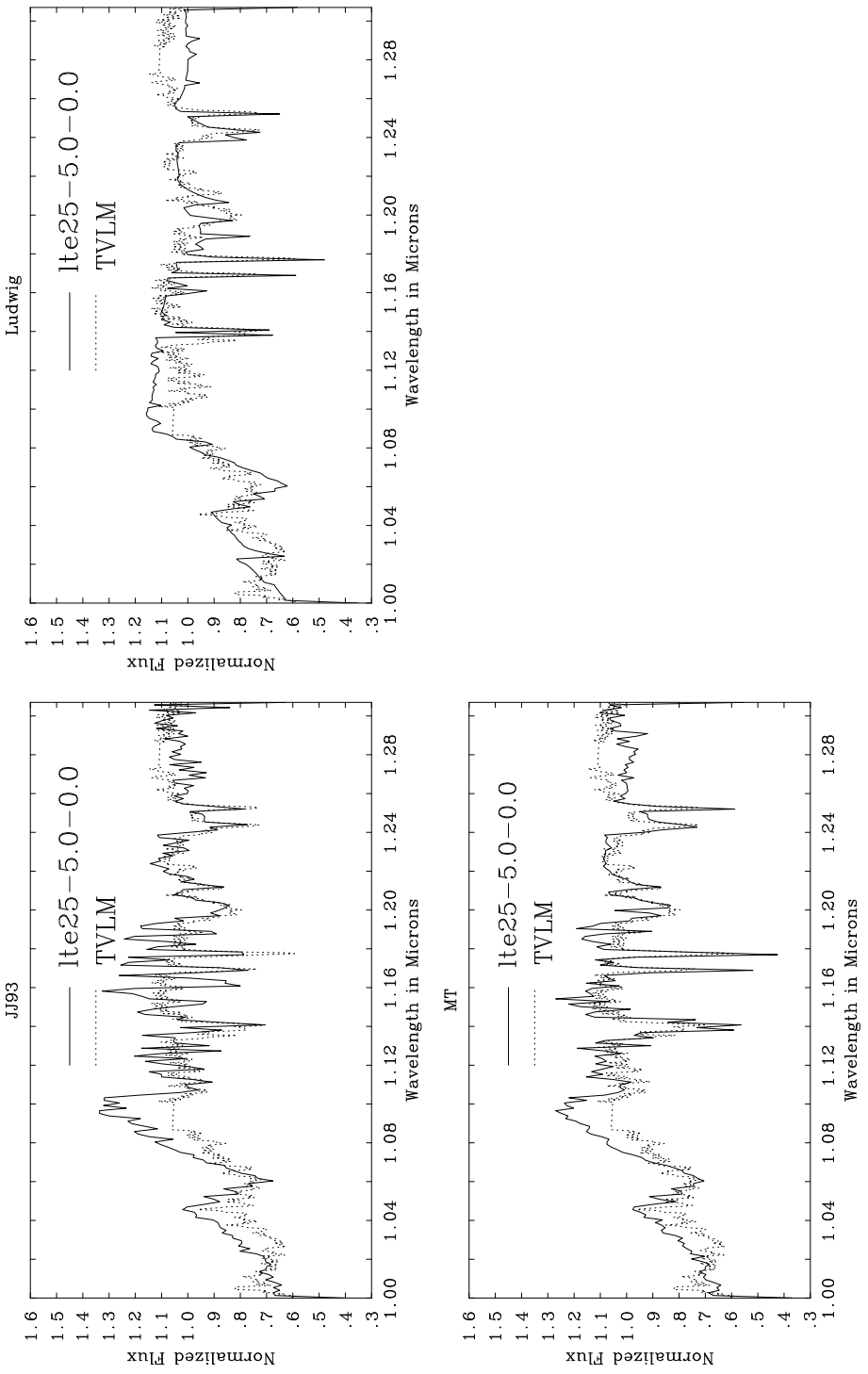

Figure 2.2: Comparison of synthetic and observed spectra as previous Figure, from 1.0 to 1.3 μm.

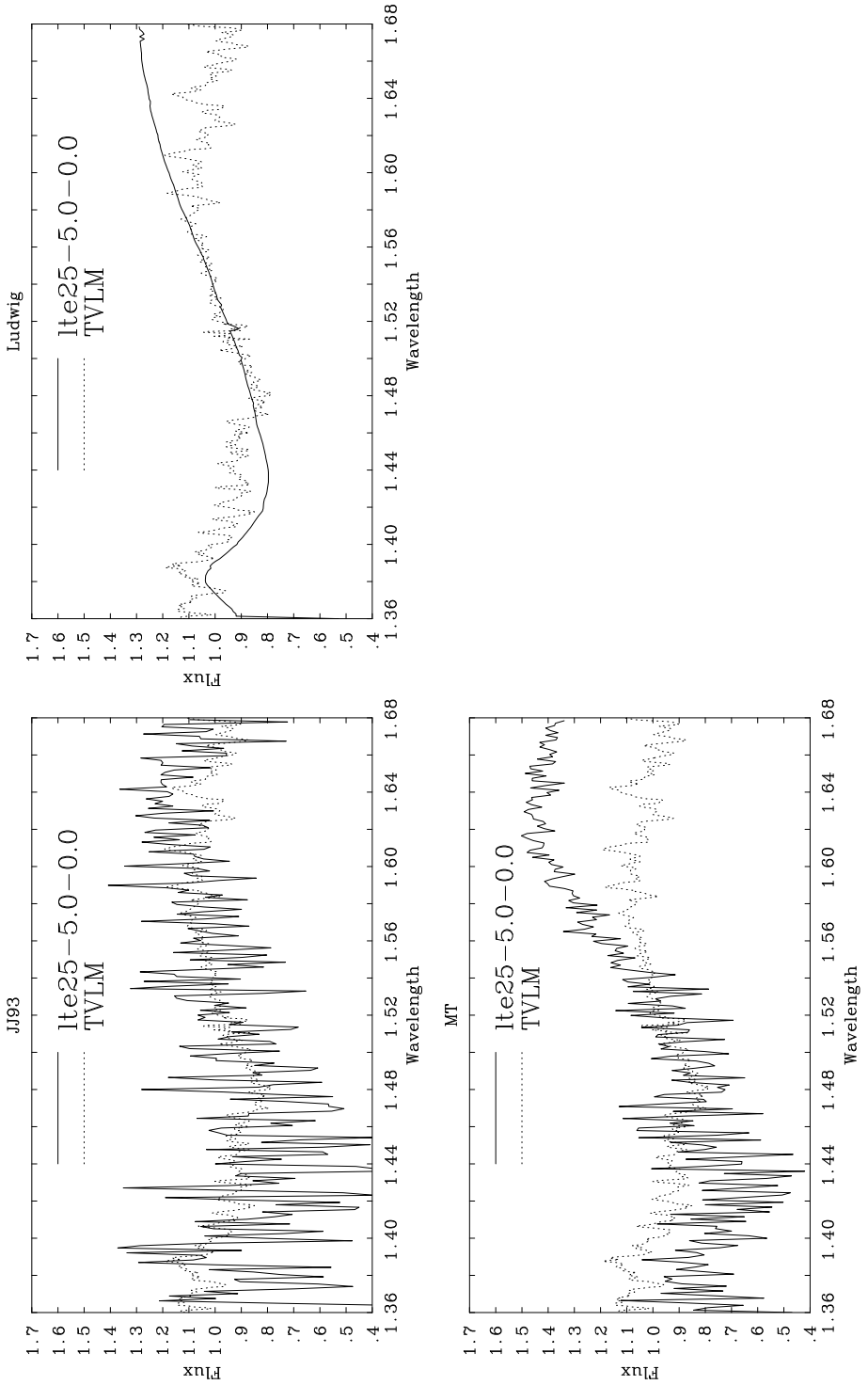

Figure 2.3: Comparison of synthetic and observed spectra from 1.38 to 1.68 μm. Here there is a strong water band centered at 1.42 μm.

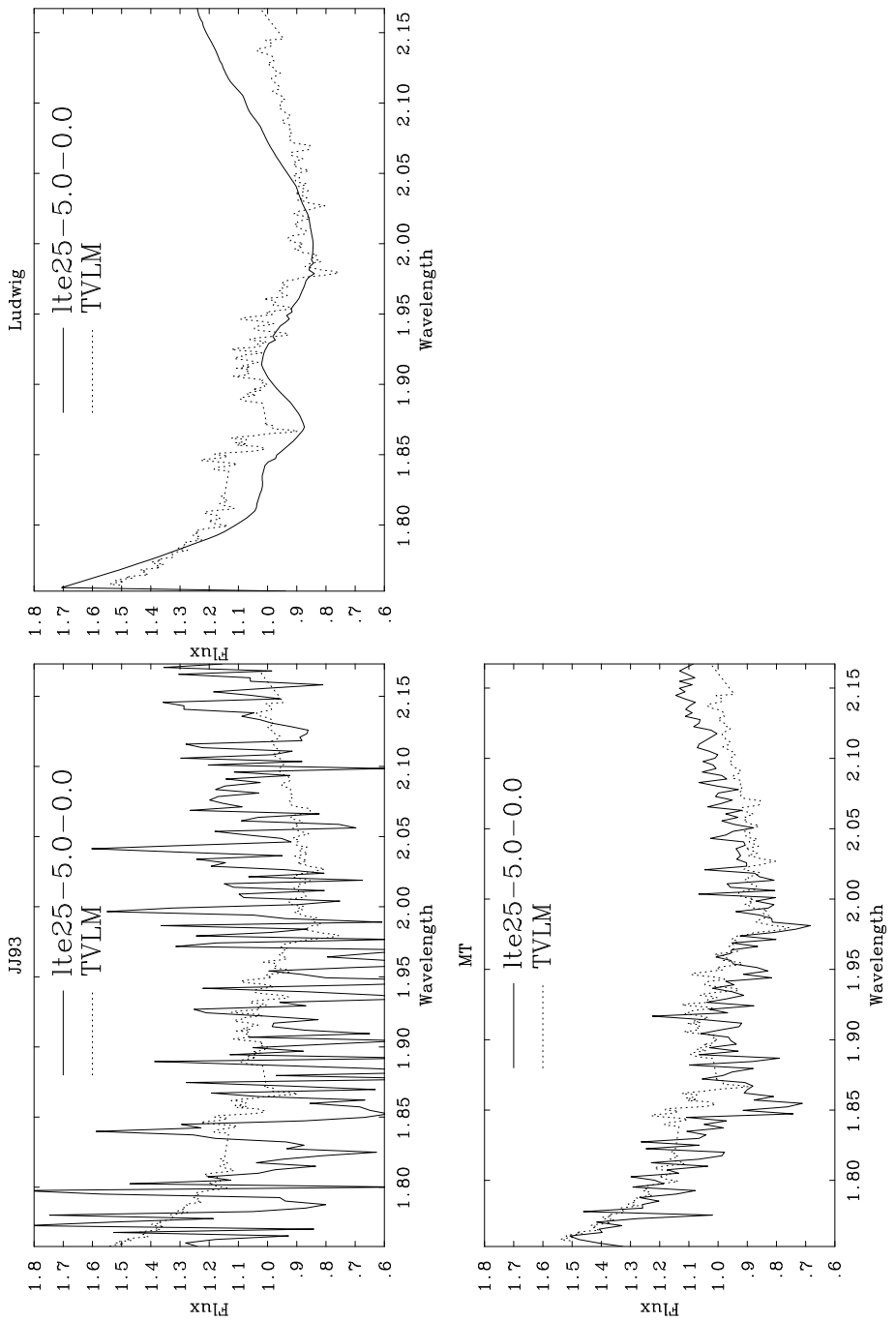

Figure 2.4: Comparison of synthetic and observed spectra from 1.75 to 2.15 μm. Here, as well, strong water bands are present.

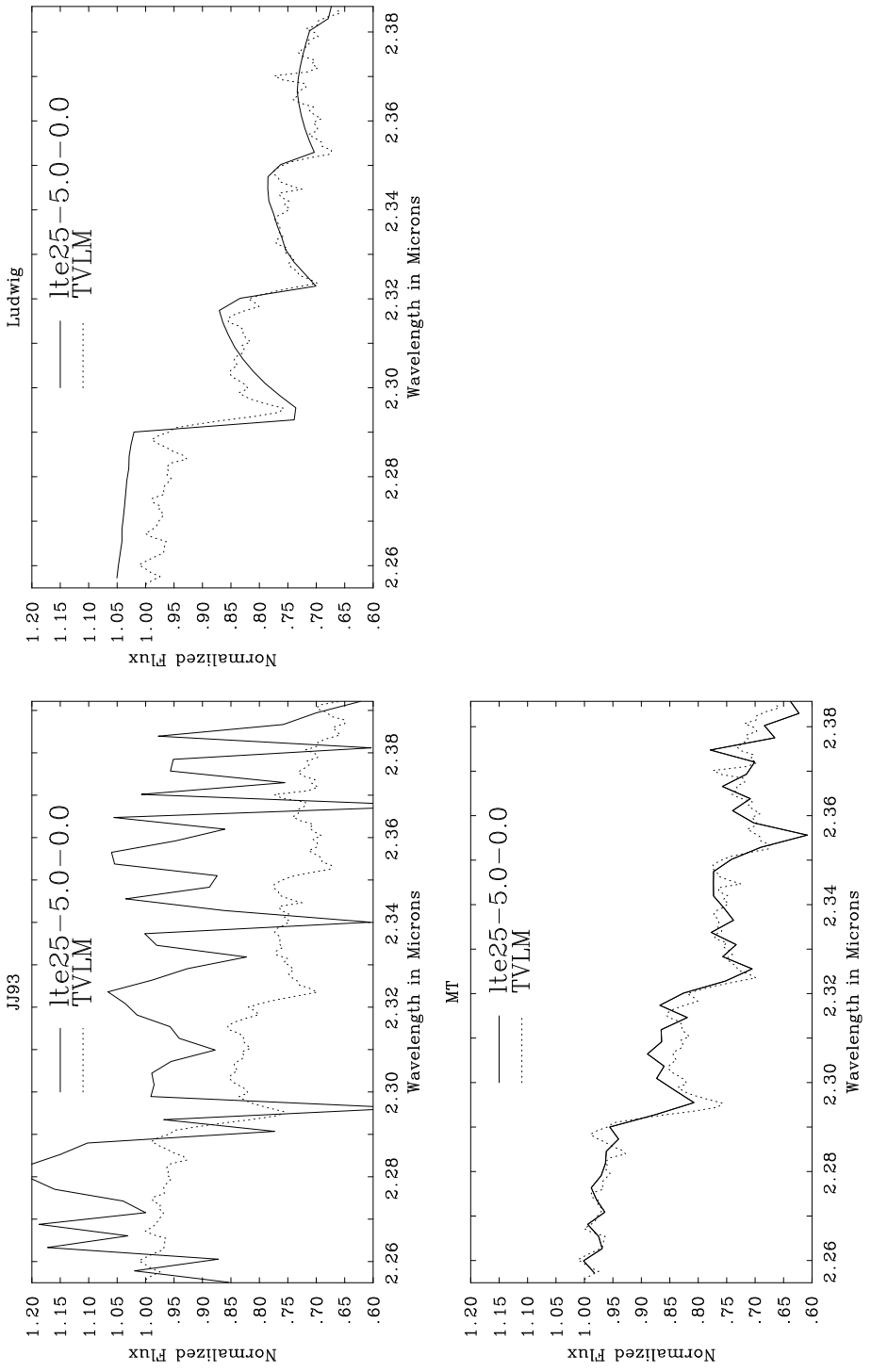

Figure 2.5: Comparison of synthetic and observed spectra from 2.25 to 2.39 μm. In this region there are strong CO bands.

Chapter 3

Calculating spectra of triatomic molecules

As discussed in Chapter 1, one of the main complications in the study of LMS is the lack of molecular data on H_2O and TiO. The water molecule can access energies as high as 45000 cm^{-1} before dissociating and accurate databases which include such high energies are not yet available.

Reproducing high temperature water spectra is a challenging and difficult task because of the complexity of the motion of asymmetric triatomic molecules.

In a molecule, the individual atoms vibrate and rotate about its center of mass, all these processes changing its state of motion. In the case of an asymmetric top molecule, such as water, the rotation of the atoms can be quite complex because their moments of inertia (I_A, I_B, I_C) are all different.

3.1 The Born-Oppenheimer approximation

The full Hamiltonian for any molecule is a very complex operator and depends on both the nuclear and electronic components. Born and Oppenheimer (1927) proposed that since the masses of the electrons are almost negligible with respect to the masses of the nuclei, the latter can be considered almost static compared to the electrons. This implies that

we can separate the nuclear and electronic wavefunctions. This approximation is known as the Born-Oppenheimer approximation (BO). According to this, the total energy is the sum of the electronic and nuclear energy i.e:

$$E_{tot} = E_{electr.} + E_{nuclei} \tag{3.1}$$

An important corollary of this approximation is that, since the electronic motion can be regarded as occurring when the nuclei are stationary, the electronic wave function can be evaluated with the nuclei clamped. A series of these calculations can be used to build up a potential energy surface upon which the nuclei move.

In order to calculate predictions for rotation-vibration energies, an accurate potential surface is necessary (Polyansky *et al*, 1996a). There are two ways of obtaining good potential surfaces: (i) *ab initio* electronic structure calculations at a grid of points and fitted to a functional form; (ii) semi-empirically by trying to fit known experimental energy levels and extrapolating the rest. The potential surface is then refined until differences between the computed and the experimental levels are minimal. Traditionally *ab initio* potential energy surfaces are, on average, accurate to within ~ 10 cm^{-1} for the band origins of water (Sutcliffe & Tennyson, 1987). A recent potential energy surface (discussed later on in this chapter and in Chapter 6) by Partridge & Schwenke (1997) gives an error of ~ 3 cm^{-1}. In general (and for water) *ab initio* BO potentials are not spectroscopically accurate.

For some molecules, the BO approximation breaks down. This happens when two electronic states are very close to each other in energy and therefore ro-vibronic effects are important. For H containing species, BO approximation also gives problems at the 1 cm^{-1} level (Zobov *et al*, 1996). The BO breakdown is important for water when spectroscopically accurate data are needed. For further details on how to construct a calculation which accounts, at least in parts, for the BO breakdown, see Zobov *et al* (1996). Zobov *et al*'s results will be used to compute a water linelist, ZVPT, described in Chapter 6.

3.2 Vibrational and Rotational Motions

Molecules vibrate, rotate and translate: in a molecule with N atoms, each atom will be represented with 3 coordinates. Then, the total number of coordinates will be 3N and the molecule will have 3N degrees of freedom being the atoms' position independent of each other. Three degrees of freedom correspond to the free translation of centre of mass of the molecule through space. This motion is separable and uses 3 degrees of freedom leaving the molecules 3N-3 internal degrees of freedom. Additionally, the molecule will rotate about the 3 principal axes using another 3 degrees of freedom. This leaves left 3N-6 vibrational degrees of freedom.

Molecules are divided into groups according to the values of their principal axes of inertia. In linear molecules the atoms lie on a straight line. $I_B = I_C$ and I_A can be approximated to zero. Non linear molecules can be divided into: (i) symmetric tops, where two principal moments of inertia are equal. This group can be subdivided into two subgroups, *prolate* molecules where $I_B = I_C$ and *oblate* molecules where $I_B = I_A$. (ii) Spherical tops where all the moments of inertia are identical. (iii) Asymmetric tops where all the moments of inertia are different. The latter is the case of the water molecule. Some asymmetric tops, such as water, can however go linear when vibrationally excited. Water accesses linear geometries at energies around 12000 cm^{-1} above the minimum. At linearity 3N-5 vibrational modes are allowed, as opposite to 3N-6. This causes problems with all theories which separate completely vibrational and rotational motions.

3.2.1 The vibrational motion

Figure 3.1 shows the vibrational modes allowed for H_2O. By convention, the three fundamental vibrations are labelled ν_1, ν_2, ν_3.

The three modes are referred to as normal modes of vibration of the molecule. In Figure 3.1 each motion is also labelled as symmetric or antisymmetric since the water molecule does have some degree of symmetry. In particular, imagine a line (at the top of Figure 3.1) which bisects the HOH angle. If we rotate the molecule about this axis

Figure 3.1: The three fundamental vibrational modes of water.

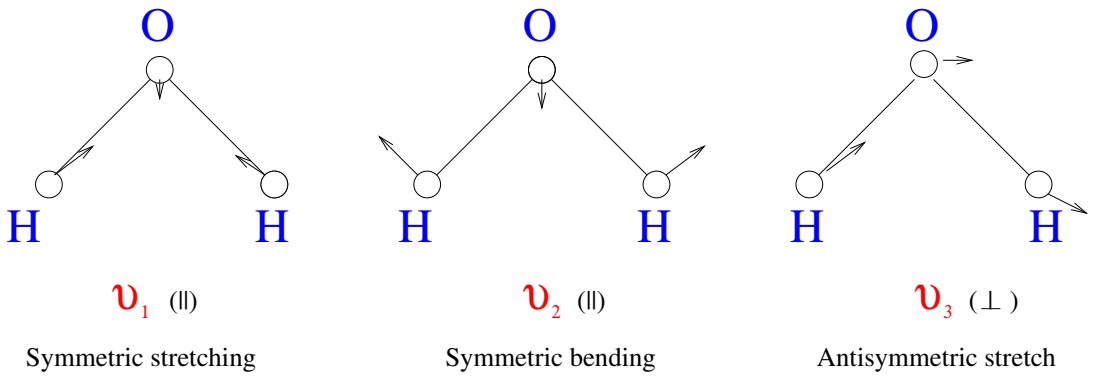

by 180 degrees its final appearance is identical with the initial one. This axis is referred to as C_2 axis since twice in every complete revolution the molecule presents an identical aspect to the observer. The first two vibrations are called symmetric because if after the vibration we rotate the molecule by 180 degrees, the aspect of the molecule does not change according to the observer. The third vibrational motion is called antisymmetric because after each vibration, if we rotate the molecule its shape changes. Respectively, these three vibrations are called: symmetric stretching, symmetric bending and antisymmetric stretching. Clearly if one of the nuclei moves, the whole molecule is likely to suffer a displacement, and it will undergo a motion which will be a mixture of angle-bending and bond-stretching.

3.2.2 The rotational motion

We have already introduced the different types of molecules according to their principal moments of inertia. When describing the rotational motion, this classification becomes of particular importance. The rotational motion is usually resolved into rotational components about the three moments of inertia (I_A, I_B, I_C) which become the three principal axes of rotation. Figure 3.2 illustrates the principal axes in the water molecule.

Rotational energy is quantized. The permitted levels can be calculated by solving the Schrödinger's equation for the system represented by the molecule. For asymmetric top

Figure 3.2: The three axes of symmetry for the water molecule. The B axis is the C_{2v} axis of symmetry.

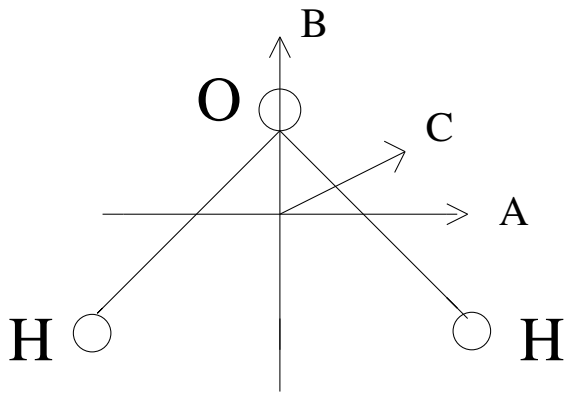

molecules, however, solving it analytically is impossible. Its values depend on the shape and size of the molecule. It is useful to introduce at this stage the rotational constants for asymmetric top molecules, A, B, C which are directly related to the moment of inertia. In fact they are equal to:

$$A = \hbar^2/2I_A; B = \hbar^2/2I_B; C = \hbar^2/2I_C \tag{3.2}$$

A prolate symmetric top corresponds to $B = C$ and an oblate symmetric top to $B = A$. The range of values of B between A and C corresponds to various conditions of asymmetry. Water represents a middle case between an oblate and prolate molecule with the dipole parallel to the B axis. Various parameters can be used to indicate the degree of asymmetry. For example, Ray's asymmetry parameter (Ray, 1932) is:

$$\kappa = \frac{2B - A - C}{A - C} \tag{3.3}$$

For an oblate, κ = 1; for a prolate κ = -1. For the water molecule in the electronic ground state, the typical values for the rotational constants are: A = 27.88061 cm^{-1}; B = 14.52161 cm^{-1}; C = 9.27776 cm^{-1} (Herzberg, 1945). Using these values, κ is -0.43623.

3.2.3 Quantum numbers

To specify the states of rotation and vibration, quantum numbers are used. Two categories of quantum numbers can be distinguished: the 'rigorous' and the 'approximate' quantum numbers. The 'rigorous' ones are:

J, the rotational quantum number;

ortho/para which define the symmetry of the H interchange (odd/even). Alternatively the quantum number q can be used to define the vibrational parity and can be 0 or 1;

p which defines the rotational parity as $(-1)^J + p$. p can be either 0 or 1. States with $p = 0$ and $p = 1$ are conventionally labelled e and f states respectively (Brown *et al*, 1975).

n which is the number of levels in each vibrational stack.

Approximate (and often used) quantum numbers are:

(v_1,v_2,v_3) for v_i quanta of excitation in mode ν_i. For example, a $(0, 0, 0)$ state is the ground vibrational state with no stretching or bending excitation. Mod(v_3,2) relates to *ortho/para*;

K_a, K_c where K_a is the projection of J on the A axis and K_c is the projection of J on the C axis.

Computational "quantum numbers" use e and f to define symmetry blocks. So for water we have ee, eo, fe and fo which are directly related to the rotational and vibrational parity of the molecule. This notation allows the computation in k-blocks where k is a semi-quantum number and is the projection of the rotational quantum number on the z–axis. At equilibrium it corresponds to K_a. Table 3.1 relates some of the rigorous quantum numbers with the approximate and computational ones. It is possible to divide the wavefunctions for each J into four symmetry blocks, except for $J = 0$ for which we have two possible states only.

The programs used throughout this thesis only use rigorous quantum numbers. Approximate numbers are then added by hand.

Table 3.1: Symmetry labels.

Sym. block	DVR	K_a	K_c	p	q	O/P
ν_3 even						
J even						
A_1	ee	even	even	0	0	P
A_2	eo	odd	even	0	1	O
B_1	fe	odd	odd	1	0	P
B_2	fo	even	odd	1	1	O
J odd						
A_1	ee	even	odd	0	0	O
A_2	eo	odd	odd	0	1	P
B_1	fe	odd	even	1	0	O
B_2	fo	even	even	1	1	P
ν_3 odd						
J even						
A_1	ee	odd	even	0	0	P
A_2	eo	even	even	0	1	O
B_1	fe	even	odd	1	0	P
B_2	fo	odd	odd	1	1	O
J odd						
A_1	ee	odd	odd	0	0	O
A_2	eo	even	odd	0	1	P
B_1	fe	even	even	1	0	O
B_2	fo	odd	even	1	1	P

3.3 Perturbation Theory

For further details on the theory discussed in this section refer to: (i) Watson (1977); (ii) Sutcliffe & Tennyson (1987); (iii) Henderson (1990) and references therein.

Computing energy levels and wavefunctions from a suitable potential surface is not trivial. The standard method of solving the vibrational and rotational motion is to use Perturbation Theory. Basically any system is considered as a small modification of a system of which the solutions are known. This method does not solve the Schrödinger's equation from first principles to extract the eigenvalues and eigenfunctions. It instead makes use of approximations for vibrational motion, such as the harmonic oscillator (Wilson *et al*, 1980) and for rotational motion, such as rigid-rotations (Townes & Schawlow, 1975).

The harmonic oscillator model considers vibrations as small displacements of the atoms forming the molecule from a global minimum along the resultant normal modes. Quantum numbers are then assigned to these modes and vibrational wavefunctions are obtained.

Energy levels are parametrised using 'force constants' for the vibrational problem and 'rotational constants' for the rotational one. The force constants are the coefficients of a Taylor expansion around the equilibrium position and they give the derivative of the potential at equilibrium (see for example Hoy *et al*, 1972). The rotational constants are the coefficients of a power series in the rotational angular momentum and its projection and again they give information about the underlying potential of the system.

The Hamiltonian of a rigid–rotor expressed in terms of the rotational constants is:

$$H_{rigid} = AJ_a^2 + BJ_b^2 + CJ_c^2 \tag{3.4}$$

where A, B and C are the rotational constants and $J_{a,b,c}$ are the angular momentum components. This is valid also when rotational constants contain contributions from vibrational effects. Quantum mechanically, equation 3.4 can be written:

$$H_{rigid} = \frac{1}{2}(A+B)\underline{J}^2 + [C - \frac{1}{2}(A+B)]J_C^2 + \frac{1}{4}(A-B)[(J_A + iJ_B)^2 + (J_A - iJ_B)^2] \tag{3.5}$$

The calculation of the energy levels reduces to the diagonalization of the Hamiltonian matrix elements for each value of J, see for example Sutcliffe & Tennyson (1987). One important result of this is that levels with J_{K_a,K_c} and J_{K_a+1,K_c} for high K_c, and J_{K_a,K_c} and J_{K_a,K_c+1} for high K_a are almost perfectly degenerate. When the molecule is not rigid, centrifugal distortions play an important role. The "model" can be improved by adding higher-degree terms to the Hamiltonian of equation 3.5. So the total Hamiltonian is expressed as the sum of the single-order Hamiltonians. If the centrifugal terms in Equation 3.5 are treated as a perturbation of the rigid–rotor Hamiltonian, an approximate expression for the energy levels can be derived from perturbation theory. Physically these higher terms arise from the expansion and distortion of the molecule by centrifugal forces.

The rotational and centrifugal constants are to be determined by fitting the eigenvalues to the observed rotational energies. The parameters obtained from the fit are then used to predict higher, unobserved, levels. Nearly all previous work on water has relied on fitting techniques based on the least-squares fitting of the pure rotational spectrum (eg Flaud *et al*, 1976, 1997).

Such techniques work for some molecules where the vibrational displacements are small. They become inappropriate when the vibrational modes involve large amplitude motions and centrifugal effects are not small.

Moreover, perturbation theories are based on the idea that vibrational and rotational motions are uncoupled to first order. Ro-vibrational coupling is then added through Coriolis contributions, again considered to be small perturbations to the ideal rigid-rotor.

Perturbation expansions can be proved to be highly inaccurate for molecules where vibrational motions have large-amplitude (Polyansky & Tennyson, 1992) and line frequencies calculated from such Hamiltonians may be out by tens or even thousands of cm^{-1}. H_2O is the classic example: it diverges for $J > 14$ in the ground vibrational state and for lower J in higher vibrational states (Polyansky, 1985).

3.4 Variational Calculations

Alternatively to techniques based on Perturbation Theory, it is possible to perform variational calculations which show much more reliable extrapolation behaviour with rotational excitation (Polyansky *et al*, 1994). Variational calculations solve the Schrödinger's equations from first principles. Ro-vibrational energy levels and wavefunctions are obtained using basis set expansions together with the variational principle (Lord Rayleigh, 1937). This principle shows that the better the representation offered by the set of basis functions, the lower the calculated energies will be. This allows one to construct and diagonalize a Hamiltonian matrix. By increasing the basis set (therefore reducing the approximation), the energies will approach the 'exact' values. Before being applied to triatomic molecules, this principle has been used for studies of diatomic ones (Suzuki, 1971, 1975). The first application to a triatomic molecule, water, was performed by Bucknell *et al* (1974). A review on early variational calculations can be found in Carney *et al* (1978).

3.4.1 FBR and DVR

Variational methods on water in the past have often employed a Finite Basis Representation (FBR) in the internal co-ordinates of the molecule, such as Radau co-ordinates (Tennyson *et al*, 1993). Radau co-ordinates are the best ones to deal with the water molecule (Schwenke, 1992a). They describe the relative atomic positions with two radii (r_1 and r_2) separated by an angle (θ). They were first proposed for planetary motion calculations (Radau, 1928).

Briefly, FBR means that the matrix elements of the Hamiltonian operator of the molecule have to be evaluated numerically. Most important, integrals over the potential matrix elements are off–diagonal. Suitable basis functions are: Morse oscillators (Laguerre polynomials) and free rotor functions (Legendre polynomials). For more details see Henderson (1990).

Based on the work by Tennyson and Sutcliffe (1982), program suites have been developed that calculate energy levels, wavefunctions and dipole transition moments for rotating

and vibrating triatomic molecules which, within the Born-Oppenheimer approximation, give variationally exact results for a given potential energy surface using FBR.

The problems with the FBR techniques are related to computer limitations. Usually it is the memory that limits the size of the chosen basis. In fact, the more functions required as the basis, the more memory will be needed to diagonalize the matrix. There are two reasons why a large number of functions may be needed: (i) if high energy states are required, more and more functions are needed to converge the higher levels; (ii) 'floppy' molecules, such as water, that can undergo very large amplitude motions which requires an extensive basis.

To solve some of the problems encountered with the FBR, Light *et al* (1985) employed the Discrete Variable Representation (DVR) technique which involves solving the nuclear problem in a discretized co-ordinate space. A full 3D DVR calculation can be handled as a series of diagonalizations and truncations (Bačič & Light, 1986) in such a way that the size of the 3D Hamiltonian diagonalisation can be greatly reduced. This is performed by considering motions in reduced co-ordinates, with the other co-ordinates fixed at the DVR points. For the water molecule, θ is kept fixed and the Hamiltonian is solved for the symmetrized radial coordinates (Fulton, 1994). This method allows the truncation of the wavefunction in regions where it will have no magnitude because the potential is very high; only the lowest energy solutions of the 2D Hamiltonian are employed as a basis for the next step reducing the overall size of the problem. For more details again refer to Bačič & Light (1986). Thus, the computational advantages of this method are: (i) the construction and diagonalization of a much reduced Hamiltonian matrix; (ii) the DVR theory makes the potential energy function totally diagonal in the DVR grid points; (iii) subsequent integrals, such as dipole matrix elements, are much quicker to calculate in a DVR (Lynas–Gray *et al*, 1995).

The size of the secular problem increases rapidly with J. To deal with high J an efficient algorithm to calculate the ro-vibrational wavefunction has to be found, for example, by using a two-step variational procedure (Tennyson & Sutcliffe, 1986). The first step is

to solve the 'vibrational' problem obtained by ignoring the off-diagonal Coriolis coupling terms. This approximation is equivalent to assuming that k, the projection of the angular momentum on the body–fixed z–axis, is a good quantum number. This give eigenfunctions of the effective, Coriolis–decoupled Hamiltonian in terms of k. $J \geq \mathrm{k} \geq \mathrm{p}$, where p is the rotational parity. The second step of the procedure then consists of using these eigenfunctions, symmetrized, as a basis for the exact effective Hamiltonian. The advantages of this procedure are the following: (i) It is not necessary to include all the solutions of the first step to obtain converged solutions for the second. The best algorithm for this is to select the intermediate basis functions according to an energy ordering criteria. (ii) The second advantage is that the secular matrix constructed for the second step has a sparse structure: all the elements are zero except for the diagonal element and one-off diagonal block linking k with k$\pm$ 1. Therefore, by storing only the non-zero elements, the core requirements are reduced by a factor of $\sim J$. iii) Finally, a sparse matrix can be rapidly and efficiently diagonalized. As will be seen (see Table 4.5), computationally it is convenient to structure the wavefunctions generated according to their k value.

FBR have been used for computation of water (eg. Miller *et al*, 1994, JJ93 and PS) and HCN (Jørgensen, 1992) opacity data. In this thesis, Chapters 5, 6 and 7, a DVR technique is applied. Also H_3^+ opacity data have been computed using DVR (Neale *et al*, 1996).

3.5 Vibration-Rotation Spectroscopy

Transitions involving changes in the vibrational as well as the rotational state of the molecule give rise to vibrational-rotational band spectra which are observed in the infrared. The vibrational and rotational motions are quantized. For an asymmetric top, there are $2J+1$ sublevels of different energy for each value of J. The atoms forming the molecule possess an internal degree of freedom or nuclear spin which introduces certain symmetry restrictions for both vibrational and rotational motions. For molecules like water, where the nuclei have a non-zero spin, the nuclear spins will affect the population of molecular

states and therefore the transition intensities. Both the symmetric and antisymmetric levels are present. The symmetric levels are those that are positive with respect to the B axis (ee and fe for J even), while the antisymmetric are those negative with respect to the B axis (eo and fo for J even). These levels have different statistical weight. For water, the antisymmetric levels have 3 times the statistical weight of the symmetric. The integrated absorption intensities can be calculated depending on temperature using the Einstein A–Coefficients, A_{if}:

$$\mid R^2 \mid = \frac{(2J^{'}+1)A_{if}}{(2J^{"}+1)\omega^3} \tag{3.6}$$

and

$$I = C\frac{\omega g(2J^{"}+1)}{Q(T)}\left(\exp(\frac{-E^{"}}{kT}) - \exp(\frac{-E^{'}}{kT})\right) \mid R^2 \mid \tag{3.7}$$

where C, the constant of proportionality, depends on the units employed. $J^{'}$ and $E^{'}$ are the rotational quantum number and the energy level of the upper state, while $J^{''}$ and $E^{''}$ are the corresponding parameters for the lower state. The energies are in cm^{-1}, as is the transition frequency $\omega(= E^{'} - E^{"})$. g is the nuclear spin degeneracy factor which for water is 1 (para) or 3 (ortho).

Associated with each vibrational level is a stack of rotational levels. Transitions can occur between rotational levels within one vibrational state as well as from different vibrational states.

If the molecule has no symmetry then all the vibrational modes are infrared active but if the molecule has a certain degree of freedom, in order to be infrared active there must be a dipole change during the vibration and this change must take place either along the line of symmetry axis ($\parallel$) or at right angle to it ($\perp$) (see Figure 3.2). Figure 3.3 shows the nature of the dipole changes for the three vibrations of water.

The selection rules for the rotational transitions of complex molecules depend on the type of vibration, $\parallel$ or $\perp$, which the molecule is undergoing. They also depend on the shape. In general, there are a very large number of possible transitions. Most of them are weak and therefore hard to observe. In fact, strictly speaking, there are no selection rules

Table 3.2: Dipole rules for the water molecule which has the dipole parallel to the B_{axis}. The $\Delta\ J = 0$ transitions correspond to the Q branch, while the $\Delta\ J = \pm 1$ are the R and P branches respectively. In terms of K_a, K_c, the strongest transitions are the ones with Δ K_a=$\pm$ 1 and $\Delta\ K_c$=$\pm$ 1.

ΔJ = 0	ΔJ = $\pm$ 1
Δ K_a=$\pm$ 1,$\pm$ 3,$\pm$ 5,... $\Delta\ K_c$=$\pm$ 1,$\pm$ 3,$\pm$5,...	
$e \leftrightarrow f$, $e \not\leftrightarrow e$, $f \not\leftrightarrow f$	$e \not\leftrightarrow f$, $e \leftrightarrow e$, $f \leftrightarrow f$

for vibrations i.e $\Delta\nu$=$\pm$n where n is any integer. However, if |n| $>$ 1 then the transitions are called "overtone" and they are usually weaker than the "fundamental" ones (n = 1). If we approximate the system to a harmonic oscillator, only $\Delta\nu$=$\pm$1 transitions are allowed.

Rotationally, the selection rules are based on which values are allowed for J, K_a, K_c. If, as in the case for water, there is no overall electron spin J and K are integer. J can be any integer but once J is fixed then it will limit the values for K_a and K_c. A transition can only occur with ΔJ = 0 (Q branch) ,+1 (R branch) and -1 (P branch). The selection rules for water in terms of K_a and K_c and e and f are listed in Table 3.2.

3.6 The water spectrum

Water is a triatomic asymmetric top molecule. At equilibrium, the water molecule has C_{2v} symmetry, with an angle of 104.55° between the two O-H bonds of length 0.957 $\AA$ at equilibrium (Halonen & Carrington, 1988).

At high temperatures (T $\geq$ 1000K), the spectrum of water contains high rotational and vibrational bands which are not measured in the laboratory. These spectra can be reproduced synthetically if the energy levels, the wavefunctions and the dipole transitions

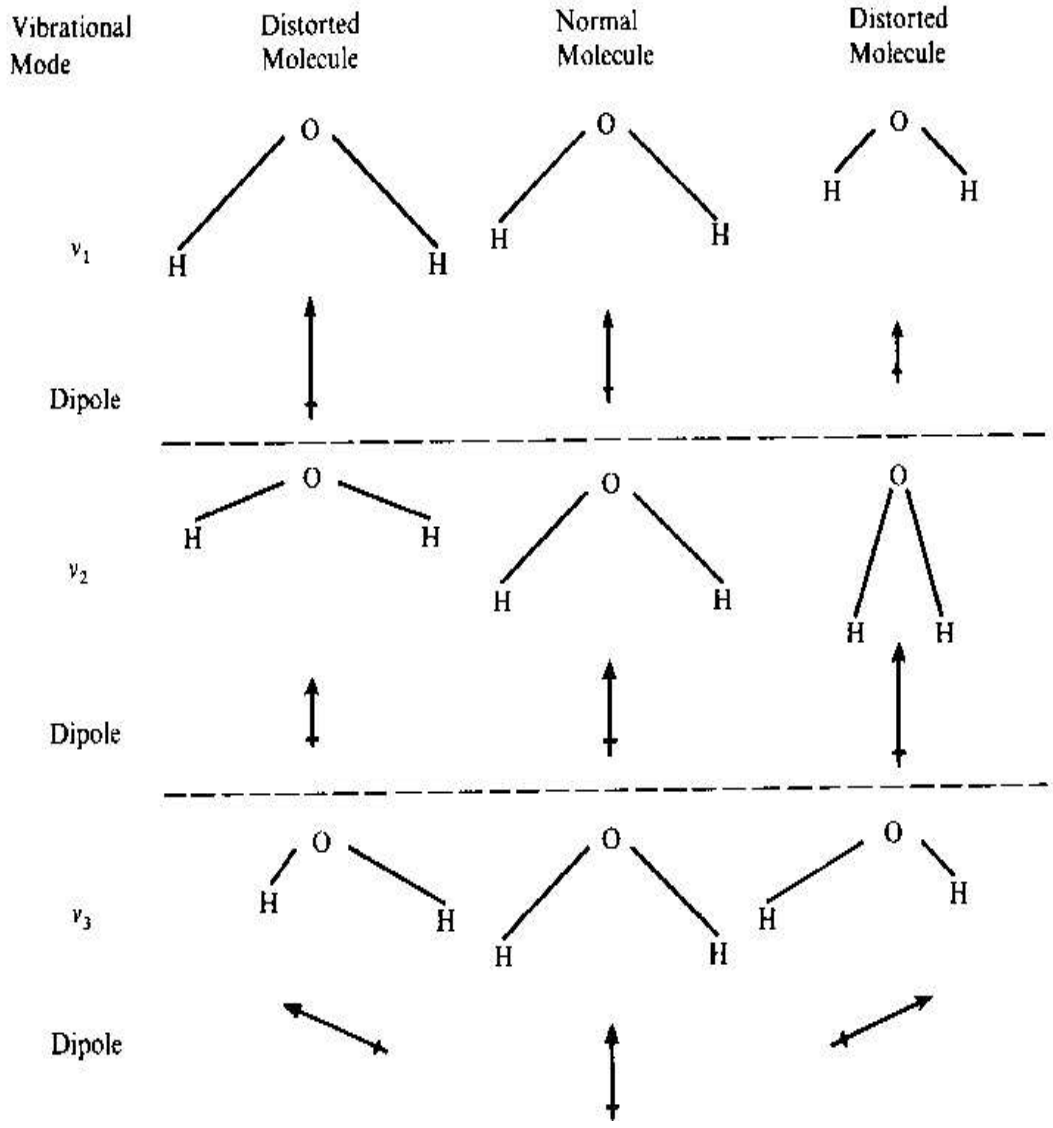

Figure 3.3: The change in the electric dipole moment produced by each vibration in the water molecule. This occurs either along (parallel) or across (perpendicular) the symmetry axis. This drawing is taken from Banwell, 1972.

of each angular momentum state J of water are calculated. Figure 3.4 show an energy level diagram for the water molecule up to $J = 4$.

Water is one of the most studied molecules. So far, there is a wide collection of data on water both experimentally and computationally. However, the amount of available data decreases dramatically as we increase the temperature at which we require those data. At room temperature (300K) experimental data are much more reliable than calculated ones while at higher temperatures, laboratory measurements fail to provide a good database. In fact, to obtain the water spectrum in absorption, equipment able to produce long paths at a uniform temperature up to 3000K and at low pressure is required. Usually, flames are a more convenient source of water vapour at high temperatures but produce emission instead of absorption spectra. It can be hard to measure transition intensities reliably in flame conditions.

3.6.1 Experimental previous work

Both room temperature and high temperature experiments on water have been performed for years. Experimentally, at low to moderate temperatures, a large amount of data are available and widely used. Here, I will mention only those works relevant to this thesis. Flaud *et al* (1976 and other works) compiled atlases (Flaud *et al*, 1981) by assembling transitions measured in a laboratory with a high resolution Fourier transform spectrometer at a limit of a resolution of ~ 0.015 cm^{-1}. The region covered is from microwave to mid–infrared. They also performed a complete analysis of the ν_1, ν_3 and $\nu_2+\nu_3$ bands. Recently, Flaud et al (1997) extended their work to the near infrared. Kauppinen et al (1979) recorded the spectrum of natural water vapour between 30 and 720 cm^{-1} with a double-beam Fourier spectrometer. The resolution achieved was ~ 0.018 cm^{-1} and the accuracy of the observed line positions was better than $\pm$ 0.001 cm^{-1} under best conditions. They observed 550 lines and they identified the strongest. Toth (1991) recorded High-resolution spectra with a Fourier-transform spectrometer covering transitions in the (010)- (000) band from 1066 to 2582 cm^{-1}. The measured line frequencies were used along with additional

Figure 3.4: A partial energy diagram for H_2O from $J = 0$ to $J = 4$. The (n,m) notation corresponds to K_A, K_B. P and O labels define the probability of the molecule to be in a particular state. O stands for *ortho* (most probable) and P stands for *para* (least probable). The allowed transitions are also depicted.

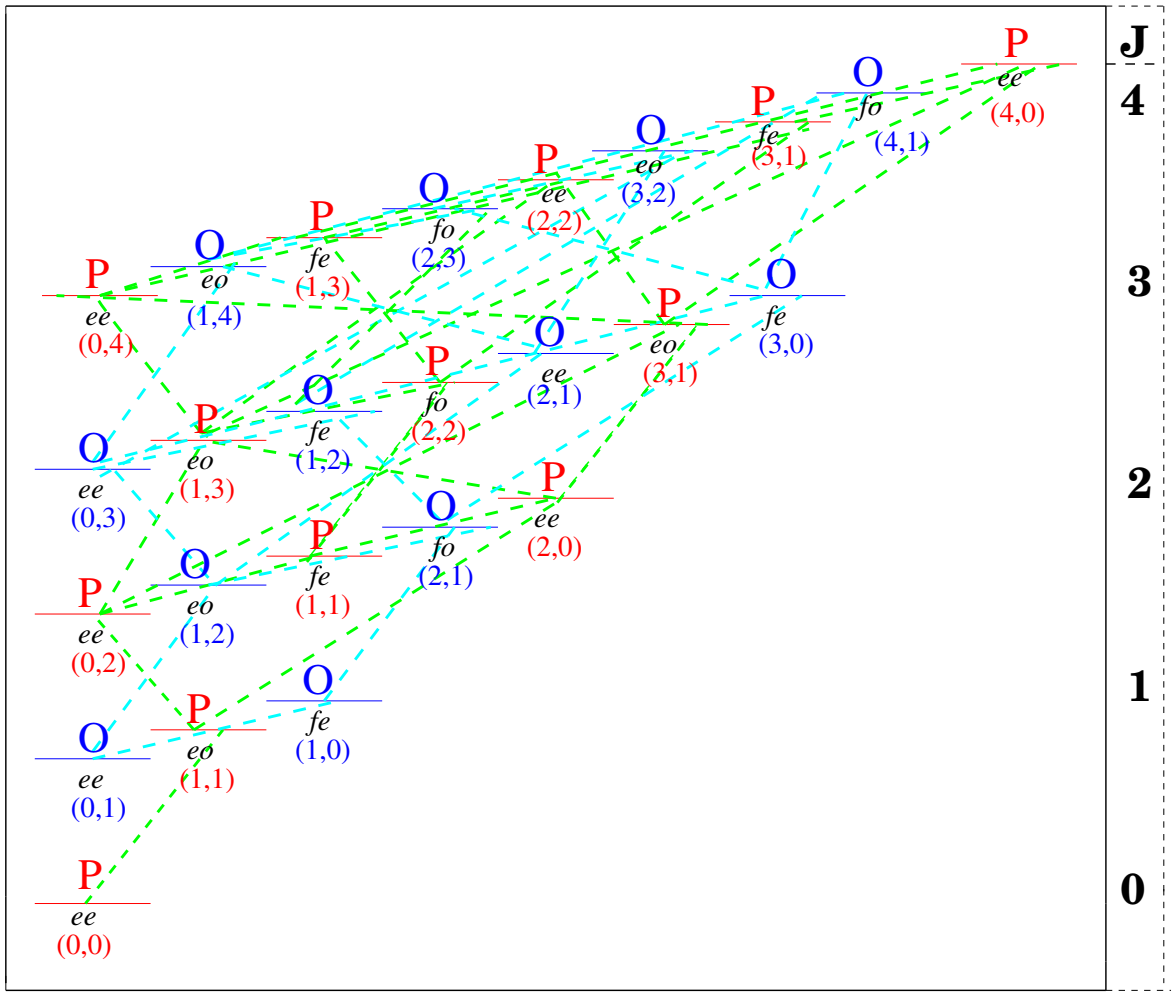

data taken from studies at microwave and far-infrared frequencies in an analysis to obtain rotational energies of levels in the (000) and (010) states.

Most of the data mentioned and many others have been used to compile the HITRAN (High-resolution transmission molecular absorption) database (Rothman *et al*, 1987, 1992; Rothman, 1996) which is a collection of transitions seen and assigned from laboratory measurements for seven principal atmospheric absorbers and twenty-one additional molecular species. It is so far the most complete experimental database. The band coverage is from the millimeter through to the visible portion of the spectrum. In the case of water it includes data measured by several groups. It contains a vast majority of transitions observed at room temperature involving the ground vibrational state and some for higher states. It covers energies up to ~ 6000 cm^{-1} and rotational levels up to $J = 20$. In general, the accuracy of the line positions is better than ± 0.005 cm^{-1} and the line intensities are accurate to $\sim 20\%$ (the accuracy decreases as the lines become weaker and with increasing J). Many weak transitions are not actually measured. In laboratory, strong transitions are observed and the line positions of many weaker ones are deduced by combination theories from the line positions of the observed ones. The intensity is retained using predictions from Perturbation Theory. This can lead to serious omissions (Polyansky *et al*, 1997d).

Recently, an extension of HITRAN has been produced, called HITEMP (Rothman *et al*, 1995 and Rothman, 1996). It is a mixture of measured and calculated transitions which also includes high vibrational bands. However, it has not yet been generally released.

At temperatures higher than 300K it becomes difficult to perform laboratory experiments. However, many groups have attempted to measure high temperature water, mainly for restricted frequency regions due to the limitation of the instruments employed. There are no 'complete' sets available. Perhaps because of possible military applications, there appears to be a 'grey' literature on hot water. An example is Mandin *et al* (1992) who measured a region from 800 to 1900 cm^{-1} of the water spectrum with a Fourier-transform flame at 2000K. They essentially covered part of the ν_2 and $2\nu_2$-ν_2 bands. However, the data are not released. They show a small portion of the emission spectrum obtained. It

lacks of accuracy in the line positioning measurements and in the intensities due mainly to the deficiency of the instrument which falls at the lower end of the spectrum.

3.6.2 Computational previous work

Much of the work on water has been concentrated in computing accurate potential surfaces (both *ab initio* and empirically fitted) and dipole surfaces. As mentioned above, the traditional way of fitting experimental data using perturbation theories is not accurate for water at high temperatures because of the large amplitude motions.

One often used approach is to construct potential energy surfaces starting from *ab initio* force constants. Electronic structure calculations give values for the potential at a grid of points. It is then necessary to interpolate analytically between these points. This is often done by means of least-squares fitting a surface of suitable functional form with adjustable parameters. *Ab initio* calculations usually deviate from experimental values by a few tens of cm^{-1} (Sutcliffe & Tennyson, 1987). This accuracy is insufficient for detailed spectroscopic studies. Potential surfaces computed using empirical force constants are, for example, Carter and Handy (1987), Jensen (1989), Polyansky *et al* (1994), and Polyansky *et al* (1996a). They have used available spectroscopic data to optimize their potential and increase the accuracy of rotation-vibration calculations (Fernley *et al*, 1991).

The calculation of reliable water data relies not only on the availability of accurate potential surfaces but also on valid dipole moment surfaces. Until recently, the best available dipole surface was an *ab initio* one by Rosenberg *et al* (1976). More recently, a number of new dipole moment surfaces have been published, for example, by Wattson and Rothman (1992), Gabriel *et al* (1993) and Jørgensen & Jensen (1993) where vibrational band strengths are computed. For a detailed comparisons between dipole surfaces see Lynas-Gray *et al* (1995).

3.6.3 Data for Opacity Calculations

With the increase in the accuracy of potential surfaces and dipole moments, several groups became involved in the computation of opacity data mainly for astronomical and atmospheric purposes. In astronomy, water vapour in the infrared is the principle source of opacity governing the energy output of cool stars (see Chapter 1). Their importance has led to a number of groups finding the opacities for this molecule.

Experimentally, Ludwig (1971) measured the "curves-of-growth" at a resolution of 20 cm^{-1} of water vapour in the temperature range from 1000K to 3000K at a total pressure of 1 atm with a strip burner 6 m long. He used a statistical band model to reduce his experimental data and yield spectral absorption coefficients which were then binned over 25 cm^{-1} in the region between 1 μm and 10 μm. These data are still widely used (see, for example Abe & Matsui, 1988). However they are at too low a resolution to be useful for the identification of water lines, or indeed reliable modeling (Allard *et al*, 1994; Schryber *et al*, 1995). In fact, coarse data like Ludwig's are inaccurate because the absorption was averaged in bins and the spectral structure within these bins has a significant influence on the model atmosphere calculations (Allard *et al*, 1994).

The available computed datasets, beside the present work, are:

(1) JJ93: The Jørgensen-Jensen (JJ93) water linelist (Jørgensen & Jensen, 1993). They computed an *ab initio* linelist using a mixture of variational and perturbation techniques. This linelist is not actually published and we have not been able to obtain detailed information on their computation.

Although JJ93 contains many transitions belonging to water, their strength is not accurate and their positions are not good enough to perform spectroscopic assignments or predict reasonably good positions of the water bands in the atmospheres of cool stars (see Chapter 2).

(2) MT linelist: The Miller and Tennyson linelist (Miller *et al*, 1994; Schryber *et al*,

1995) has been computed using the FBR program suite TRIATOM (Tennyson *et al*, 1993). MT used a spectroscopically determined potential energy surface by Jensen (1989) and a dipole surface from Wattson & Rothman (1992). The calculations are variational and they use FBR. They used Radau (Tennyson *et al*, 1993) for the radial co-ordinates; Morse-like oscillators for the radial co-ordinate stretching basis functions and associated Legendre functions for the bending co-ordinate basis functions. The body-fixed z axis was chosen to be parallel to r_1 which meant that *ortho/para* states could not be correctly identified. In fact, while the angular symmetrization is consistent with embedding the body–fixed z–axis along either r_1 or r_2, the radial symmetrization is only achieved with the z–axis embedded along the bisector of r_1 and r_2.

The MT contains 6.4 million lines, rotational states up to $J = 30$ and energy levels up to at least 11000 cm^{-1}.

The MT linelist has been included in model atmosphere for (i) M dwarfs, such as VB10 (Allard *et al*, 1994) and (ii) cool brown dwarfs. In fact, it is with the MT linelist that Allard *et al* (1996) modelled the first and coolest brown dwarf yet discovered, Gl 229B (Nakajima *et al*, 1995; Oppenheimer *et al*, 1995). However, the energy cut–off of the MT linelist is too low and overall the accuracy of the energy levels is not high enough to give a good representation of stellar energy output shortward of around 2 μm (Jones *et al*, 1995 and Chapter 2 of this thesis). The MT linelist will be also discussed in Chapter 5.

Some of the data listed above, both experimental and computed, have been used in Chapters 5,6 and 7 for comparisons with our computed data.

Spectroscopically, the MT linelist and JJ93 are of little use. In fact, they were not designed to be used spectroscopically. HITRAN, on the other hand, although accurate, is insufficient. More accurate data are definitely needed for both spectroscopic assignments and modelling.

Technical developments (Tennyson & Sutcliffe, 1992) and use of more accurate potential energy surfaces (Polyansky *et al*, 1994) have allowed us to significantly improve the accuracy of the MT calculations. We have computed three new linelists with different

purposes : VTP1, ZVPT and VT2 (not yet complete). The results are shown in Chapters 5,6 and 7.

Contemporaneously with this work, new laboratory measurements of hot water vapour became available. They are, so far, the best available experimental data. They have been measured by Bernath's group in Canada (see Wallace *et al*, 1995 and Polyansky *et al*, 1996b and 1997d). They recorded an emission spectrum at a temperature of 1550 C° in the ranges of 373 to 933 cm^{-1} and at 1000 C° in the range of 900 to 2000 cm^{-1}, using the Bruker IFS 120 HR Fourier transform spectrometer. These measurements will be discussed in Chapter 6 together with ZVPT.

Computationally, new work has also been developed during the course of this project: a new linelist has been computed by Partridge and Schwenke (1997, PS herein) from NASA Ames Laboratory. It contains 300 million transitions and should have served the same purpose of VT2: accounting for the opacity in cool stars. However, we have analysed their linelist (see Chapter 7) and come to the conclusion that the completion of VT2 is still vital.

In the course of the thesis I will show why we have computed more than one water linelist and I will address some of the main applications of VTP1, ZVPT and VT2.

Chapter 4

Calculations on Water: an overview

Based on the Tennyson–Sutcliffe approach, a suite of programs (Tennyson *et al*, 1995) has been developed to calculate vibration-rotation wavefunctions employing a Discrete Variable Representation (DVR) on a grid in coordinate space. This method is very efficient for generating large quantities of data as underlined in the previous chapter.

In this chapter, I will describe briefly the program suite and I will present some test calculations aimed at finding the best parameters for the purpose of computing opacity data for the water molecule.

4.1 The program: DVR3D

The final version of DVR3D used for the purpose of this work was modified, as discussed later, throughout the course of this project. However, the structure of the program is essentially unchanged. The program suite DVR3D is a 'collection' of four programs. It was published by Tennyson *et al* (1995) and followed a previous suite written for the same purpose called TRIATOM (Tennyson *et al*, 1993). The main difference between TRIATOM and DVR3D is the change from FBR to DVR method (see Chapter 3).

DVR3D calculates the energy levels, wavefunctions and dipole transition moments

for rotating and vibrating triatomic molecules. Two subroutines need to be supplied to compute the potential energy surface and the dipole surface at given points. A few of DVR3D's characteristics are listed below: (1) it approaches the vibrational problem by using an exact Hamiltonian within the Born-Oppenheimer approximation. (2) It uses internal coordinates, either scattering (Jacobi) or Radau (Tennyson *et al*, 1995). (3) Rotationally excited states are treated using an efficient two–steps algorithm (Tennyson & Sutcliffe, 1986). (4) It uses a Discrete Variable Representation (DVR) based on Gauss–Legendre and Gauss–Laguerre quadrature for all the coordinates. (5) The vibrational step uses successive diagonalization and truncation (Bačič & Light, 1986). (6) In the case of water, it calculates dipole transition intensities using full symmetry which distinguish between wavefunctions of *ortho* and *para* states.

The four programs are briefly described below:

DVR3DRJ: calculates the bound vibrational or Coriolis decoupled ro-vibrational wavefunctions using an exact (within the Born-Oppenheimer approximation) Hamiltonian. For $J > 0$ this is the starting point for construction of the full wavefunctions.

ROTLEV3B: performs the second step in a two-step variational calculation for the bound ro-vibrational levels of a triatomic molecule giving as an output the energy levels for each angular momentum state J and their wavefunctions. A difference between this program and ROTLEVD in TRIATOM is the coordinates used. Instead of having the z–axis parallel to r_1 (or r_2), it places the molecule, in an $x - z$ plane and requires the x–axis to bisect θ and the z–axis to lie on the plane of the molecule perpendicular to x while y is such that (x, y, z) form a right–handed frame. In this way, the treatment of the r_1 and r_2 coordinates are identical, allowing them to be properly symmetrized. Hence wavefunctions for water can be identified (Tennyson & Sutcliffe, 1992).

DIPOLE3: computes the dipole transition strength for each transition, using only rigorous, symmetry based selection rules (see Chapter 3).

The parameters involved in these 3 sub–programs which are relevant to understanding part of the current work will be fully described shortly. Refer to Tennyson *et al* (1995) for a full detailed description.

SPECTRA: takes the outputs from DIPOLE3 and ROTLEV3B to calculate the absorption (or emission) linestrengths at any frequency, and the partition function if required. The final output contains the intensities for every wavelength at several temperatures (arbitrary input parameter). This subprogram was taken from TRIATOM and modified to suit our needs.

Table 4.1 summarizes the essential input parameters for the DVR3DRJ and ROTLEV3B subprograms. Most of these parameters have been tested; the results are given in this chapter.

The choice of the input parameters is essential since it determines the 'quality' of the energy levels and wavefunctions. In order to determine the latter, tests need to be performed to quantify the convergence of the calculated energy levels and their comparison with experimental or previously calculated ones. Although DVR is not fully variational, we still used the Variational Principle to estimate the convergence: if the same potential surface is employed, the most accurate set of energy levels should be the one that on average has the lower values for each energy.

Table 4.1: Some input parameters for DVR3DRJ and ROTLEV3B.

DVR3DRJ		ROTLEV3B	
Grid size (NPNT2)	number of DVR points in r_2 from Gauss-associate Laguerre quadrature	NVIB	number of vibrational levels from DVR3DRJ to be read for each k-block
Angular points (NALF)	number of DVR points in θ from Gauss-(associate) Laguerre quadrature.		
Angular momentum (JROT)	rotational angular momentum quantum number J	NEVAL	number of eigenvalues requested for the first parity
NEVAL	number of eigenvalues and eigenvectors requested	KMIN	decides the parity to be calculated (=0 for f;1 for e;=2 for both)
Hamiltonian (MAX3D)	maximum dimension of final Hamiltonian	IBASS	size of the final Hamiltonian
IPAR	parity of the molecule =0 for *para* and =1 for *ortho*	NEVAL2	number of eigenvalues required for the second parity
RE1 (r_e), DISS1 (D_e), WE2 (ω_e)	Morse–like functions parameters		

4.2 Previous work with DVR3D

The program suite DVR3D, suitable for calculations on triatomic molecules using the Cray/YMP8 (Rutherford Laboratory) had only been used previously for the water molecule in limited tests. In particular, Fulton (1994) performed several calculations using the Jensen (1989) potential. He used two sets of the Morse oscillator-like functions, defined by Tennyson *et al* (1995), $r_e = 2.06a_h$, $D_e = 0.14E_h$ and $\omega_e = 0.014E_h$ and $r_e = 2.55a_h$, $D_e = 0.25E_h$ and $\omega_e = 0.007E_h$. He used 24 grid points for the radial coordinates and 40 for the angle. This choice of parameters was taken from an earlier DVR1D calculation (Henderson & Tennyson, 1993). The size of the final Hamiltonian was 4300, corresponding to a cut-off energy of 84318.4 cm^{-1}. All calculations were performed for the rotational level $J = 0$. These tests showed improvements over previously calculated band origins (Fernley *et al*, 1991). However, they were not extensive enough to determine accurately the best choice of input parameters for calculating the energy levels for higher rotational and vibrational states.

DVR3D has also been used succesfully to calculate a complete H_3^+ linelist (Neale *et al*, 1996) and a high temperature partition function (Neale & Tennyson, 1995).

For testing purposes, we used the same potential energy surface as Fulton (1994). For the computation of the linelists different potential energy surfaces have been used. They will be discussed later. Initially, tests were performed to optimize the choice of the input parameters which is strongly related to the convergence of the calculated energy levels. Several calculations have been performed where the energy levels have been compared to the previous work described above and to experimental work.

4.3 Testing the input parameters for the first step: DVR3DRJ

We started with the parameters involved in the first step of the variational computation of the wavefunction (DVR3DRJ). The first tests were performed by varying alternately (i) the radial grid size (NPNT2); (ii) the size of the Hamiltonian (MAX3D); (iii) and

the three parameters: r_e, D_e and ω_e. The number of DVR points in θ was chosen to be 40. This parameter had been tested by Henderson (1991) and used in earlier work (Fernley *et al*, 1991; Fulton, 1994). We used the Jensen (1989) potential energy surface as in Fulton (1994). These parameters are all directly related to the accuracy of the results. The tests were performed for the rotational levels of $J = 0$, $J = 1$, $J = 6$ and $J = 20$.

4.3.1 Test on NPNT2

We first tested the grid size. It is important because it represents the truncation of the radial basis functions and therefore it plays an important role in determining the convergence of the energy levels. In theory, the bigger the size of the grid is, the better the calculation can get. In practice, a limit has to be imposed due to computer related limitations. In fact, the memory and the CPU time required are directly proportional to the size of the grid: as far as memory is concerned, we find an increase of 9% when passing from grid size of 24 to 28 and a 24% when we change from 28 to 36. We find similar behaviour for the CPU time. The limit of the grid size had therefore to be chosen by testing several sizes of grids until a compromise between convergence and computer limitations was reached. For this test, the parameters used to characterize the Morse oscillator-like functions were an equilibrium radius $r_e = 2.06a_0$, a dissociation energy $D_e = 0.14E_h$ and a fundamental frequency $\omega_e = 0.014E_h$. The size of the final Hamiltonian was 2700.

We found a direct correlation between the convergence and the increase in the number of levels. Fulton (1994) had indirectly tested the variability of the grid size (24 and 40); however he included another variable, the basis set, and the two calculations were performed with two different basis sets. Nevertheless, Fulton already noted that the limitation on the grid size implies that some high energy states had wavefunctions that were going out of the grid leading to incorrectly converged energies. He also demonstrated how this problem can be solved by employing a new set of basis functions (as shown later in this chapter).

We performed the tests with grids sizes of 24, 28, 32, 36 and 40. The aim was to find the smallest grid that would give good convergence. For example if the difference in energy between levels calculated using 40 and 24 grid points is minimal for all the excited states considered, than the 24 grid could have been taken for the computation of any linelist. Table 4.2 lists a few selected band origins for $J = 0$ for grid sizes of 24, 28 and 36 for the even parity calculation compared with Fulton's results. Table 4.3 lists a few selected band origins of the odd parity for grid size of 28 and 40.

Table 4.2: Comparison of some of the eigenvalues for $J = 0$, even parity for grid sizes of 24, 28 and 36.

n^o	(ν_1, ν_2, ν_3)	E_{24}	E_{28}	E_{36}	E_{24}(Fulton)
2	(0,0,0)	1594.341	1594.341	1594.341	1594.512
30	(2,4,0)	13453.730	13453.730	13453.730	13453.730
153	(3,2,4)	25440.245	25440.244	25440.244	25440.245
188	(4,10,0)	27430.534	27430.390	27419.668	27430.645
191	(4,1,4)	27536.986	27527.247	27526.215	27526.162
200	(2,15,0)	28033.875	28031.998	28031.530	...

In Figures 4.1 and 4.2, differences in energy levels between 24 and 28, 28 and 36 are plotted, again for $J = 0$.

A larger number of grid points definitely gives a better convergence for higher vibrational energy levels. For the first 140 vibrational even states up to an energy of 23381.0621 cm^{-1} the grid size used makes no difference. In fact the numerical value of the energy level is the same up to the 4^{th} decimal point for 28 and 40. In general for energies higher than 25000 cm^{-1}, the differences among grids becomes more evident. In general, up to 20000cm^{-1}, the convergence is within 0.001 cm^{-1}, while it gets worse (within 0.01cm^{-1}) for higher states. As we will see later, both 40 and 28 have been used to produce water linelists.

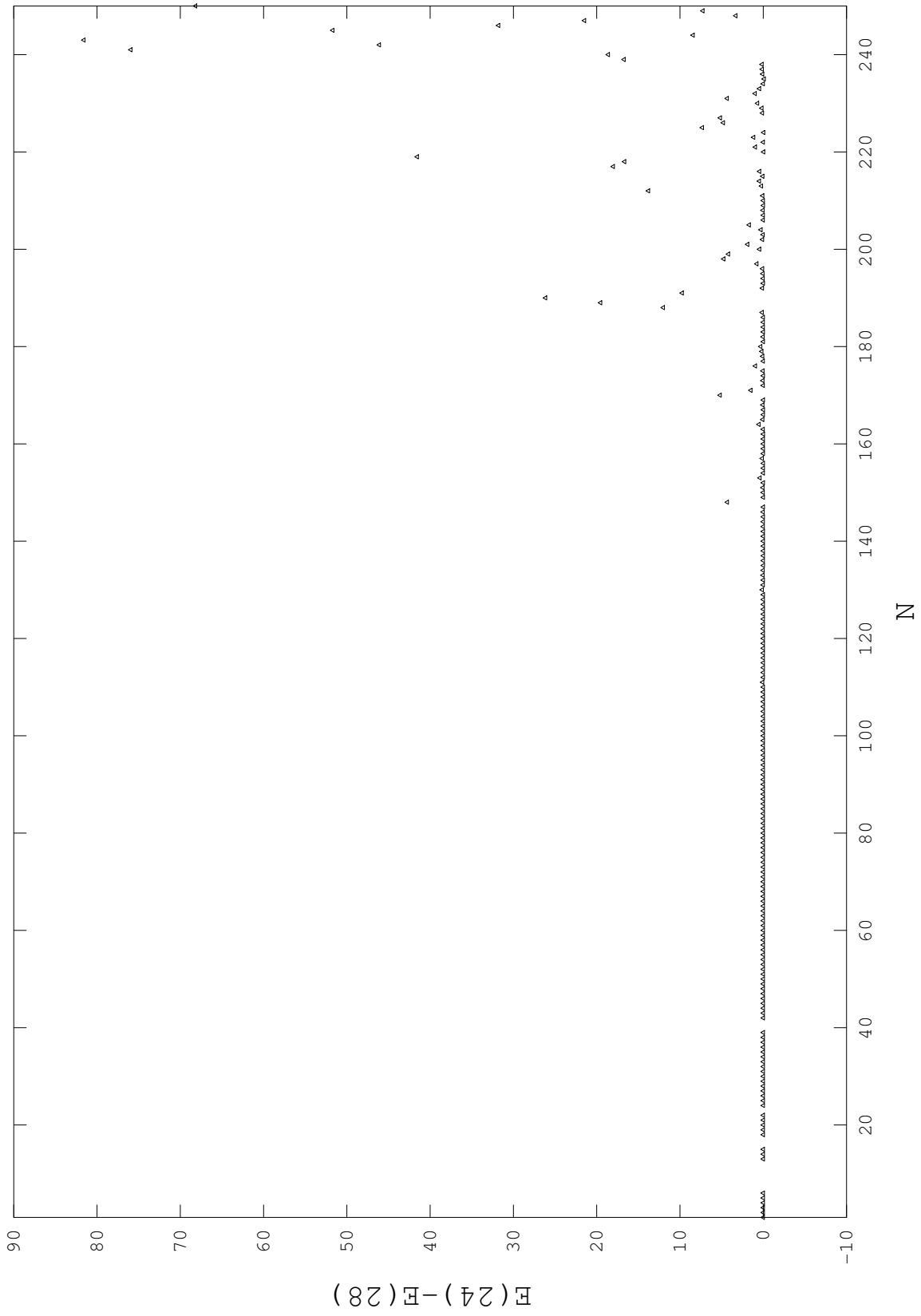

Figure 4.1: Difference in energy levels between a grid size (NPNT2) of 24 and a grid size of 28 for $J = 0$.

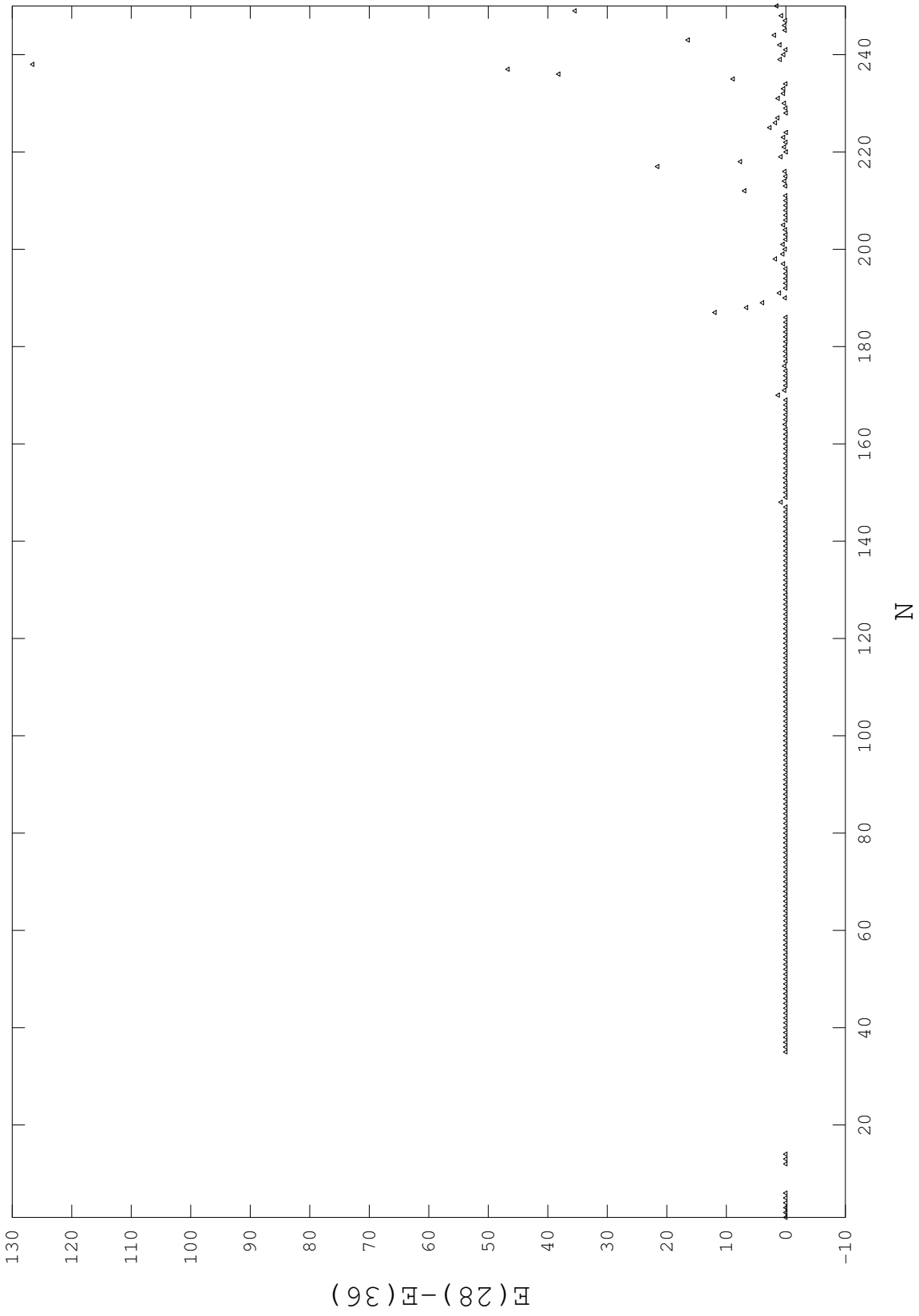

Figure 4.2: Difference in energy levels (in cm^{-1}) between a grid size (NPNT2) of 28 and a grid size of 36 for $J = 0$.

Table 4.3: Comparison of some of the eigenvalues for $J = 0$ odd for grid sizes of 28 and 40.

n^o	(ν_1, ν_2, ν_3)	E_{28}	E_{40}
1	(0,0,1)	3751.5427	3751.5427
30	(2,4,1)	16536.9252	16536.9262
60	(0,2,5)	20906.4264	20906.4260
100	(3,8,1)	24694.7673	24694.7637
111	(6,1,1)	25499.3252	25499.3177
129	(7,0,1)	26860.0866	26860.0727
134	(4,7,1)	27076.8343	27076.8312

4.3.2 Test on MAX3D

The second parameter to be tested was the size of the Hamiltonian. The DVR Hamiltonian is based on a finite basis representation and its truncation relates to the accuracy of the Hamiltonian and to the overall problem size. MAX3D needs to be carefully chosen to maximise convergence. A truncation is an approximation. A bigger MAX3D implies a smaller approximation. The CPU time is directly proportional to the cube of the size of the Hamiltonian. Several values for the Hamiltonian for the calculation of the rotational levels of $J = 0$, $J = 1$ and $J = 6$ have been employed. In particular, (i) $H = 1500$, 2000 and 2700 for $J = 0$ and $J = 1$; (ii) $H = 800$ and 1000 for $J = 1$; (iii) $H = 1600$ and 2100 for $J = 6$. After the first test, where we ran DVR3DRJ for $J = 1$ for the even parity, we found that, by changing H from 1500 to 2000, the first 50 eigenvalues up to the 4th decimal point did not differ. This implies that if the requirement of the linelist is to include only the ground vibrational state transitions then a small size of Hamiltonian as well as a small grid will be sufficient which would be computationally cheap. Subsequent tests requiring 300 and 500 eigenvalues were performed with $H = 800$, 1000, 1500. We noticed an obvious increase in the requirements of filespace when changing from 300 to 500 eigenvalues and

of CPU time when increasing the Hamiltonian. We found that the convergence between the three values of the Hamiltonian was very good. We repeated some of the tests for $J = 6$ rotational state and we found the same good convergence. The lower vibrational states (up to ~ 13000 cm^{-1}) are the same for all the values tried for the Hamiltonian. Up to 21000 cm^{-1} the energy levels converge up to the third decimal place, while as we get to 25000 cm^{-1} the difference can became as big as few wavenumbers. Figure 4.3 shows the difference between energy levels calculated with a Hamiltonian of 1600 and 1800 for $J = 6$. We again found that the size of the Hamiltonian needed to be chosen according to the requirements of the linelist to be computed.

4.3.3 Tests on the basis functions

Finally, to obtain good convergence the choice of the basis functions is probably of primary importance. An earlier calculation (Fernley *et al*, 1991) performed with the previous DVR1D (Henderson & Tennyson, 1993) program used $r_e = 2.06a_0$, $D_e = 0.14E_h$ and $\omega_e = 0.014E_h$ (referred to as 'old' herein). Fulton (1994) already tested these parameters against a new set, $r_e = 2.55a_0$, $D_e = 0.25E_h$ and $\omega_e = 0.007E_h$ (referred to as 'new' herein). He noticed that with the old parameters certain high energy states had wavefunctions that tried to access geometries not represented by the grid. The grid size was fixed at 24. We have extensively repeated the tests with various combinations for $J = 0$, $J = 1$ and $J = 6$ at 24, 28, 36 and 40 radial points for both of the two sets.

An example of our tests is shown in Table 4.4. Figure 4.4 shows the difference in energy levels between old and new parameters for a grid size of 36 for J=0. We find that, within the same potential, the new parameters give better results for energies belonging to high vibrational levels in agreement with Fulton.

4.3.4 Testing the parameters for the second step: ROTLEV3B

The input parameters for ROTLEV3B depend on the rotational quantum number. The three parameters to be chosen for each J are: NEVAL, NEVAL2, IBASS. NEVAL (the

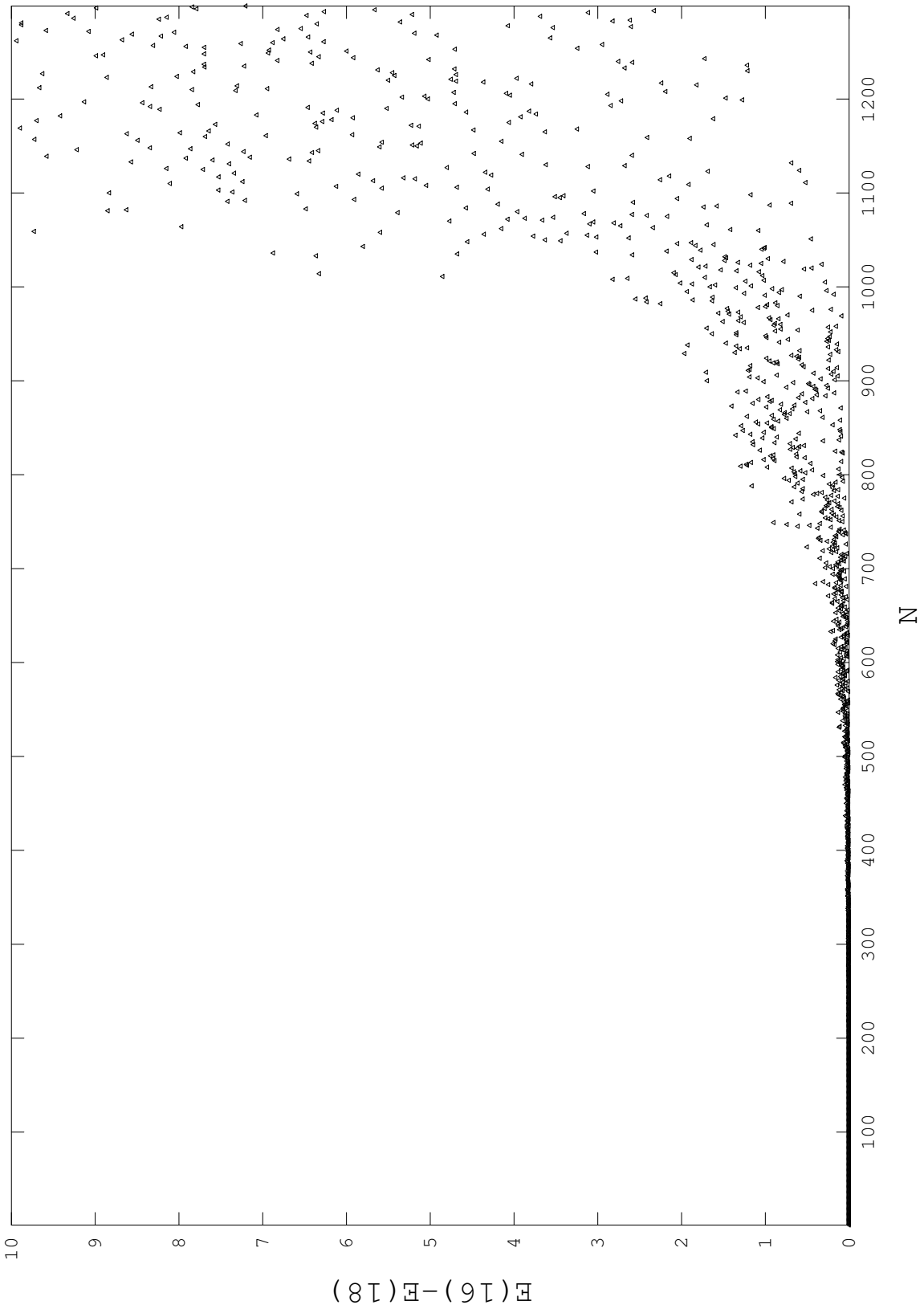

Figure 4.3: Difference in energy levels (in cm^{-1}) between a calculation performed with a Hamiltonian (MAX3D) of 1600 and one of 1800 for $J = 6$.

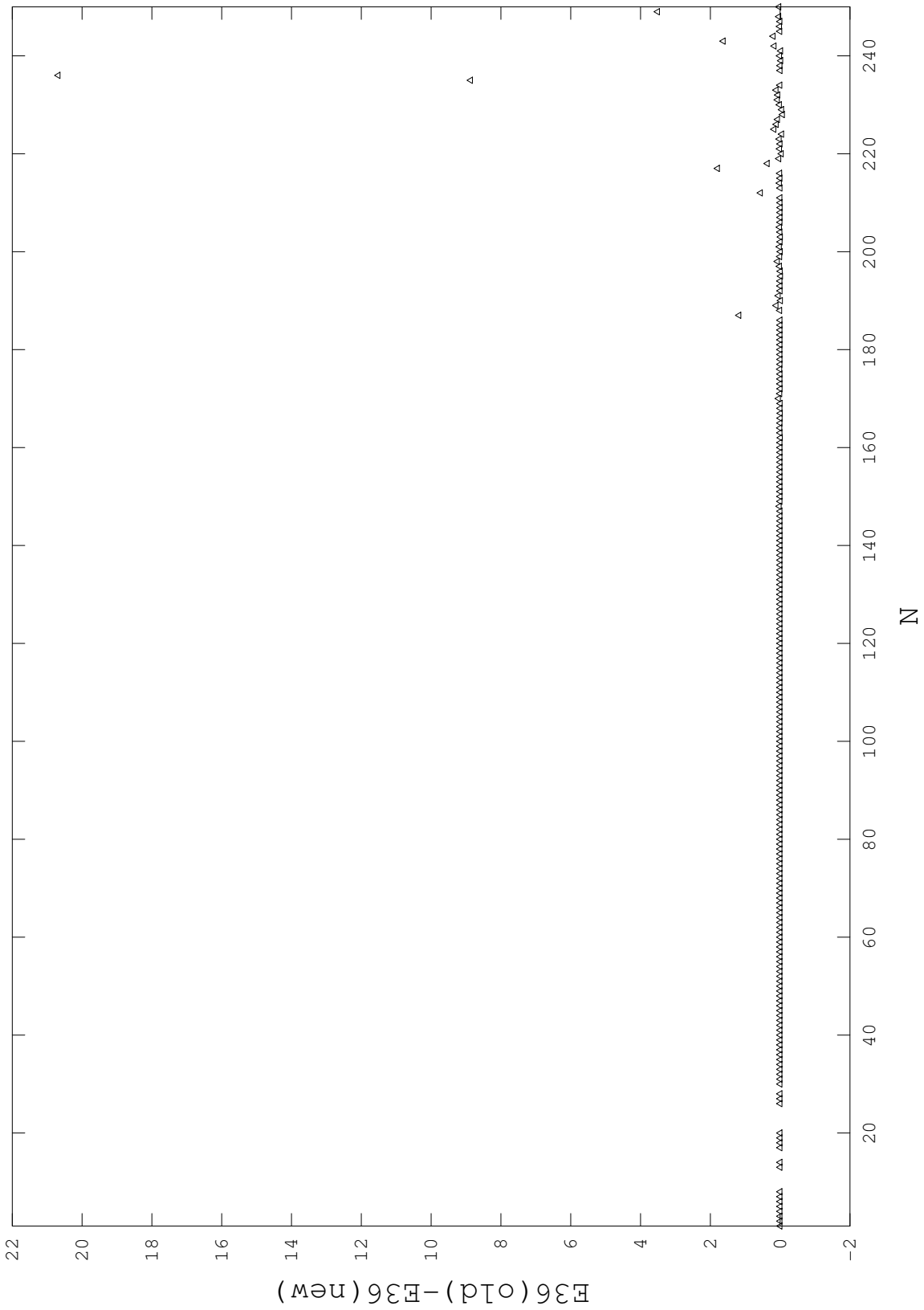

Figure 4.4: Difference in energy levels (in cm^{-1}) for a computation performed with 'old' and 'new' basis functions for $J = 0$ and a grid size of 36.

number of e states calculated for any J, *ortho* or *para*) and NEVAL2 (the number of f states calculated for any J, *ortho* or *para*) can differ since we find that, corresponding to a certain energy cut-off, there are more e states than f states (see Table 7.2 in Chapter 7). NEVAL and NEVAL2 need to be chosen carefully since the CPU time increases with NEVAL for a fixed grid size. Storage is also proportional to the values of NEVAL and NEVAL2: the number of wavefunctions required depends on the energy cut-off. The size of the wavefunctions is equal to the number of stored levels times the number of grid points times the number of k–blocks. For example, for a cut-off energy of 30000 cm^{-1} (necessary to model cool stars' atmospheres), wavefunctions for $J = 8$ have a total size of $\sim$ 4 Gb. The choice of NEVAL and NEVAL2 also influences the CPU time and memory of the computation of the dipoles as we will discuss later.

However, the criterion for choosing NEVAL is simply based on the maximum value for the energy required and we had to adopt an empirical law where NEVAL and NEVAL2 where chosen according to the relations of respectively n $\times$ (J+1) and J/(J+1)$\times$ NEVAL. IBASS represents the size of the second step Hamiltonian. We have tested it using an empirical law as well: its size should be chosen according to an m $\times$ (J+1) law. We found, even more than for the other parameters, that the choice is highly based on the requirements. The higher the upper energy level required is for each J, the higher m and n have to be. For our tests we adopted m = 150, 200, 300 and n = 5, 100, 300. In general we consistently found that we require m = 300 and n $\sim$150 to calculate energy levels up to 30000 cm^{-1}.

4.4 Improvements to the suite DVR3D over the course of the project

The computation of molecular linelists can be a very extensive and expensive one. Before embarking on the computation of VT2, we were not fully aware of the CPU time, storage space and memory requirements. Estimating *a priori* was a difficult task.

Table 4.4: Comparison of some eigenvalues for $J = 0$ for various parameters.

NPNT	28	28	24	24	36	36	40
	r_e=2.06	r_e=2.55	r_e=2.06	r_e=2.55	r_e=2.06	r_e=2.55	r_e=2.55
	D_e=0.14	D_e=0.25	D_e=0.14	D_e=0.25	D_e=0.14	D_e=0.25	D_e=0.25
n^o	ω_e=0.014	ω_e=0.007	ω_e=0.014	ω_e=0.007	ω_e=0.014	ω_e=0.007	ω_e=0.007
1	4630.401	4630.401	4630.401	4630.401	4630.401	4630.401	4630.401
20	15233.281	15233.280	15233.281	15233.244	15233.281	15233.281	15233.281
70	23295.657	23295.656	23295.657	23295.626	23295.657	23295.657	23295.657
100	26175.646	26175.645	26175.646	26175.608	26175.646	26175.646	26175.646
170	31087.807	31085.404	31092.992	31066.988	31086.524	31086.570	31086.526
200	32621.955	32621.828	32622.413	32621.880	32621.845	32621.837	32621.845

Throughout the computation of VTP1 and VT2 linelists, improvements and changes have been made to the suite.

While computing VTP1, we found some physical problems in the published version of SPECTRA (Tennyson *et al*, 1993): (i) some of the *ortho* and *para* pairs had swapped intensities according to certain symmetry rules; (ii) some transitions were missing. The missing transitions were due to a problem related to the cut-off intensity assumed by the program while the swapping of particular symmetries was related to inappropriate symmetry handling in the published version of the program SPECTRA. Some transitions, specifically, for $\Delta J = +1$ from J odd to J even, from e(odd) to e(even), *ortho* and *para* transitions were swapped. The problem has been fixed by correcting the formula calculating those particular transitions.

This problem did not come out in the computation of the MT linelist because it did not distinguish between *ortho* and *para* as there the program did not use any symmetry.

Also, the data handling in the published version of SPECTRA has been changed. Originally, the program required the entire linelist to be read and stored in before any

filtering (eg. wavelength region or intensity cut–off). The program has been rewritten to allow pre-filtering. This change was essential given the size of the linelists being processed.

During the computation of VT2, several problems concerning the CPU time, storage and memory handling were encountered. No physical problems have been found. Because of the CPU time, the memory requirement and the storage space needed, the following changes had to be made:

ROTLEV3B: options have been implemented so that the construction of the wavefunction can be done in separate steps. The Hamiltonian construction, the diagonalization and the transformation (back to the original DVR grid) of each parity can now be computed separately. This increased the number of jobs per wavefunction but allowed us to make use of the only available computer facility by fitting the jobs the memory, CPU time and storage limitations. The way the wavefunctions are written out has been changed as shown in Table 4.5. This was necessary to reduce I/O usage in DIPOLE3.

During the course of the computation, the Cray/YMP8 we were running the codes on was replaced by a Cray/J90 with the advantage of a large increase of processors (from 8 to 32) which then allowed multitasking. Library routines have been replaced to suit the new system using the BLAS (basic linear algebra subroutines) which provide standard matrix operation routines optimized for any given computer architecture. On the Cray J90 these are implemented as part of the ISML library (http://www.vni.com/products/imsl/specs.html) and automatically multitask code with high efficiency.

DIPOLE3 underwent several changes during the project. In general, it has been rewritten to (i) handle the new layout of the wavefunction from ROTLEV3B; (ii) to reduce I/O; (iii) to allow excellent multitasking. More specifically, new options have been implemented in DIPOLE3 to allow the choice of particular states or particular k–blocks to calculate the dipole transitions between wavefunctions. The number of blocks can be calculated *a priori* with the following formula:

$$(j^{'} + j^{''} + min(j^{'}, j^{''})) - 2 \tag{4.1}$$

where $j^{'} = J^{'} + \mathrm{KMIN}^{'}$, $j^{"} = J^{"} + \mathrm{KMIN}^{"}$ and $min(j^{'}, j^{''})$ is the smallest value between $j^{'}$ and $j^{"}$. KMIN is 0 for f and 1 for e calculations.

The advantage of these implementations are computer related: calculating dipole transitions between thousands of energy levels is computationally difficult.

SPECTRA: several options have been implemented, among which, are most importantly, input parameters that give the choice of: (i) wavelength or frequency regions for which the spectrum needs to be calculated. (ii) The inclusion in the output file of the energy levels, quantum numbers and spin degeneracy. (iii) The cut-off intensity to be calculated and written out. (iv) A choice between relative (to the maximum) or absolute intensity.

The program suite with relevant documentation is available via WWW (http://www.tampa.phys.ucl.ac.uk/).

4.5 Concluding remarks

In the course of this thesis, we use the DVR3D suite to calculate three water linelists. We have carefully chosen the input parameters according to the tests that we have described in the course of this chapter. For VTP1 we are mainly interested in the energy levels belonging to the ground vibrational state (this justifies the choice of the 'old' values for the basis set parameters). According to our conclusions for the testing we are confident we can calculate the required energy levels by calculating $\sim J + 3$ levels (NEVAL and NEVAL2 = 1(J+3)) up to $J = 6$ for both parities. After that, n varied from 3 to 20 according to J.

For ZVPT we are interested in the energy levels belonging to the (000), (100), (010), (020), (001), (030) vibrational states. We chose the numbers of eigenvalues and eigenvectors for each J in order to include states belonging to those vibrational bands. In practice, that meant including all the energy levels up to 17000 cm^{-1} for each J.

For VT2 we are interested in obtaining energy levels up to 30000 cm^{-1} at the possible expense of spectroscopic inaccuracy as the energy increases. Again, NEVAL and NEVAL2 needed to be varied with J.

The computational cost of VTP1 and ZVPT is trivial compared to VT2. VTP1 took $\sim$ 150 hours Cray/YMP8 CPU time. ZVPT took $\sim$ 250 hours on the Cray/J90. VT2 is not yet completed but we estimate that it will take in total more than 6000 hours Cray/YMP8 hours. This large difference in computational costs is due to the relationships of the CPU time with (i) the radial grid size; (ii) NEVAL and NEVAL2; (iii) the maximum dimension and the final size of the Hamiltonian.

Table 4.5: A graphical representation of the changes in the way the wavefunction was written out from ROTLEV3B (from top to bottom). k is the projection of J onto body-fixed z–axis. Each k block contains a limited number of basis functions selected. *nbass* is the size of the Hamiltonian for each energy level (here an example with 5 energy levels) within each block. *mbass* is the maximum size of the vibrational problem. The new layout of the wavefunction is computationally advantageous in that all the energy levels do not need to be read for each block.

NEVAL	k=0	k=1	k=2		
1	nbass(1,0)	nbass(1,1)	nbass(1,2)		
2	nbass(2,0)	nbass(2,1)	nbass(2,2)		
3	nbass(3,0)	nbass(3,1)	nbass(3,2)		
4	nbass(4,0)	nbass(4,1)	nbass(4,2)		
5	nbass(5,0)	nbass(5,1)	nbass(5,2)		
	mbass(NEVAL)= nbass(k=1) + nbass(k=2) + etc...				
⇓					
k_{block}	NEVAL				
	1	2	3	4	5
0	nbass(0,1)	nbass (0,2)	nbass(0,3)	nbass(0,4)	nbass(0,5)
1	nbass(1,1)	nbass(1,2)	nbass(1,3)	nbass(1,4)	nbass(1,5)
2	nbass(2,1)	nbass(2,2)	nbass(2,3)	nbass(2,4)	nbass(2,5)
	mbass= nbass(k) × NEVAL				

Table 4.6: List of input parameters for the three linelists (i) VTP1, (ii) ZVPT, (iii) VT2. For NEVAL and NEVAL2, n varied even within each linelist so it will be discussed in the text.

	VTP1	ZVPT	VT2
Radial points(NPNT2):	21	28	40
Angular size(NALF):	40	40	40
H(MAX3D):	1000	1000	2000
r_e	$2.06a_0$	$2.06a_0$	$2.55a_0$
D_e	$0.14E_h$	$0.14E_h$	$0.25E_h$
ω_e	$0.014E_h$	$0.014E_h$	$0.007E_h$
IBASS	200(J+1)	150(J+1)	300(J+1)
NEVAL and NEVAL2	n(J+3)	nJ	nJ

Chapter 5

A first Spectroscopic linelist: VTP1

Recently, high resolution spectra of Sunspots showed the presence of very dense forests of water lines (Wallace *et al*, 1995). Water lines can reach a density of 50 lines per cm^{-1} and making the process of identification very difficult (see Chapter 6 for further details). To assign these transitions never identified before, a new spectroscopically accurate water linelist was needed. This was the major reason for computing VTP1. Secondly, it would have been a unambiguous test of the new version of the DVR3D program suite.

In this Chapter I present VTP1 and its applications.

VTP1 is a calculated linelist. It does not cover high vibrational bands but it does cover high rotational levels. It contains 230,000 lines, many fewer levels than MT. However, it is spectroscopically accurate and it also includes higher rotational levels. The present linelist is designed for spectroscopic analysis.

VTP1 can be used for studying water spectra, particularly of hot rotational states, like in masers (Yates *et al*, 1995) and in other hot molecular environments including magnetodynamic shocks, circumstellar outflows and active galactic nuclei. However, it is not complete enough to give opacities for modelling cool stellar atmospheres.

5.1 Parameters employed

The choice of the potential and dipole surface is essential in determining the accuracy of the line positioning and strength. For this linelist, the energy and wavefunctions were generated using the PJT1 potential of Polyansky *et al* (1994). This potential was determined by fits to spectroscopic data and is particularly accurate for energy levels belonging to low vibrational states. The observed rotational levels of the ground state are reproduced with a standard deviation of only 0.03 cm^{-1}. However, PJT1 is less accurate for higher states. For further details, refer to Polyansky *et al* (1994).

We have tested PJT1 *a posteriori* by comparing the first 300 energy levels of selected ($J = 0$, $J = 1$ and $J = 6$) calculated with PJT1 with energy levels calculated with a previously published potential surface from Jensen (1989). Jensen used his MORBID Hamiltonian (Jensen, 1988) to fit his potential. The MORBID (Morse Oscillator rigid bender internal dynamics) Hamiltonian uses an approximate kinetic energy approach.

In Table 5.1 we compare some energy levels up to the 95th for $J = 0$ (even) calculated with the suite DVR3D, employing the same parameters, with the two different potentials. For the first 4 levels we have also listed the experimental energy values according to HITRAN. The latter does not contain many energy levels belonging to vibrational states other than the ground one. Therefore only the first few levels for each J could be compared with HITRAN. From the comparisons of the first few levels for $J = 0$, $J = 1$ and $J = 6$ with the experimental values, we find that PJT1 is significantly better then the two previous potentials reaching an accuracy of ~ 0.1 cm^{-1}. This value was estimated by taking the average absolute difference between experimental levels and calculated ones for each of the three J.

Dipole transitions were calculated using the spectroscopically determined dipole surfaces of Wattson and Rothman (1992). This dipole surface has been used before (Miller *et al*, 1994) and so we limited the test to a quick comparison among the $J = 2$ dipole transitions with the ones from MT linelist and found consistency.

We used a DVR grid of 40 points based on Gauss-(associated) Legendre polynomials in

the θ coordinate. For the radial coordinates we used the same radial basis set parameters as MT (see Fernley *et al*, 1991) and a DVR grid of 21 points. This number of grid points is sufficient to obtain good convergence for low lying vibrational levels but needs extending to converge high vibrational states (Fulton, 1994). In the first vibrational step, we selected 500 eigenvectors out of a 1000 dimension secular problem (i.e the maximum dimension of the final Hamiltonian matrix). For the ro-vibrational problem, the size of the Hamiltonian varied with J as $200 \times (J+1)$. The number of eigenvalues obtained varied with J as $n(J+3)$ as explained in Chapter 4. We ensured that all the energies belonging to the ground vibrational state were included.

5.2 Computation of the linelist

Wavefunctions were computed and used to generate a list of all possible dipole allowed transitions following the rigorous symmetry rules listed in Chapter 3. The use of properly symmetrized wavefunctions was necessary to account correctly for the nuclear spin statistics. As a consequence, *ortho/para* doublets, very close in frequency, have been resolved with the correct intensity ratio. This feature is not present in the MT linelist.

The aim of this work was to compute all the wavefunctions for rotational angular momenta as high as $J = 38$ including all the energy levels belonging to the ground vibrational state, (000). Our final linelist actually includes higher vibrational states and more specifically some of the levels for the (100), (001), (011), (010), (021), and (101) states. For high J ($J \geq 10$) we found that it was necessary to consider energies of up to 12000 cm^{-1} above the $J = 0$ ground state.

The computation took 76 jobs for creating the wavefunctions and 228 jobs to calculate the transitions on the Cray/YMP8 at Rutherford Appleton Laboratory. The total CPU time consumed amounted to $\sim$ 150 hours where 20 hours were taken for the dipoles and the remaining for the creation of the wavefunctions. The maximum memory required was 15 Mw and the filespace needed at any time was $\sim$ 10Gb.

During the computation, we performed some checks on the outputs. In order to test

Table 5.1: Comparisons of energy levels (for $J = 0$) calculated with three different potential energy surfaces. The first four levels are also compared with experimental energies.

n^o	Jensen	PJT1	Exp. (HITRAN)
1	1594.3409	1594.6986	1594.7480
2	3152.0499	3151.6107	3151.6300
3	3656.5277	3657.1371	3657.0540
4	4667.7495	4667.0182	4666.7930
10	7539.8747	7536.8669	...
15	9719.8645	9720.7776	...
20	10869.4461	10868.9177	...
25	12144.5925	12139.1844	...
30	13453.7303	13451.4246	...
35	13911.8750	13910.4413	...
40	14859.0683	14863.9843	...
45	15744.2790	15742.9675	...
50	16525.5923	16527.0043	...
55	17054.8774	17063.9734	...
60	17542.6032	17528.4769	...
65	18257.4956	18257.0249	...
70	18684.8247	18734.1380	...
75	19376.5919	19382.8750	...
80	19757.2311	19815.6698	...
85	20398.3559	20406.7872	...
90	20731.8103	20767.9885	...
95	21277.7448	21280.1144	...

the frequencies we used a tabulated list of relative intensities versus frequencies of laboratory measurements performed by Kauppinen *et al* (1979), later used in comparison with VTP1 linelist at T = 300K. At this temperature, laboratory measurements are spectroscopically accurate and therefore give very precise frequencies. For wavefunctions and dipole transitions up to $J = 8$ we ran the subprogram SPECTRA using a temperature of 300K and compared the resulting frequencies and intensities with the "Kauppinen" set and found that some transitions were missing and that some *ortho* and *para* transitions were swapped. To fix these problems we corrected SPECTRA in the way we described in Chapter 4.

An alternative method of checking our results was by comparison with available experimental and theoretical data. We compared the energy levels produced by our DVR method against the ones in the MT linelist and the HITRAN database (Rothman *et al*, 1987). In general, the VTP1 levels are a major improvement over the MT energy levels (see Table 5.2).

It is interesting to point out some of the improvements of the VTP1 over the MT linelist: the MT linelist was calculated with the basis set program suite TRIATOM (Tennyson *et al*, 1993) using an older potential energy surface (Jensen, 1989) which had a high standard deviation (6.4 cm^{-1}). Moreover, for high rotational states ($J \geq 20$), studies (Polyansky *et al*, 1994) have shown that Jensen's potential can give errors of up to 30 cm^{-1}. This problem is exacerbated in MT's calculation due to poor convergence at high J (up to 10 cm^{-1}) (Miller *et al*, 1994). With the DVR method, the convergence is much better and is essentially independent of J.

Our accuracy tests suggest that errors in our linelist should only be apparent in observations made at a resolving power, $\frac{\lambda}{\Delta\lambda}$, greater than 17000. However, we note that the tests performed on hot transitions rely on a small sample of lines which have been assigned to the high temperature laboratory measurements (Polyansky *et al*, 1996b).

Table 5.2: Comparison of a sample of calculated energy levels with observed ones from the HITRAN database. Calculations are VTP1 (this work) and MT (Miller *et al*, 1994). See text for details.

$(\nu_1\nu_2\nu_3)$	J	VTP1	Obs	Obs - Calc	
				VTP1	MT
010	0	1594.6986	1594.7480	0.0494	-1.0613
010	1	1618.6243	1618.5590	-0.0653	-1.0612
020	1	3175.6319	3175.4410	-0.1909	-1.1337
100	1	3680.5329	3680.4541	-0.0788	-1.8220
000	2	70.0909	70.0910	0.0001	-1.2371
010	2	1664.9133	1664.9710	0.0577	-1.0596
100	2	3750.5293	3750.4639	-0.0654	-1.8210
000	3	136.7599	136.7620	0.0021	-1.2375
010	3	1731.8466	1731.8979	0.0513	-1.0742
010	3	1907.6644	1907.6169	-0.0475	-1.0773
001	3	4030.1858	4030.3059	0.1201	-1.3980
000	4	222.0535	222.0520	-0.0015	-1.2405
010	4	1817.4053	1817.4510	0.0457	-1.0918
000	11	2144.0347	2144.0470	0.0123	-1.2849

5.3 Results

Our linelist contains 230,000 lines which is too many to tabulate usefully here. An illustrative portion of the linelist is given in Table 5.4. The various parameters in Table 5.4 have been defined in Chapter 3 but for convenience we give them here: $J^{'}$ and $E^{'}$ are the rotational quantum number and the energy level of the upper state, while $J^{''}$ and $E^{''}$ are the corresponding parameters for the lower state. The energies are in cm^{-1} as is the transition frequency $\omega(= E^{'} - E^{"})$. g is the nuclear spin degeneracy factor which for water is 1 (para) or 3 (ortho). The Einstein Coefficient, A_{if}, is in s^{-1}. It can be used directly to calculate the transition probabilities

$$\mid R^2 \mid = \frac{(2J^{'}+1)A_{if}}{(2J^{"}+1)\omega^3} \tag{5.1}$$

and the integrated absorption intensities depending on the temperature chosen

$$I = C\frac{\omega g(2J^{"}+1)}{Q(T)}\left(\exp(\frac{-E^{"}}{kT}) - \exp(\frac{-E^{'}}{kT})\right) \mid R^2 \mid \tag{5.2}$$

where C is the constant of proportionality equal to 7.9920×10^{11} for the intensity in cm $mole^{-1}$, or equal to 3.5656×10^{7} at STP for the intensity in $cm^{-2}atm^{-1}$.

We have compared VTP1 with all the available public (and non public) data and also with data not yet published (HITEMP, Rothman 1996, private communications). Our comparisons include:

1) An extensive comparison of the energy levels from (i) VTP1, (ii) MORBID calculations (Polyansky, private comunications), (iii) HITRAN and (iv) HITEMP.

2) A graphical comparison of VTP1 with available laboratory data at room temperature for 2 independent sets, HITRAN and a table from Kauppinen *et al* (1979)

3) A comparison of a small portion of a high temperature Fourier Spectrum from Mandin *et al* (1992) and a comparison of VTP1 at several temperatures with unpublished spectra of HITEMP.

5.3.1 Energy levels comparison

The symmetry nomenclature employed by DVR3D is different to those employed by the comparison sets of data. HITRAN/HITEMP uses approximate quantum numbers. Energy levels computed with the MORBID approach are labelled with some approximate quantum numbers and some artificial ones directly related to approximate quantum numbers. Table 3.1 in Chapter 3 relates all the different nomenclatures (see also Figure 3.4 from Chapter 3).

By developing a general reversible transformation rule between VTP1, MORBID and HITRAN/HITEMP, we wrote a program to assign the standard quantum numbers to VTP1 and to intercompare energy levels. The program is built up of several subroutines, each with many options according to the user's needs. The general aim was not only to compare *all* the energy levels belonging to every rotational and vibrational state but also to facilitate the comparison by dividing the energy levels files from different sets into (i) individual rotational levels (ii) individual symmetry blocks (iii) individual vibrational bands and so on. Table 5.3 shows an example of such a comparison for the vibrational band (000) for every rotational level up to $J = 5$.

VTP1 is closer to experimental values than MORBID for the ground vibrational level. In fact, for (0,0,0) VTP1 is accurate within ~ 0.0004 cm^{-1}. However as the vibrational states increase, the accuracy of VTP1 decreases with respect to MORBID. Note that although HITEMP is a computed linelist, levels present in HITRAN have been used in the place of computed one. Our tests imply that this has not always been done correctly.

5.3.2 Comparisons at T = 300K

We calculated a VTP1 spectrum at room temperature (300K) and compared it with a spectrum obtained experimentally by Kauppinen *et al* (1979). Laboratory data at low temperature are very reliable and so a match between calculated and observed spectra at room temperature would confirm the quality of the data. Figure 5.1 shows such a comparison. For visual reasons we plotted the laboratory measurements in the positive direction,

Table 5.3: Comparison of energy levels from various sets belonging to the rotational states from $J = 0$ to $J = 5$ for the (0,0,0) vibrational state.

J	1 - p	O/P	K_a	K_c	(ν_1, ν_2, ν_3)	VTP1	HITRAN	HITEMP	MORBID
0	0	1	0	0	000	0.00000	0.0000	0.0000	0.000
1	0	1	0	1	000	23.79438	23.7940	23.7944	23.7907
2	0	1	2	0	000	136.16195	136.1640	136.1639	136.1524
3	0	1	2	1	000	212.15427	212.1560	212.1564	212.1345
3	0	3	3	1	000	285.21499	285.2190	285.2194	285.1988
3	1	1	3	0	000	285.41422	285.4190	285.4186	285.3981
4	0	1	2	2	000	315.77703	315.7790	315.7796	315.7404
4	0	1	4	0	000	488.12678	488.1340	488.1343	488.1045
4	0	3	3	2	000	382.51269	382.5170	382.5169	382.4900
4	1	1	3	1	000	383.83821	383.8430	383.8425	383.8163
4	1	3	4	1	000	488.10030	488.1080	488.1078	488.1045
5	0	1	2	3	000	446.50737	446.5110	446.5107	446.4461
5	0	1	4	1	000	610.33405	610.3410	610.3413	610.3167
5	0	3	3	3	000	503.96396	503.9680	503.9680	503.9287
5	0	3	5	1	000	742.06276	742.0730	742.0731	742.0365
5	1	1	3	2	000	508.80750	508.8120	508.8120	508.7741
5	1	1	5	0	000	742.06603	742.0760	742.0764	742.0398
5	1	3	4	2	000	610.10733	610.1140	610.1145	610.0895

while the calculated spectrum is plotted in the negative direction. The relative laboratory intensities are normalized to match the absolute calculated ones since the original data were normalized to unity. The match is almost perfect and certainly falls within the expected error bars. We also compared the same data with HITRAN database (Figure 5.2): again the HITRAN spectrum is plotted in the positive direction. In this case both sets of intensities are absolute.

Figures 5.1 and 5.2 show that at low temperature, VTP1 linelist is sufficient for assigning water lines and for reproducing the measurements.

5.3.3 Higher temperatures comparisons.

There is much less data available for comparison at higher temperatures. However, Mandin *et al* (1992) published a high resolution, Fourier-transform flame spectrum with a temperature in the region of 2000 K. A comparison with a water spectrum generated with the VTP1 at this temperature is shown in Figure 5.3. Mandin *et al* made no claims about intensity; indeed there is a pronounced drop in intensity at the lower end of the spectrum which is probably due to loss of instrumental sensitivity at these frequencies. In the calculated spectrum there are some missing transitions with respect to the flame spectrum probably belonging to higher vibrational states. However, the observed line positions are again in good agreement with ours.

Since completion of VTP1, we have become aware of a new linelist, not yet generally available (Rothman, private communication, 1996), called HITEMP, see discussion in Rothman *et al* (1995). The hot water lines in this linelist come from theoretical calculations similar to ours (Wattson & Rothman 1992). We have undertaken some comparisons between the two linelists and in general we find excellent agreement. For instance, line intensities are within 5% for the cases compared. The comparisons were made at the following temperatures:

1) T = 1000K (Figure 5.4)

2) T = 1500K (Figure 5.5)

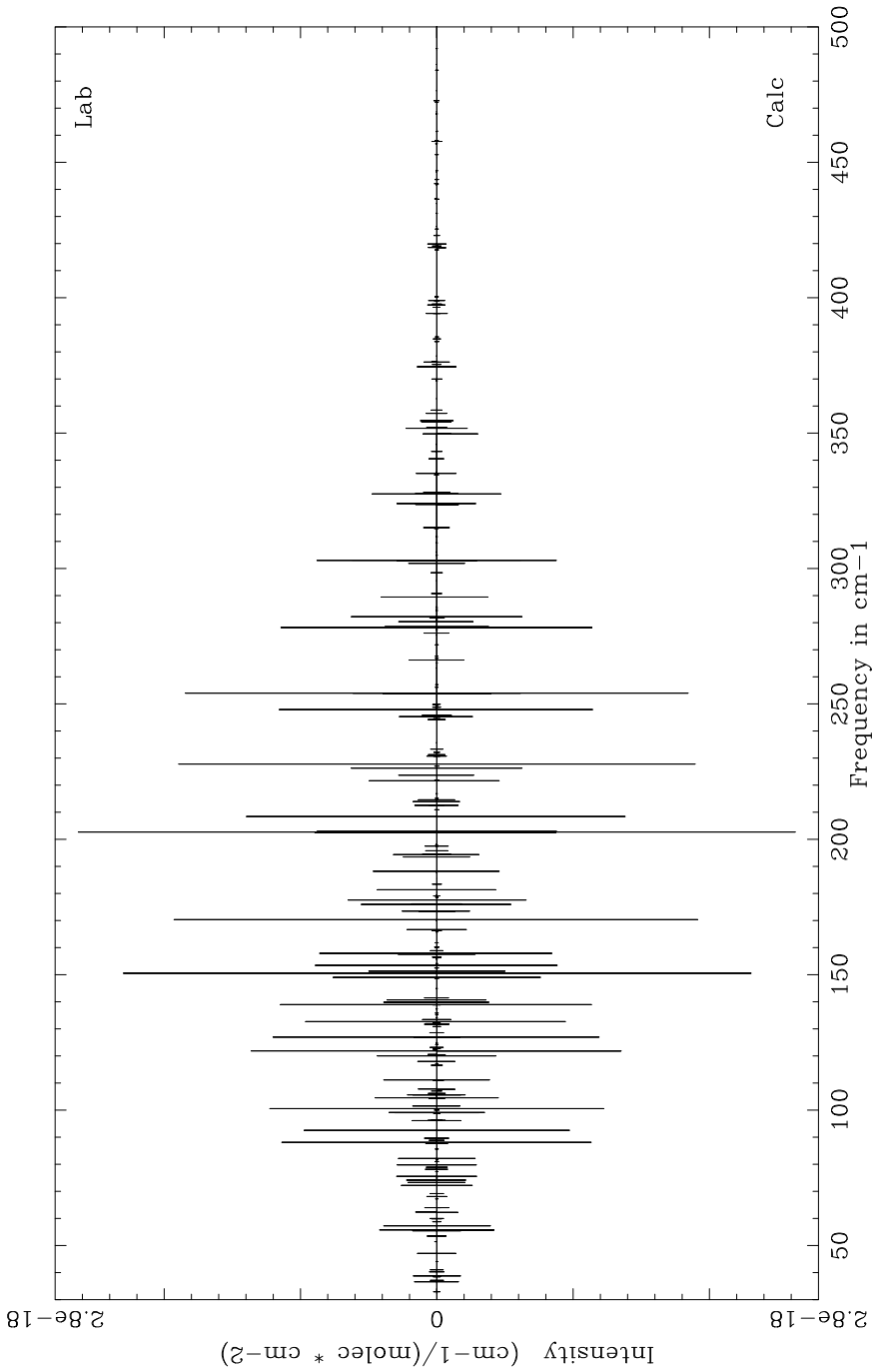

Figure 5.1: Comparison of the water absorption spectrum at T=300K. Upper: laboratory spectrum (Kauppinen *et al*, 1979); lower: generated using the VTP1 linelist. The laboratory spectrum has been normalised to the strongest transition in the calculated spectrum.

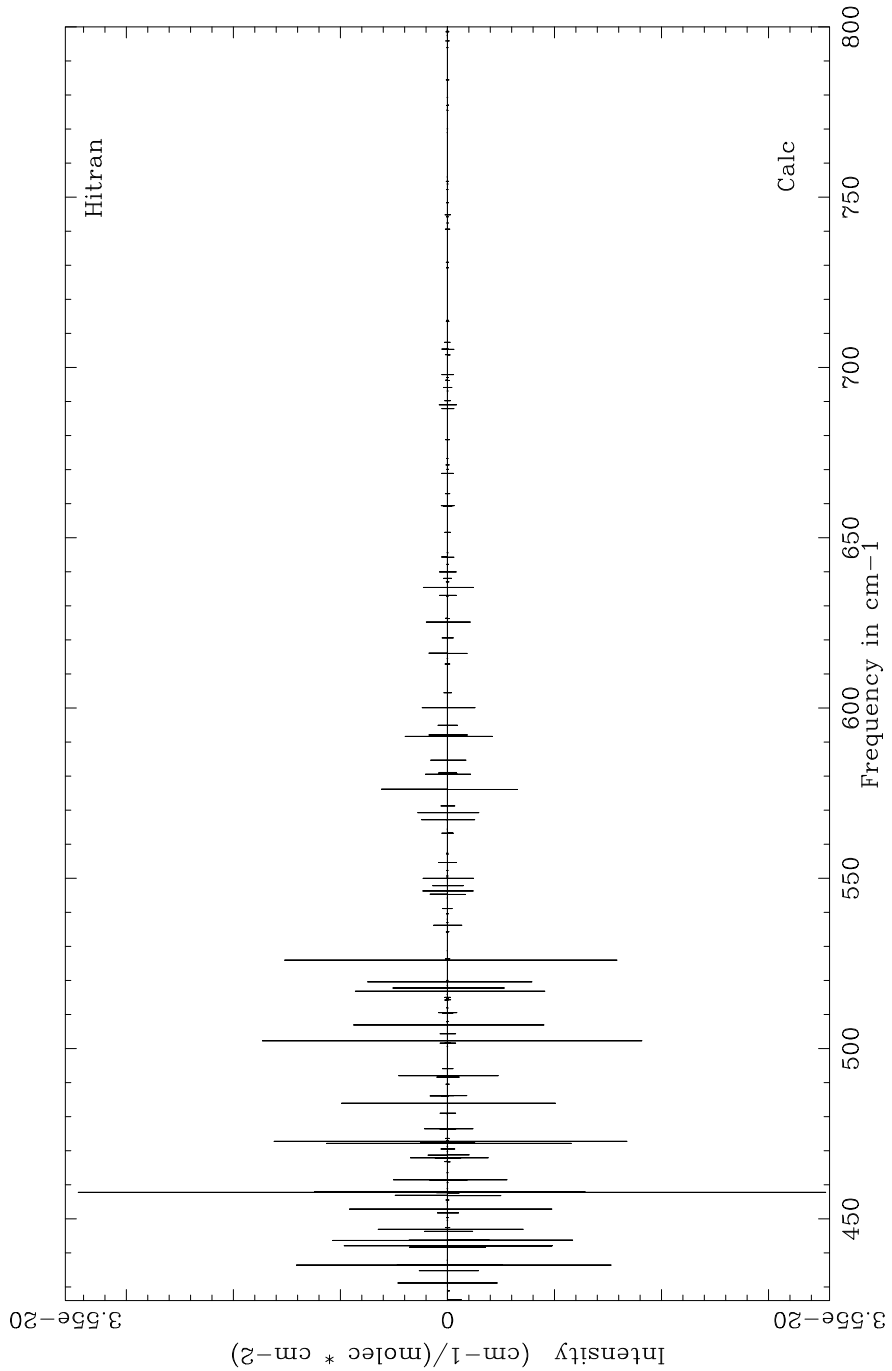

Figure 5.2: Comparison of the calculated water absorption spectrum at T=300K. Upper: generated using the HITRAN database; lower: generated using the VTP1 linelist.

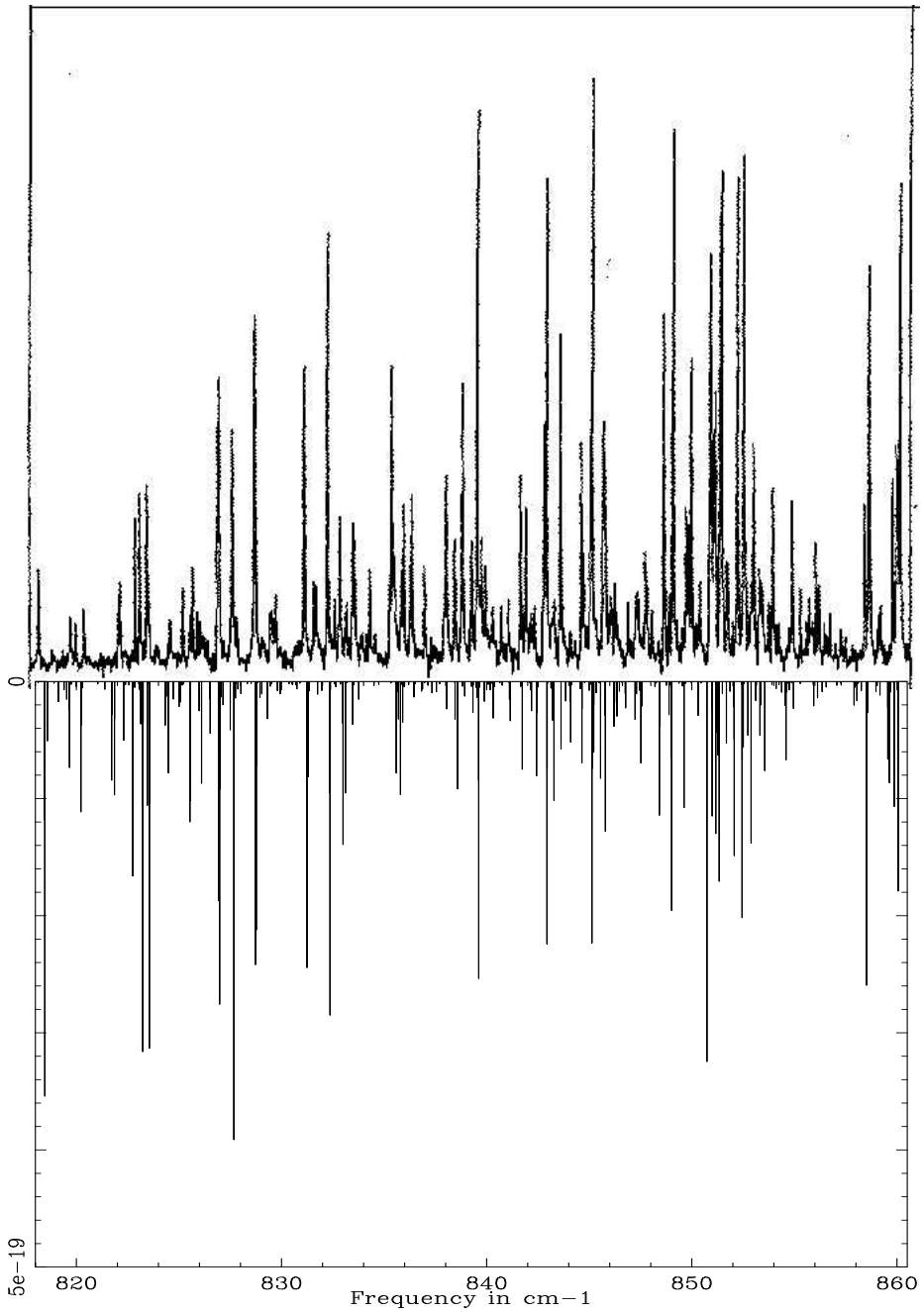

Figure 5.3: H_2O emission spectrum in the pure rotation bands region. Upper: flame spectrum of Mandin *et al* (1992) for which the intensity scale is not uniform as a function of frequency; lower: spectrum generated using the VTP1 linelist and $T = 2000$K, absolute intensities are given in units of $\mathrm{cm}^{-1}/(\mathrm{mol.} * \mathrm{cm}^2)$.

3) T = 2000K (Figure 5.6)

4) T = 2500K (Figure 5.7)

5) T = 3000K (Figure 5.8)

At T = 1000K, the comparison is outstanding: the line positioning is exact within 1%. As the temperature increases we note that VTP1 is missing high vibrational transitions as expected and the line positions agree within 5%.

5.4 Use of VTP1

This water linelist has many applications both in astronomy and in molecular spectroscopy.

Hot water is predicted theoretically to be formed in warm post-shock gas in dissociative and non-dissociative shocks in molecular clouds such as those in Orion. At higher temperature, water is thought to have a dominant role in the cooling process (Draine *et al*, 1983). Furthermore, Neufeld and Melnick (1987) demonstrated that many far-infrared H_2O rotational transitions are potentially observable. In fact, recent ISO observations confirmed the presence of water vapour in star forming regions like Whydrae (Neufeld *et al*, 1996, Barlow *et al*, 1996). Theoretical models for physical and chemical conditions in circumstellar outflows predict that large quantities of water should be produced in oxygen-rich outflows (Chen & Neufeld 1995). Finally, over the last ten years, water maser emission in extragalactic sources has been observed, mainly where nuclear activity was present (Neufeld *et al*, 1994). For analysing, modelling and predicting spectra from all these sources, reliable hot water data like VTP1 are essential.

The entire linelist is available via either our group world wide web page on http: www.tampa.phys.ucl.ac.uk/jonny/ or anonymous ftp to jonny.phys.ucl.ac.uk by looking into the directory pub/astrodata/water/vtp1. The list has been split into 10 files based on frequency in cm^{-1}: for example file w294 contains transitions from 0 to 294 cm^{-1}, file w587 from 294 to 587 cm^{-1} and so on.

Originally, VTP1 was conceived for assigning water lines in the Sunspots and in the

laboratory (see Chapter 6 for further details). However, although quite spectroscopically accurate, the errors in the line positions were not systematic enough for these spectroscopic assignments. This problem was solved by using an *ab initio* potential surface. With this new potential we calculated a new linelist ZVPT described and discussed in the next chapter. ZVPT is less acurate than VTP1 but it is systematic in its errors.

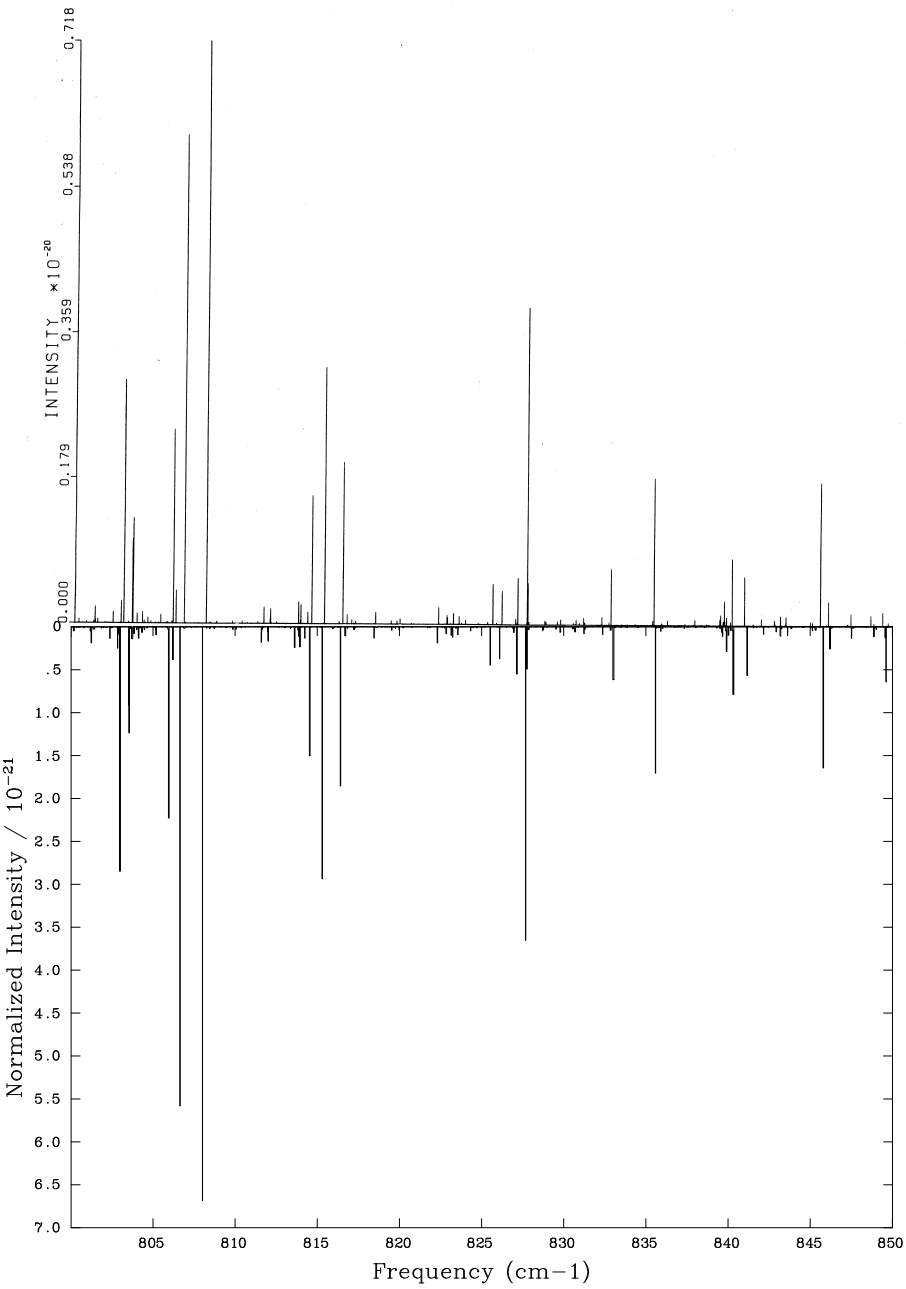

Figure 5.4: Top: HITEMP spectrum at 1000K. The graph has been kindly provided in hardcopy by Rothman (private communications 1996). Bottom: VTP1 spectrum at 1000K. The slight depositioning is not due to difference in frequency but to graphiocal problems in scaling VTP1 to fit a scanned picture of the HITEMP spectrum.

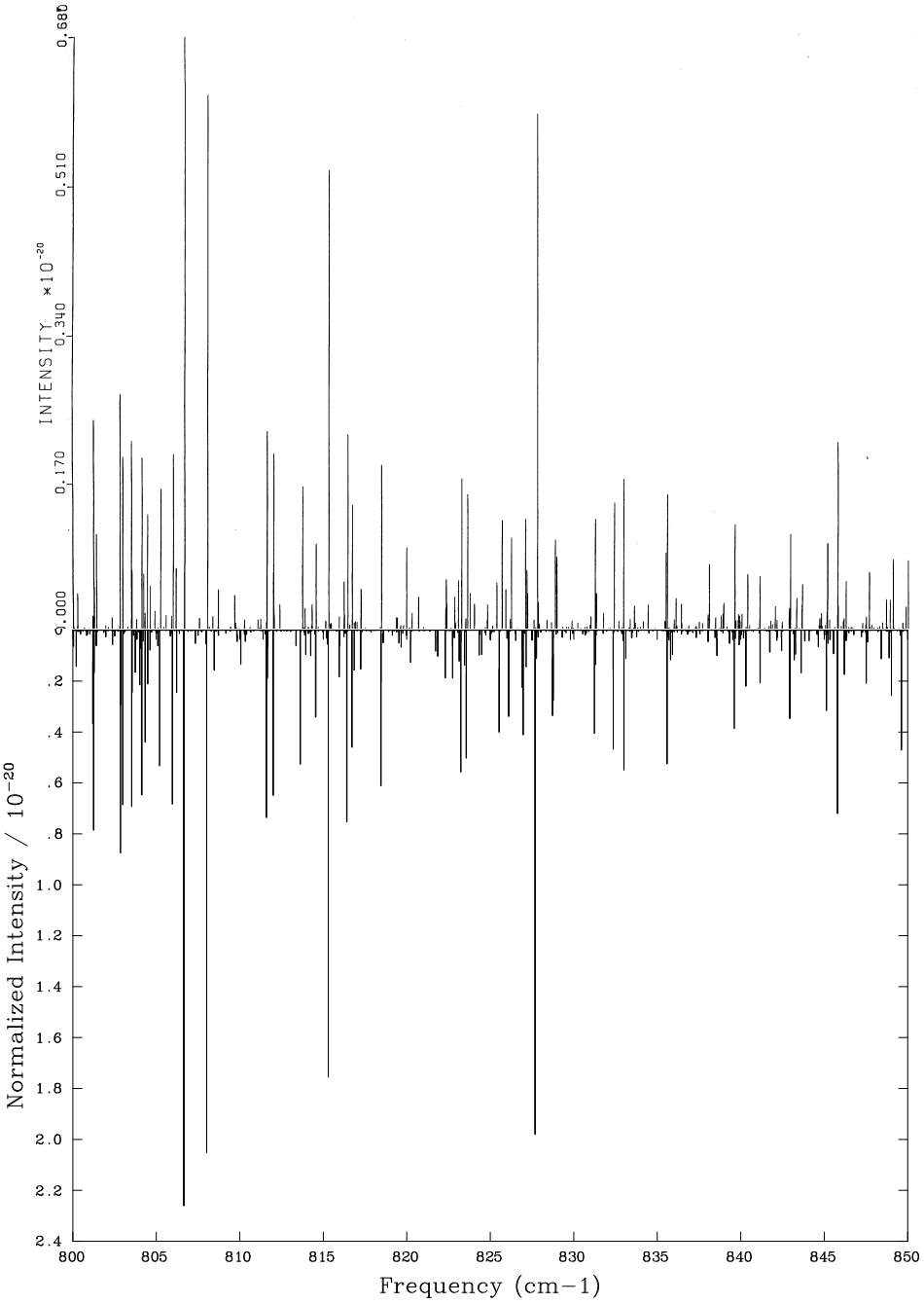

Figure 5.5: Top: HITEMP spectrum at 1500K. Bottom: VTP1 at 1500K.

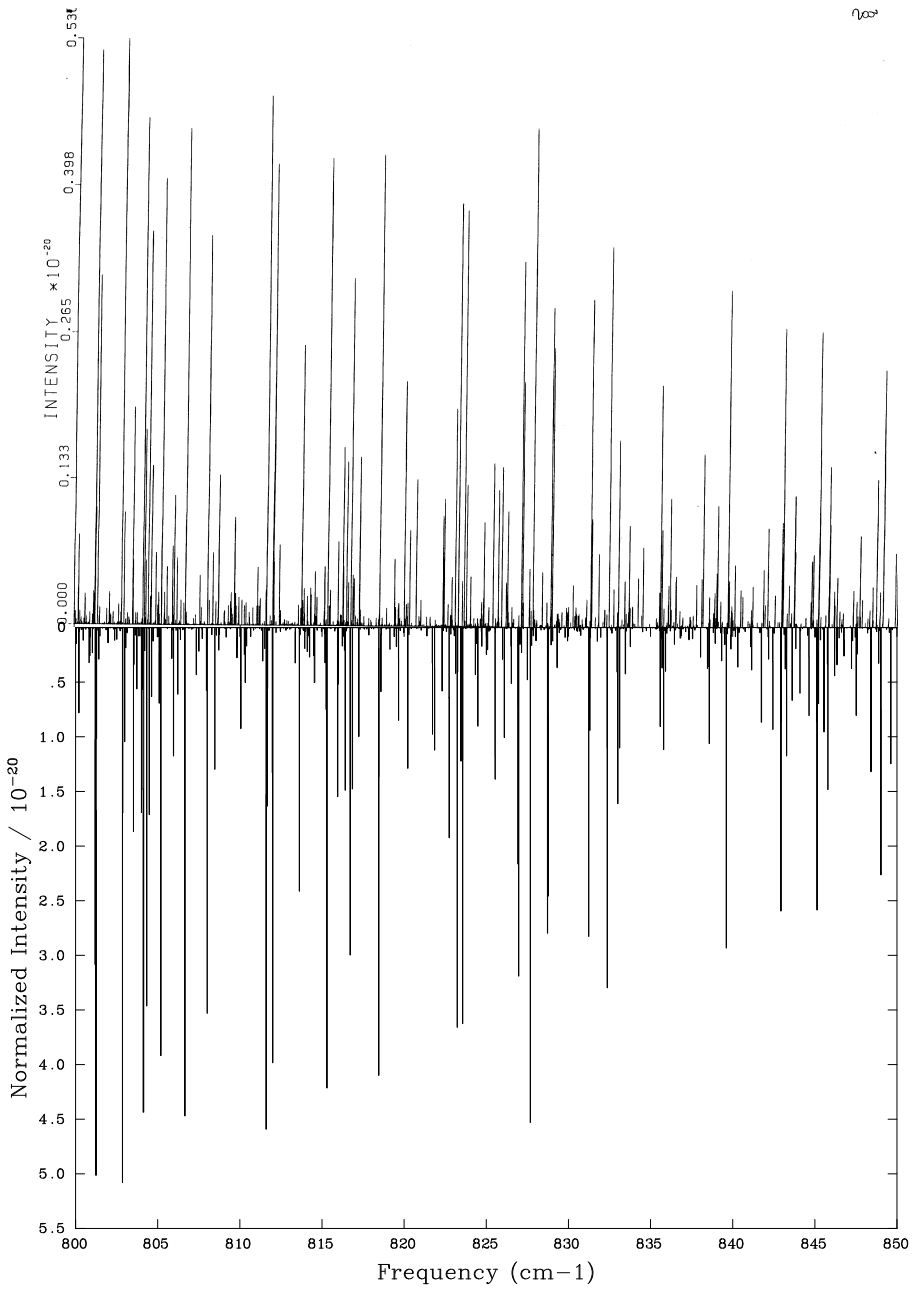

Figure 5.6: Top: HITEMP spectrum at 2000K. Bottom: VTP1 at 2000K.

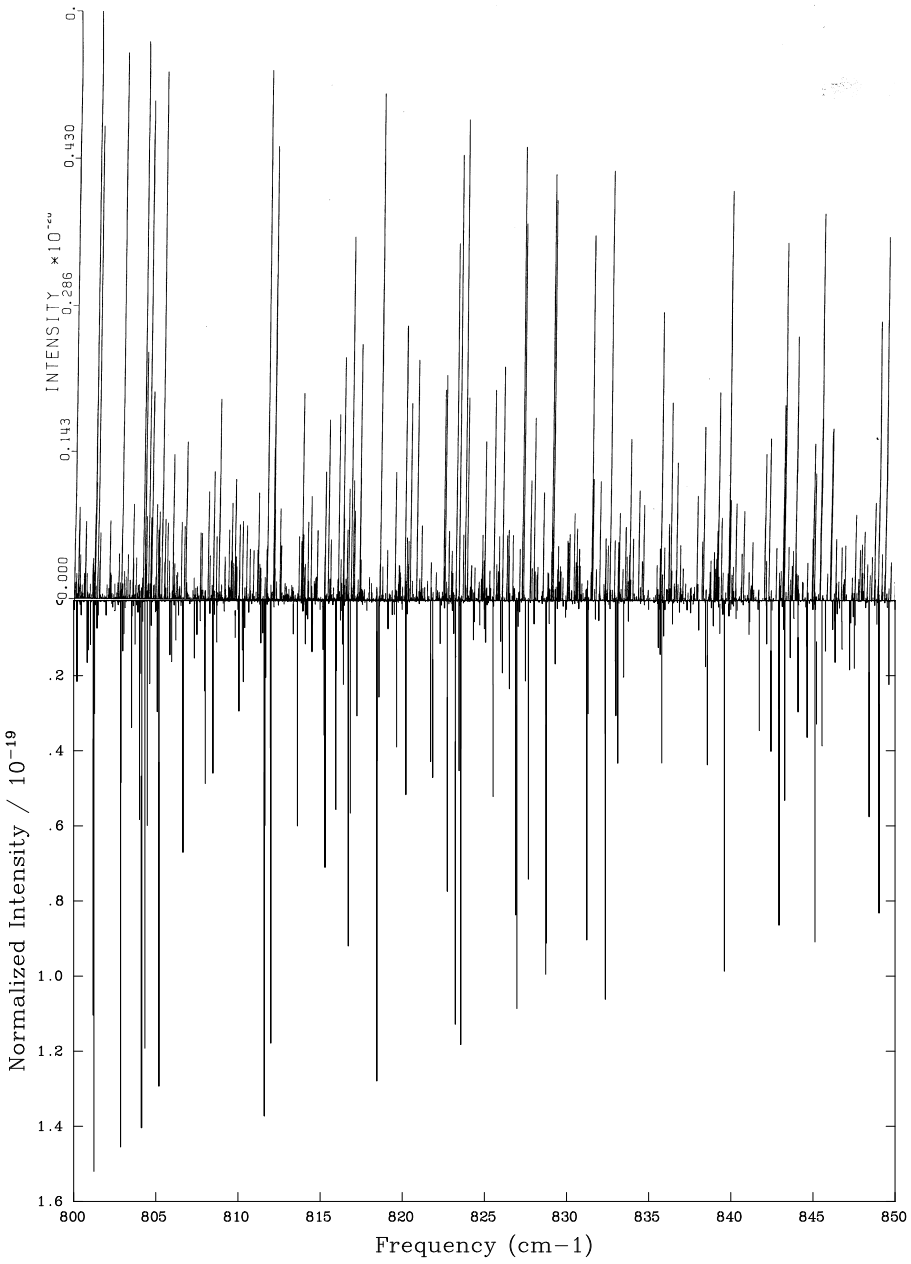

Figure 5.7: Top: HITEMP spectrum at 2500K. Bottom: VTP1 at 2500K.

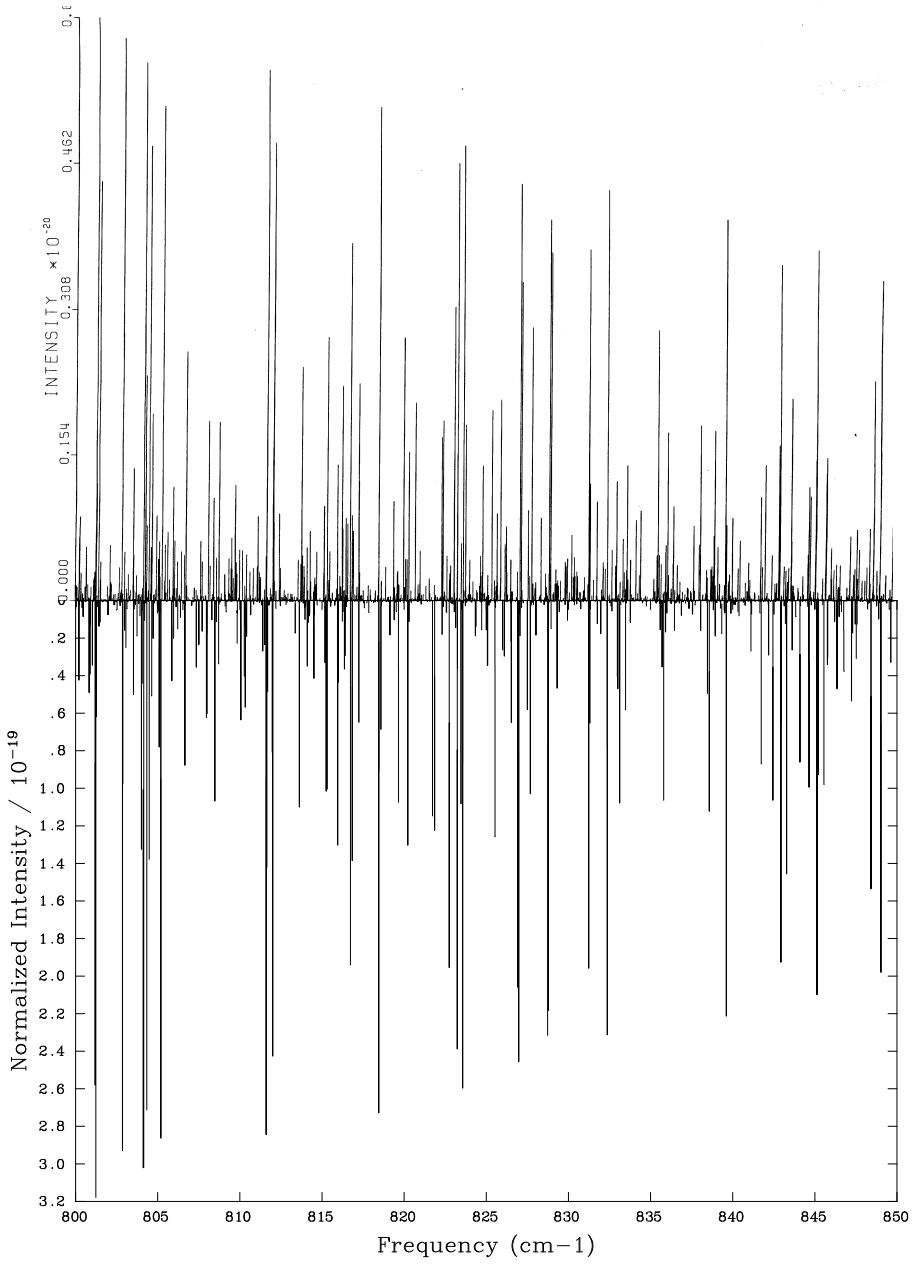

Figure 5.8: Top: HITEMP spectrum at 3000K. Bottom: VTP1 at 3000K.

Table 5.4: A sample of output from the VTP1 water linelist

J"	E"	J′	E′	g	ω	A_{if}
15	7219.7758	16	7219.7664	3	0.00944	0.29297E-14
21	9866.5985	21	9866.5702	1	0.02828	0.17378E-12
23	8181.6862	22	8181.6307	3	0.05549	0.10877E-15
15	9685.0104	15	9684.9441	1	0.06633	0.55787E-17
4	1922.8695	5	1922.7950	1	0.07457	0.56702E-11
17	9028.4692	18	9028.3509	1	0.11832	0.23194E-16
18	8438.5499	19	8438.4201	1	0.12983	0.13021E-12
15	6938.8815	14	6938.7360	3	0.14549	0.15747E-15
4	3598.7126	5	3598.5495	1	0.16308	0.14296E-09
17	9712.2928	16	9712.1121	3	0.18078	0.45226E-21
9	2904.6030	10	2904.4189	1	0.18404	0.48356E-10
18	9945.7933	17	9945.5767	3	0.21652	0.15836E-17
19	8478.8283	18	8478.6024	1	0.22587	0.91786E-16
19	8478.8283	18	8478.6024	1	0.22587	0.91795E-16
16	9106.8766	16	9106.6499	3	0.22671	0.17487E-10
23	7704.5736	23	7704.3268	1	0.24681	0.28430E-12
15	9526.0973	16	9525.8396	1	0.25773	0.62094E-21
16	9814.7779	16	9814.5087	1	0.26919	0.47118E-14
15	9144.5890	15	9144.3109	1	0.27813	0.57340E-19
22	6219.8393	21	6219.5360	3	0.30330	0.17593E-09
18	6581.2302	17	6580.9125	1	0.31771	0.14342E-20
18	6869.0323	17	6868.6956	1	0.33676	0.31519E-14
4	1908.0028	3	1907.6644	1	0.33838	0.60864E-09
15	5339.8335	15	5339.4940	1	0.33945	0.75710E-17
19	6779.2503	18	6778.9063	1	0.34407	0.22194E-15

16	8991.2922	15	8990.9471	1	0.34513	0.19625E-17
18	6869.0323	17	6868.6843	3	0.34800	0.34790E-14
16	9296.4229	17	9296.0269	1	0.39599	0.31366E-13
21	7933.5123	22	7933.1111	3	0.40123	0.61338E-11
20	9926.8347	20	9926.4118	3	0.42282	0.39977E-13

Chapter 6

Computation of the the ZVPT linelist

For the first time, in 1970, Hall identified water lines in Sunspots in the K window (Hall, 1970). Benedict made some water line assignments in Hall's spectra but this work was never completed and published. The next attempt to perform a complete analysis of the Sunspot was by Wallace and Livingston (1992) who published a spectral atlas of a dark sunspot umbra in the region 1970–8640 cm^{-1} (1.16 to 5.1 μm). They obtained umbral spectra with the 1-meter Fourier transform spectrometer on Kitt Peak. They found that the spectra contained large absorption bands of water vapour. This is not very surprising considering that the temperature of the Sunspots is $\sim$ 3200K. They identified many absorption features belonging to the L window using the French laboratory measurements (Flaud *et al*, 1976; Camy-Peyret *et al*, 1977).

Later, Wallace *et al* (1995, 1996) were able to demonstrate that hot water was responsible for the dense lines in the M band (10-20 μm) sunspot spectrum (again collected in an atlas, Wallace *et al*, 1994). These bands have been identified as transitions of water by directly comparing them to high-temperature laboratory emission spectra (Wallace *et al*, 1995). The laboratory spectrum was obtained to confirm that the sunspot features were indeed due to water (Wallace *et al*, 1995). Details of the laboratory emission spectrum

can be found in Polyansky *et al* (1996b) and in Chapter 5. This spectrum has a similar resolution ($\Delta\tilde{\nu} \sim 0.01$ cm^{-1}) to the sunspot spectrum but is much less crowded because of the lower temperature. While many of the water lines in the sunspot spectrum are blended, the lines in the laboratory spectrum are nearly all well resolved. Polyansky *et al* (1996b) assigned some transitions involving high rotational quantum numbers J and K_a to an emission spectrum recorded at 1800 K in the M window. The method used to assign these laboratory spectra was perturbational. In some cases Polyansky *et al* found more than one candidate per line. They underlined that this is due to the limitation of the perturbational methods and pointed out that more accurate variational calculations are needed for better assignments.

Further assignments could also be made with VTP1 but we found that, although accurate, the errors in this linelist were not systematic enough for making reliable assignments. This will be discussed in the course of this chapter. We therefore computed a new linelist employing the very high quality *ab initio* BO potential energy surface by Partridge and Schwenke (PS, Schwenke, 1996). With this new linelist, the M and K windows of hot water in a sunspot have been assigned.

6.1 Parameters employed

The PS potential surface has been corrected for the mass-dependent adiabatic correction to the BO approximation. This correction was included by addition of a mass-dependent *ab initio* adiabatic surface (Zobov *et al*, 1996). An approximate allowance for the non-adiabatic correction was included by the use of an H atom mass of 1.007551 amu, mid-way between that of H and a bare proton (Zobov *et al*, 1996) and an O atom of 15.990526 amu. We employed the dipole surface of Wattson & Rothman (1992) as used for VTP1. Temperature dependent spectra were generated using the adapted version of program SPECTRA (Tennyson *et al*, 1993 and Chapter 4).

We used a DVR grid of 40 points based on Gauss-(associated) Legendre polynomials in the θ coordinate. For the radial coordinates, we used a DVR grid of 21 points with

radial basis set parameters of $r_e = 2.06a_0$, $D_e = 0.14E_h$ and $\omega_e = 0.014E_h$. Again, as for VTP1, this number of grid points is sufficient to obtain good convergence for low–lying vibrational levels.

In the first 'vibrational' step, we diagonalised a series of final secular problems of dimension 1000 from which we retained the lowest 500 eigenvalues and eigenvectors. For given J, the full ro-vibrational problem was solved using a basis of the $150 \times (J+1)$ lowest solutions from the first step.

We calculated energy levels, wavefunctions and dipole transitions from $J = 0$ to $J = 33$ with the following cut-off energies:

1. $J = 0$ to $J = 19$: 12000 cm^{-1}
2. $J = 20$ to $J = 33$: 22000 cm^{-1}

After completion of this work, and after the first assignments of the M window, we realized that higher energies were required in order to assign fully the laboratory spectrum and the infrared solar spectrum. We did not have sufficient Cray time to extend fully the linelist but we computed further energy levels with different cut-off energies according to J. We have therefore computed eigenvalues with energies of up to at least 18000 cm^{-1} for $J \leq 25$; for $J = 25$ this corresponds to the lowest 500 eigenvalues for each symmetry block. For $25 \leq J \leq 33$ eigenenergies up to 23000 cm^{-1} were computed, corresponding to 320 eigenvalues per symmetry block for $J = 33$. These criteria ensured that we covered all the energy levels belonging to the (000), (100), (010), (020), (001), (030) vibrational states. Low K_a states of many higher vibrational bands are also included.

6.2 Tests and comparisons with previous sets of energy levels

We have performed several checks and comparisons between ZVPT and experimental and calculated databases. In particular, we were interested in comparing it with VTP1.

Taking into account the large amount of data we had for VTP1, ZVPT and HITRAN, we have divided our comparison into vibrational bands. For each vibrational band, we compared their energy levels. Tables 6.1 and 6.2 show some comparisons for few energy levels belonging to the (010) and (100) vibrational bands.

Table 6.1 lists the energy levels belonging to (010) with rotational levels from J=10 to J=15. The table lists only 3 levels per J. This table is complemented with Figure 6.1 where the differences between linelists are quantized. Table 6.2 gives only the difference between HITRAN and ZVPT and HITRAN and VTP1 from $J = 0$ to $J = 17$ for the (100) vibrational state. VTP1, as expected, is the most accurate. Figure 6.1 shows the accuracy curves for VTP1 and ZVPT. The number of levels chosen for each J depended on the number of energy levels available in the HITRAN database. Within each J we have averaged the absolute difference between each calculated linelist and HITRAN. Both linelists show non-linearity in their errors with respect to HITRAN so, at first sight, since more spectroscopically accurate, VTP1 could be considered the best one for assignments.

However, we note that, due to the incompleteness of HITRAN together with the possibility that levels from different branches might be of different accuracy, this statistic could be biased. Therefore we have also plotted the same curve for each J for energy levels belonging to *one* branch only. A branch is a set of levels defined by $(v_1,v_2,v_3)J_{K_aK_c}$ for which J varies but K_a or K_c is constant. In Figure 6.2 we have chosen $K_c = J$. In fact, although not spectroscopically accurate, Figure 6.2 shows that ZVPT is more systematic in its inaccuracy: the error increases very slowly and systematically with J within the same branch. With VTP1 the error distribution is much steeper, although less erratic than that found with PS (see Figure 7.6 in Chapter 7). Note that for $J = K_c \sim 10$, the ZVPT results appear erratic but this is almost certianly due to mis–assignments in HITRAN (Polyansky *et al*, 1997d)

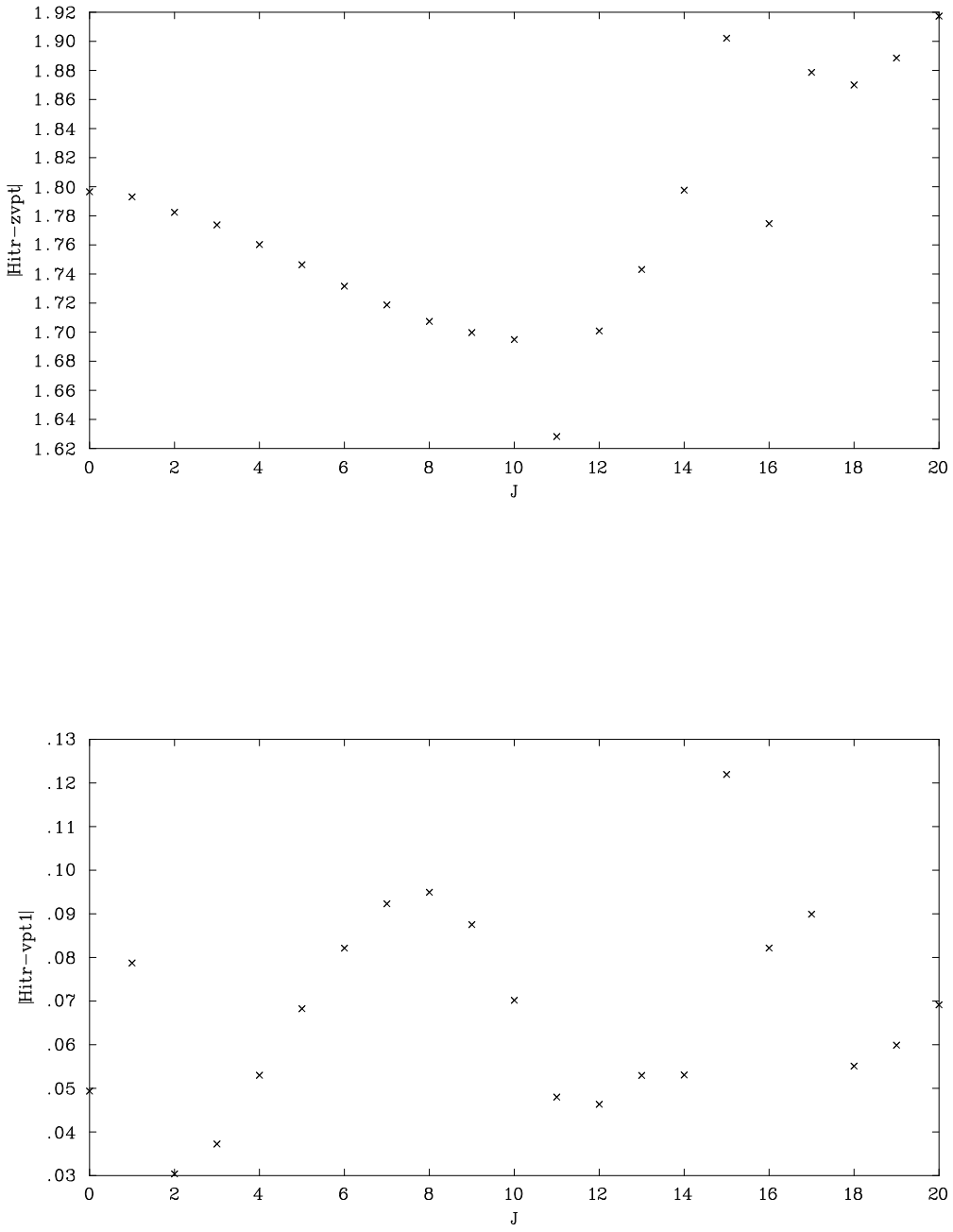

Figure 6.1: Top: $|ZVPT - HITRAN|$ in cm^{-1} as a function of J. Bottom: $|VTP1 - HITRAN|$ in cm^{-1} as a function of J. The energy levels belong to the (0,1,0) vibrational state. The difference plotted for each J corresponds to the averaged differences between energy levels belonging to each J.

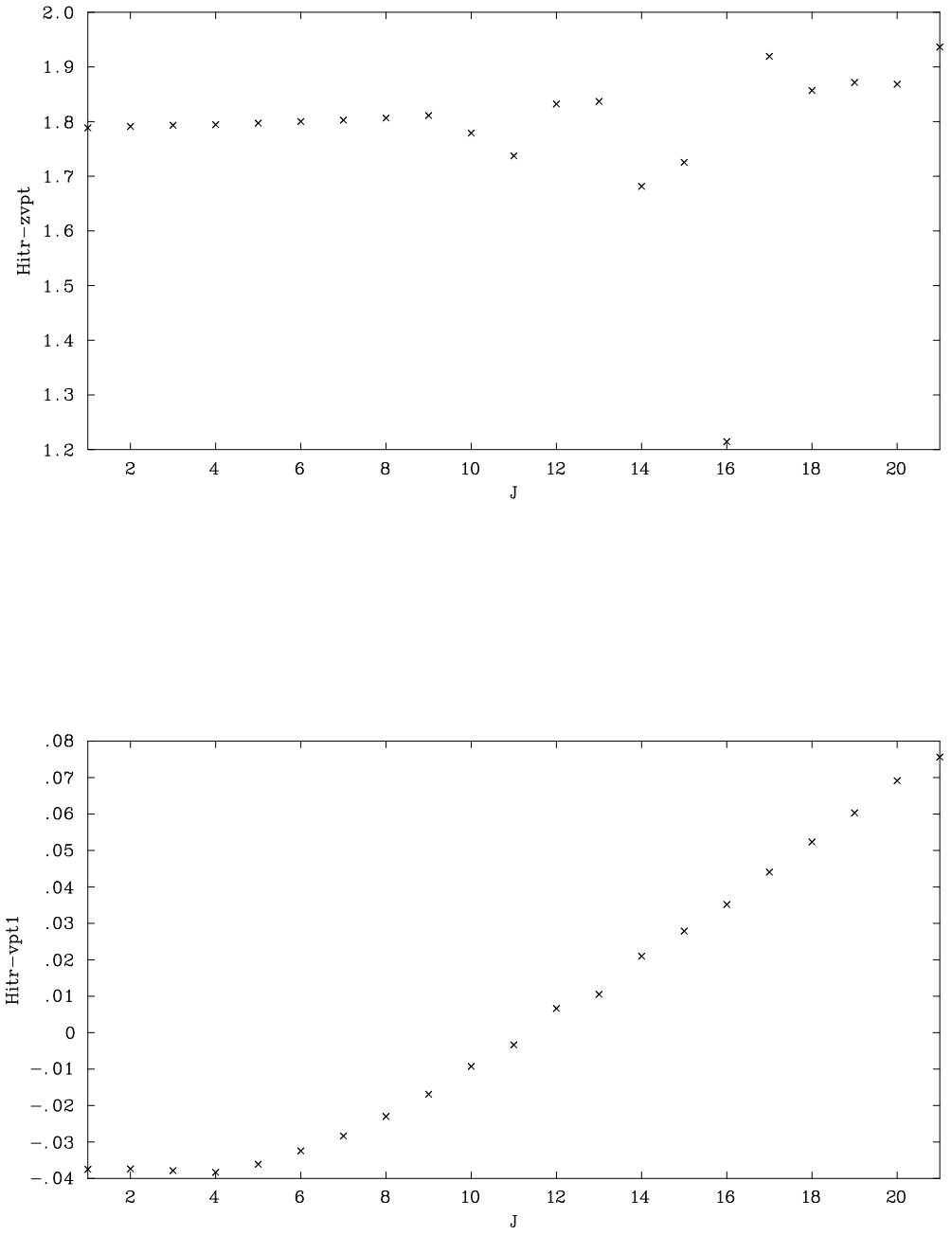

Figure 6.2: Top: $ZVPT - HITRAN$ in cm^{-1} as a function of J. Bottom: $VTP1 - HITRAN$ in cm^{-1} as a function of J for energy levels belonging to the (0,1,0) vibrational state for the branch where $K_c = J$.

Table 6.1: Comparison of energy levels belonging to the (010) vibrational state from different computed databases

J	K_a	K_c	ZVPT	VTP1	HITRAN
10	0	10	2706.91565	2705.08883	2705.09700
10	2	8	3060.20263	3058.35820	3058.40100
10	4	6	3255.52495	3253.70387	3253.73900
11	2	9	3316.65881	3314.83215	3314.85700
11	4	7	3537.68307	3535.82473	3535.87100
11	6	5	3834.83576	3833.20847	3833.14600
12	0	12	3146.40171	3144.57608	3144.57300
12	2	10	3589.47059	3587.65823	3587.66900
12	4	8	3845.24801	3843.36817	3843.41400
13	0	13	3392.96713	3391.14091	3391.13100
13	2	11	3878.89557	3877.09326	3877.09000
13	4	9	4175.89874	4174.01490	4174.03800
14	0	14	3657.33352	3655.50566	3655.48600
14	2	12	4185.20153	4183.40540	4183.39200
14	4	10	4527.11811	4525.24574	4525.24300
15	0	15	3939.43332	3937.60268	3937.57500
15	2	13	4508.55433	4506.76122	4506.73700
15	4	11	4896.47971	4894.62885	4894.58300

Table 6.2: The σ of ZVPT and VTP1 with respect to Hitran for the (100) vibrational state.

J	K_a	K_c	ZVPT-HITRAN	VTP1-HITRAN
0	0	0	3.35499	0.08315
1	0	1	3.35766	0.07895
1	1	1	3.34751	0.07700
1	1	0	3.35519	0.14180
2	1	2	3.35039	0.06970
2	1	1	3.35600	0.06545
2	2	1	3.32491	0.06050
3	2	2	3.33114	0.04823
4	1	4	3.35731	0.04356
4	1	3	3.37197	0.02552
4	2	3	3.33906	0.03125
5	2	4	3.34763	0.00914
6	1	6	3.36444	0.00371
6	2	5	3.35452	-0.01916
7	2	6	3.36137	-0.05180
8	1	8	3.37266	-0.04960
8	1	7	3.37766	-0.08785
8	2	7	3.36797	-0.08844
9	2	8	3.37399	-0.13054
10	1	10	3.38489	-0.11898
10	1	9	3.38241	-0.16367
10	2	9	3.37971	-0.18218
11	1	11	3.39337	-0.17343
11	2	10	3.38796	-0.25536

12	2	10	3.41804	-0.34991
12	1	12	3.36279	0.00423
12	3	10	3.14363	0.68266
12	1	11	3.40309	-0.27607
12	3	9	3.48602	-0.52883
12	2	11	3.36725	-0.59196
12	4	9	3.41011	-0.20132
13	0	13	3.39856	-0.18296
13	2	11	3.42792	-0.42798
13	1	13	3.41826	-0.16757
13	3	11	3.40279	-0.11598
13	5	9	3.43236	-0.29794
13	1	12	3.33719	-0.66216
13	3	10	3.49041	-0.59779
13	5	8	3.51324	-0.63173
13	2	12	3.38787	-0.14773
13	4	10	3.43077	-0.27275
13	6	8	2.98036	-0.05878
14	0	14	3.41722	-0.23236
14	2	12	3.44767	-0.64869
14	4	10	3.87307	-0.88119
14	6	8	3.43938	-0.59232
14	1	14	3.41557	-0.23475
14	3	12	3.42089	-0.26452
14	5	10	3.44933	-0.42004
14	7	8	3.23293	-0.28916
14	1	13	3.40627	-0.22196
14	3	11	3.54840	-0.63729

14	5	9	3.59607	-0.80438
14	7	7	3.27207	-0.34095
14	2	13	3.41217	-0.24768
14	4	11	3.45255	-0.34451
14	6	9	3.25585	0.03827
14	8	7	3.20554	-0.29179
15	0	15	3.42548	-0.28313
15	2	13	3.42538	-0.16850
15	4	11	4.12775	-0.84036
15	6	9	3.54915	-0.85441
15	8	7	3.25088	-0.36030
15	1	15	3.42626	-0.28313
15	3	13	3.45185	-0.33467
15	5	11	3.53067	-0.46675
15	7	9	3.12800	-0.45429
15	1	14	3.42690	-0.30309
15	3	12	3.50868	-0.88934
15	5	10	3.65501	-0.95087
15	7	8	3.35203	-0.47752
15	2	14	3.45096	-0.28581
15	6	10	3.54920	-0.18937
16	0	16	3.44130	-0.32642
16	1	16	3.44165	-0.32642
16	7	10	3.19907	-0.27532
16	1	15	3.43259	-0.37116
16	2	15	3.44339	-0.36264
16	6	11	3.68342	-0.35296
17	0	17	3.46063	-0.36801

17	1	17	3.46075	-0.36801

6.3 Applications: Sunspots' assignments

With the aid of ZVPT we have been able to assign the infrared spectrum of hot water in a sunspot. This was done using intensity information in the calculations and spectra, and by following branches so that systematic errors in the calculations were removed. The atlases, published by Wallace *et al* (1994, 1995, 1996), cover from mid–to near infrared. Many regions are affected by Telluric and other species (such as SiO) absorption. We have concentrated on M and K bands. The regions where most of the assignments were made are: (i) 750–1010 cm^{-1} (10–13 μm) and (ii) 4600–5100 cm^{-1} (2.17–1.96 μm), where the spectrum is dominated by hot water absorption. In total, we have assigned 1687 sunspot lines in the M window and 485 in the K window.

These assignments were performed by Polyansky *et al* (1997a,b,c) in stages. First, all the transitions between energy levels known previously were assigned. These assignments were called trivial. Second, we computed ZVPT spectra at the appropriate temperature to assign the rest of the spectrum. The sunspot spectrum was divided into four echelons on the basis of intensity: strong transitions with 6 – 8% absorption; medium transitions with 4 – 6% absorption; weak absorptions with 2 – 4% absorption; and poorly resolved structure at the less than 2% absorption level. Most of the assignments have been made in the strong and medium transitions, but we believe that extension of our calculations to higher vibrational states will allow assignment of the weaker transitions. Third, the spectrum was analysed in terms of branches. The use of branches was crucially seeded by known data at low temperature. In fact, with ZVPT, once one level of a particular branch was assigned, the next member of a branch could be predicted with an accuracy of ~ 0.02 cm^{-1}. For transitions observed both in laboratory and in Sunspots, a crude confirmation of the assignments was obtained by comparing the ratios of line intensities with that estimated from Boltzmann distributions at the appropriate temperatures. Figs 6.3 to 6.6

show such assignments for several regions of the M window. Figure 6.7 show an example of K window assignment.

Figure 6.3 shows the region 771.5–775.5 cm^{-1} where transitions belonging to three distinct vibrational bands can be observed.

The region covered by Figure 6.4 is 841–849.5 cm^{-1}. We have an example of the so called "splitting": two high K_a transitions, which one would expect to be strongly overlapped, are instead split, presumably by Coriolis interactions with levels of a different vibrational state (Polyansky *et al*, 1997d).

In Figure 6.5, the region 872.5–875.3 cm^{-1} is shown. With this Figure we illustrate the congested nature of the sunspot spectrum.

Figure 6.6 (924.2–925.6 cm^{-1}) shows a region of the spectrum that is sensitive to higher water levels and therefore many of the lines that we assign are not seen in the cooler laboratory spectrum.

Figure 6.7 (4890–4930 cm^{-1}) is an example of the transitions assigned in the K window. It can be seen that these assignments include all of the strong absorption features in the spectral region of interest. Of the 10 vibrational bands for which transitions have been assigned, only (011) − (000) and (021) − (010) have been observed previously in the laboratory or in space (Rothman *et al*, 1992).

Full details of the assignments can be found in Polyansky *et al* (1997a, 1997b, 1997c).

Summaries of the assignments are shown in Tables 6.3 and 6.4. They show that the range of previously known experimental data on this system has been greatly extended.

ZVPT has proved to be already extremely valuable. This linelist, like VTP1, will shortly be available on the web and we hope it will fulfill many spectroscopic needs.

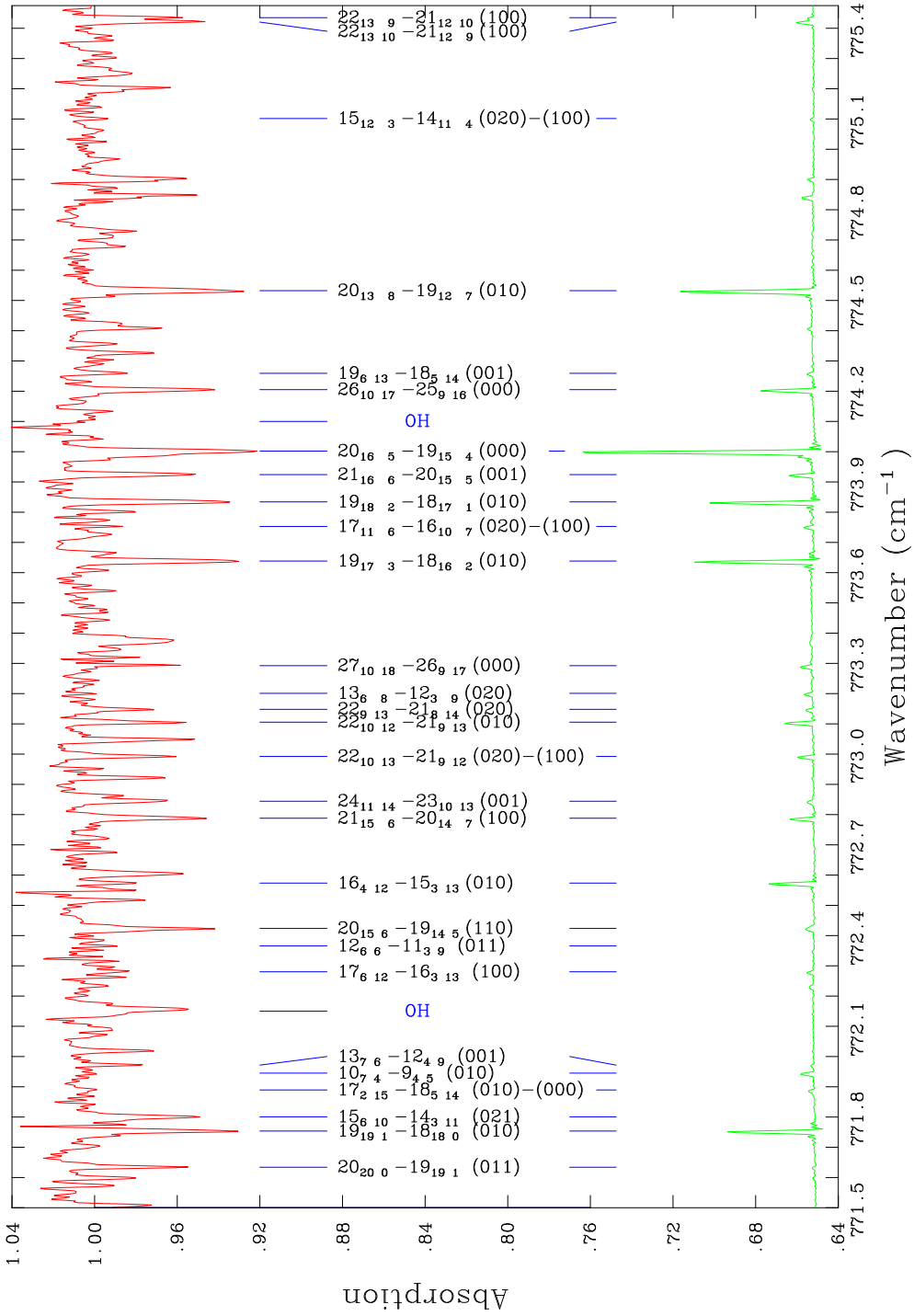

Figure 6.3: Top: part of the sunspot spectrum of Wallace *et al* (1995). The region covered is from 771.5 to 775.5 cm^{-1}. Quantum number assignments, given as $J_{K_aK_c}$ (upper)–$J_{K_aK_c}$ (lower) for various vibrational states (labelled using standard notation $(v_1v_2v_3)$), are marked. Bottom: the corresponding part of the laboratory spectrum (Polyansky *et al*, 1996b). For convenience, we have normalized the intensity.

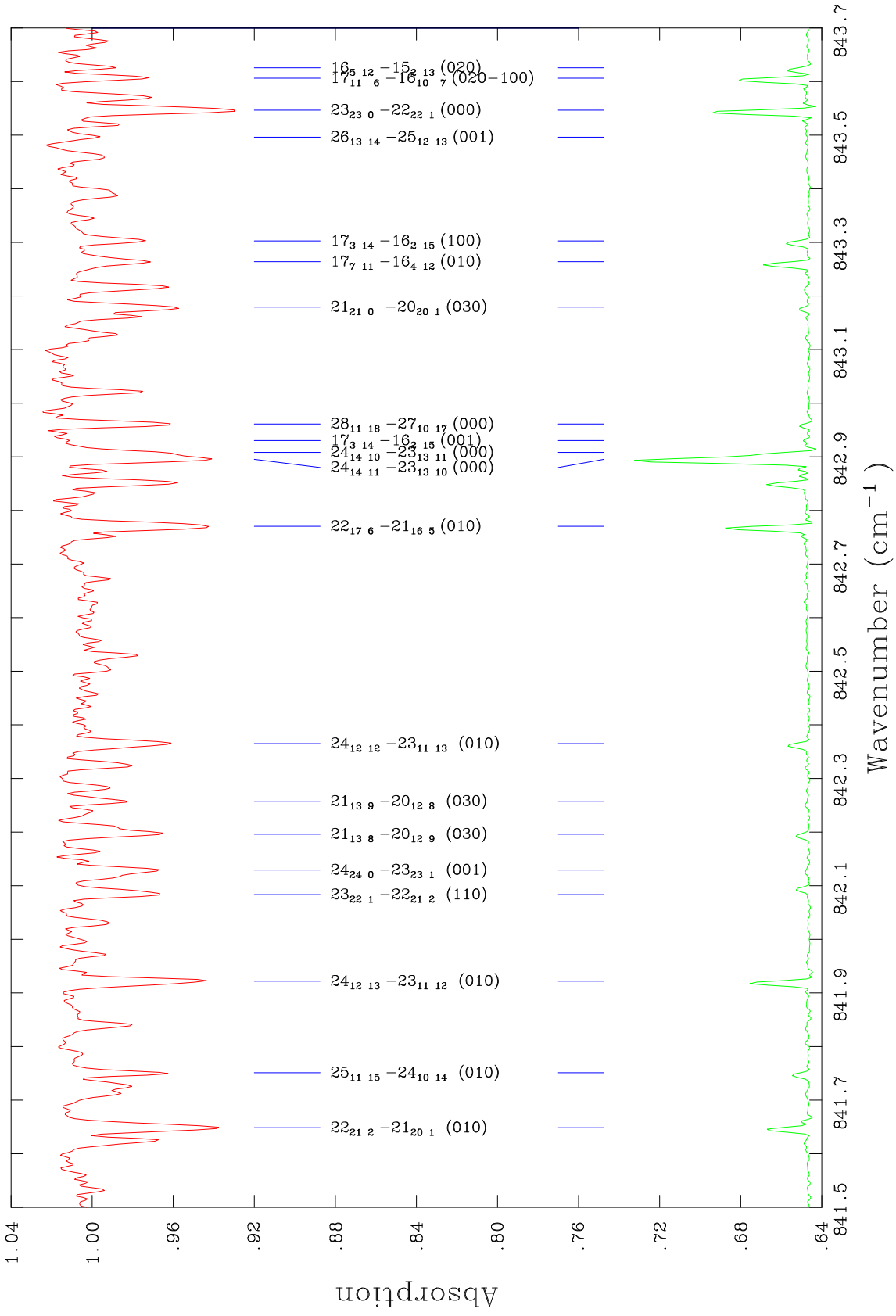

Figure 6.4: Top: part of the sunspot spectrum of Wallace *et al* (1995) from 841.5 to 849.5 cm^{-1}. Bottom: the corresponding laboratory spectrum.

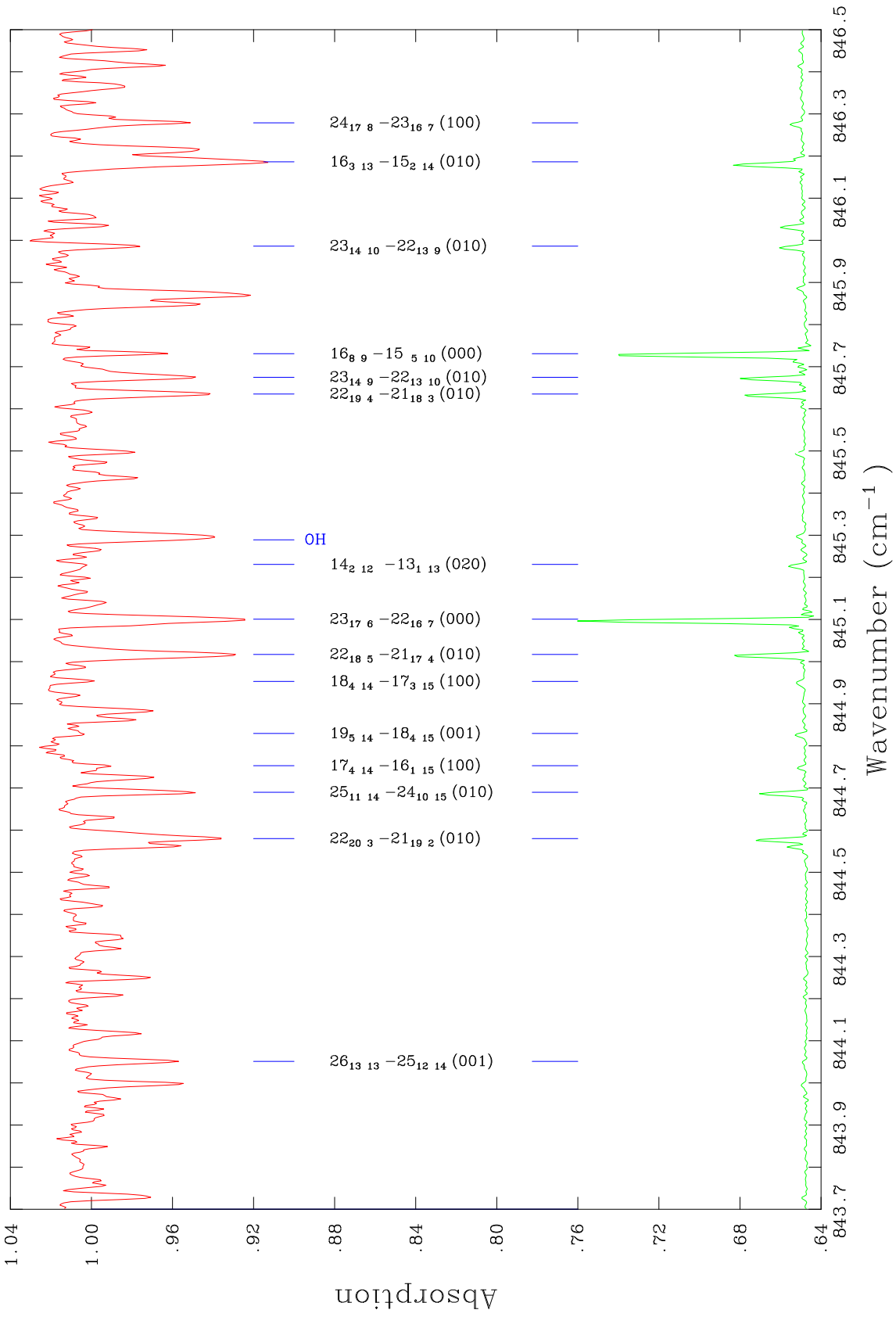
$24_{17\ 8} - 23_{16\ 7}$ (100)
$16_{3\ 13} - 15_{2\ 14}$ (010)
$23_{14\ 10} - 22_{13\ 9}$ (010)
$16_{8\ 9} - 15_{5\ 10}$ (000)
$23_{14\ 9} - 22_{13\ 10}$ (010)
$22_{19\ 4} - 21_{18\ 3}$ (010)
OH
$14_{2\ 12} - 13_{1\ 13}$ (020)
$23_{17\ 6} - 22_{16\ 7}$ (000)
$22_{18\ 5} - 21_{17\ 4}$ (010)
$18_{4\ 14} - 17_{3\ 15}$ (100)
$19_{5\ 14} - 18_{4\ 15}$ (001)
$17_{4\ 14} - 16_{1\ 15}$ (100)
$25_{11\ 14} - 24_{10\ 15}$ (010)
$22_{20\ 3} - 21_{19\ 2}$ (010)
$26_{13\ 13} - 25_{12\ 14}$ (001)
Absorption
1.04
1.00
.96
.92
.88
.84
.80
.76
.72
.68
.64
Wavenumber (cm^{-1})
843.7
843.9
844.1
844.3
844.5
844.7
844.9
845.1
845.3
845.5
845.7
845.9
846.1
846.3
846.5

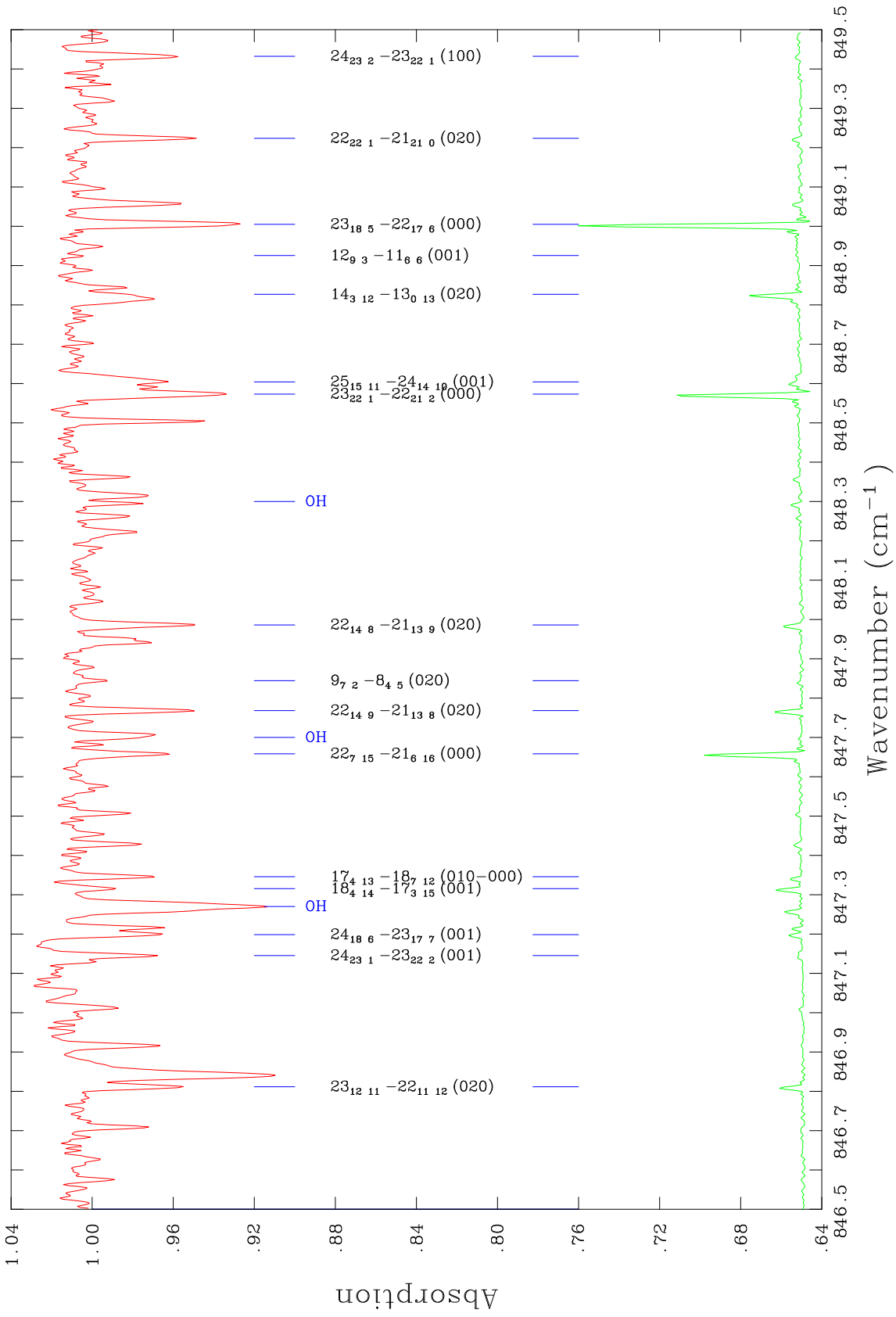
$24_{23\ 2} - 23_{22\ 1}$ (100)
$22_{22\ 1} - 21_{21\ 0}$ (020)
$23_{18\ 5} - 22_{17\ 6}$ (000)
$12_{9\ 3} - 11_{6\ 6}$ (001)
$14_{3\ 12} - 13_{0\ 13}$ (020)
$25_{15\ 11} - 24_{14\ 10}$ (001)
$23_{22\ 1} - 22_{21\ 2}$ (000)
OH
$22_{14\ 8} - 21_{13\ 9}$ (020)
$9_{7\ 2} - 8_{4\ 5}$ (020)
$22_{14\ 9} - 21_{13\ 8}$ (020)
OH
$22_{7\ 15} - 21_{6\ 16}$ (000)
$17_{4\ 13} - 18_{7\ 12}$ (010−000)
$18_{4\ 14} - 17_{3\ 15}$ (001)
OH
$24_{18\ 6} - 23_{17\ 7}$ (001)
$24_{23\ 1} - 23_{22\ 2}$ (001)
$23_{12\ 11} - 22_{11\ 12}$ (020)
Absorption
1.04
1.00
.96
.92
.88
.84
.80
.76
.72
.68
.64
846.5
846.7
846.9
847.1
847.3
847.5
847.7
847.9
848.1
848.3
848.5
848.7
848.9
849.1
849.3
849.5
Wavenumber (cm^{-1})

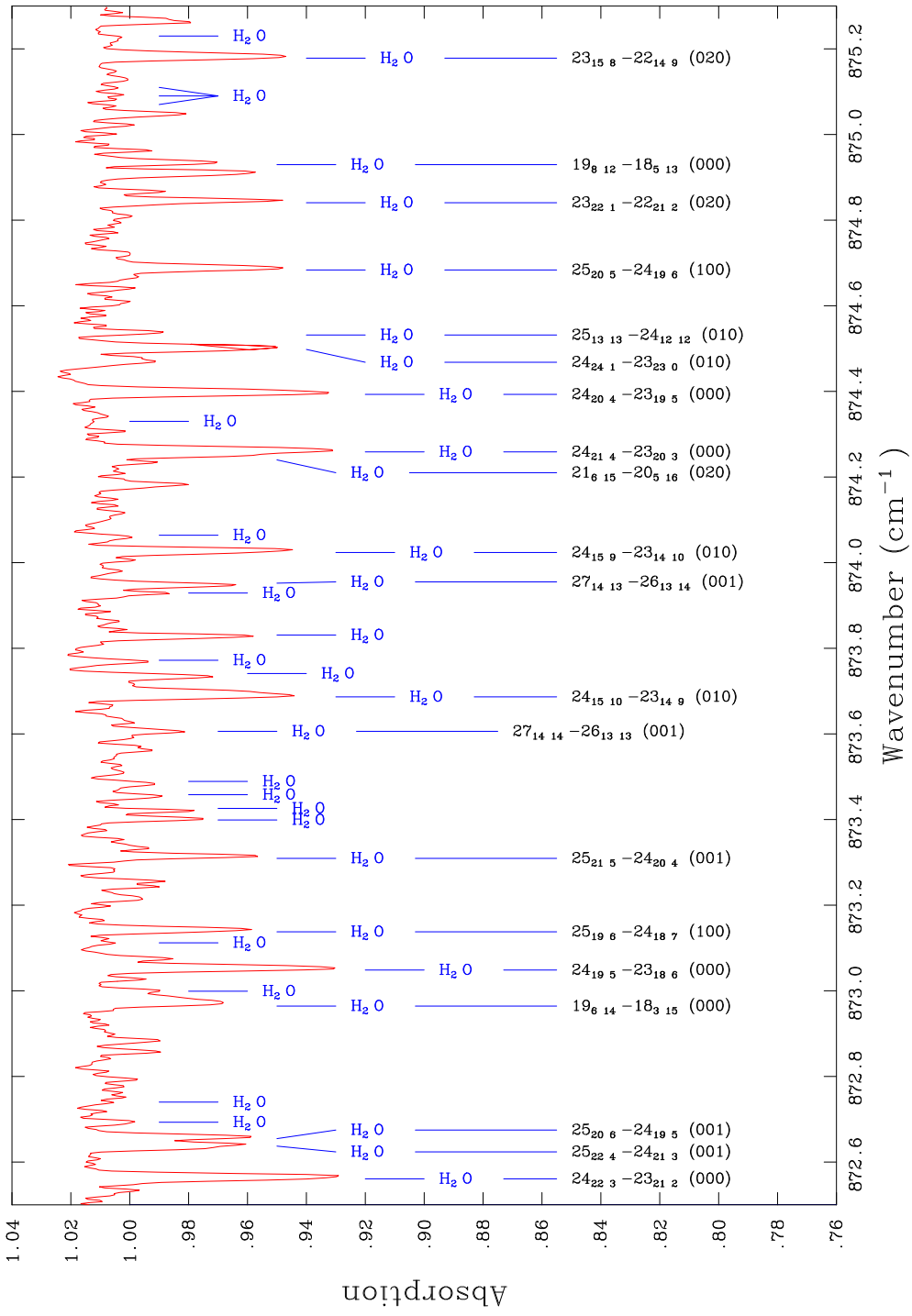

Figure 6.5: Part of the sunspot spectrum of Wallace *et al* from 872.5 to 875.3 cm^{-1} region. Features previously associated with water by comparison with laboratory spectra are labelled H_2O.

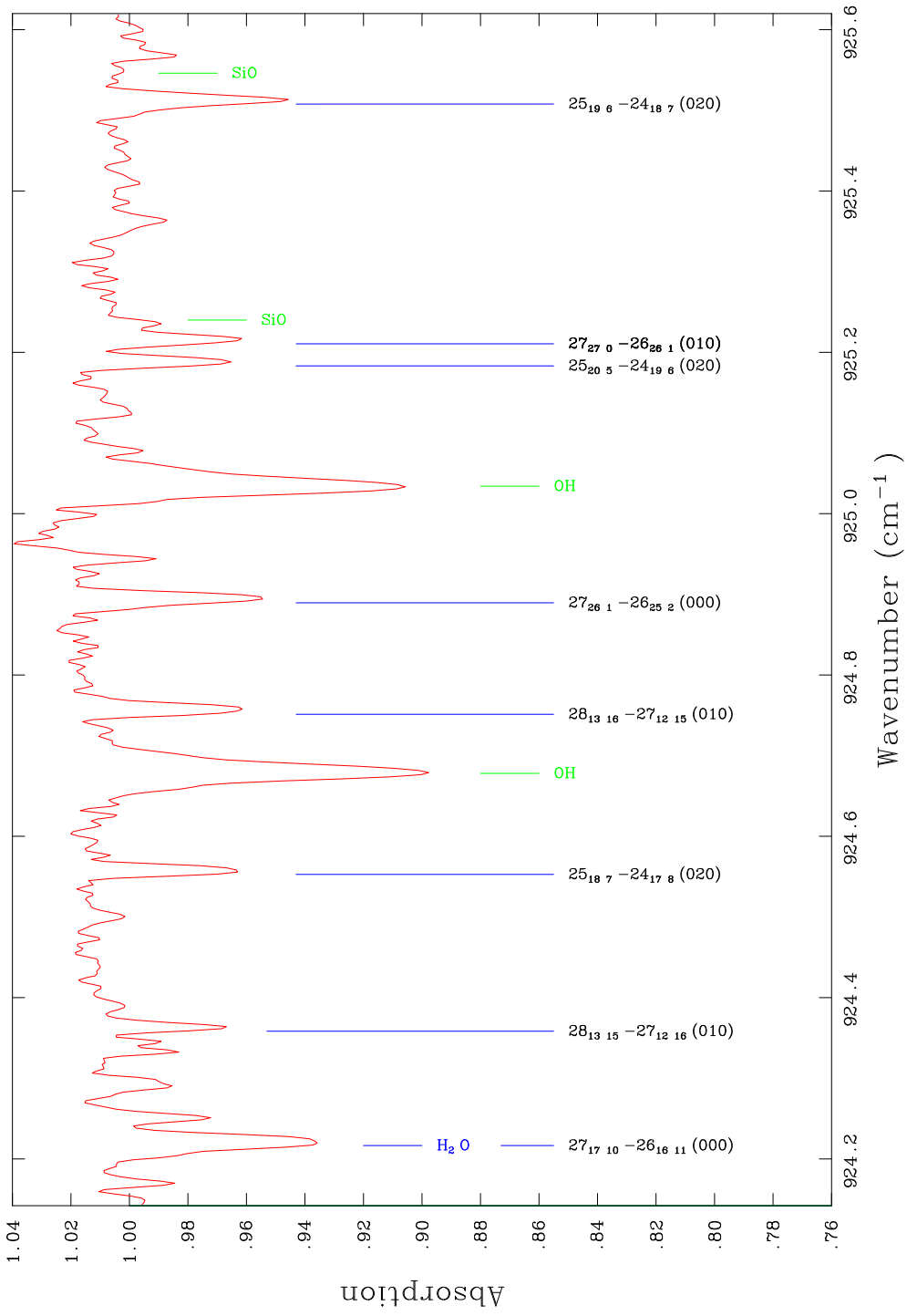

Figure 6.6: Part of the sunspot spectrum of Wallace *et al* from 984.2 to 925.6 cm^{-1}. The only feature previously associated with water by comparison with laboratory spectra is labelled 'H_2O'.Assignments for the features of 'SiO' and 'OH' are well known.

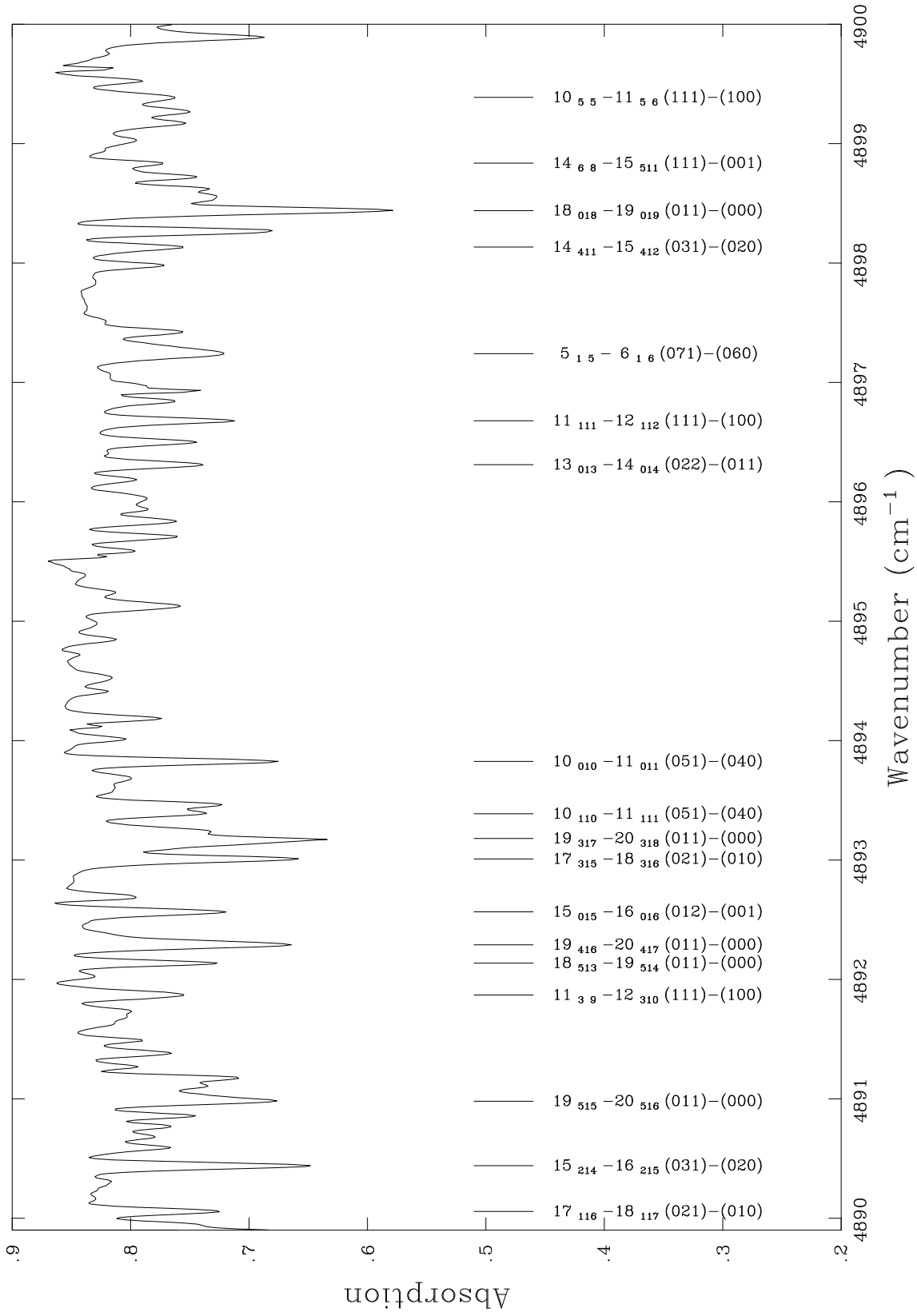

Figure 6.7: Part of the sunspot spectrum of Wallace *et al* from 4890 to 4900 cm^{-1}.

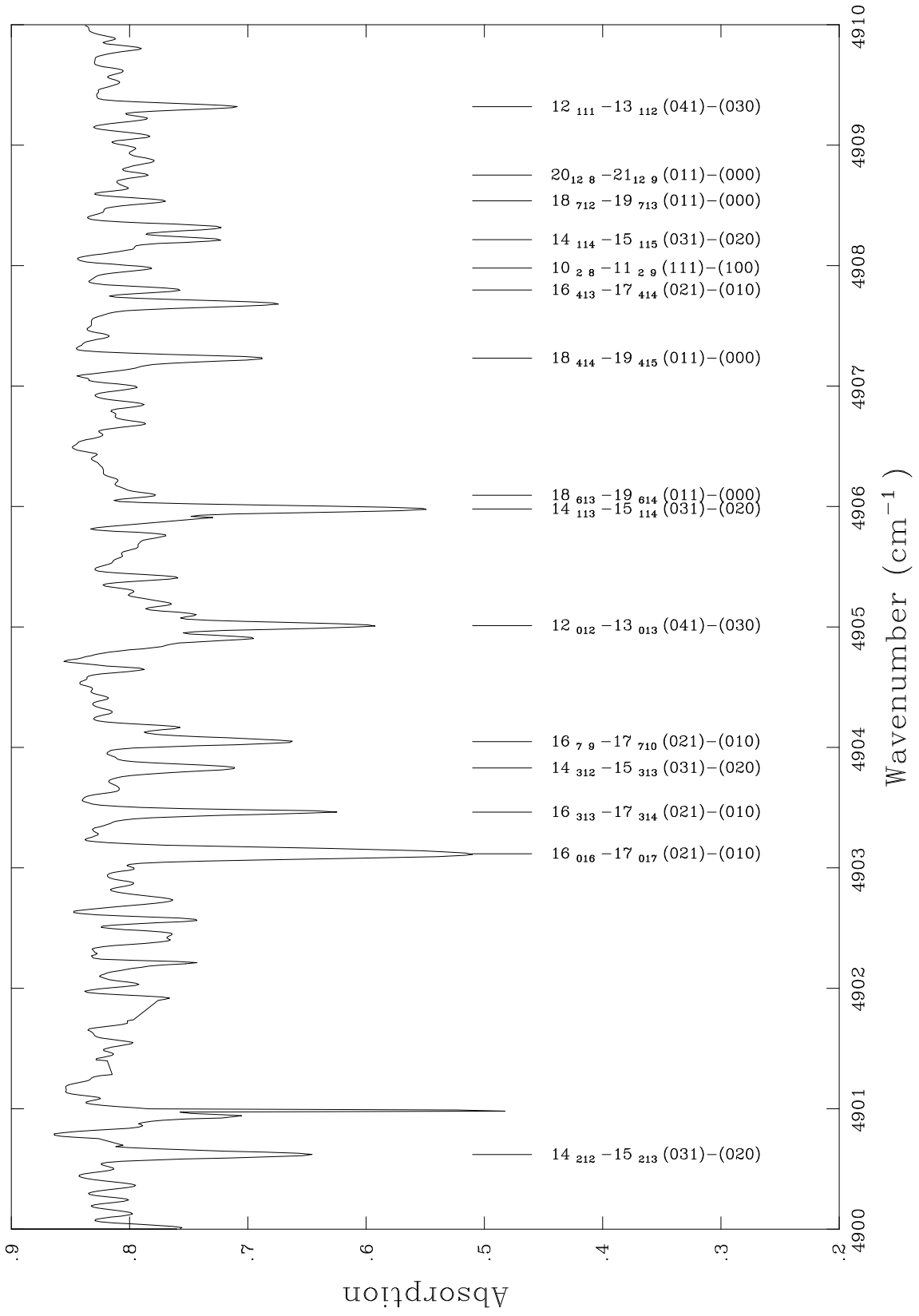
12 111 −13 112 (041)−(030)
20 12 8 −21 12 9 (011)−(000)
18 712 −19 713 (011)−(000)
14 114 −15 115 (031)−(020)
10 2 8 −11 2 9 (111)−(100)
16 413 −17 414 (021)−(010)
18 414 −19 415 (011)−(000)
18 613 −19 614 (011)−(000)
14 113 −15 114 (031)−(020)
12 012 −13 013 (041)−(030)
16 7 9 −17 710 (021)−(010)
14 312 −15 313 (031)−(020)
16 313 −17 314 (021)−(010)
16 016 −17 017 (021)−(010)
14 212 −15 213 (031)−(020)
Absorption
.9
.8
.7
.6
.5
.4
.3
.2
4900
4901
4902
4903
4904
4905
4906
4907
4908
4909
4910
Wavenumber (cm−1)

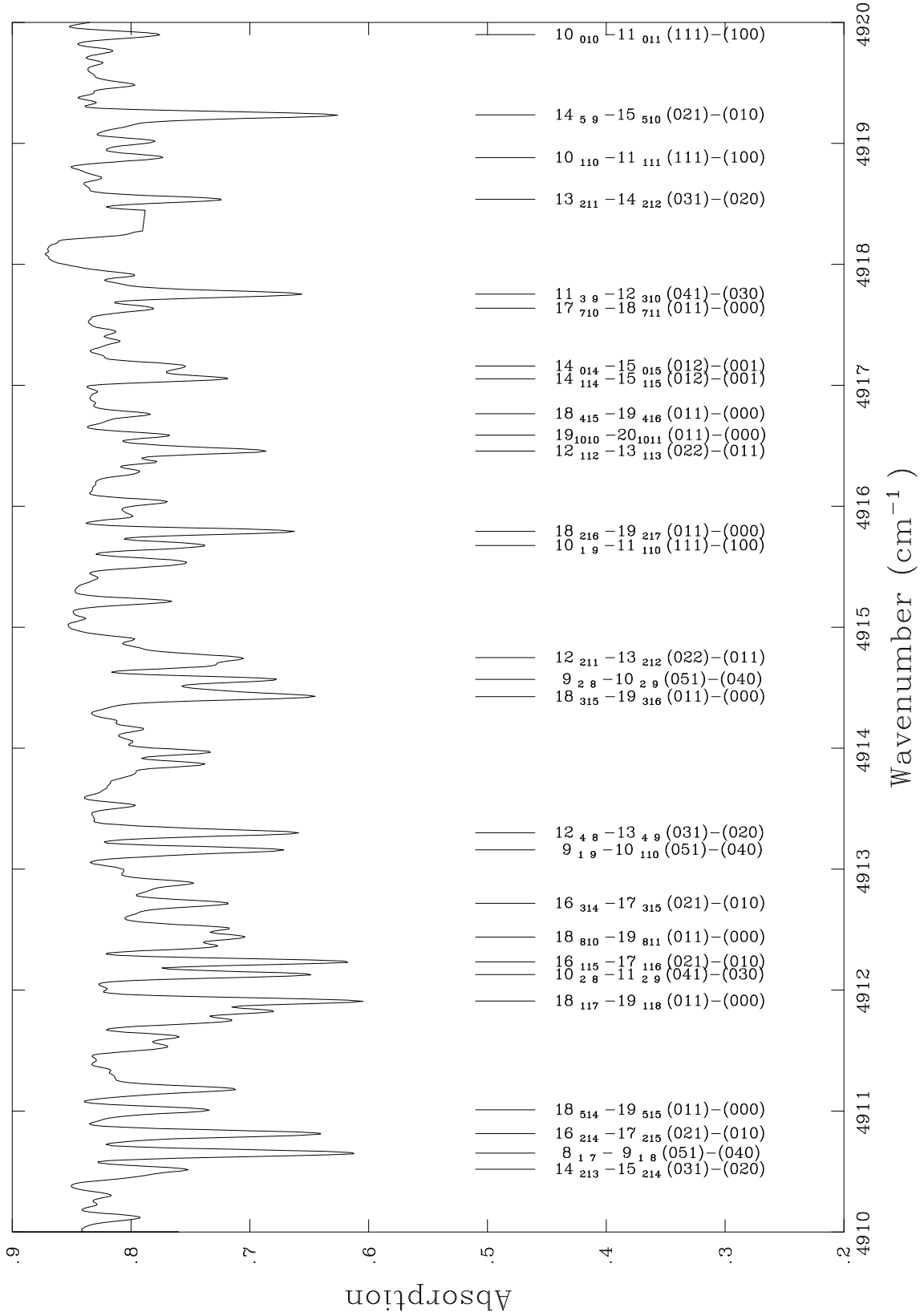
10 010 −11 011 (111)−(100)
14 5 9 −15 510 (021)−(010)
10 110 −11 111 (111)−(100)
13 211 −14 212 (031)−(020)
11 3 9 −12 310 (041)−(030)
17 710 −18 711 (011)−(000)
14 014 −15 015 (012)−(001)
14 114 −15 115 (012)−(001)
18 415 −19 416 (011)−(000)
19 1010 −20 1011 (011)−(000)
12 112 −13 113 (022)−(011)
18 216 −19 217 (011)−(000)
10 1 9 −11 110 (111)−(100)
12 211 −13 212 (022)−(011)
9 2 8 −10 2 9 (051)−(040)
18 315 −19 316 (011)−(000)
12 4 8 −13 4 9 (031)−(020)
9 1 9 −10 110 (051)−(040)
16 314 −17 315 (021)−(010)
18 810 −19 811 (011)−(000)
16 115 −17 116 (021)−(010)
10 2 8 −11 2 9 (041)−(030)
18 117 −19 118 (011)−(000)
18 514 −19 515 (011)−(000)
16 214 −17 215 (021)−(010)
8 1 7 − 9 1 8 (051)−(040)
14 213 −15 214 (031)−(020)
Absorption
.9
.8
.7
.6
.5
.4
.3
.2
4910
4911
4912
4913
4914
4915
4916
4917
4918
4919
4920
Wavenumber (cm−1)

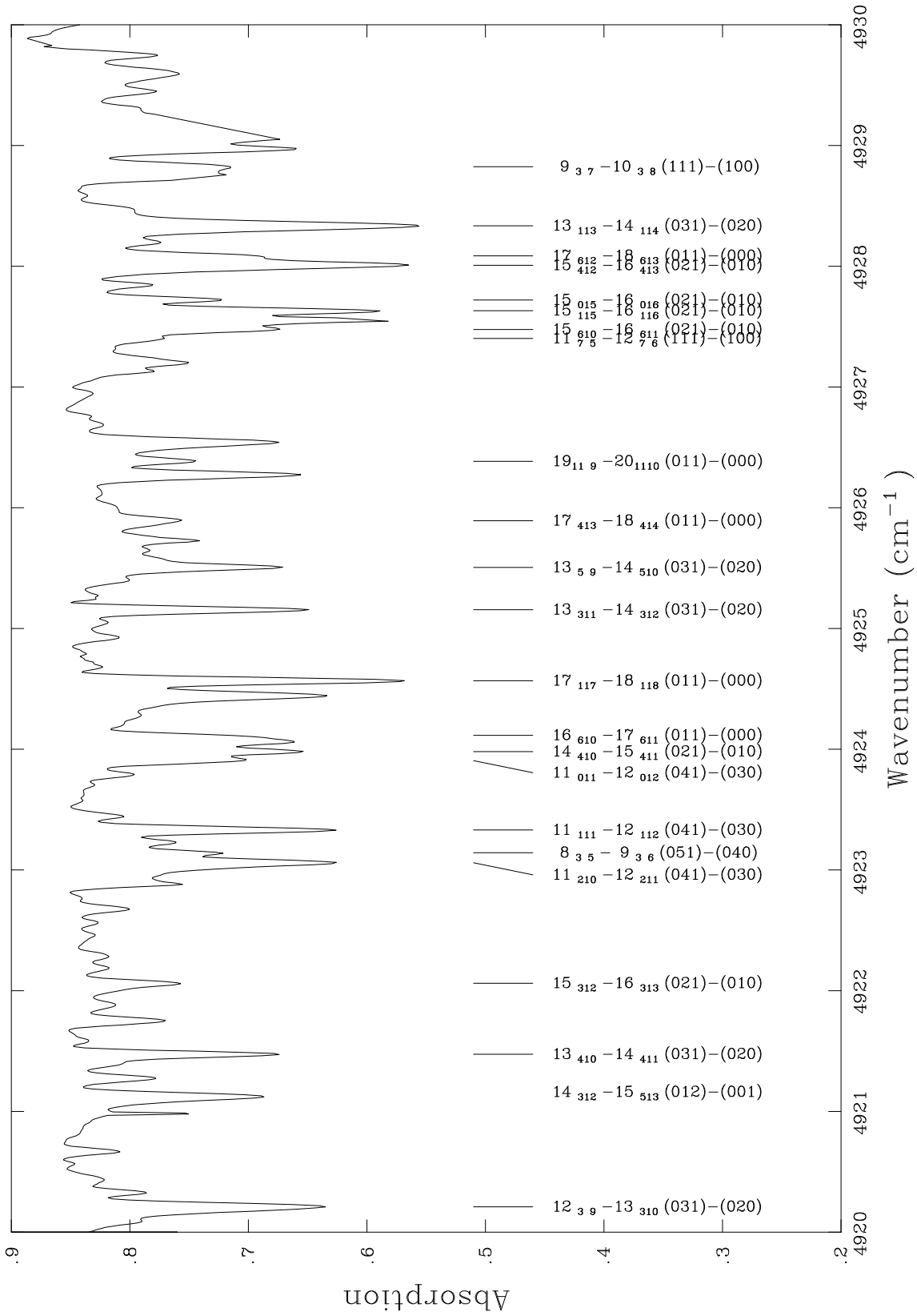
9 3 7 −10 3 8 (111)−(100)
13 113 −14 114 (031)−(020)
17 612 −18 613 (011)−(000)
15 412 −16 413 (021)−(010)
15 015 −16 016 (021)−(010)
15 115 −16 116 (021)−(010)
15 610 −16 611 (021)−(010)
11 7 5 −12 7 6 (111)−(100)
19 11 9 −20 1110 (011)−(000)
17 413 −18 414 (011)−(000)
13 5 9 −14 510 (031)−(020)
13 311 −14 312 (031)−(020)
17 117 −18 118 (011)−(000)
16 610 −17 611 (011)−(000)
14 410 −15 411 (021)−(010)
11 011 −12 012 (041)−(030)
11 111 −12 112 (041)−(030)
8 3 5 − 9 3 6 (051)−(040)
11 210 −12 211 (041)−(030)
15 312 −16 313 (021)−(010)
13 410 −14 411 (031)−(020)
14 312 −15 513 (012)−(001)
12 3 9 −13 310 (031)−(020)
Absorption
.9
.8
.7
.6
.5
.4
.3
.2
4920
4921
4922
4923
4924
4925
4926
4927
4928
4929
4930
Wavenumber (cm−1)

Table 6.3: Highest energy level, E, observed previously and assigned in this work as a function of vibrational state. For this work, calculated values of the energy levels are given. Until now, transitions involving high K_a levels have proved particularly hard to assign. For a full list of assigned transitions see Polyansky *et al* (1997c)

Band	Previous			This work		
	J	K_a	E (cm^{-1})	J	K_a	E (cm^{-1})
(000)	35	1	11656[1]	33	33	21111
(010)	30	2	10866[2]	31	31	21223
(020)	15	3	6346[3]	30	30	22340
(100)	30	1	12203[1]	28	28	19552
(001)	34	1	14618[1]	28	28	19514
(030)	14	2	7361[4]	28	27	22243
(110)	15	6	8720[5]	24	24	17995
(011)	30	1	13838[1]	26	26	19723
(040)	12	1	7689[6]	13	12	11512
(050)	–	–	–	4	4	9785

[1]Flaud & Camy-Peyret (1976)

[2]Camy-Peyret *et al* (1977)

[3]Toth (1993)

[4]Flaud *et al* (1977)

[5]Rothman *et al* (1992)

[6]Toth (1994)

Table 6.4: Summary of water transitions assigned in the 4600 – 5100 cm^{-1} region of the sunspot spectrum of Wallace and Livingston (1992). Given are the number of transitions, N, for a particular band, the highest calculated energy level involved, E^{max}, and corresponding rotational assignment. The calculated vibrational band origin, $E(J = 0)$, are given for both vibrational states involved in each band.

Band	$E^{max}(cm^{-1})$	JK_aK_c	$E(J = 0)(cm^{-1})$	N
011 − 000	13842	30 0 30	5335 − 0	144
021 − 010	14820	29 1 29	6876 − 1596	103
031 − 020	15315	27 1 27	8379 − 3154	119
041 − 030	15882	25 1 25	9839 − 4670	26
051 − 040	16066	22 0 22	11249 − 6138	14
061 − 050	15959	18 0 18	12592 − 7546	22
071 − 060	15309	11 1 11	13841 − 8874	6
012 − 001	13659	22 1 22	9007 − 3758	20
022 − 011	12784	15 0 15	10529 − 5335	14
111 − 100	13850	23 1 23	8813 − 3660	17

Chapter 7

The Computation of the VT2 linelist

VTP1 and ZVPT, discussed respectively in Chapters 5 and 6, although spectroscopically accurate, are not complete enough to be used as opacity data for the modelling of cool stellar atmospheres.

The major motivation of my work was to compute a linelist, VT2, which could solve the water opacity problem in cool stellar atmospheres. In this chapter I will discuss (i) the improvements in the potential surface and in the codes from MT (computed with TRIATOM) to VT2 (computed with DVR3D); (ii) the refinement of the input parameters together with the choice of a much larger sets of energies for each J; (iii) the PS linelist with respect to VT2, ZVPT and indeed some regenerated (UCL)PS data.

During the course of this project, started three years ago, we have encountered a series of computational problems, mainly due to the limited power of the computers available. This led to a huge delay in the accomplishment of VT2, during which improvements on the potential surfaces were developed and urgent needs for spectroscopic data led us to compute smaller linelists (VTP1 and ZVPT) which served specific purposes.

As mentioned in Chapter 3, in the last few months a new extended opacity dataset

was computed by the Nasa Ames group (Partridge & Schwenke, 1997, PS), which adds to the available opacity data sets used for modelling of cool stars atmosphere (Allard *et al*, 1997).

Nevertheless, VT2 is still needed as I will show in the course of this Chapter. The PS linelist, although a great improvement still has not solved some of the problems caused by the inexact treatment of the water opacity in the model atmospheres.

7.1 Input parameters

The potential used is PJT2 by Polyansky *et al* (1995). This potential is not as accurate for the ground state as PJT1, however, it is very reliable (the most reliable when we started the computation) for higher vibrational states.

The dipole surface used is *ab initio* from Gabriel *et al* (1993). They used a 130 contracted Gaussian type orbitals (GTOs) basis and the coupled electron pairs approximation (CEPA-1), which is a high correlation technique. This dipole surface was chosen over others, e.g. Wattson and Rothman (1992) and two of Jørgensen and Jensen (1993), because compared with them it seems to give the best results (see Lynas-Gray *et al*, 1995).

For a complete calculation which will give an accurate description for the hot water vapour transitions seen at temperatures applicable to cool stellar atmospheres (up to 5000K), it is necessary to compute all levels up to at least 30000cm^{-1} above the ground state for J up to 42 (Partridge & Schwenke, 1997). The aim is to give an accurate representation for transitions longward of 0.2 μm with convergence better than 0.1 cm^{-1}. The inputs parameters we are using are listed in Table 7.1.

Table 7.1: Parameters employed for the full calculation of the water linelist. See Chapter 4 for definitions.

H	r_e/a_0	D_e/E_h	ω_e/E_h	IBASS	NPNT2	NALF
2000	2.55	0.25	0.007	300(J+1)	40	40

The number of eigenvalues and vectors required were chosen depending on J, such that 30000 cm^{-1} was always reached. For the ground rotational level, $J = 0$, we obtained 500 levels for the states of both even and odd parity. There is no general formula for deciding how many levels are required in order to reach 30000 cm^{-1} for the e parity but again varies with J. For the number of levels required for the f parity, we applied the formula:

$$NEVAL2 = NEVAL \times \frac{J}{J+1}$$

where NEVAL is the number of levels chosen for the calculation of the e parity and NEVAL2 is the number of levels chosen for the calculation of the f parity. Table 7.2 lists how many levels needed to be calculated in order to reach 30000 cm^{-1} for each J. We have listed *only* the J for which we have computed the wavefunctions. The third column refer to the number of levels calculated by the PS linelist (see later). The necessary number of levels ($NEVAL$) increases with J until $J = 16$ and then decreases again. This is also shown in Figure 7.1. The choice of parameters is justified and explained in Chapter 3.

7.2 Computational Problems

In September 1994 we had been awarded 2000 CPU time hours with the Supercomputer Cray YMP8 (later J90) at Rutherford Appleton Laboratory. During the course of the computation, we have encountered many computational problems. All of them were related to either (i) the limited computers resources available or/and (ii) the inadequacy of the codes for large calculations again within the capability of the computers available. The computer related problems were to do with 1) 'space' limits and 2) CPU time requirements. There are three types of space that concerned us: (i) the physical temporary space where the jobs were running (ii) the 'virtual' space where wavefunctions and other smaller files were archived; (iii) memory space needed to run each job. We will discuss them in turn. During the course of the computation the computer we were using has been replaced. Originally we used the Cray/YMP8. In February 1996 the YMP8 was replaced with the J90. The plan was to compute at first all the wavefunctions with increasing J

Table 7.2: NEVAL for each symmetry block of each J[1].

J	VT2	PS	J	VT2	PS
0	153	201	15	2099 1895	1622 1474
	115	150		2087 1935	1601 1518
1	416 235	347 197	16	2125 1935	1627 1502
	415	346 146		2090 1940	1608 1503
2	644 404	536 337	17	2121 1961	1633 1490
	587 406	487 339		2106 1926	1614 1528
3	802 557	670 471	18	2083 1947	1616 1498
	794 624	666 518		2067 1947	1601 1500
4	1010 775	841 646	19	2081 1880	1611 1476
	955 773	793 643		2075 1939	1594 1506
5	1148 915	953 761	20	2056 1887	1574 1459
	1147 970	948 806		2027 2898	1550 1459
6	1335 1102	1101 912	21	2006 1833	1543 1417
	1280 1104	1054 916		1997 1866	1520 1444
7	1453 1223	1189 1008	22	1902 1742	1493 1384
	1450 1276	1197 1051		1891 1773	1479 1386
8	1608 1557	1318 1138	23	1886 1731	1460 1327
	1381 1396	1274 1138		1875 1753	1446 1357
9	1705 1476	1387 1207	24	1821 1674	1389 1284
	1696 1525	1381 1250		1796 1685	1375 1287
10	1824 1524	1483 1307	25	1733 1596	1321 1215
	1604 1601	1441 1312		1710 1617	1316 1234
11	1891 1670	1532 1357	26	1660 1589	1258 1160
	1886 1721	1524 1395		1640 1534	1238 1165
12	1985 1772	1601 1431	27	1560 1430	1188 1089
	1934 1776	1566 1440		1530 1460	1177 1106
13	2026 1811	1631 1467	28	1474 1353	1121 1025
	2019 1861	1623 1504		1456 1362	1101 1028
14	2091 1876	1601 1516			
	2036 1881	1580 1521			

[1]The top left number corresponds to an ee block followed by fo.

The bottom left number corresponds to an eo block followed by an fe.

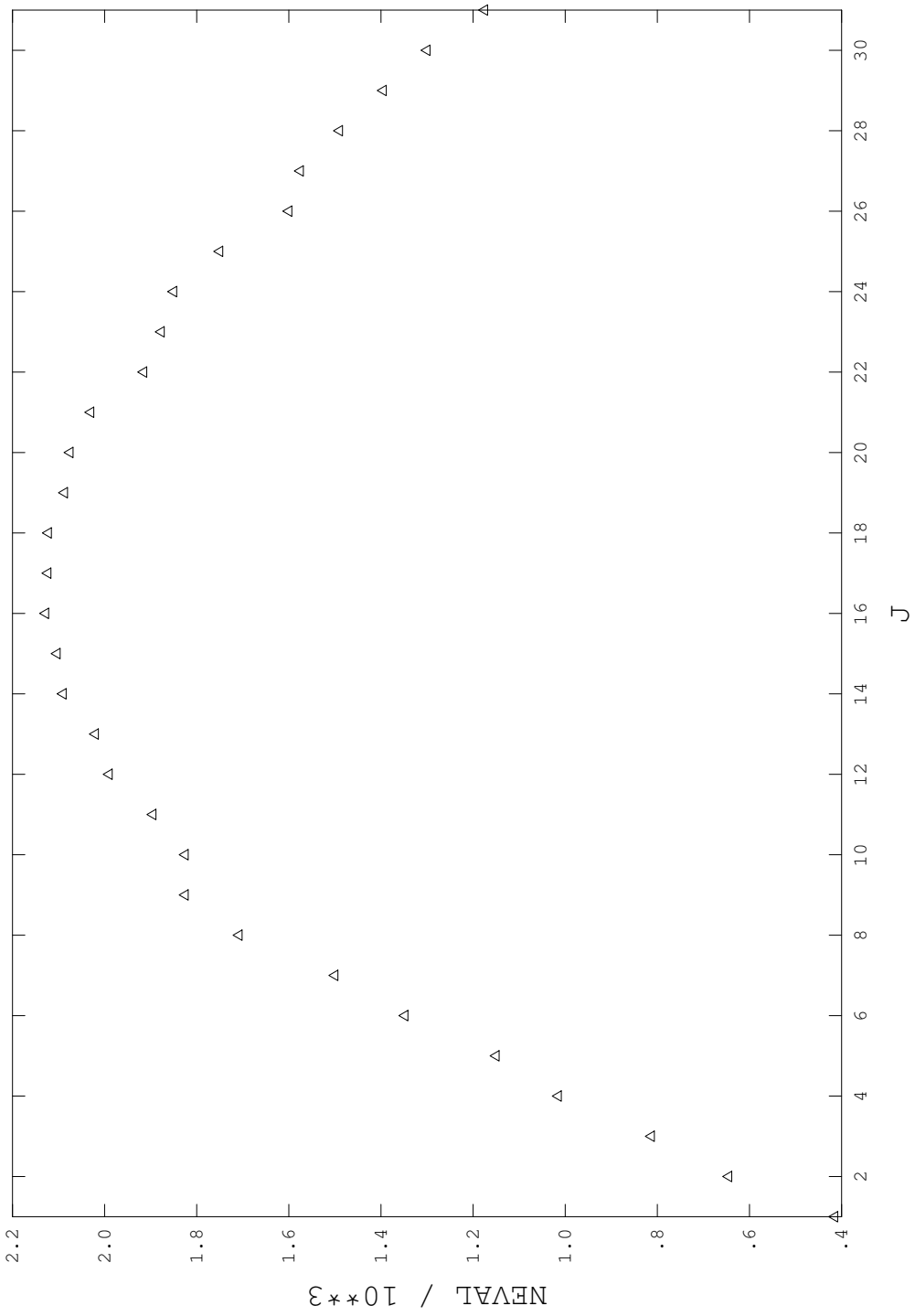

Figure 7.1: Number of energy levels required for each J to reach 30000cm^{-1} for VT2.

Table 7.3: Example of computer requirements for a $J = 17$ calculation. ROTLEV3B has been split up in 4 steps: HAM, construction of the Hamiltonian for both e and f parity. DIA, diagonalization of both the matrices for both e and f. TRA, transformation and creation of the wavefunctions computed *separately* for e and f. The dipole transition involving $J = 17$ used as an example is $16ee \rightarrow 17eo$.

	DVR3DRJ	ROTLEV3B			DIPOLE3
		HAM.	DIA.	TRA. (x2)	
Mem. (Mw)	8	103	30	80	150
CPU (hrs)	7	18	70	2	100
Filesp. (Gb)	4	6	15	15	20

and then to produce the dipoles as we did for VTP1 and ZVPT.

Most of our problems can be explained by the large amount of data used. So far, nearly 2 Tera bytes of space is being used. Most of it is in the "virtual tapes" archive. Some (55Gb) is on line. More specifically: DVR3DJ provides two identical files containing the vibrational wavefunctions necessary for ROTLEV3B to calculate rotationally excited states. These two files increase in size with J and with NEVAL. For VT2, they can get as big as 10Gb. ROTLEV3B creates as outputs 2 wavefunctions that can be as large as 15Gb each. The ROTLEV3B files increase in size with the increase in NEVAL and J. In Table 7.3 we show an example of a complete run, from the creation of the wavefunction to the computation of the dipole transitions (not employing the latest version of DIPOLE3, see Section 4.4 and later in this Chapter for details), for $J = 17$.

7.2.1 YMP8 calculations

During the first half of 1995 we slowly managed to produce more than half of the wavefunctions required. We encountered many unforseen problems. The user support at the Rutherford Appleton Laboratory were very helpful in trying to lighten the problems which

were, however, never solved completely. One of the problems was the temporary directory where the jobs were running. It often became full and as a consequence the jobs crashed before ending. The temporary files created by the codes were not enough to account for these crashes. The temporary directory was around 40Gb of size. All together, one of our job can require from 5Gb to 25Gb of space to run successfully.

A second problem was the CPU time required to compute a single wavefunction. It often exceeded the maximum time allowed for each jobs by the limits of the batch queues[1]

None of the queues available were suitable, either because of the CPU time or the memory space or the filespace limitations. We partly solved both of the problems described above by (i) adjusting ROTLEV3B. We split it into 4 subprograms (Hamiltonian construction; diagonalization with an option of doing only e or f; transformation and creation of the wavefunction). See Chapter 2 for details. (ii) Using a new YMP8 queue, created exclusively to compute VT2, called MOLQ with increased limits. (iii) Increasing the amount of permanent space from where input files could be assigned. This allowed us slowly to complete more than half of the wavefunctions. However, from June 1995 the number of jobs successfully executed decreased by a large amount. Around September 1995, we basically had to stop our computation, until the new machine, the $J90$ arrived. This forced stop was due to the temporary directory being almost always full. Until its closure, apart from a brief period during Christmas 1995, the YMP8 was not capable of running any reasonably large job.

7.2.2 The J90 computation

From February 1996 the YMP8 has been replaced with a new machine, the J90. Although with a 50% slower clock speed, it turns out to be much better in that it uses 32 processes as opposed to 8. Along with the arrival of the J90, a new queue was introduced: the MULTI8 queue. The latter prioritizes efficiently multitasked jobs. The codes had to be

[1] the Cray at Rutherford Laboratory had set up 9 queues with different time, memory and filespace limitations. The maximum CPU time, memory and filespace allowed were respectively: 86400, 100Mw and 10Gb.

Table 7.4: List of computed and missing dipole transitions.

J	$\Delta J = 0$	$\Delta J = 1$
0		$\star$
1	$\times$	$\star$
2	$\star$	$\star$
3	$\star$	$\star$
4	$\star$	$\star$
5	$\star$	$\star$
6	$\star$	$\star$
7	$\star$	$\star$
8	$\star$	$\star$
9	$\star$	$\times$
10–40	$\times$	$\times$

changed in order to make the most of this multi–process machine (see Section 4.4). In particular we improved DIPOLE3. The code was restructured to allow it to multi–task efficiently. Indeed large production runs typically use 7.9 out of 8 possible processors.

Unfortunately by this time, all the CPU time that we had been awarded was finished. A lot of it had been lost because of computer crashes caused by the problems described above.

7.3 Where we have got to

Up to date, we have managed to construct the first-step Hamiltonian (DVR3DJ) for every J until 35. Wavefunctions have been created up to $J = 28$. Finally we have computed all the dipole transitions up to $J = 9$. In Table 7.4 we have a list of the dipoles computed and the ones missing.

The number of transitions already calculated was unexpected! Estimating from the

energy levels computed up to $J = 28$, we believe that we will have ~ 700 million transitions. Figures 7.2 and 7.3 show water spectra at T = 300K computed with VT2. The frequency regions covered are (i) 0 to 700 cm^{-1} and (ii) 1300 to 1430 cm^{-1}. Due to the number of transitions, it was necessary to smooth it by fitting a Gaussian profile evaluated at an arbitrary grid of points with a FWHM of 0.005 cm^{-1}. At higher temperatures, weaker transitions belonging to higher vibrational bands, important in the modelling of cool stars' atmospheres, are also present!

7.4 Comparisons with PS linelist

7.4.1 The PS linelist

By the time we had partially computed VT2, the PS linelist became public. Partridge & Schwenke computed an *ab initio* linelist using a high quality potential energy surface empirically refined and an *ab initio* dipole surface (Partridge & Schwenke, 1997). The method employed to compute the linelist is variational using the FBR method of Schwenke (1992b). PS optimized their *ab initio* potential using experimental line positions for low–lying rotational levels ($J \leq 5$) taken from HITRAN. In the calculation of their full linelist PS truncated the basis set used for the variational calculations for $J > 4$ at the level of their $J = 4$ calculations.

We have performed comparisons and tests with PS and our linelists. In particular, (i) We have compared PS energy levels with VT2 ones and with energy levels for $J = 17$ and 28 computed with DVR3D using PS potential energy surface and VT2 parameters. (ii) We have compared PS energy levels with ZVPT ones. We also have computed a partial linelist, UCLPS, using ZVPT parameters and PS potential surface and used it for further comparisons. (iii) We have attempted to use the PS linelist in model atmosphere calculations using the model atmosphere code PHOENIX (Allard & Hauschildt, 1995).

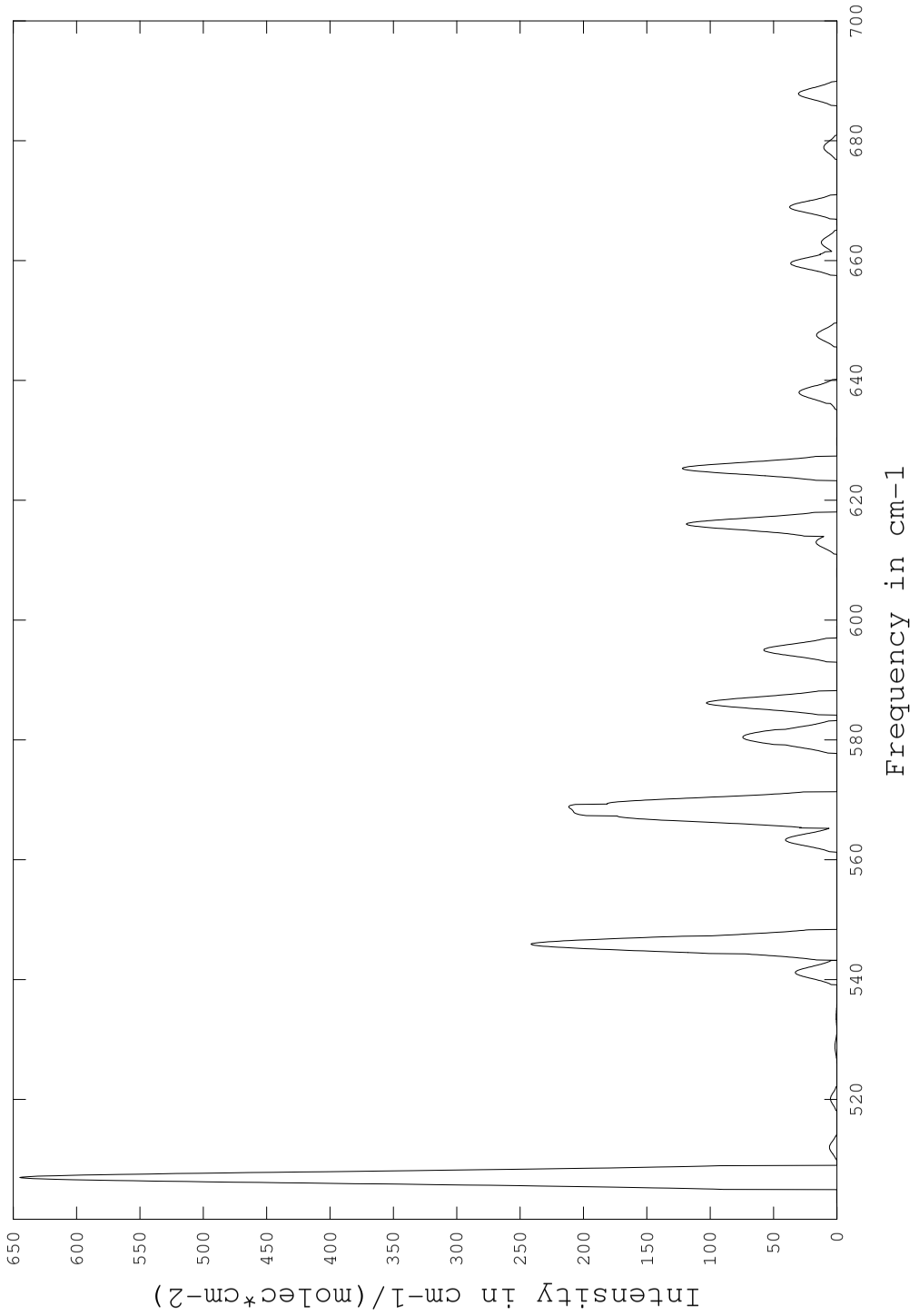

Figure 7.2: A partial water spectrum at 300K computed with VT2.

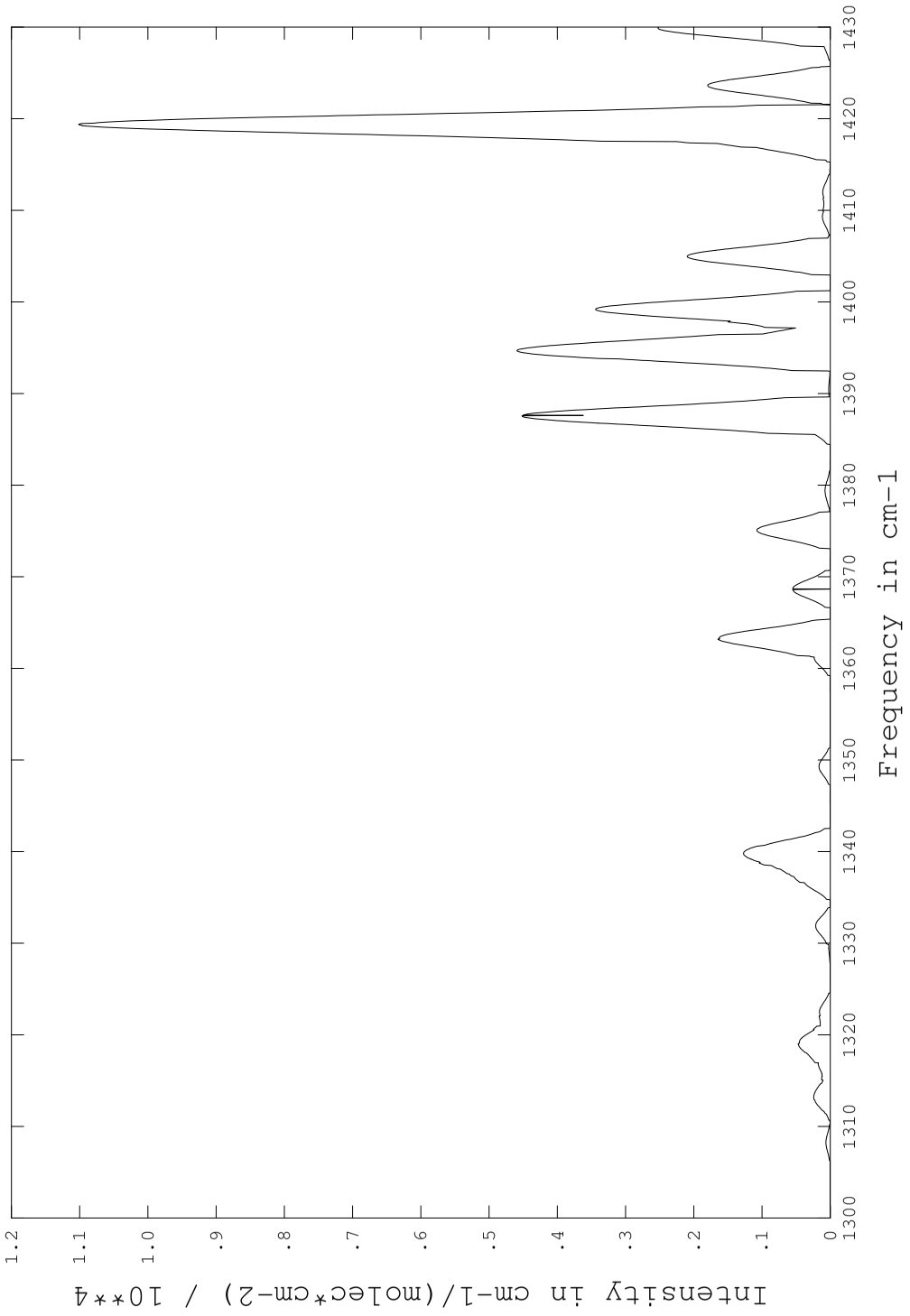

Figure 7.3: A partial water spectrum at 300K computed with VT2.

7.4.2 Energy levels comparisons with VT2

In Table 7.2 we have listed the number of energy levels calculated in VT2 and PS for each J. We find two problems with the PS linelist: (i) first of all, it does not reach 30000 cm^{-1} for any J apart from $J = 0$. On average they get to 28000 cm^{-1}. (ii) Secondly, even by cutting our energy levels to 28000 cm^{-1}, we still have more levels than they have for high J. For example, for $J = 17$ we need 100 energy levels more than they do to reach 28000 cm^{-1}. From the number of energy levels missing for each J we estimate that they omitted $\sim$ 30 % transitions up to $J = 10$; $\sim$ 50% up to $J = 20$; and $\sim$ 60% up to $J = 28$.

To perform tests independently of the potential energy surface employed, we also computed a new sets of levels for $J = 17$ and 28 using the PS potential energy surface and the same masses as PS. The parameters employed are the same as for VT2. This was done to test the variational convergence within the same potential energy surface. Examples of energy levels comparisons with VT2 and the new calculations are shown in Figures 7.4 and 7.5. We again note a 'lack' of levels for the PS linelist. For both $J = 17$ and $J = 28$ the calculations performed with the PS potential energy surface are in perfect agreement with VT2 which suggests that the lack of states in the PS linelist is due to poor convergence and not to differences in the potential energy surface used. In fact, close examination of the parameters of the PS calculation strongly suggests that their decision not to increase the size of the calculation beyond that used for $J = 4$ has resulted in poorly converged calculations for higher states with high J. This decision undoubtedly saved them from some of the computational problems that we have experienced.

7.4.3 Energy levels comparisons with UCLPS and ZVPT

We have compared energy levels taken from (i) ZVPT and (ii) UCLPS with PS. UCLPS is a partial linelist computed with the PS potential and masses but ZVPT parameters using DVR3D. Table 7.5 gives a comparison of the observed $J = 24$ rotational levels of the manifold of the (001) vibrational state. For low J energy levels, PS's calculations give superb results, reproducing experiment with a much higher accuracy than either ZVPT

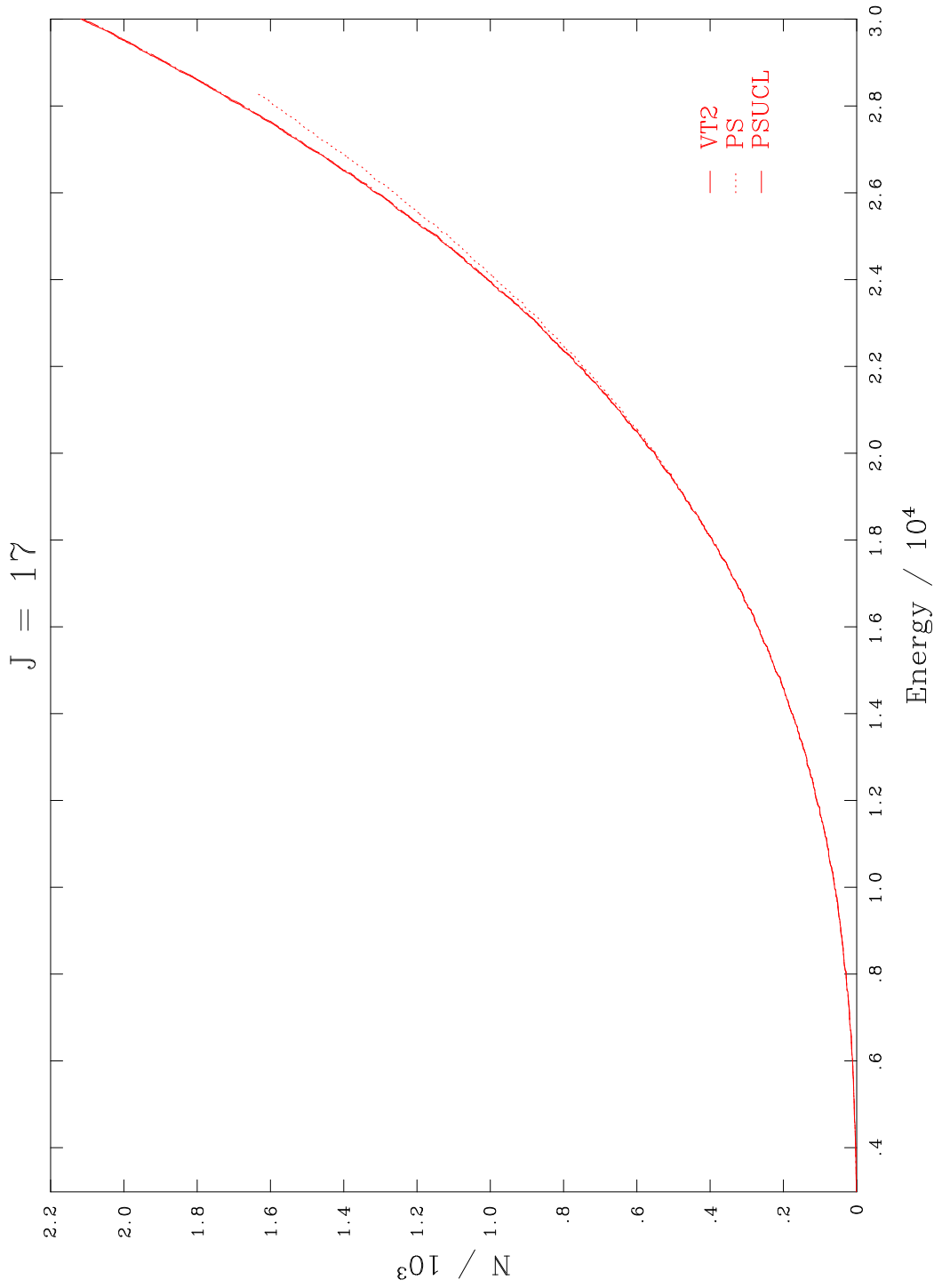

Figure 7.4: Number of energy levels as a function of Energy for PS (dotted) and VT2(continuous) linelist for $J = 17$. The PS linelist does not arrive until 30000 cm^{-1}.

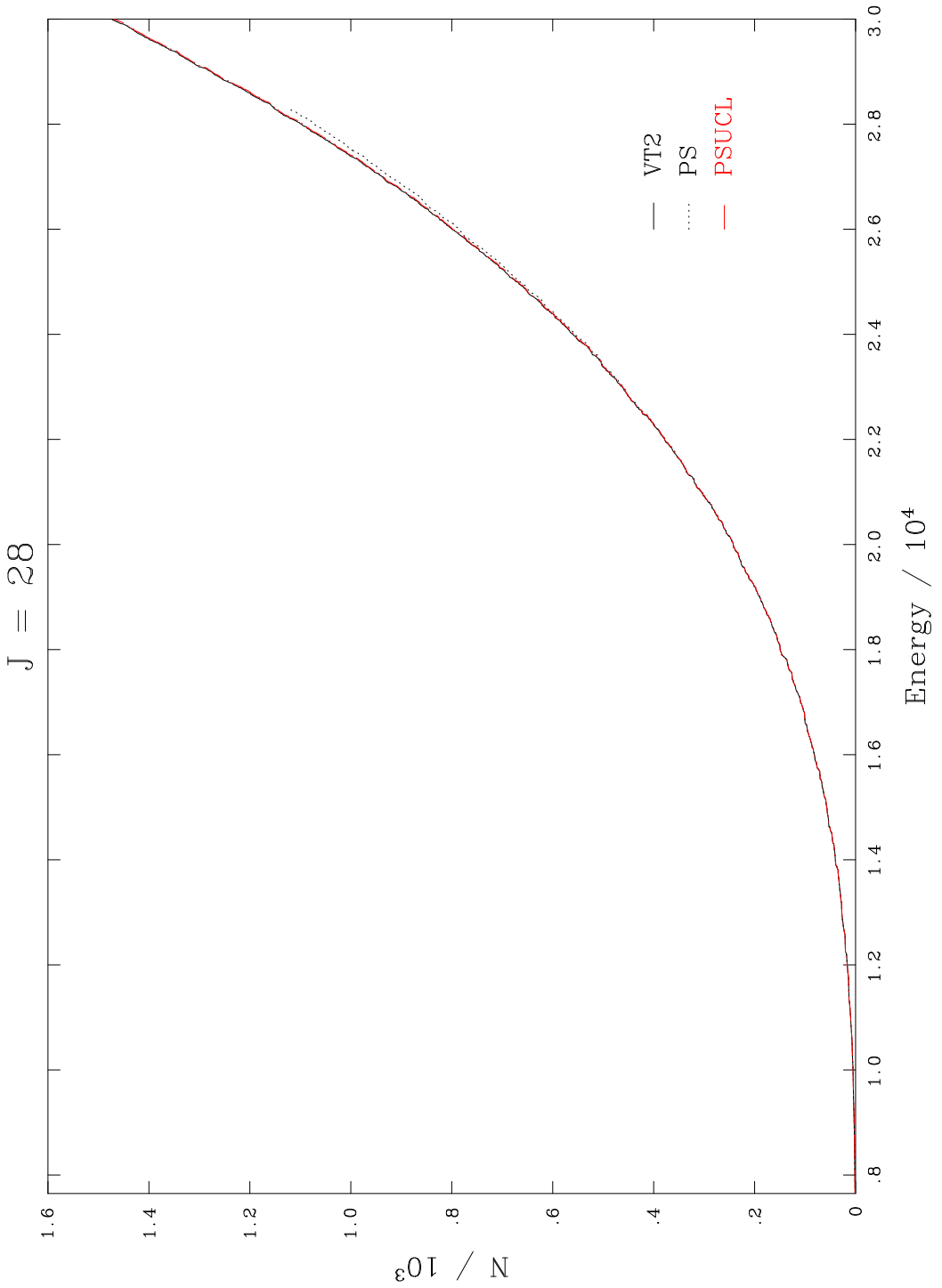

Figure 7.5: Number of energy levels as a function of Energy for PS (dotted) and VT2(continuous) linelist for $J = 28$. As for Figure 7.4, Ps does not reach 30000 cm^{-1}.

or VTP1. However for higher rotational states, particularly those with $J > 20$, we find that a very high proportion of rotational states which one expects to be degenerate in fact show significant splittings in the PS linelist. This splitting is not shown in ZVPT, VTP1 or in UCLPS.

Table 7.5: Energy levels for $J = 24$ rotational levels of the (001) state in cm^{-1}. Experimental levels with $K_a \leq 3$ are from Flaud *et al* (1976). Levels with $K_a \geq 11$ are from Polyansky *et al* (1996). Calculated energy levels are from Partridge and Schwenke (PS), UCLPS and ZVPT.

J K_a K_c	Expt	PS	UCLPS	ZVPT
24 0 24	9379.493	9379.670	9379.656	9382.131
24 1 24	9379.493	9379.683	9379.656	9382.131
24 1 23	9803.442	9803.603	9803.590	9806.080
24 2 23	9803.442	9803.617	9803.590	9806.078
24 2 22	10183.350	10183.505	10183.486	10186.063
24 3 22	10183.350	10183.518	10183.486	10186.063
24 3 21	10529.434	10529.524	10529.505	10532.189
24 11 14	12297.529	12297.917	12296.525	12300.930
24 11 13	12299.281	12299.417	12299.346	12302.453
24 12 13	12554.999	12555.164	12555.078	12558.089
24 12 12	12555.210	12555.382	12555.276	12558.289
24 13 12	12826.246	12826.479	12826.360	12829.316
24 13 11	12826.324	12826.500	12826.390	12829.348
24 14 11	13108.367	13108.519	13108.393	13111.322
24 14 10	13108.364	13108.563	13108.406	13111.334
24 15 10	13398.573	13398.727	13398.552	13401.474
24 15 9	13398.573	13398.712	13398.553	13401.474

24 16 9	13693.277	13693.357	13693.171	13696.166
24 16 8	13693.277	13693.391	13693.171	13696.166
24 17 8	13991.433	13991.673	13991.437	13994.475
24 17 7	13991.433	13991.654	13991.437	13994.475
24 18 7	14290.330	14290.464	14290.220	14293.346
24 18 6	14290.330	14290.748	14290.220	14293.346
24 19 6	14587.427	14587.749	14587.336	14590.581
24 19 5	14587.427	14587.619	14587.336	14590.581
24 20 5	14880.626	14880.682	14880.407	14883.806
24 20 4	14880.626	14881.115	14880.407	14883.806
24 21 4	15167.074	15167.817	15166.816	15170.402
24 21 3	15167.074	15167.088	15166.816	15170.402
24 22 3	15443.810	15443.745	15443.505	15447.310
24 22 2	15443.810	15444.066	15443.505	15447.310
24 23 2	15707.030	15707.345	15706.651	15710.700
24 23 1	15707.023	15706.805	15706.651	15710.700
24 24 1	15951.702	15951.273	15951.150	15955.438
24 24 0	15951.702	15951.285	15951.150	15955.438

It is clear from Table 7.5 that PS's linelist systematically gives splittings which appear to be artificial. In particular for the levels with high K_a and with K_c odd, all lie below the ones with K_c even levels with which they should be quasi-degenerate. Since PS truncated their variational rotation-vibration calculations at 7,500 energy-selected basis functions independent of the rotational parity, this means that the K_c odd (f parity) calculations will contain states of higher cut-off energy that the K_c even (e parity) calculation. Because of the variational principle, the K_c odd states will be better converged and hence lower in energy.

This artificial splitting of lines has two possible consequences. The first is that it

is more difficult to use the linelist for assignments. The second consequence is perhaps more subtle. As with VT2, a major objective of PS was to construct a list of over 300 million water transitions in order to model the atmospheres of cool stars. An important consideration in these radiative transport models is how the line absorptions fill in the gaps in the spectrum. Two transitions which, to within their linewidth, are coincident will have a rather different effect than two well-separated transitions. In the latter case the overall stellar opacity will be overestimated. For T $\sim$ 2000–4000 K, Boltzmann considerations suggest that transitions involving states with J = 20–30 are the dominant sources of opacity. Artificially doubling the number of lines for these J values could have serious consequences for the opacity prediction.

Figure 7.6 also shows how the errors behave along a branch for ZVPT and PS. For all J, our results give a systematic error for each branch which is quite large, $\sim$ 2–3 cm^{-1}, however, although, for low J, PS's linelist gives very little residual error, as J increases along a branch, the change in the error becomes larger and erratic. This is in contrast with the smaller and smooth error of ZVPT calculations.

7.4.4 Model atmospheres' comparisons

We have attempted to use the PS linelist in model atmosphere calculations. We have used the same version of the code PHOENIX previously used to make the comparisons with the star TVLM.

Figures 7.7 a) and b) show such a comparison.

The fit obtained with the PS linelist is definitely an improvement. However, it still seems unable to reproduce the H band (from 1.3 to 1.75 μm) properly: it overestimates the strength of water centered at 1.4 μm. However is water really the problem? As mentioned in Chapter 1, it has been proposed recently that dust might form in the atmospheres of the coolest dwarfs. Tsuji *et al* (1996a,b) show that if dust is included, temperatures in the photospheres are much more elevated in all the models. This implies that the cooling caused by the molecules is less than expected in dust-free models. This would

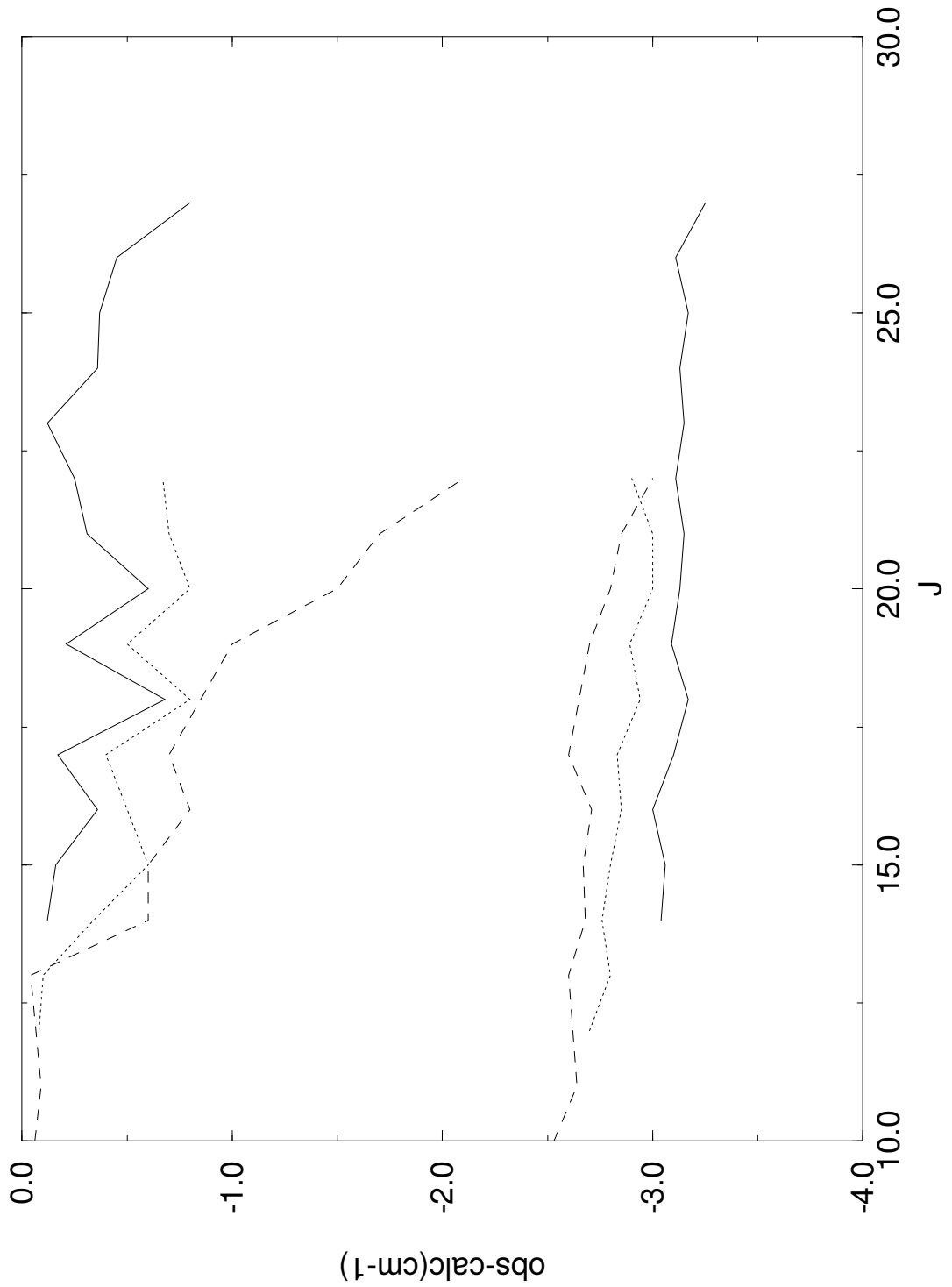

Figure 7.6: Comparison of typical band errors (observed minus calculated). Solid line: (031) − (020) $J = K_c$; dotted line: (041) − (030) $J = K_c$; dashed line: (051) − (040) $J = K_c$. Upper lines are the errors obtained using PS linelist; lower lines using ZVPT.

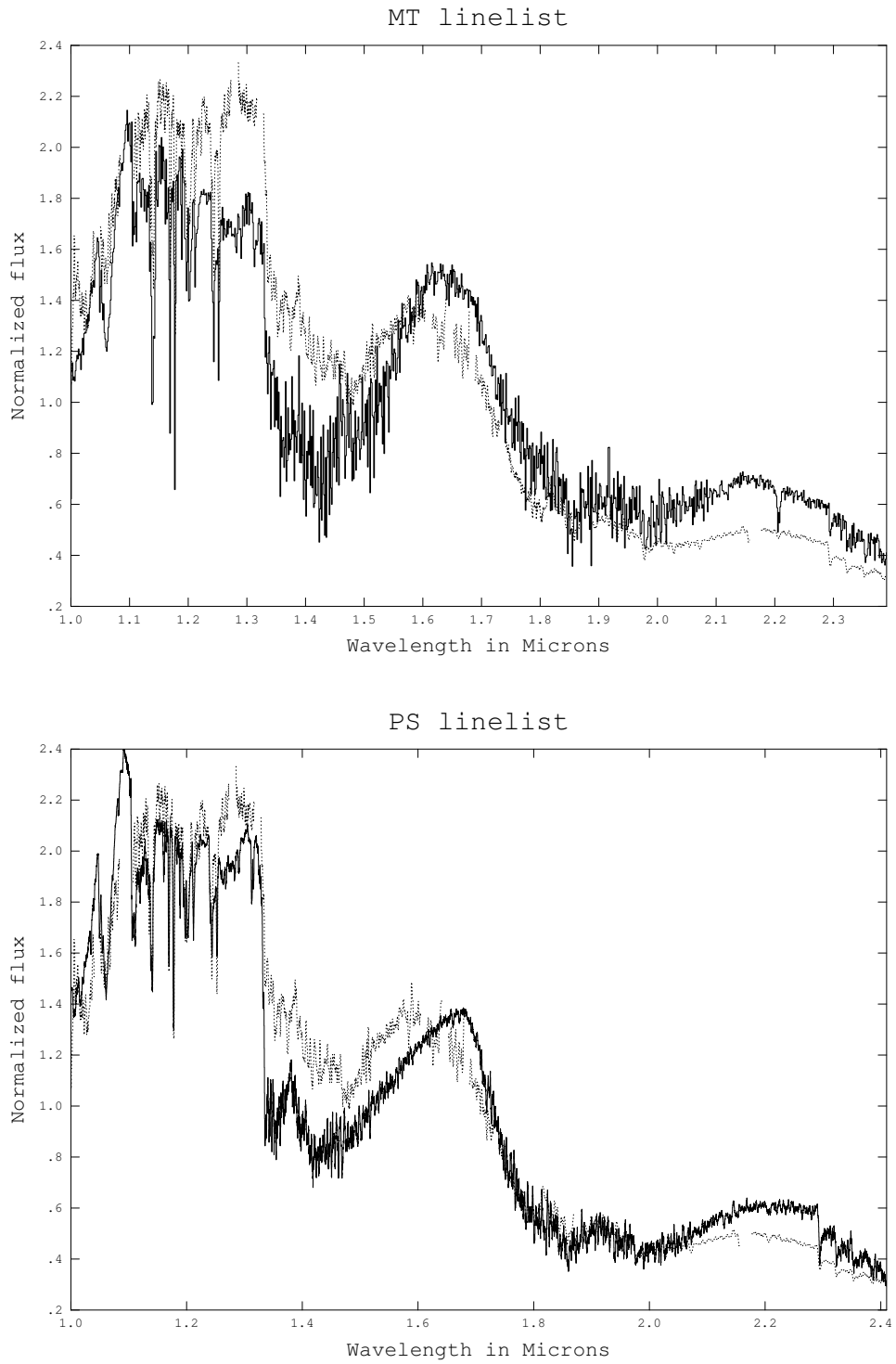

Figure 7.7: Comparisons of observed and synthetic spectra for the star TVLM. The models were computed at T_{eff} = 2500 K, [M/H] = 0.0, log g = 5.0. Top: the model includes the MT linelist for the opacity of water. Bottom: the model includes the PS linelist. The dotted curve is the observed spectrum

therefore decrease the strength of the water bands. Dust, however, has not yet been *directly* observed, despite claims of indirect observations (Jones *et al*, 1997; Tsuji *et al*, 1996b). Many models now are trying to include dust. Comparisons with observations are still, however, controversial. In fact, while for very cool objects dusty models, including the PS linelist, seem to reproduce very well the SED (Ruiz *et al*, 1997), at higher temperatures, where dust is not thought to be very important, the models still fail. In fact, models of the M dwarf VB10 (T $\sim$ 2800K, see Chapter 8), used before to test the models (Allard *et al*, 1994) actually gave worse results than those obtained with the MT linelist (Allard, private communications).

7.5 Conclusions

The VT2 project was motivated by the urgent need of reliable data on hot water mainly for modelling of cool stellar atmospheres. The high cost both in computer and clock time of the computation of linelists when high vibrational states need to be included, was unforseen. In fact, the VT2 linelist had to be suspended for the following reasons:
(i) we had run out of computer time and (ii) we were aware that Partridge and Schwenke, from NASA Ames, had a complete linelist. In this chapter we have proved that the PS linelist, although superior so far to all the available opacity data sets, is still not accurate enough to reproduce the water opacity in the M dwarfs' atmospheres. For the above reason together with many requests from modelling groups, we decided to resume the VT2 calculations. Tennyson (private communications) has recently reprogrammed DIPOLE3B, using a method suggested by Schwenke (1992b) to deal with all three coordinates within a DVR. This reduces computer time by nearly a third. Recently we have obtained 4000 YMP8 CPU hours to complete VT2. It should be finished by December 1997 and will be included in the latest model atmospheres codes.

Chapter 8

Observational Data

As explained in Chapter 1, due to the complexity of cool star atmospheres, a combination of reliable model atmospheres and high quality spectroscopy is necessary in order to determine their temperatures and luminosities, and eventually their mass function. With the improvement of infrared instrumentation, a high Signal to Noise (S/N) is now feasible. This implies that more details of the molecular and atomic lines of the spectra will be resolved.

During the nights of the 11th, the 14th and the 16th of May 1995, we observed several cool stars (in particular, M dwarfs) with the Cooled Grating Spectrometer 4 (CGS4) on the UK Infrared Telescope on Mauna Kea, Hawaii. In this Chapter we present the observations and their reduction. A lot of these data are still being analysed.

8.1 The observations: the sample chosen

We have observed a number of M dwarfs. The stars chosen for the observations range widely in temperatures and metallicities, and therefore constitute a good sample.

The instrument used, CGS4 (http://www.jach.hawaii.edu/UKIRT.new/instruments-/cgs4/handbook.html), has recently been improved allowing a much higher resolution.

In general, the signal to noise, which is defined as the amount of real flux from the source with respect to the total noise introduced by the instrument and by the sky, was

usually ≥ 50. Comparison sky spectra were obtained by nodding the telescope so that the object was measured successively in two rows of the array, separated by 30 arcsec. We aimed to observe throughout the three near infrared bands J, H and K. The 75 line mm^{-1} grating was used with central grating wavelengths of 1.135 μm ($\Delta\lambda$=0.34), 1.415 μm ($\Delta\lambda$=0.259), 1.635 μm ($\Delta\lambda$=0.33) and 2.07 μm ($\Delta\lambda$=0.675) for each target. The coverage, resolution and integration times for each star are listed in Table 8.1. Throughout this Chapter I will list the sample in a spectral type order (therefore effective temperature order), where known.

Table 8.1: Central wavelength and wavelength coverage, resolution, dates of the observations and integration times.

	Object	λ_{cen} (μm)	$\Delta\lambda$ (μm)	Date	Exp. Time (total) sec.
1	CM Dra	1.135	0.00044	14/05/95	17
		1.415	0.00044	14/05/95	10
		1.635	0.00044	14/05/95	15
		2.07	0.00088	14/05/95	10
		1.415	0.00044	16/05/95	15
		2.07	0.00088	16/05/95	10
2	Gl 299	1.415	0.00044	16/05/95	10
		1.635	0.00044	16/05/95	10
		2.07	0.00088	16/05/95	6
3	VB10	3.81		16/05/95	2.4
4	GJ 1111	1.135	0.00044	12/05/95	10
		1.415	0.00044	11/05/95	10
		1.635	0.00044	11/05/95	10
		2.07	0.00088	14/05/95	5
5	TVLM 513–4546	1.135	0.00044	16/05/95	20
		1.415	0.00044	16/05/95	15

		1.635	0.00044	16/05/95	20
		2.07	0.00088	16/05/95	20
6	Gl 569B	1.135	0.00044	12/05/95	1.25
		1.415	0.00044	16/05/95	3
		1.635	0.00044	16/05/95	3
		2.07	0.00088	16/05/95	1.75
7	GD 165B	1.135	0.00044	12/05/95	20
		1.135	0.00044	14/05/95	25
		1.415	0.00044	14/05/95	30
		1.635	0.00044	14/05/95	1.5
		2.07	0.00088	16/05/95	20
8	LHS 318	1.135	0.00044	12/05/95	2
9	Z12401–3041	1.135	0.00044	14/05/95	5
10	LHS 2238	1.135	0.00044	14/05/95	5
11	F16048	1.135	0.00044	14/05/95	1.5
12	F16156	1.135	0.00044	14/05/95	1.2
13	LHS 3768	1.135	0.00044	16/05/95	20

Each grating position overlaps with the previous and the next at the two ends which ensures reliable coverage of the whole region.

8.1.1 The sample

We have observed 13 stars, some of them not in all the 4 wavelength positions. For each of them we have observed at least one standard at each grating. A brief description of each target is given below:

(1) CM Dra: it is the least massive eclipsing binary known. It will be fully discussed and analyzed in Chapter 9.

(2) Gl 299: it is a subdwarf with metallicity of $\sim$ -1.5 (Monet *et al*, 1992) or $\leq$ -2.0

(Saumon *et al*, 1994). Its temperature is higher than 3000K (Jones *et al*, 1996). For technical problems we succeeded in observing this object only at the central wavelengths 1.415, 1.635 and 2.07 μm.

(3) GJ 1111: this is a young disk object. The Disk Population is intermediate between Populations I and II (see Chapter 1). It is believed that GJ1111 is still contracting onto the main sequence and so it probably has a metallicity higher than the solar values and a low value of log g (Jones *et al*, 1996). This target has been observed and discussed before (see for example, Jones *et. al*, 1996; Leggett 1992; Leggett *et al*, 1996; Tinney *et al*, 1993).

(4) VB10: this is classified as an old disk object and lies close to the main sequence defined by Monet *et al* (1992) suggesting a solar metallicity. It has been classified as an M8 V object (Kirkpatrick *et al*, 1993). Mass and surface gravity have not been determined.

(5) TVLM 513: it is a very low-mass M dwarf discovered by Tinney *et al* (1993). Based on its photometric colours and parallax (Tinney *et al*, 1995) and the conversion to bolometric magnitude (Jones *et al*, 1995b), TVLM 513 has a M_{bol} of 13.95$\pm$0.25. Its well determined luminosity, likely youth and solar-type metallicity (based on $v_{tan} = 4.0 \pm 0.4$) can be used to predict an expected effective temperature. Using solar-metallicity evolutionary model calculations for M dwarfs $T_{\rm eff} \sim 2250$ K (based on model X of Burrows *et al*, 1993b) or $\sim$ 2150 K (based on Baraffe *et al*, 1995).

(6) Gl 569B: it was discovered by Forrest *et al* (1988) together with its companion YD M dwarf Gl 569A. It is a cooling brown dwarf candidate. From the distance (known through the parallax of Gl 569A), we know that it is overluminous by 0.65 mag with respect to stars with the same colours and spectral type. This is thought to be due to a low value of log g and a solar-type metallicity (Jones *et al*, 1996). However, there is no strong evidence for it to be a young cooling brown dwarf.

(7) GD 165B: discovered by Zuckerman and Becklin (1987), this is a good brown dwarf candidate. It has a white dwarf companion whose age is at least 0.5 Gyr (Jones *et al*, 1994). GD 165B is separated from the white dwarf by 100AU so it is unlikely that its surface composition has been influenced by the evolution of the primary. Therefore, solar

abundances are assumed. Using the models of Burrows *et al* (1993b), GD 165B's surface gravity must lie between 5.25 and 5.45. It is considered a good brown dwarf candidate because of its sub-luminosity. It has been observed before by Jones *et al* (1994, 1996) and Kirkpatrick *et al* (1993). Recently, this object acquired more importance since Tsuji *et al* (1996b) found almost clear evidence of the presence of dust in its photosphere.

(8) LHS 318: we observed this object only at the central wavelength of 1.135 μm. This is a high proper motion star. No references could be found apart from the bolometric apparent magnitude (m_b=16.1) from the Simbad database.

(9) F16156, (11) Z12401–304 and (12) F16048: these objects, unknown to Simbad database, are IRAS[1] sources. Their K magnitude is:

F16156–283: ~ 5

Z12401–304: ~ 6

F16048–314: ~ 9

Comparing their spectra is significant in that the K band is a good indicator of changes in effective temperature. However, we observed these sources only at the central wavelength of 1.135 μm.

(10) LHS 2238: it is a high proper motion star. Its spectral type has not been determined yet. The only two references found were (i) Kirkpatrick *et al* (1995) who observed the object but did not publish the spectrum; (ii) Lee (1984) who performed a proper-motion survey and estimated the photograpic magnitude to be 15.24.

During the observations of GD 165B (7) and GL569 B(6), we encountered several technical problems with the instrument due mainly to the dichroic mirror not being in the correct position. As a result, the spectra obtained are highly affected by noise.

TVLM 513 (5) and GL 569B (6) are very interesting because of their similarity and well known parameters. A direct comparison of their SED and, moreover, a detailed analysis

[1]The Infrared Astronomical Satellite (IRAS) was a joint project of the US, UK and the Netherlands designed to perform a reliable survey of infrared point sources. For more details refer to http://www.ipac.caltech.edu/ipac/iras

of their spectral signature could be a tool in: 1) accurately determining their log g. 2) providing a test for the latest atmospheric models. We have attempted a spectral analysis of these stars which is not presented in this thesis. For more details, see Viti *et al* (1997b).

Also in Table 8.2 I list the information available for most of the targets. The entries missing from the table are the ones for which we could not find references in the literature or in the Simbad database.

8.1.2 Standards

Standards have been carefully chosen in order to remove from the observations the effects of atmospheric absorption. For each target, we chose an A0 or B9 standard which was within 4 degrees where possible. Table 8.3 lists the respective standards for each target.

The choice of those standards to remove telluric bands of water, oxygen, carbon dioxide and methane was based on the expectation that such stars have no features in common with M dwarfs and are in general mainly featureless except for some hydrogen lines. The airmass difference between object and standard used never exceeded 0.05 and so we are confident that the spectra have good cancellation of atmospheric features. Some of the hydrogen lines introduced into the spectrum when dividing by the standard had, however, to be removed manually.

8.2 Data reduction

The data reduction has been performed with the following packages:

(i) CGS4DR (Puxley *et al*, 1992).

(ii) FIGARO, SPECDRE, KAPPA, DIPSO packages provided and supported by Starlink.

Both the object and the standard were wavelength calibrated by using arc lines of krypton, argon and xenon. The accuracy of the calibration is around 0.5×10^{-3} μm.

Table 8.2: The spectral type, when known, the V magnitude, the infrared photometry, the metallicity, the effective temperature and the surface gravity of each target.

	Object	Sp Type[a]	M_v[b]	J-H[c]	H-K[c]	K[c]	M/H[d]	T_{eff}[e]	log g[f]
1	CM Dra	M4e	12.9	0.56	0.28	7.84	$\leq$ -0.5	3150	5.0
2	Gl 299	M4	13.65	0.47	0.28	7.64	-1.5	3120	5.15
3	VB10	dM8e	17.30	0.66	0.44	8.80	0.0	2750	5.18
4	GJ 1111	dM6.5e	16.99	0.58	0.36	7.26	0.0	2600	5.2–5.3
5	TVLM 513	M8.5V	..	0.65	0.54	10.77	0.0	2400	5.0
6	Gl 569B	M8.5	..	..	..	..	0.0	2360	4.97
7	GD 165B	$>$ dM10	..	1.02	0.61	14.17	0.0	1860	5.4

[a] For objects 2, 4, 6 and 7 see Jones *et al* (1996); for objects 3 and 5 see Kirkaptrick ; *et al* (1995);for object 1 see Lacy (1977).

[b] For object 5 see Tinney *et al* (1993); for objects 2 and 4 see Leggett *et al* (1996); for object 1 see Lacy (1977).

[c] For objects 3 and 7 see Jones *et al* (1994); for object 5 see Tinney *et al* (1993); for objects 2 and 4 see Leggett *et al* (1996); for object 1 see Lacy (1977).

[d] For objects 2, 3, 4, 6 and 7 see Jones *et al* (1996); for object 5 see Tinney *et al* (1993); for object 1 see Lacy *et al* (1977).

[e] For object 3 see Jones *et al* (1995); for object 7 see Jones *et al* (1994); for objects 2, 4 and 6 see Jones *et al* (1996); for object 5 see Tinney *et al* (1993); for object 1 see Lacy 1977.

[f] For all the objects see Jones *et al* (1996).

Table 8.3: Standards used.

	Target	Standard	V_{mag}	Spectral type
1	CM Dra	SAO29931	5.70	A2p
2	Gl 299	SAO116244	5.7	A0
3	GJ 1111	SAO80113	5.98	B9.5
		BS3449	4.66	A1
4	VB10	SAO124155	8.12	A0
5	TVLM 513	SAO101379	6.0	A0
6	Gl 569B	SAO101293	5.8	A0
7	GD 165B	SAO101137	6.0	A5
8	LHS 318	SAO82166	5.8	A2
9	F16156	SAO184301	4.9	A0
10	LHS 2238	SAO43344	5.8	A2
11	Z12401–3024	BS4874	4.9	A0
12	F16048	SAO184301	4.9	A0

8.2.1 Sky Subtraction

The sky subtraction was obtained with standard routines which eliminate any residual sky emission due to the variance of sky brightness between object and sky pairs. For some of the targets, mainly the ones in close binaries, it was very difficult to get rid of the residual sky without affecting the signal. The latter was spread among three rows. To extract the spectrum from the sky subtracted signal, an Optimal Extraction technique (Horne, 1986) was used. This combines the rows using weights based on the spatial profile of the stellar image. We found that this technique is very efficient for single objects but is faulty for close binaries. In fact, the rows where the signal from the primary target is collected are much affected by the signal from the secondary, usually 'brighter'. In some of these cases, we empirically found it best to simply extract the three rows or even just the central row. In the latter case we obviously might have lost some of the signal, which would then affect the absolute flux calibration, but we believed that, for most of the targets, we preserved the correct spectral energy distribution of the object. The targets for which this was done are:

GD 165B for the 2^{nd} (λ_c=1.415 μm) and for 3^{rd} position (λ_c=1.635 μm);

GL 569B for the 1^{st} position (λ_c=1.135 μm). We find that the SED of the latter is still contaminated by the primary target.

8.2.2 Flux Calibration

The flux calibration was obtained by using the standard stars which were more or less of known spectral shape and brigthness. In general, the procedure consists of dividing the object spectrum by the spectrum of the standard and then by multiplying it by the known flux of the standard at each wavelength. The routine that we used to follow this procedure was IRFLUX, from the FIGARO package. The information required from this routine are the temperature of the standard and its magnitude at a particular band. This process also removed the atmospheric absorption features from the object spectrum. The airmasses of the object and the standard have to be close so that they have the same

extinction coefficient. As long as the standards do not have common features with the targets, the flux calibration should leave the deep, strong molecular bands and the atomic features unaltered.

Once the flux calibration for each wavelength position has been performed, the J, H and K bands, divided into four regions, could be joined. In the overlapping regions, the spectral features and the continuum are in fact well reproduced but we note that the flux levels between different spectral regions were not in agreement. The percentage of disagrement varied with the targets and on average corresponds to $\sim$10 %. These disagreements could be the results of weather variations while observing, such as wind effects. In fact, we believe that the the target 'moved' along the slit. As 'extreme' cases, we also found that for the observations centered at 1.135 μm for GD 165B, and 1.415 μm for GD 165B and CM Dra, the rows where most of the signal was supposed to be, were not the ones corresponding to the original position of the target in the slit.

The overlapping regions where therefore combined by adjusting the flux levels for each band. Where known, we took the photometry from the literature to obtain the right flux level for J, H and K (for example CM Dra, see Chapter 9).

8.3 The reduced spectra

Figure 8.1 shows the reduced complete spectra for some of the objects with decreasing effective temperature (known from literature) from top to bottom. Figure 8.2 shows the reduced spectra of the rest of the targets in the available positions. From this sample, spectral features such as (i) water bands and (ii) strong atomic lines, are already indicators of metallicity and effective temperature changes without even having to do a thorough spectral analysis. A complete analysis has, so far, only been done for the binary system CM Dra (Chapter 9 and Viti *et al*, 1997a) and partly for TVLM 513-4546 and GL 569b (Viti *et al*, 1997b). We have identified the strong features in the spectra using line identifications from Leggett *et al* (1996) and Jones *et al* (1996). It can be seen that most of the dominant features in the JHK bands are due to water vapour bands and carbon monoxide.

In particular, in the region from 0.96 to 2.4 μm, there are two strong water absorption bands centered at 1.4 and 1.9 μm. In Jones *et al* (1994, 1995), it was shown that water vapour opacities become more dominant as the effective temperature decreases. In fact, although the continuum is not very sensitive to small ($\sim$ 100 K) changes in effective temperature, the water bands are. Therefore, they can be used as a tool for interpolating an effective temperature scale. Without claiming any detailed spectral analysis, we can see from Figure 8.1 how sensitive water and any atomic structure is as a function of ΔT_{eff}. Changes in metallicity are not so obvious in the infrared since water is a single metal species. Figure 8.3 is an example of a water band (Left plot) and some Na I and K I lines for the stars in Figure 8.1. All these features are dependent on the temperature, metallicity and surface gravity. Although the targets are not very different in spectral type, we notice how the above features change. A detailed spectral analysis of the single resolved features can therefore be a very useful tool in determining an effective temperature, metallicity and surface gravity scales.

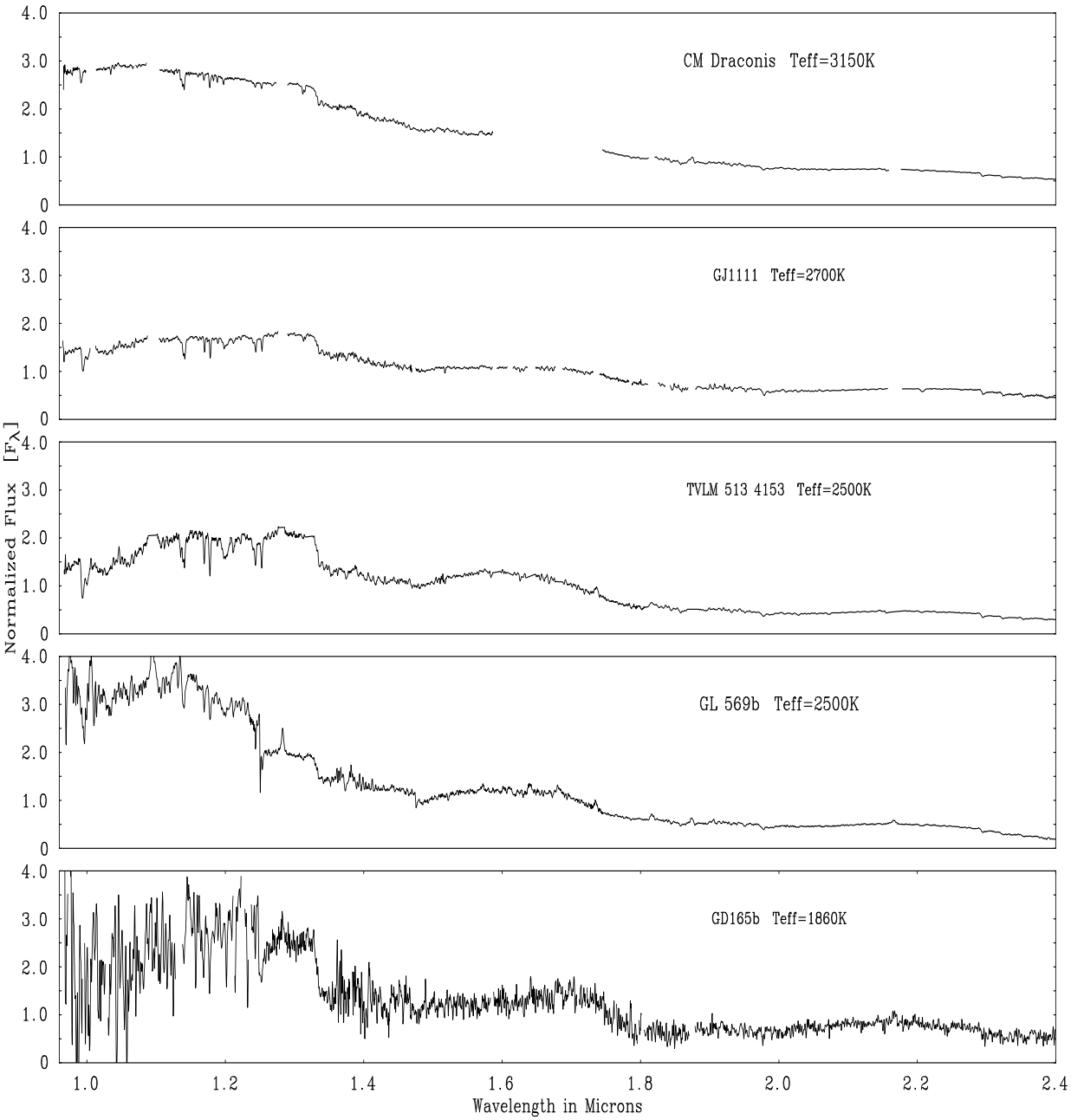

Figure 8.1: A spectral sequence of M dwarfs of different effective temperatures and metallicities: the effective temperature decreases from top to bottom.

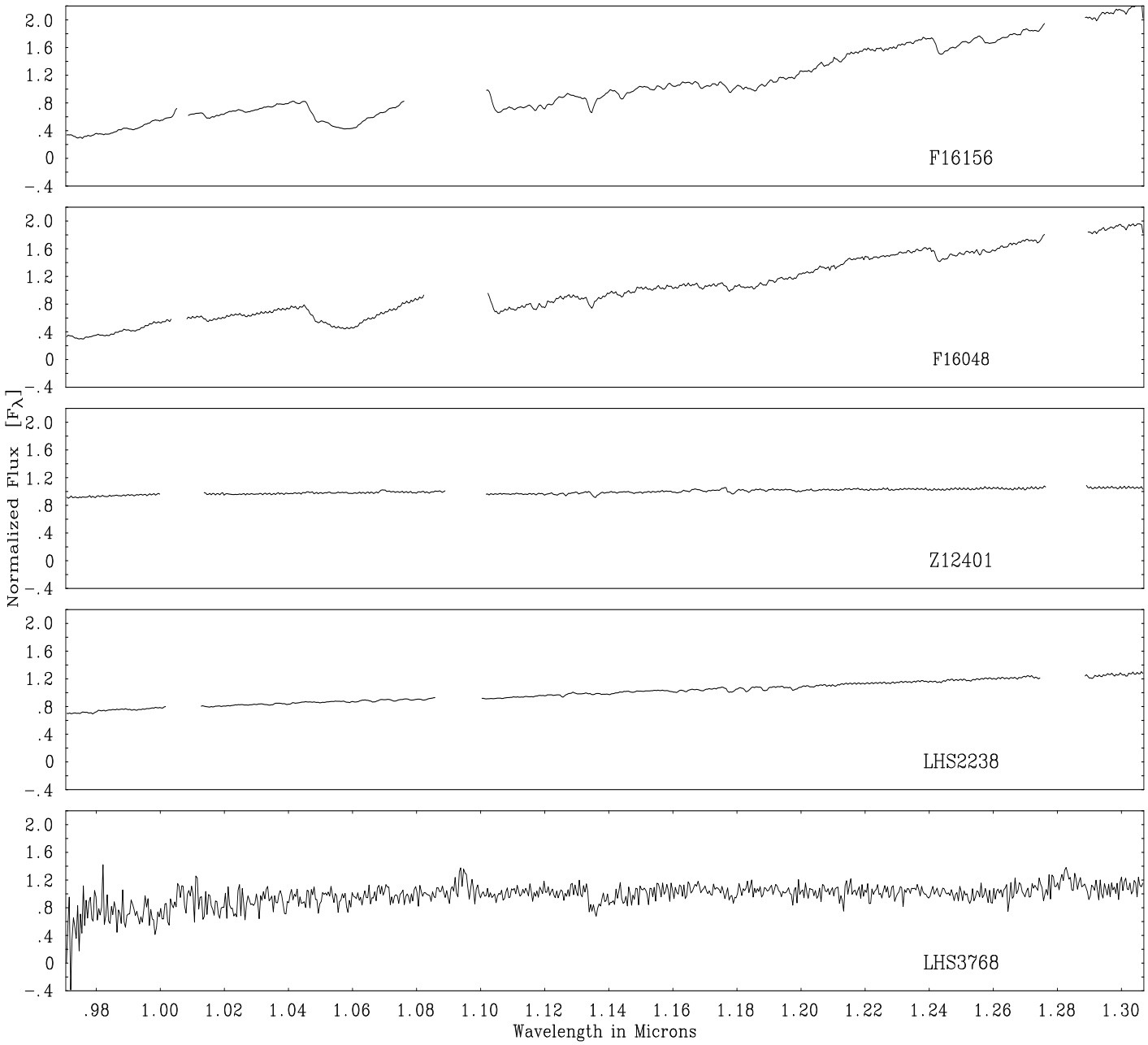

Figure 8.2: A spectral sequence of M dwarfs form 0.97 to 1.307 μm. Hydrogen emission lines introduces by the standard have been manually removed (gaps).

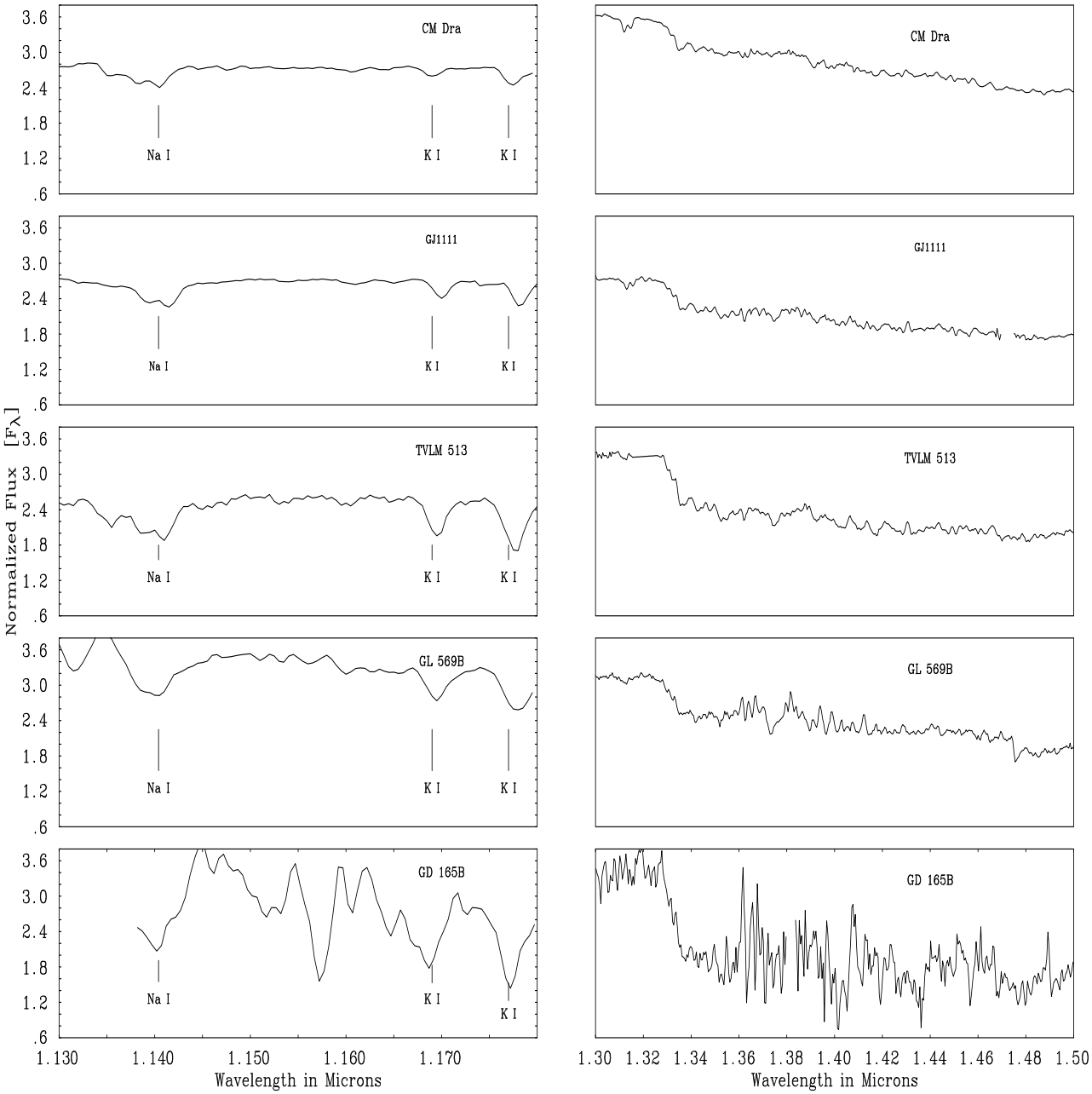

Figure 8.3: Left: 1.13–1.18 μm. A Na I line and two K I lines are labelled. Right: 1.3–1.5 μm where there is a strong water band, centered at 1.4 μm.

Chapter 9

The eclipsing binary system CM Draconis

Among the M dwarfs observed and reduced (see Chapter 8), CM Draconis (CM Dra, hereafter) is the most remarkable one because it is an eclipsing binary where the two components are almost twins. In this Chapter we compare infrared and optical observations of CM Dra with synthetic spectra computed using the stellar atmosphere code PHOENIX (Allard & Hauschildt, 1995). We explore different methods to derive the effective temperature and metallicity of the system using spectral information and the photometry of the system. By doing so, we also find the fundamental problems both with the modelling of LMS and the observations.

9.1 Brief history of CM Draconis

There are few observations of known-mass low mass stars. Parameters such as effective temperatures, masses and metallicities, vital in determining positions in the H-R diagrams, remain controversial.

CM Dra (hereafter, CM Dra) is the lowest mass main-sequence eclipsing binary known (RA =16:34:24, Dec = 57:09:00 J2000, V = 12.9 mag). It has a short period of 1.268 days (Metcalfe *et al*, 1996), a large space velocity (163 km s^{-1}) and low flaring rate

which suggest it belongs to Population II (Lacy, 1977). Paczynski & Sienkiewicz (1984) point out that CM Dra could be an important system for cosmology because its initial helium abundance can be determined from models of its structure. Because it is one of the faintest, smallest and least massive eclipsing main-sequence binaries so far known, its colour-luminosity relationship is a prime indicator of what happens to very low mass stars at the bottom of the main sequence.

Some of the fundamental physical properties of the components of CM Dra have already been determined accurately. Most important are the individual masses of $M_{\rm A} = 0.2307\pm$ 0.0010 and $M_{\rm B} = 0.2136\pm$ 0.0010 $M_{\odot}$ and radii of $R_{\rm A} = 0.2516\pm$ 0.0020 and $R_{\rm B} = 0.2347\pm$ 0.0019 $R_{\odot}$ (Metcalfe *et al*, 1996), surface gravities of $\log g = 4.999 \pm 0.007$ for CM Dra A and $\log g = 5.028 \pm 0.007$ for CM Dra B (Jones *et al*, 1996). The precision of these values far exceeds those known for any other M dwarf and means that CM Dra should be an excellent system for comparison with model calculations. This gave us the motivation to improve the current values for the metallicity and effective temperature of the system.

Lacy (1977) found the temperature to be 3150±100 K using a parallax of 0.069 ± 0.005arcsec. Chabrier & Baraffe (1995, hereafter, CB95) argued that the effective temperature of CM Dra is 3300 K based on a comparison between evolutionary models and observations. Assuming $T_{\rm eff}$ to be 3300K, they then recalculated the parallax to be 0.063, different from the value adopted by Lacy. We note that the 'current' value for the parallax is 0.0692 ± 0.0025 arcsec (van Altena *et al*, 1995). CB95 also indirectly investigated the metallicity of CM Dra finding agreement over a range of values. They found agreement between models and observations for metallicities of $-0.5 \leq [M/H] \leq 0.0$ for 3086 $< T_{\rm eff} <$3366 K, where [M/H] is the ratio of metal abundance to hydrogen content in the star. However, the only published spectrum of CM Dra lends support for CM Dra to belong to Population II. Rucinski (1978) intercompared optical Mg, MgH and TiO features of CM Dra with six other M dwarfs and concluded that it may be a subdwarf but noted that the accuracy of determination is low. Finally Gizis (1997) spectroscopically classified a series of M-dwarfs and M-subdwarfs and found CM Dra to have a solar metallicity using

spectra over the range 0.62 μm $\leq \lambda \leq$ 0.74 μm.

A modern spectral measurement covering a wide spectral range is thus desirable to determine reliably the metallicity and the effective temperature. Here we make such a study by comparing observed spectra from 0.40 to 2.41 μm with synthetic spectra computed for a wide range of effective temperatures and metallicities. We adopt a two-step direct approach:

1) attempt a general flux distribution fit to the models 2) attempt a detailed spectral analysis of restricted regions of the spectra.

The observations and data reduction procedures are described in Section 9.2. The models used are discussed in Section 9.3. Sections 9.4–7 present the analysis performed and finally in Section 9.8 we summarize the results obtained.

9.2 Observations

Figure 9.1 shows the spectrum of CM Dra from 0.40 to 2.41 μm. In the infrared spectrum (from 0.96 to 2.41 μm) the small gaps represent regions where hydrogen emission lines, introduced by the standards, were manually removed. We did not manage to observe the bigger region centered around 1.635 μm due to a problem with the rotation of the dichroic in CGS4. We therefore adopted the differential magnitudes from Lacy (1977) to obtain the absolute flux of the H band.

9.2.1 Infrared observations

CM Dra was observed, along with other M dwarfs, on the nights of 1995 May 14 and 16 with the Cooled Grating Spectrometer 4 (CGS4, http://www.jach.hawaii.edu/UKIRT.new/-instruments/cgs4/handbook.html) on the UK Infrared Telescope (UKIRT) on Mauna Kea, Hawaii.

The data reduction is described in Chapter 8. The coverage, resolution and integration times of the observations are listed in Table 9.1. Each grating position overlaps with the previous and the next at the two ends which ensures reliable coverage of the whole region.

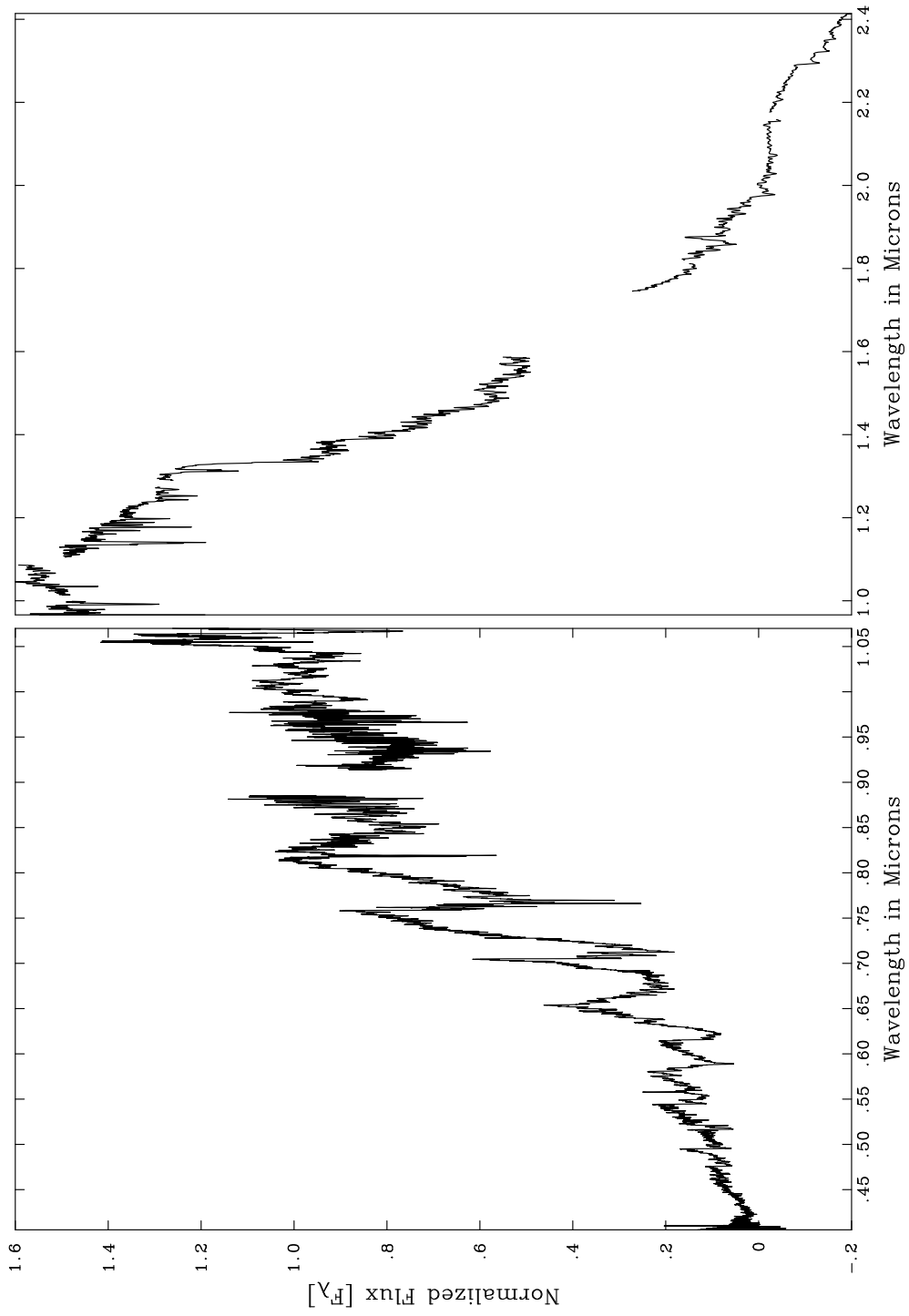

Figure 9.1: Spectrum of CM Dra. Left Plot: optical spectrum from 0.4056 to 1.007 μm. Right Plot: Infrared spectrum from 0.97 to 2.41 μm. The region between 1.587 and 1.747 μm has not been observed. The smaller gaps are due to the hydrogen lines removed by hand.

Table 9.1: Central wavelength and wavelength coverage, resolution, dates of the observations and integration times.

λ_{cen}	λ_{range}	$\Delta\lambda$	Date	Int.Time(total)
μm	μm	μm		minutes
1.135	$0.96 - 1.3$	0.00044	14/05/95	17
1.415	$1.249 - 1.508$	0.00044	14/05/95	10
1.635	$1.47 - 1.8$	0.00044	14/05/95	15
2.07	$1.739 - 2.414$	0.00088	14/05/95	10
1.415	$1.249 - 1.508$	0.00044	16/05/95	15
2.07	$1.739 - 2.414$	0.00088	16/05/95	10

To remove telluric bands of water, oxygen, carbon dioxide and methane, we observed an A2 star, SAO29931 and used it as a standard. Such stars are not expected to have any features in common with stars like CM Dra and are mainly featureless except for some hydrogen lines. The airmass difference between object and standard used never exceeded 0.05 and so we are confident that the spectra have good cancellation of atmospheric features. Some of the hydrogen lines introduced into the spectrum when dividing by the standard had, however, to be removed manually. The accuracy of the wavelength calibration is around 0.5×10^{-3} μm.

9.2.2 Optical Observations

Observations were taken during the night of 1996 July 20 at the Steward Observatory 90 inch Bok Telescope located at Kitt Peak by A. Schweitzer (private communications, see Viti *et al*, 1997a). He used a Boller & Chivens Spectrograph with an echellette configuration consisting of 180 lines/mm grating and a prism as cross–dispersor. The detector was a 1200 x 800 Loral CCD. The wavelength region covered is from 0.4 to 1.0 μm at an average resolution, $\lambda/\Delta\lambda$ of 6000. The integration time of the observations was 900 seconds. Six

orders were joined and they were all overlapping apart from the region around 0.90 μm. To remove telluric features and instrumental fringes the Oke standard stars (Oke, 1990; Colina & Bohlin, 1994), SAO29931 (A2), BD33+2642 (B2) and BD25+4655 (O) have been used. BD33+2642 and BD25+4655 were also used to flux calibrate the spectrum although the absolute flux calibration is not reliable since the night was not photometric due to the presence of cirrus clouds.

To obtain an absolute calibration we have calibrated the single orders using Lacy's photometry (1977). Both the object and the standards were wavelength calibrated by using arc lines of HeAr. The wavelength calibration is accurate to $\sim 0.01 \times 10^{-3}\,\mu$m. The data reduction was performed using the IRAF package.

We can not entirely rely on the reddest part of the optical spectrum because:
1) many telluric features are difficult to remove and cause substantial noise. Some contaminate important atomic lines such as the Na I 0.819 μm and the potassium KI 0.768 μm doublet;
2) from 0.84 μm to 1.0 μm we did not manage to correct completely for strong instrumental fringes.

9.2.3 Phase information

Our spectroscopic measurements of CM Dra were made at a variety of different phases causing the spectra on which this analysis is based to be composite with different spectral regions having different relative contributions from the A and B component. We calculated the phase at which the system was during the observations.
For the UKIRT observations: for the first night (14 May 1995) we observed the regions centered at 1.135, 1.415, 1.635 μm when one component is fully visible together with ∼85% of the other. During the integration time of the observation of the region centered at 2.07 μm one component was fully visible together with ∼80% of the other. The 2nd night of observations (16 May 1995) we observed the regions centered at 1.415 and 2.07 μm when

one component was fully visible together with ∼60% of the other. The optical region was also observed during the latter phase.

We note that when integrating the flux density, as described below, and when performing the spectral analysis we have not taken account of the phase at which spectral observations of CM Dra were made. We choose not to use this information because (1) we do not feel confident that our spectral photometry is better than 30 percent and (2) the components will be very similar, for example the measurements of Lacy (1977), on which much of this analysis depends, could not distinguish a difference in the temperature between A and B.

9.3 Models employed for the analysis

Model spectra were computed for this project with the model atmosphere code PHOENIX using direct opacity sampling treatment of the opacity of H_2O as described in Allard *et al* (1994). The data used here include the MT (Schryber, 1995; Miller *et al*, 1994) water vapour linelist and the Collins-Jørgensen TiO line list (Collins & Faÿ, 1974; Jørgensen, 1994). Since the surface gravity of the CM Dra pair is close to $\log g = 5.0$, we have investigated model spectra in the effective temperature and metallicity parameter spaces for this value of gravity only.

We have also used the more recent NextGen model structures (which became available after completion of this work). We have undertaken some tests with these latest models. Although we noticed improvements in particular in the optical fit which is most sensitive to changes in the model structure, we find no difference in the results of our analysis, in particular in the infrared. An extensive review of the models and their properties can be found in Allard *et al* (1997).

In this work we use model temperatures from 3000 to 3400 K and metallicities from [M/H]= −1.0 to +0.2. For $T_{\rm eff} = 3150$K, two models at [M/H]= −1.5 and −2.0 were also computed. The parameters represent the probable extremes of metallicity and effective temperature of CM Dra. The rotational velocity has also been calculated with the latest

values for the period and radii yielding a value of $v_{\rm rot} = 10 \pm 0.02$ km s^{-1}, in agreement with Metcalfe *et al* (1996). This means that any change induced by rotation in the models would be negligible at the resolution of our observations as even our highest resolution observations only have a resolution of 50 km s^{-1}.

Jones *et al* (1996) investigated the sensitivity of observations of M dwarfs and a previous generation of these models to changes in effective temperature and gravity over a small region from 1.16 to 1.22 μm. With similar resolution data, we first investigate the sensitivity of the synthetic spectra to changes in temperature and metallicity for the region from 1.0 to 2.4 μm, noting that, unlike the study of Jones *et al* (1996), the precision to which the gravity is known for CM Dra means that we can ignore it as a variable in the analysis. Figure 9.2(a–d) shows samples of such an investigation. In (a) and (c), two models have been normalized to have the same mean value and over plotted; in (b) and (d) the two models have been divided by one another. The models were selected in such a way to show the two extremes in each parameter. From Figure 9.2(a–b) it can be seen that change in temperature affects the water absorption (see for example the regions centered at 1.4 μm and 1.9 μm). Water gets dissociated at high temperatures and the absorption bands are weaker. Figure 9.2 show some sensitivity to change in metallicity; however the weaker absorption lines, which are not affected as much by blending effects, seem to be sensitive enough to variations in the metallicity for us to discriminate between models. Significant metallicity-sensitivity can be seen in the prominent 2.21 μm Na I and 2.29 μm CO band features.

9.4 CM Dra Parameters

We adopt the recently derived values for the radii of CM Dra from Metcalfe *et al* (1996) to calculate an effective temperature for the system. To derive the total luminosity we adopt a parallax of 0.0692 ± 0.0025 arcsec (van Altena *et al*, 1995). We obtain the total absolute flux of the system by integrating the flux density over the total spectral region from 0.1 to 100 μm obtained by normalizing the infrared and optical observed spectra to

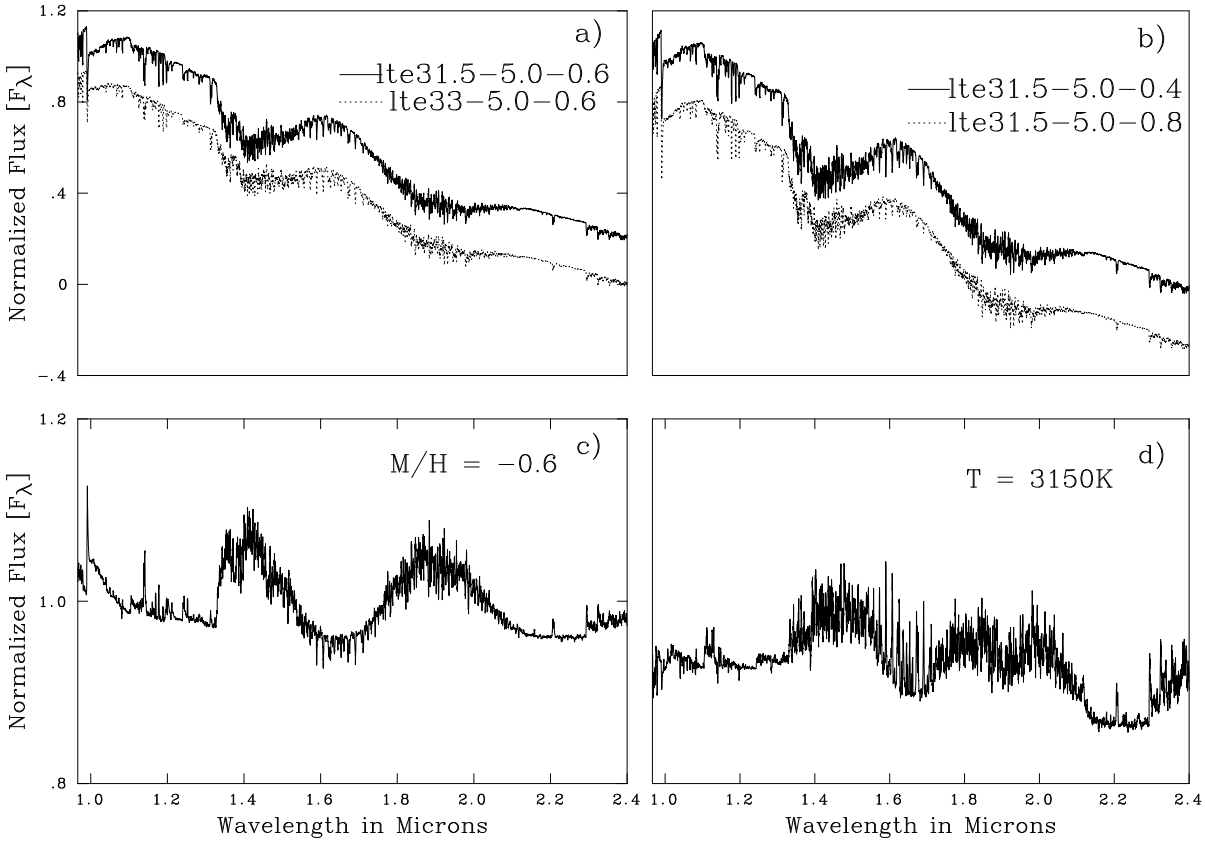

Figure 9.2: Sensitivity of the models to changes in $T_{\rm eff}$ and [M/H]. The different models are distinguished using the notation lteTT-G.G-Z.Z, where lte = local thermodynamic equilibrium assuming ζ(LTE) = 2 km s^{-1}, TT = $T_{\rm eff}/100$, G.G = log g (surface gravity), Z.Z = [M/H] (metallicity), where [M] $\equiv$ log M_{star} – log $M_{\odot}$ for any abundance quantity M. Top left: comparison of the $T_{\rm eff}$=3150 K model with the $T_{\rm eff}$=3300 K one at a fixed metallicity, [M/H]= −0.6. The y axis of the 3300 K model has been shifted by 0 .2 for clarity. Bottom left: the 3150 K model divided by the 3300 K one. Top and bottom right: same as left but comparing [M/H]= −0.4 with [M/H]= −0.8 for a fixed $T_{\rm eff}$=3150K.

Lacy's photometry for the ultraviolet and far infrared bands and by adding the rest of a synthetic spectrum (we used a $T_{\rm eff}$=3300K, [M/H]= -0.8 model). In particular, we do not consider the flux calibration of the optical and infrared spectra sufficient to warrant adjustments of each spectrum to allow for the orbital phase (discussed above). Figure 9.3 shows the overall observed spectral energy distribution (SED) of CM Dra.

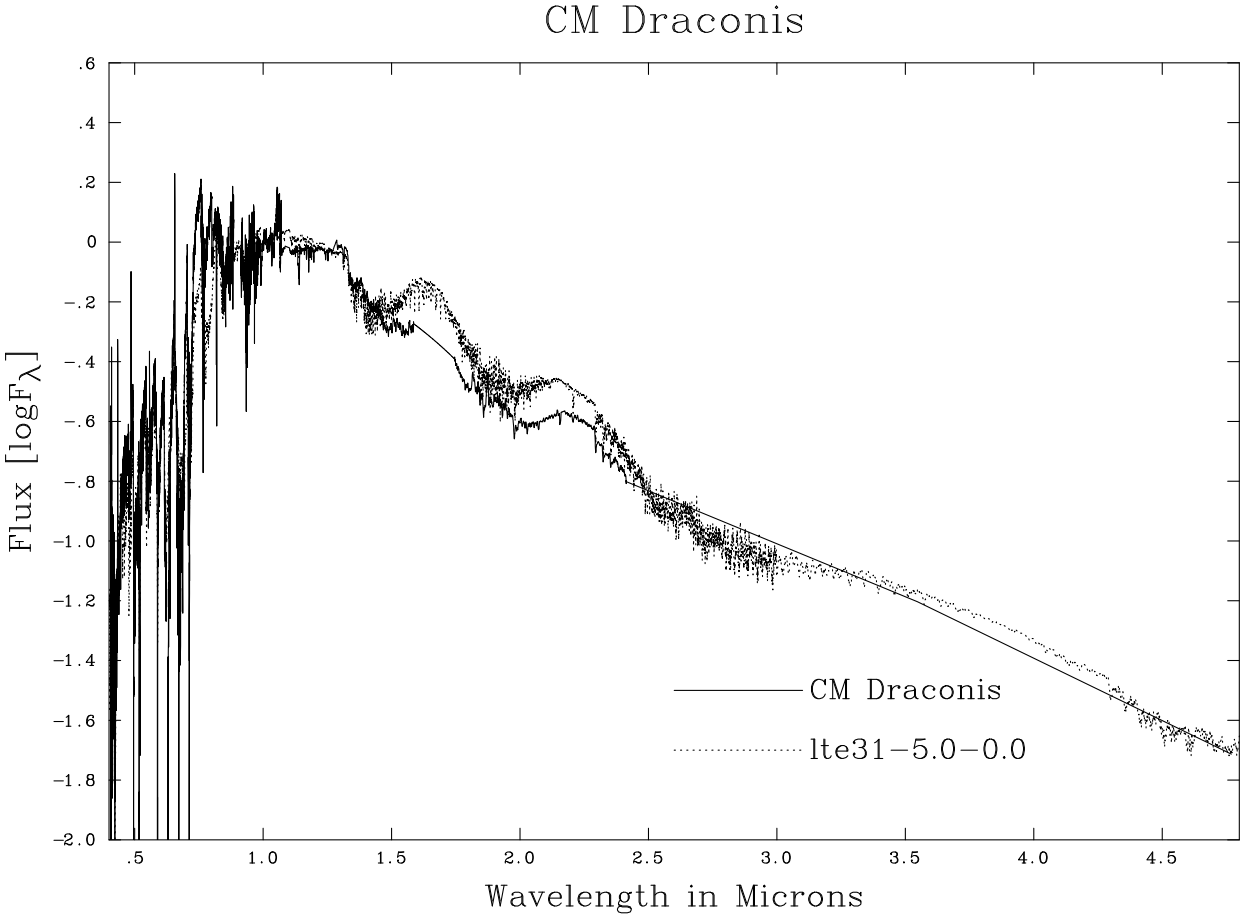

Figure 9.3: Overall spectral energy distribution for CM Dra from 0.4 to 5.0 μm, obtained by joining the observed optical and infrared spectra, is compared with a solar metallicity model at $T_{\rm eff}$=3100K.

We thus derive a total luminosity of $9.3600 \times 10^{-3} \pm 0.670 \times 10^{-3} L_\odot$ (L_A=$4.9981 \times 10^{-3} L_\odot \pm 0.504 \times 10^{-3} L_\odot$ and L_B=$4.3619 \times 10^{-3} L_\odot \pm 0.441 \times 10^{-3} L_\odot$). This implies an effective temperature for CM Dra A and CM Dra B of respectively of 3073 $\pm$ 57 K and

Table 9.2: Luminosities, effective temperatures, rotational velocity and orbital velocities of CM Dra A and B

	L ($L_\odot$)		T_{eff} (K)		v_{rot}(km)	V_{orb}(km)
	This work	Lacy (1977)	This work	Lacy (1977)		
A	$(4.9981 \pm 0.504) \times 10^{-3}$	$(5.5 \pm 0.8) \times 10^{-3}$	3073 ± 57	3150 ± 100	10	5.7124
B	$(4.3619 \pm 0.441) \times 10^{-3}$	$(4.8 \pm 0.7) \times 10^{-3}$	3076 ± 57	3150 ± 100		5.3287

3076 ± 57 K. Lacy calculated the effective temperature to be 3150 ± 100K. By employing the more accurate values for the radii by Metcalfe *et al* we have reduced the error by 40%. With the new values of the radii and period from Metcalfe *et al* (1996) we also calculated the orbital velocities of the two components. See Table 9.2 for a summary of CM Dra parameters.

9.5 Spectral analysis of the "optical" region

The optical observations were at slightly lower resolution than the models, therefore we matched the latter to the instrumental resolution by smoothing with a triangular function and resampling. This mimics the effect of detection by the square pixels used by the detector and three times oversampling employed for the observations. The smoothing was performed using routines within the KAPPA and SPECDRE Starlink packages. We attempt an analysis divided in two sections: the general flux distribution comparison and a more detailed spectral analysis.

9.5.1 General Flux distribution analysis

We have compared by eye the SED of CM Dra with most of the computed models. More specifically at every temperature for metallicities of [M/H]=-1.0,-0.8,-0.6,-0.4,-0.2, 0.0. Figure 9.4(a-f)– 9.8(a-f) show such comparisons.

We tried to find the best match in metallicity for each effective temperature and vice versa. We found that the best model fit is reached at low temperature, as low as 3000K.

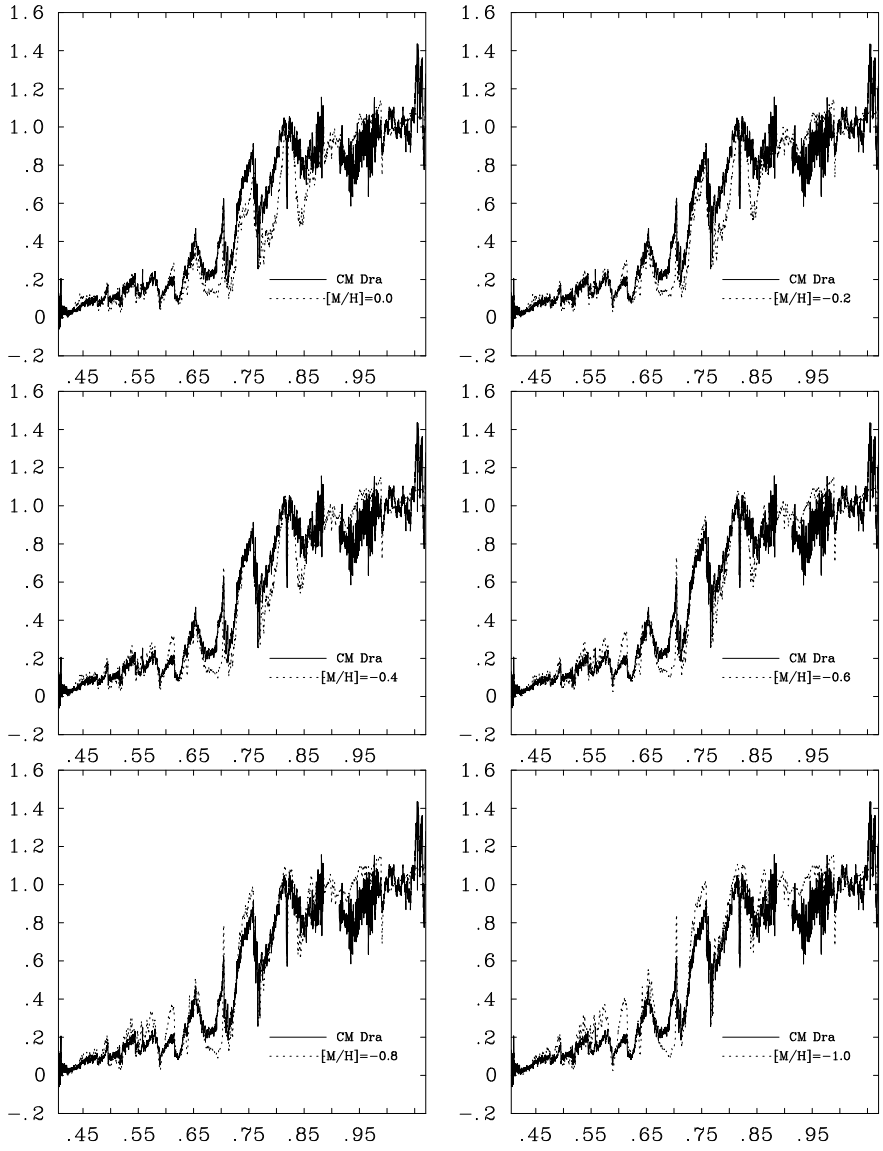

Figure 9.4: SED comparisons between observed spectra and models at T_{eff}=3000K for [M/H]=-1.0,-0.8,-0.6,-0.4,-0.2,0.0

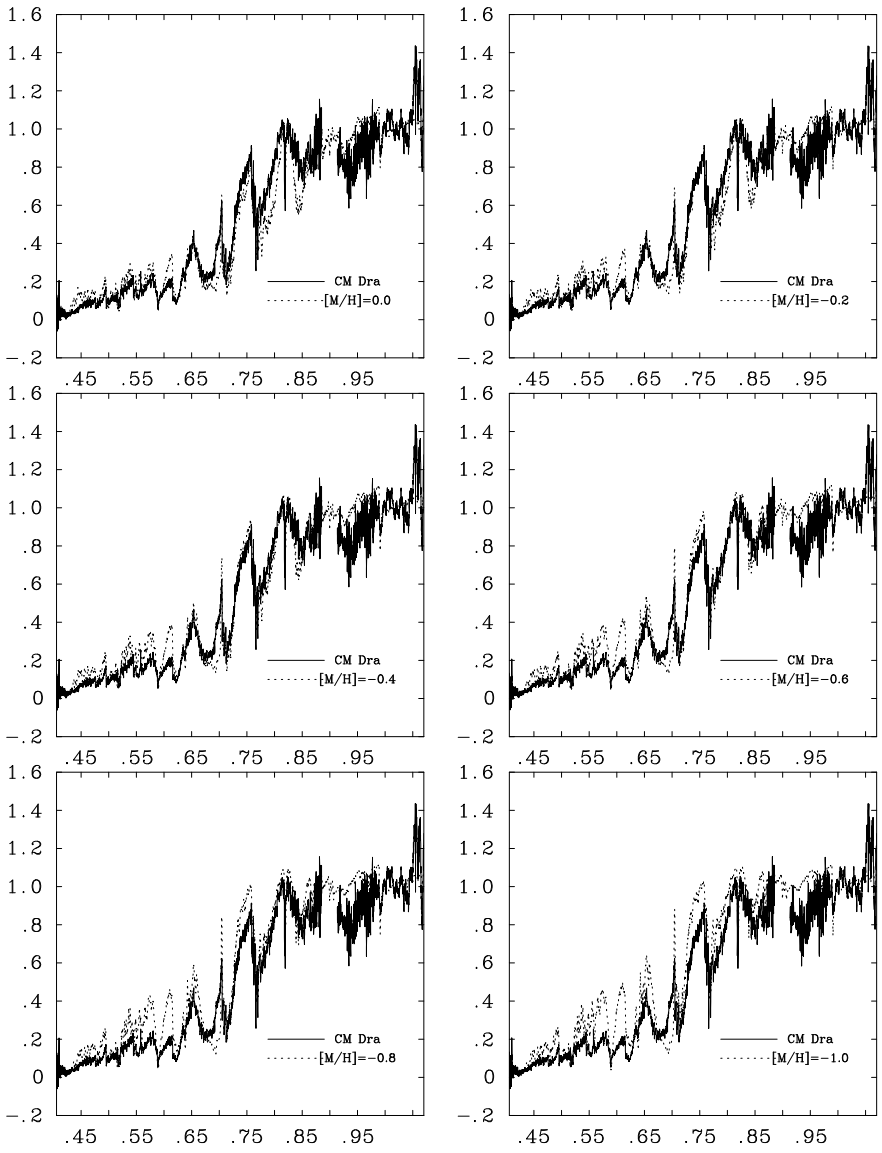

Figure 9.5: SED comparisons between observed spectra and models at T_{eff}=3100K for [M/H]=-1.0,-0.8,-0.6,-0.4,-0.2,0.0

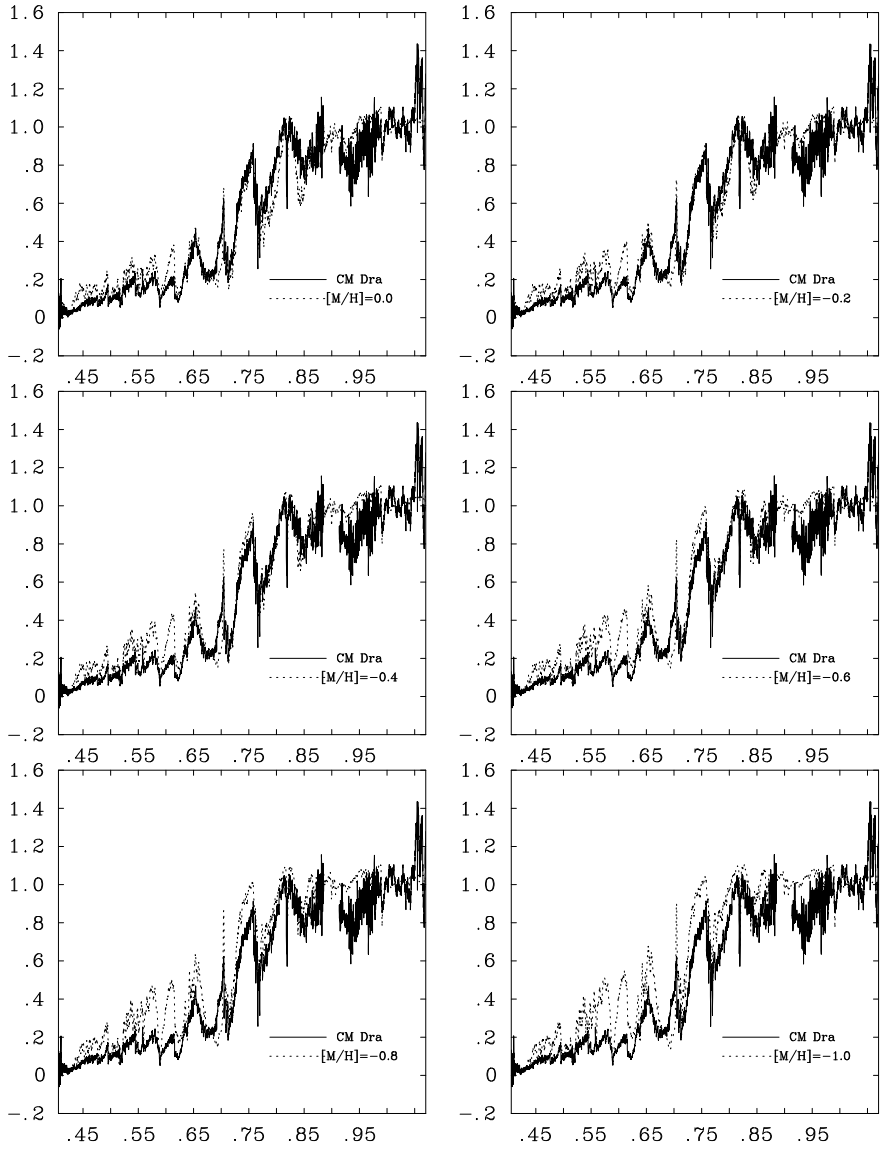

Figure 9.6: SED comparisons between observed spectra and models at T_{eff}=3150K for [M/H]=-1.0,-0.8,-0.6,-0.4,-0.2,0.0

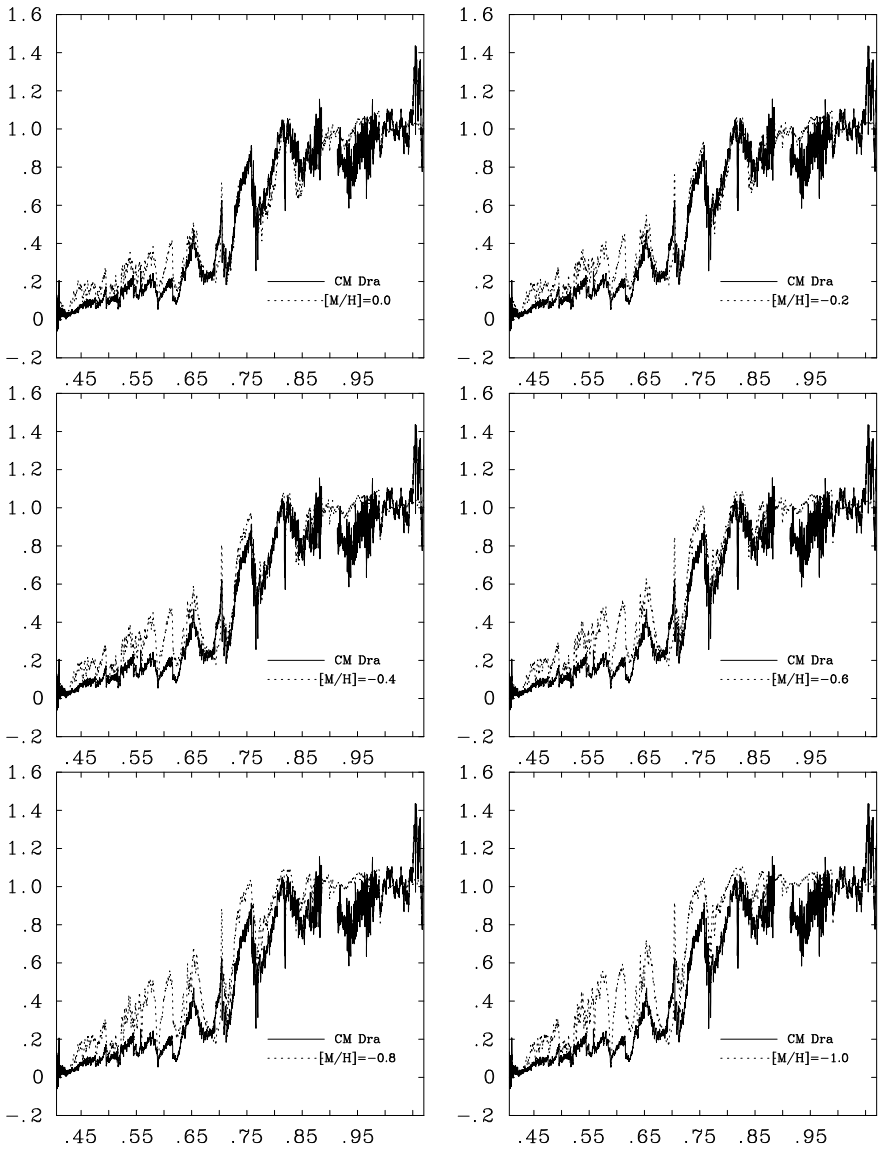

Figure 9.7: SED comparisons between observed spectra and models at T_{eff}=3200K for [M/H]=-1.0,-0.8,-0.6,-0.4,-0.2,0.0

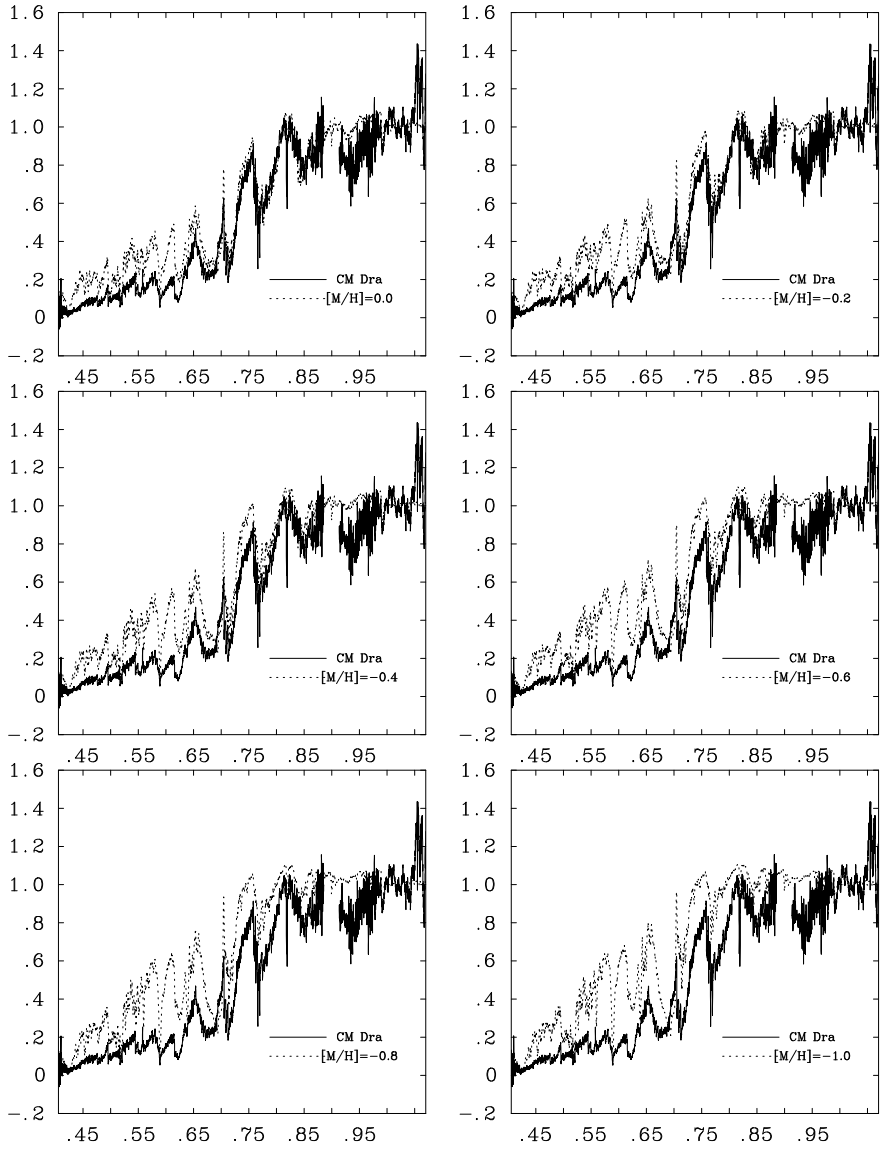

Figure 9.8: SED comparisons between observed spectra and models at T_{eff}=3300K for [M/H]=-1.0,-0.8,-0.6,-0.4,-0.2,0.0

For low temperatures models, some absorption bands are better fitted by low metallicity models. For example, the synthetic flux around ~ 0.72 μm (which is due to a band of TiO) is too high in models at solar metallicities. High temperature models give a worse fit for low metallicities: for example for $T_{\rm eff} \geq 3150$ K, the Na I line absorption feature at 0.58 μm is better matched by the solar metallicity model.

$T_{\rm eff}$	3000	3100	3150	3200	3300	3400	
0.0						$\star$	
-0.2				$\star$			
-0.4			$\star$		$\star$		
-0.6		$\star$					
-0.8	$\star$						
-1.0	$\star$						

$[M/H]$	$+0.2$	0.0	-0.2	-0.4	-0.6	-0.8	-1.0
3000							
3100							$\star$
3150				$\star$	$\star$	$\star$	$\star$
3200	$\star$	$\star$	$\star$	$\star$		$\star$	
3300		$\star$	$\star$				
3400							

Table 9.3: Top: best metallicity match within each effective temperature from a SED comparison with the optical observed region. Bottom: best effective temperature match within each metallicity from a SED comparison with the optical observed region.

Table 9.3 shows the best matches reached by keeping one parameter fixed. These comparisons were made twice:

1. by making use only of the normalized optical spectrum.

2. by making use of the normalized infrared and optical spectra together.

9.5.2 Detailed Spectral Analysis

Due to the presence of many telluric features, the 0.87–0.91 μm region was excluded. The sample of lines was chosen from the line identifications provided as a feature of the models. In the region 0.41–0.87 μm we found two very metallicity sensitive doublets: the KI 0.768 μm doublet and the Na I 0.819 μm doublet. Figures 9.9(a–f)- 9.13(a–f) show the two doublets for all the possible combinations. Also, Figures 9.14(a–f)- 9.18(a–f) show another region chosen for our spectral analysis with the strongest lines marked. We have performed this type of comparisons throughout the optical spectrum.

Within each temperature we found the best metallicity match; the results are given in Table 9.4.

Table 9.4: Best metallicity match within each effective temperature after a detailed spectral analysis of the optical observed region.

$T_{\rm eff}$	3000	3100	3150	3200	3300	3400
0.0						
−0.2						
−0.4					⋆	⋆
−0.6	⋆	⋆	⋆	⋆		
−0.8				⋆		
−1.0						

In general, the best metallicity lies between –0.6 and –0.8. However, with increasing temperature the fits to low metallicity models ($\leq$ –0.4) get worse.

Choosing the best metallicity within each temperature, we compared the different temperatures and found $\sim$ 3200 K models give the best match.

Above 0.92 μm, we found a sensitive FeH absorption band centered at $\sim$ 0.99 μm: this band appears independent enough of the continuum to try a profile fit. The results of this fit are as follows:

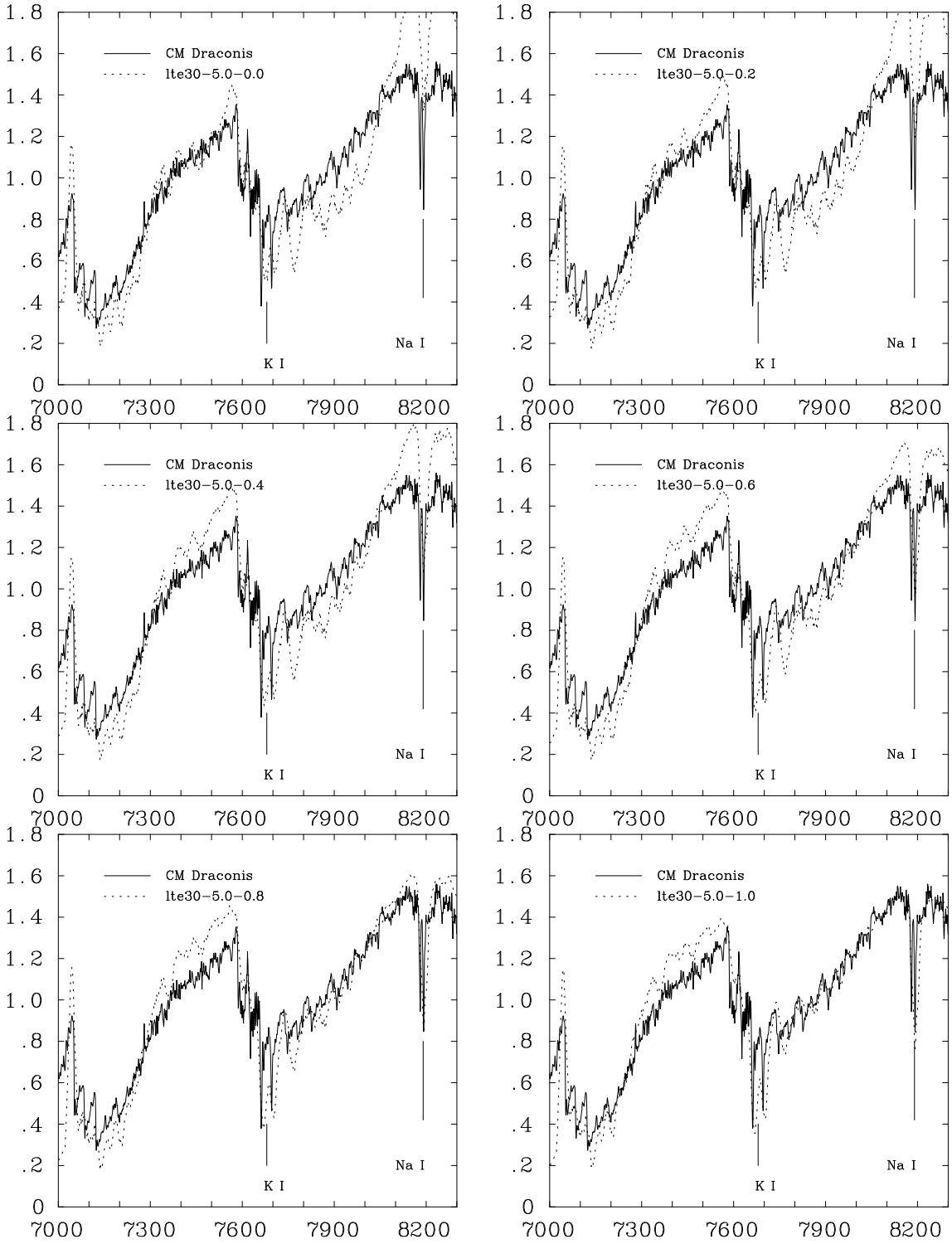

Figure 9.9: Comparison of observed spectrum with models at T_{eff}=3000 K for all the metallicities for the region 7000–8300 $\dot{A}$. The two strongest lines are shown.

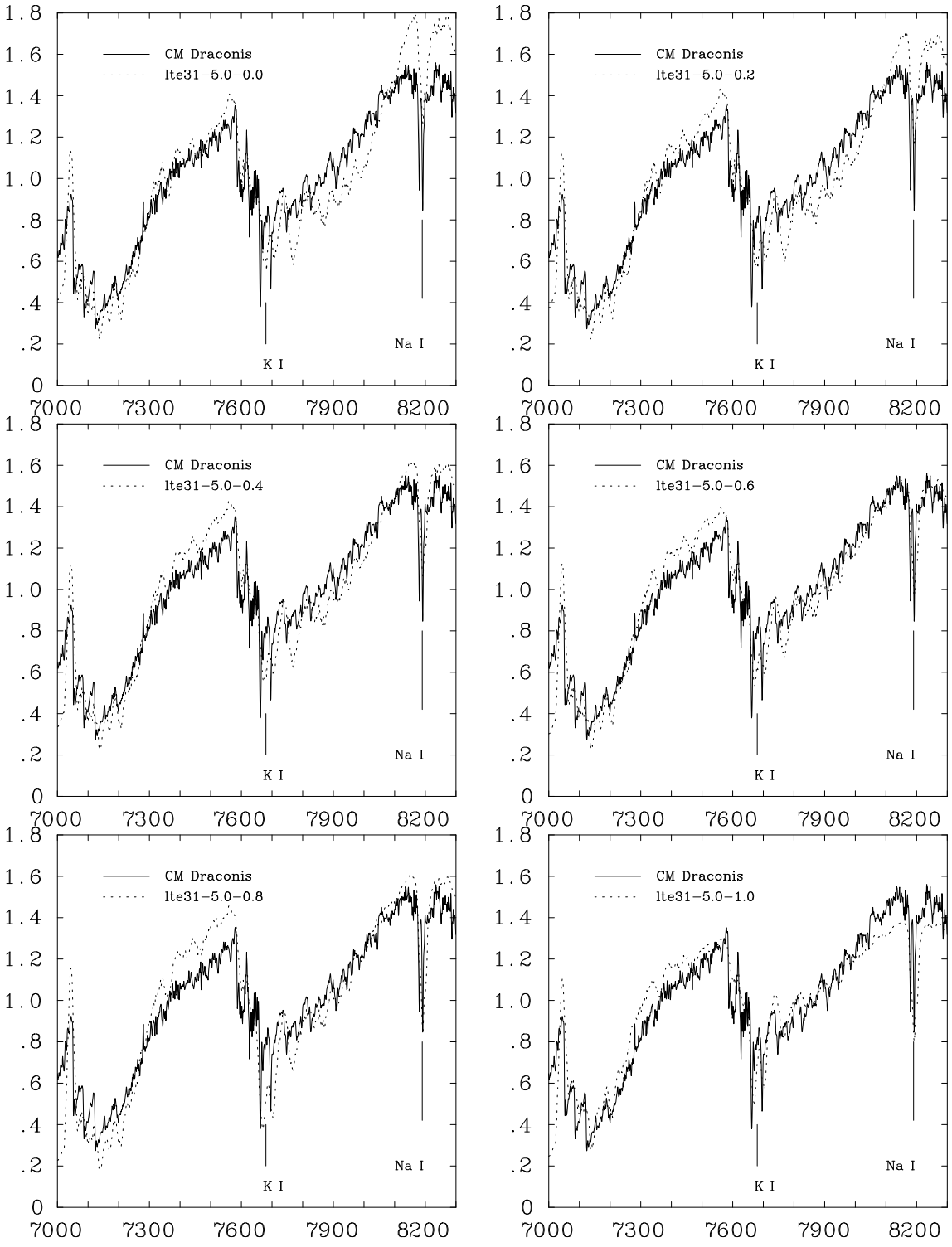

Figure 9.10: Comparison of observed spectrum with models at T_{eff}=3100 K in the region 7000–8300 $\dot{A}$

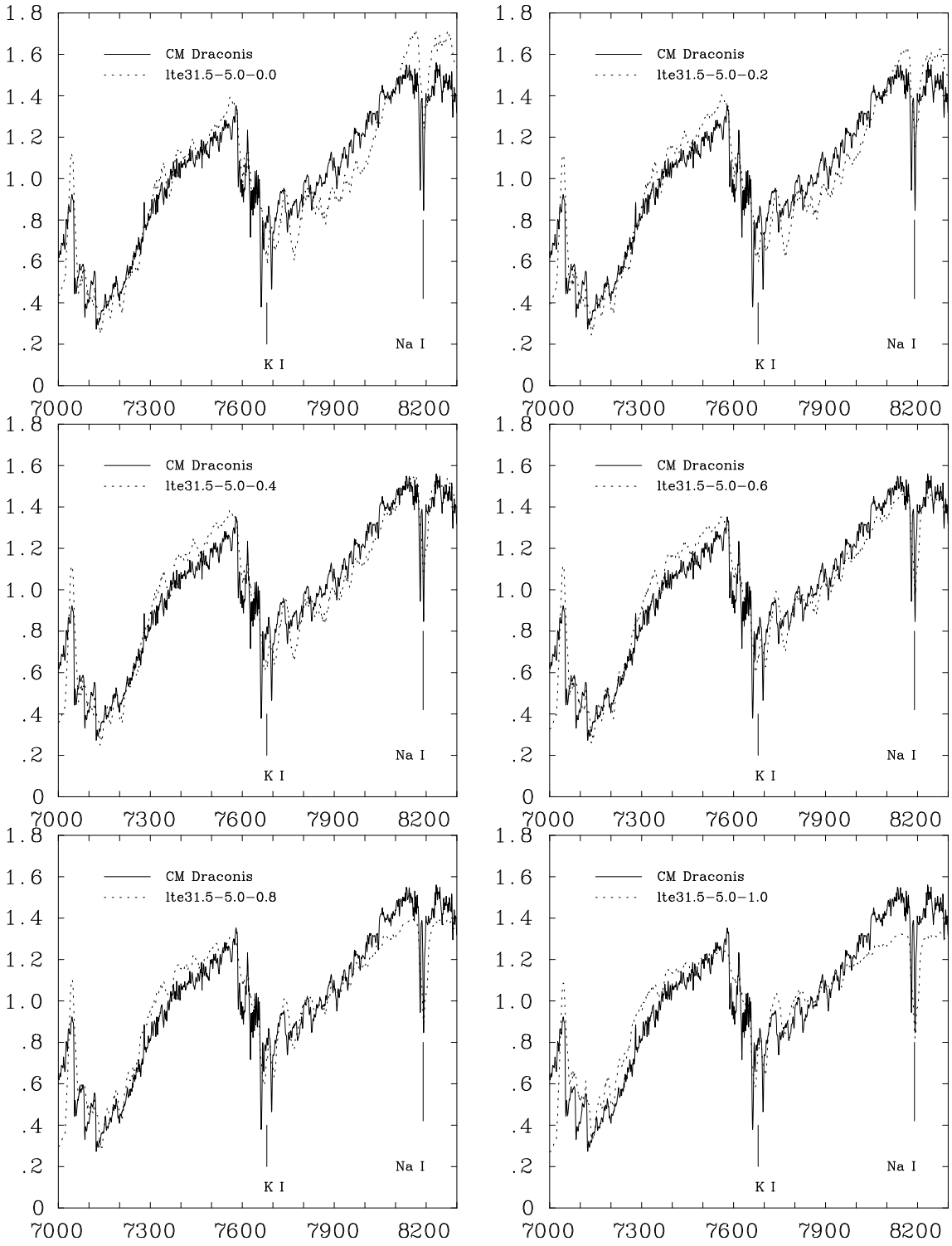

Figure 9.11: Comparison of observed spectrum with models at T_{eff}=3150 K in the region 7000–8300 $\dot{A}$

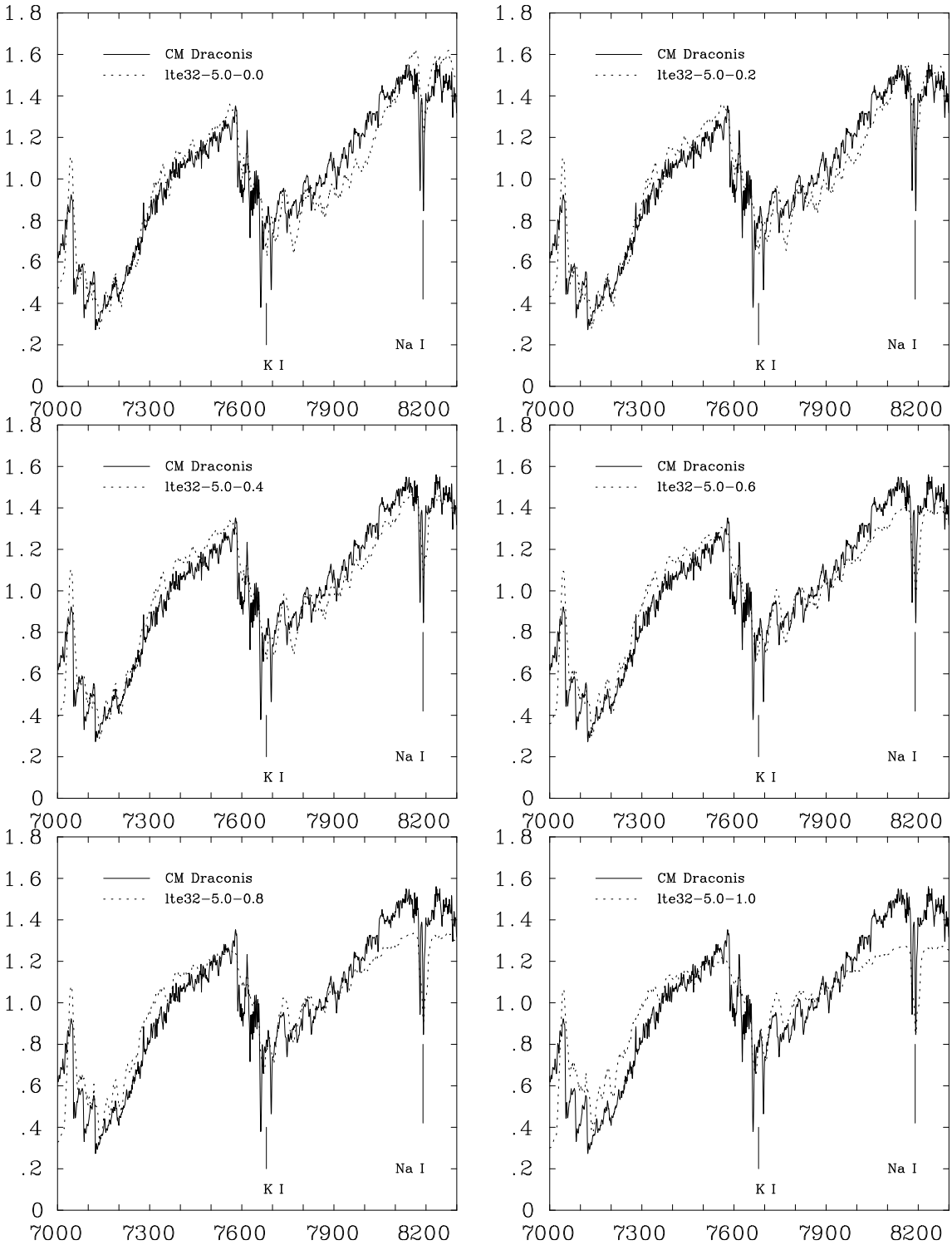

Figure 9.12: Comparison of observed spectrum with models at T_{eff}=3200 K in the region 7000–8300 $\dot{A}$

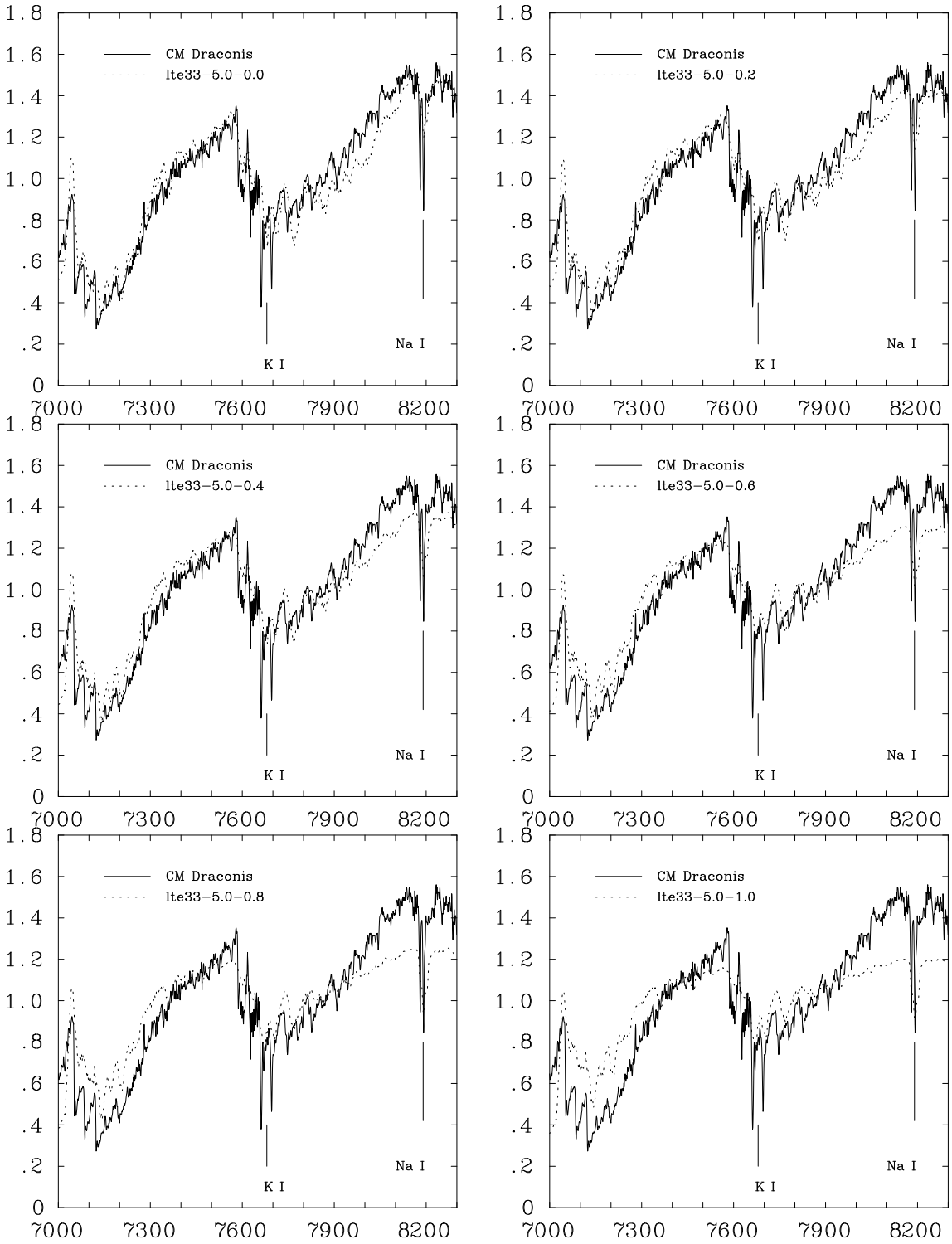

Figure 9.13: Comparison of observed spectrum with models at T_{eff}=3300 K in the region 7000–8300 $\dot{A}$

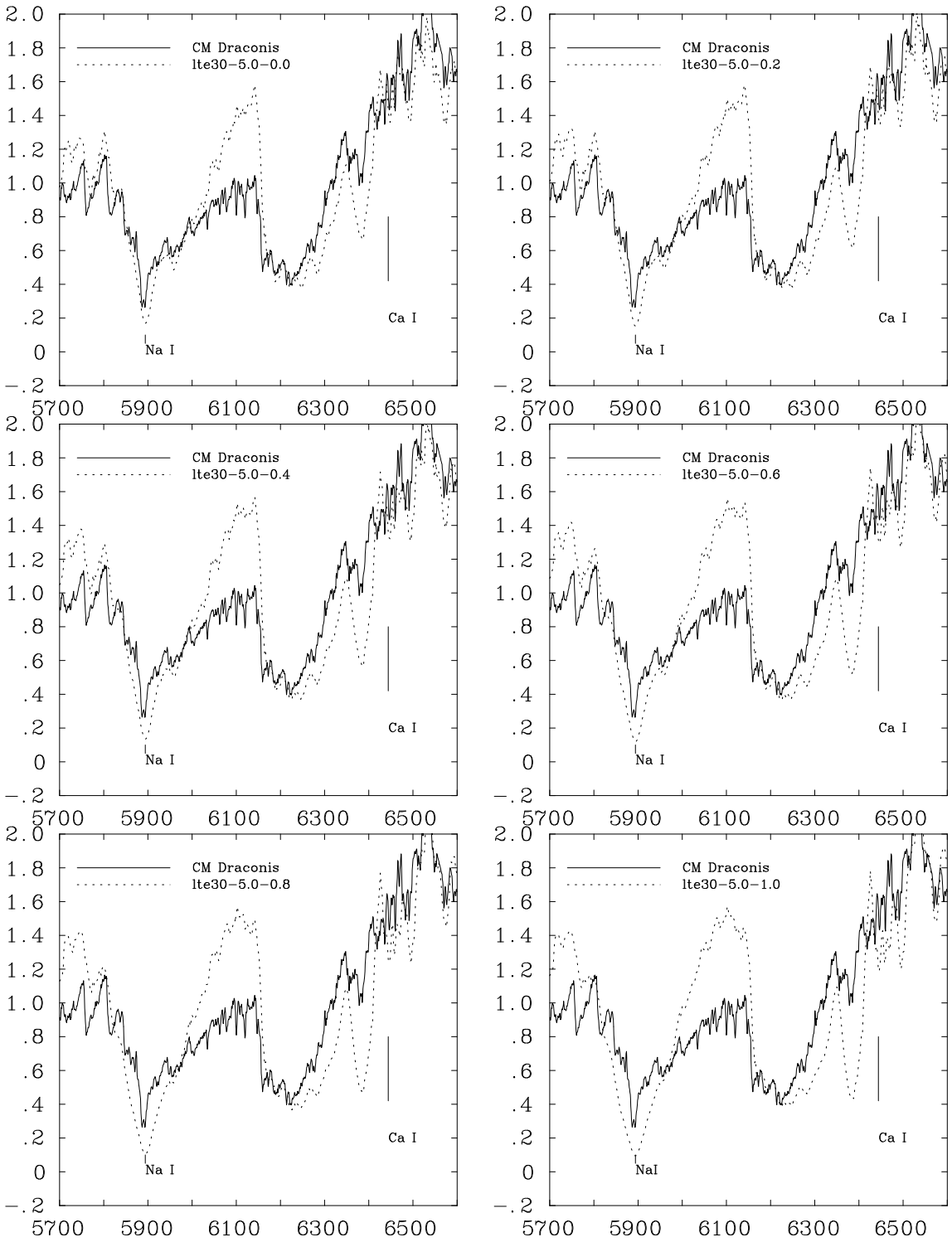

Figure 9.14: Comparison of synthetic and observed spectra in the region 5700–6500 $\dot{A}$ for T_{eff}=3000 K

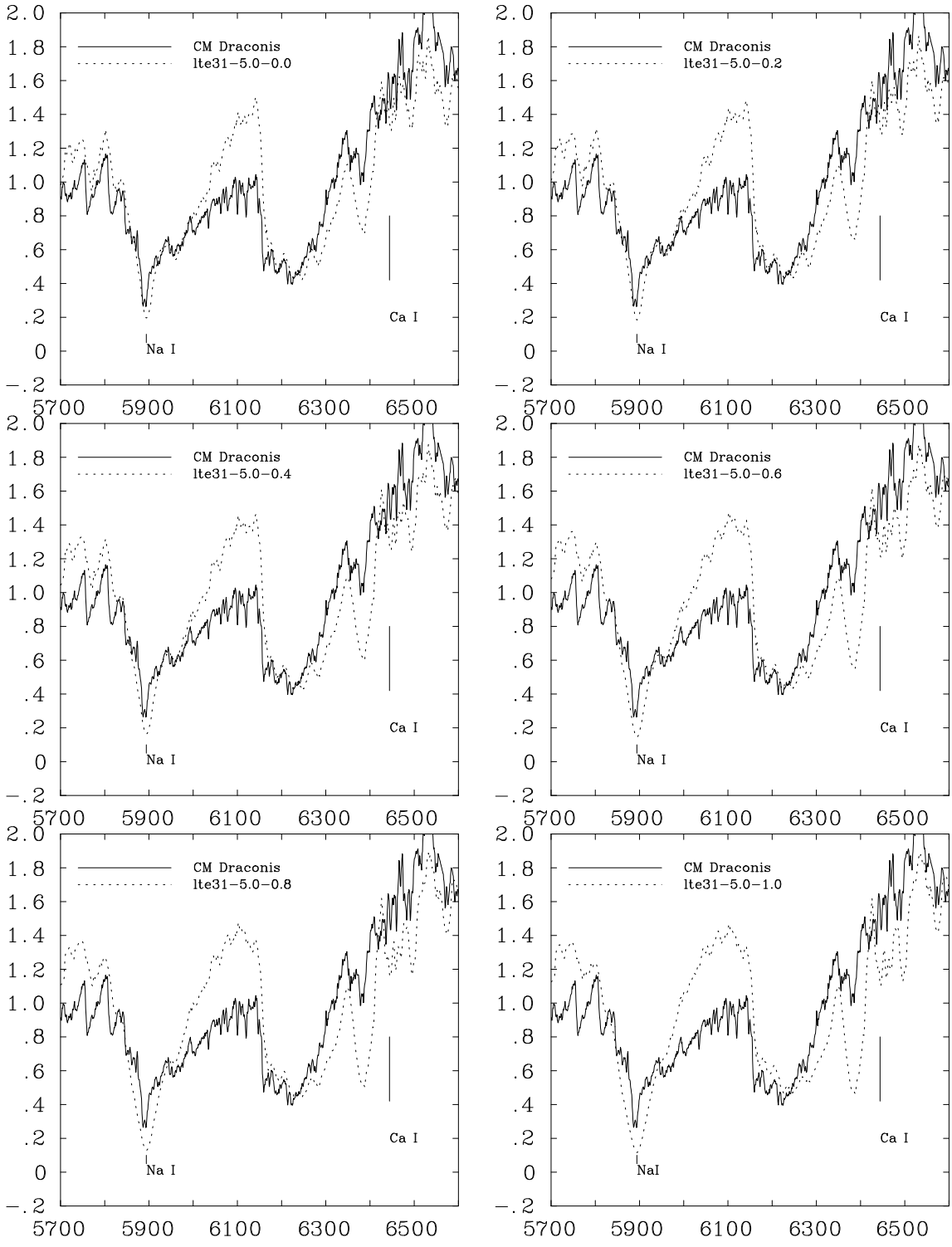

Figure 9.15: Comparison of observed spectrum with models at T_{eff}=3100 K in the region 5700–6500 $\dot{A}$

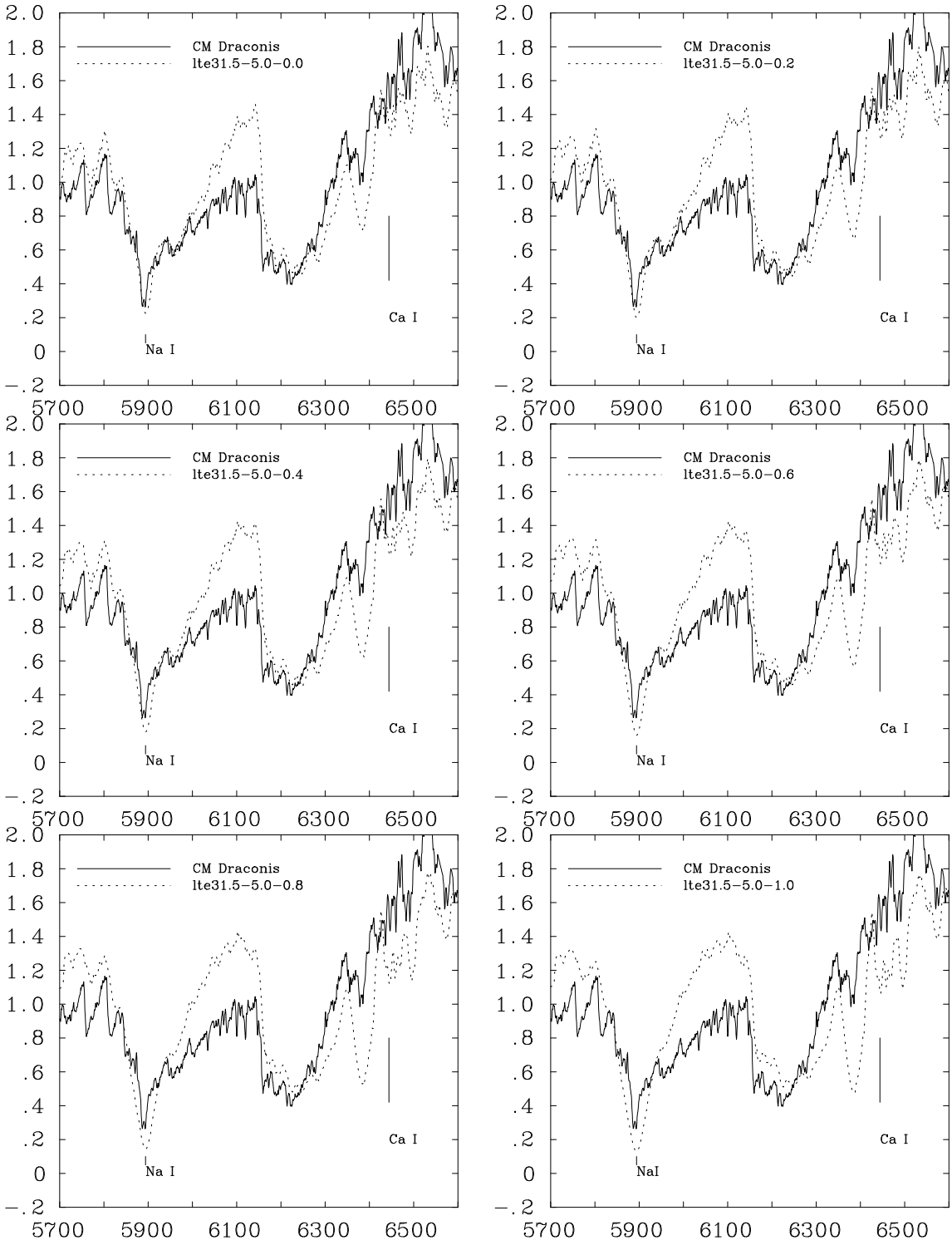

Figure 9.16: Comparison of observed spectrum with models at T_{eff}=3150 K in the region 5700–6500 $\dot{A}$

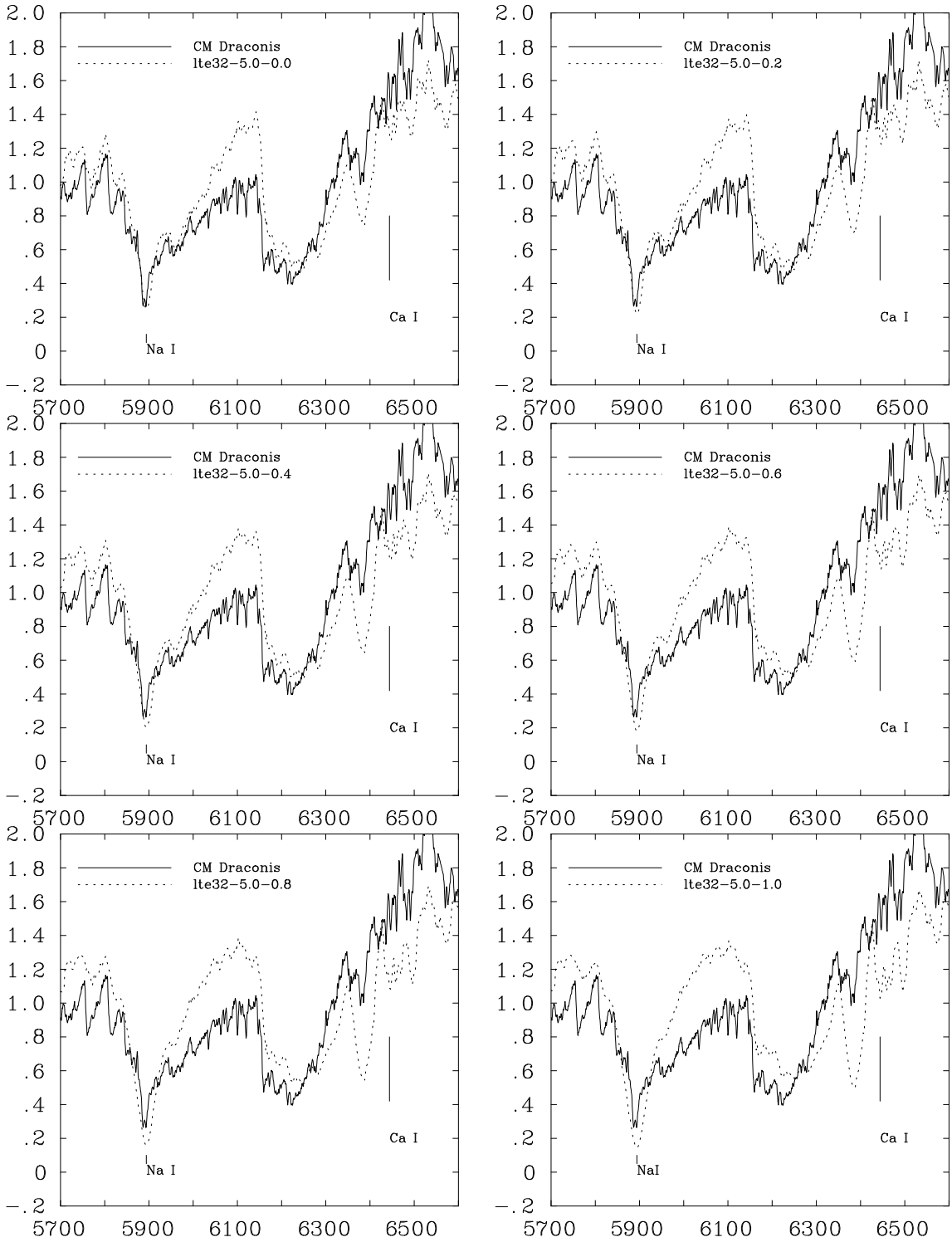

Figure 9.17: Comparison of observed spectrum with models at T_{eff}=3200 K in the region 5700–6500 $\dot{A}$

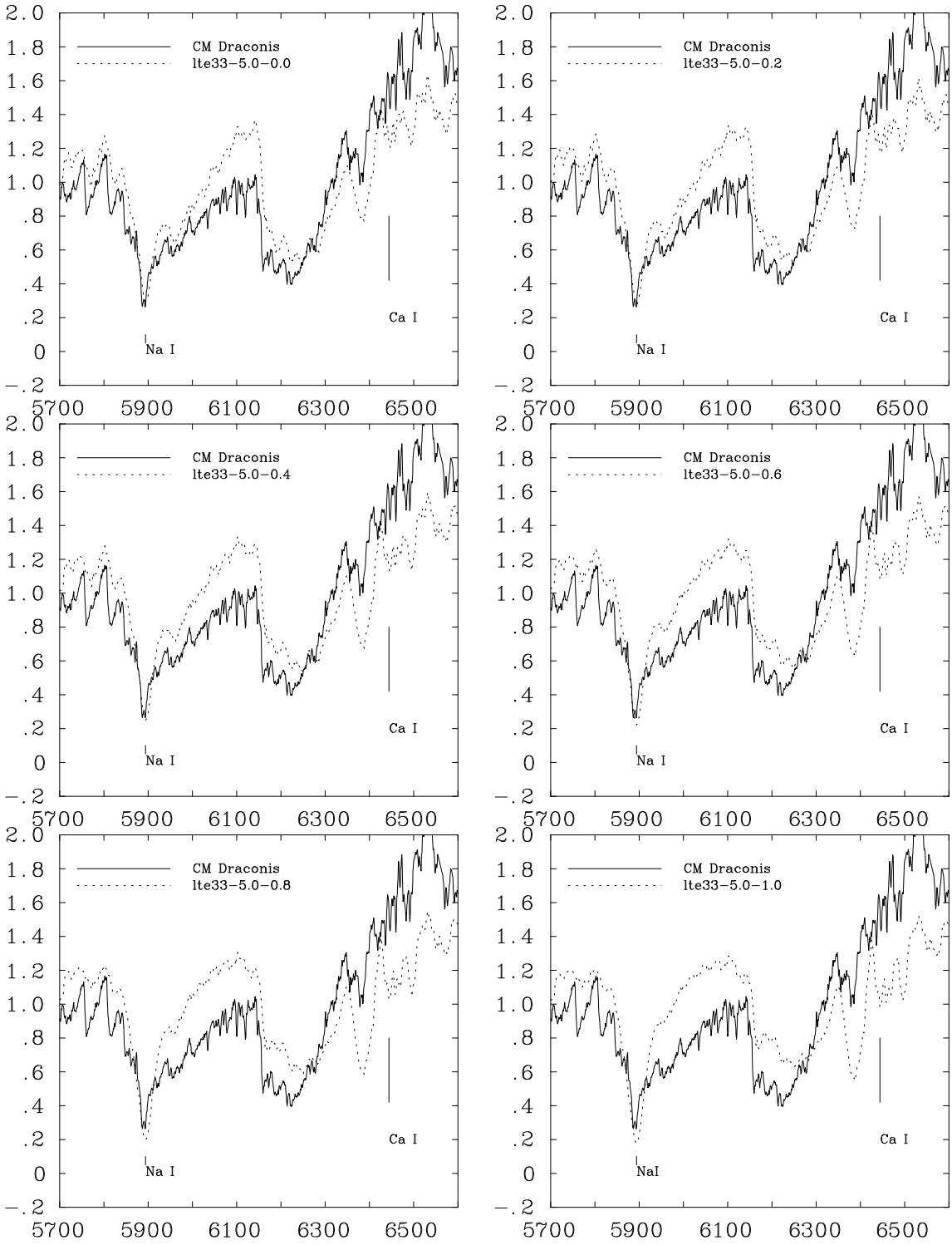

Figure 9.18: Comparison of observed spectrum with models at T_{eff}=3300 K in the region 5700–6500 $\dot{A}$

1) For every temperature apart from $T_{\rm eff}$ = 3300 K, the best fit is obtained at solar metallicities. The rest of the metallicities give a too strong FeH band. 2) Increasing the temperature causes the difference arising from a change in metallicity to decrease. 3) At $T_{\rm eff}$ = 3300 K, the solar metallicity model under-represents the FeH band, while the –0.6/–0.8 models give the best fit. However at this temperature the sensitivity of the FeH line to changes in metallicity is very small. Figure 9.19 shows the fit to the FeH line for $T_{\rm eff}$ = 3100 K at [M/H]= $0.0, -1.0$ and for $T_{\rm eff}$ = 3300 K at [M/H]= $0.0, -0.8$. We note that the models do not use a FeH linelist but the JOLA (Just Overlapping Line Approximation, Allard & Hauschildt, 1995) with astrophysical f values, which is not very accurate and therefore the modeled FeH bands cannot presently be used as reliable indicators.

In summary from the analysis of the optical spectrum we find that low temperature models ($T_{\rm eff}$ ∼3000K) of solar metallicity give a generally better SED fit. This is in agreement with the effective temperature derived previously from the luminosity and radii, and in agreement with published optical colors of CM Dra which place the system on the red edge of the disk main sequence. Yet the detailed spectral analysis of the atomic lines in the optical spectrum leads to a higher temperature; T_{eff}=∼ 3200K, and a metallicity of ∼ –0.6 seems to be generally the best match for many atomic lines.

9.6 Spectral analysis of the "infrared" region

The synthetic infrared spectra were computed at much higher resolution than the observations, so we matched them to the instrumental resolution by smoothing with a triangular function. The smoothing was performed in the same way as for the optical comparisons. Although the coverage, resolution and signal-to-noise of the observations is unprecedented for M dwarf observations, it is still not high enough to detect many of the weak absorption features which are very important in determining the best model fit. In addition, the water line list that we have used in the models is incomplete and, therefore, cannot completely reproduce the IR pseudo-continuum. We performed our analysis in three parts.

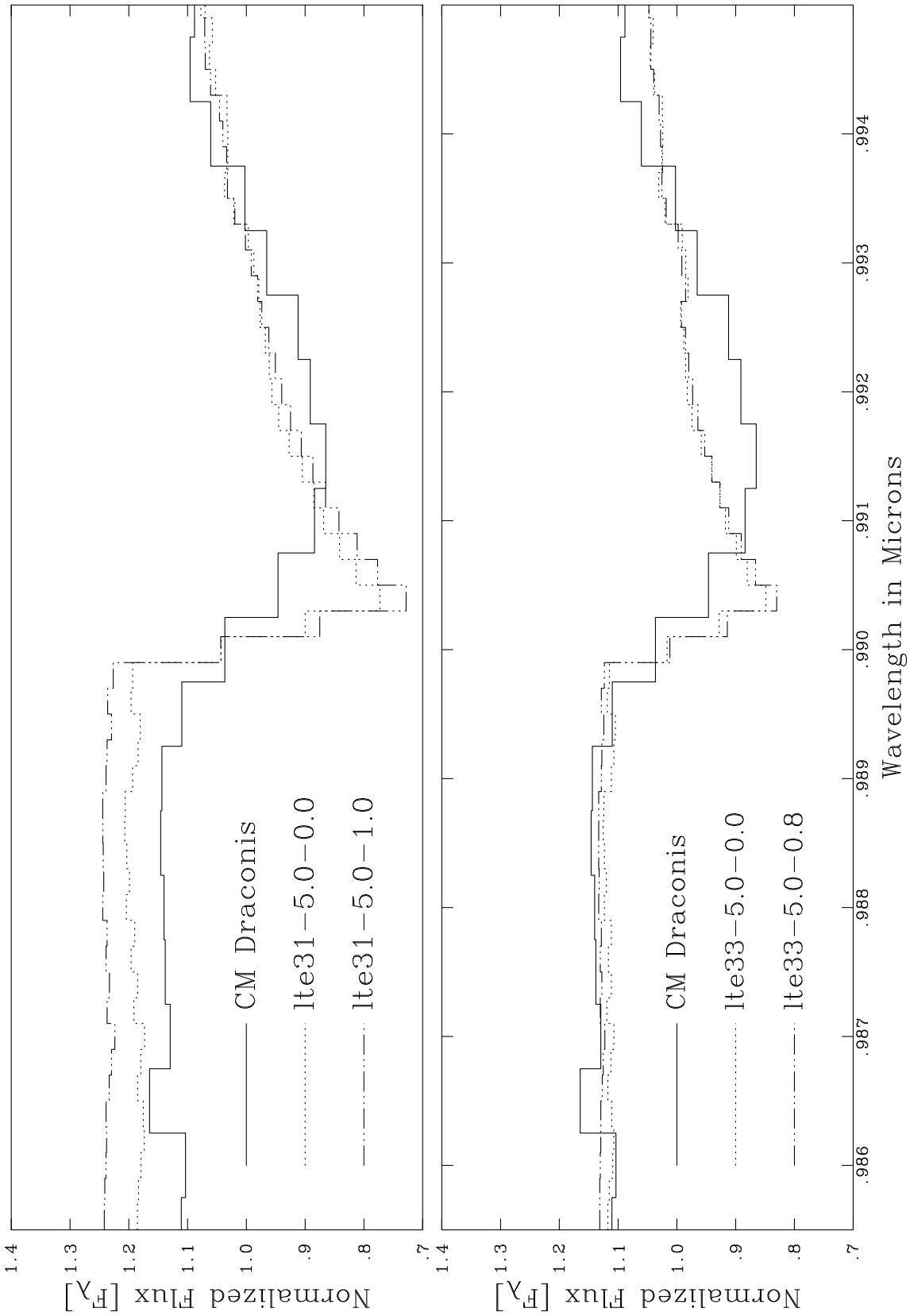

Figure 9.19: Fit to the FeH band centered at ~ 0.992 μm for the $T_{\rm eff}$=3100K, [M/H]= $0.0, -1.0$ models (top plot) and for the $T_{\rm eff}$=3300K, [M/H]= $0.0, -0.8$ models (bottom plot).

- Comparison of the general flux distribution of all the models with observations. This reduced the range of possible metallicities.

- Analysis of the strong, clearly visible metal lines identified by Leggett *et al* (1996). This step reduced the range of possible temperatures.

- Finally we identified several weak lines found in the synthetic spectra. By careful analysis of their match with the observed lines we found the best match for effective temperature and metallicity.

9.6.1 General flux distribution comparison

The infrared spectral distribution of CM Dra is much steeper than that of typical disk M dwarfs with a J-K color of nearly 0.2 mag bluer, at the same I-J color, than the bulk of the M dwarf sample of Leggett (1992). Figures 9.20(a–g)- 9.24(a–g) show the infrared SED comparison between all the synthetic and observed spectra.

For a given temperature, low metallicities reproduce the IR flux distribution better than the high ones. In fact we found that for all temperatures the best metallicity ranges seem to be for [M/H]≤ -0.4. However at very low metallicities ([M/H]≤ -1.5) the flux distribution match worsens. Figure 9.25 shows a model computed at $T_{\rm eff} = 3150$ K and [M/H]$= -2.0$.

The water bands longward of 1.60 μm are too weak and the CO bands in the region from 2.29 to 2.40 μm are not well reproduced. Table 9.5 shows the best metallicity for each effective temperature and the best effective temperature for each metallicity.

The fits are performed by eye, avoiding spectral regions which we know are not reproduced adequately by the models. Although the general flux distribution of the observed spectrum is reasonably well matched by the models, we do not believe that the line-by-line comparison is accurate enough for a χ^2 fit to be useful.

The above analysis does not absolutely rule out any of the trial effective temperatures, although 3000 K and 3100 K models give a worse match. Our results appear to be in

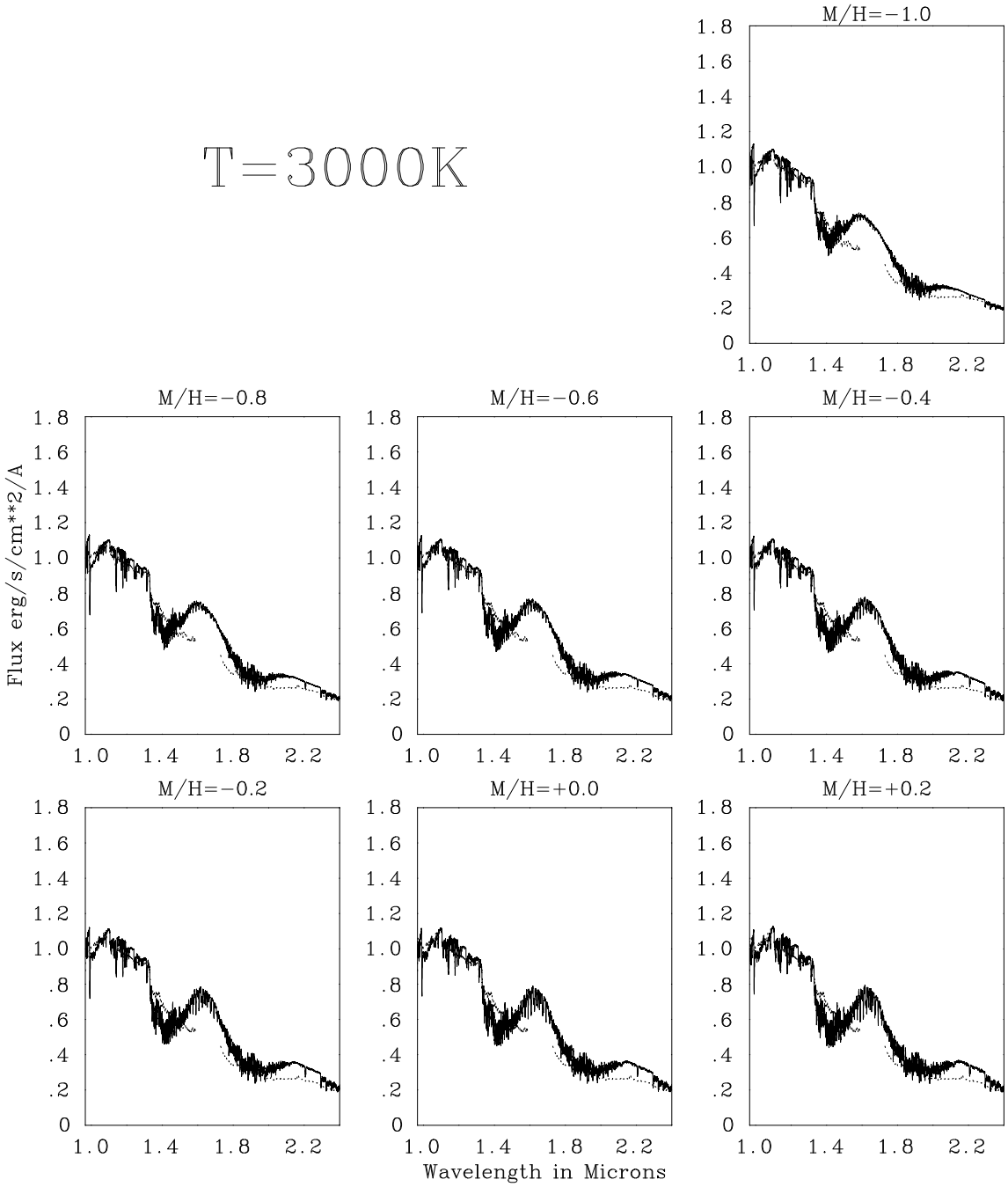

Figure 9.20: Spectral energy distribution (SED) comparisons between synthetic and observed spectra from 1.0–2.4 μm for T_{eff}=3000 K

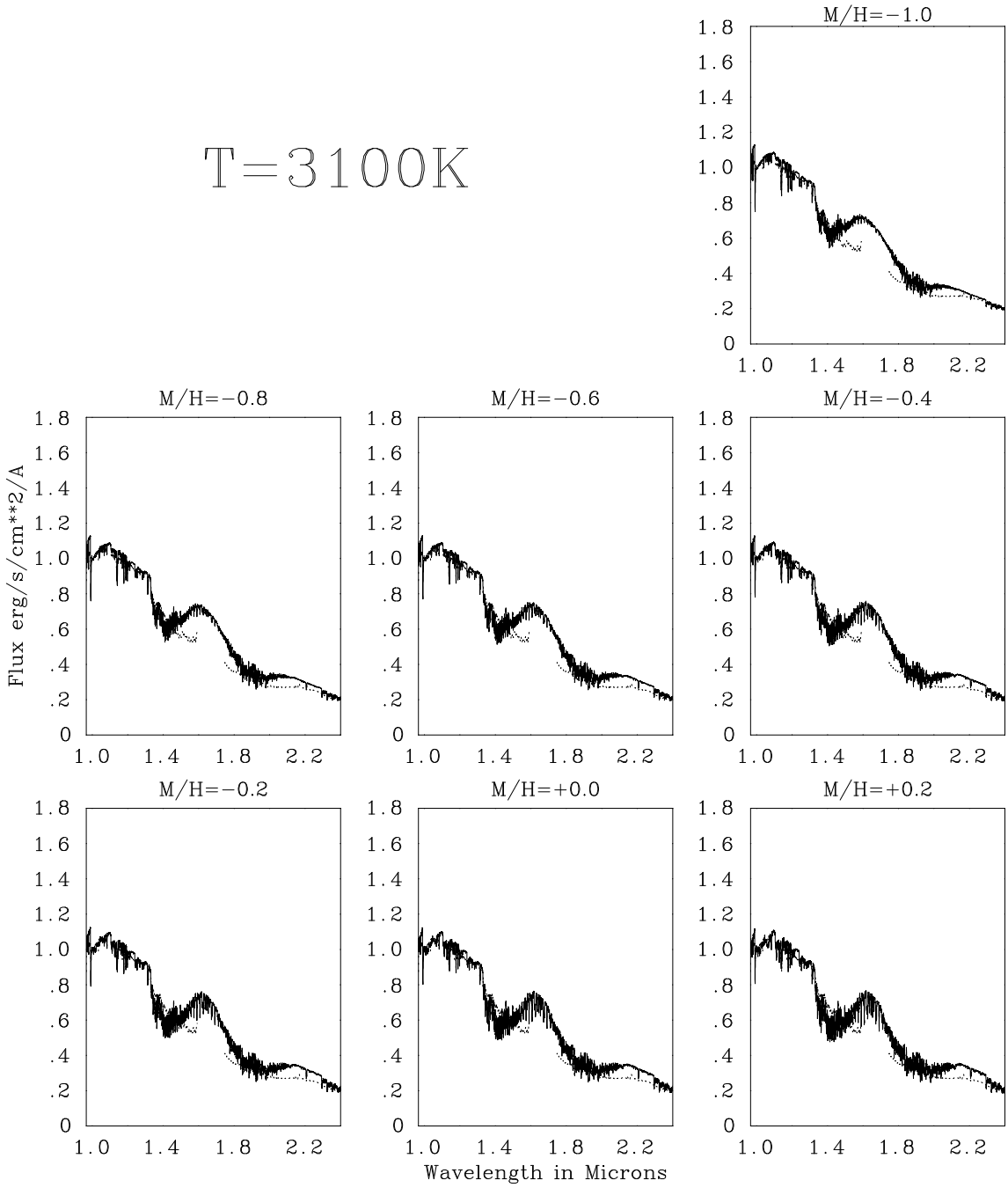

Figure 9.21: Infrared SED comparison at T_{eff}=3100 K

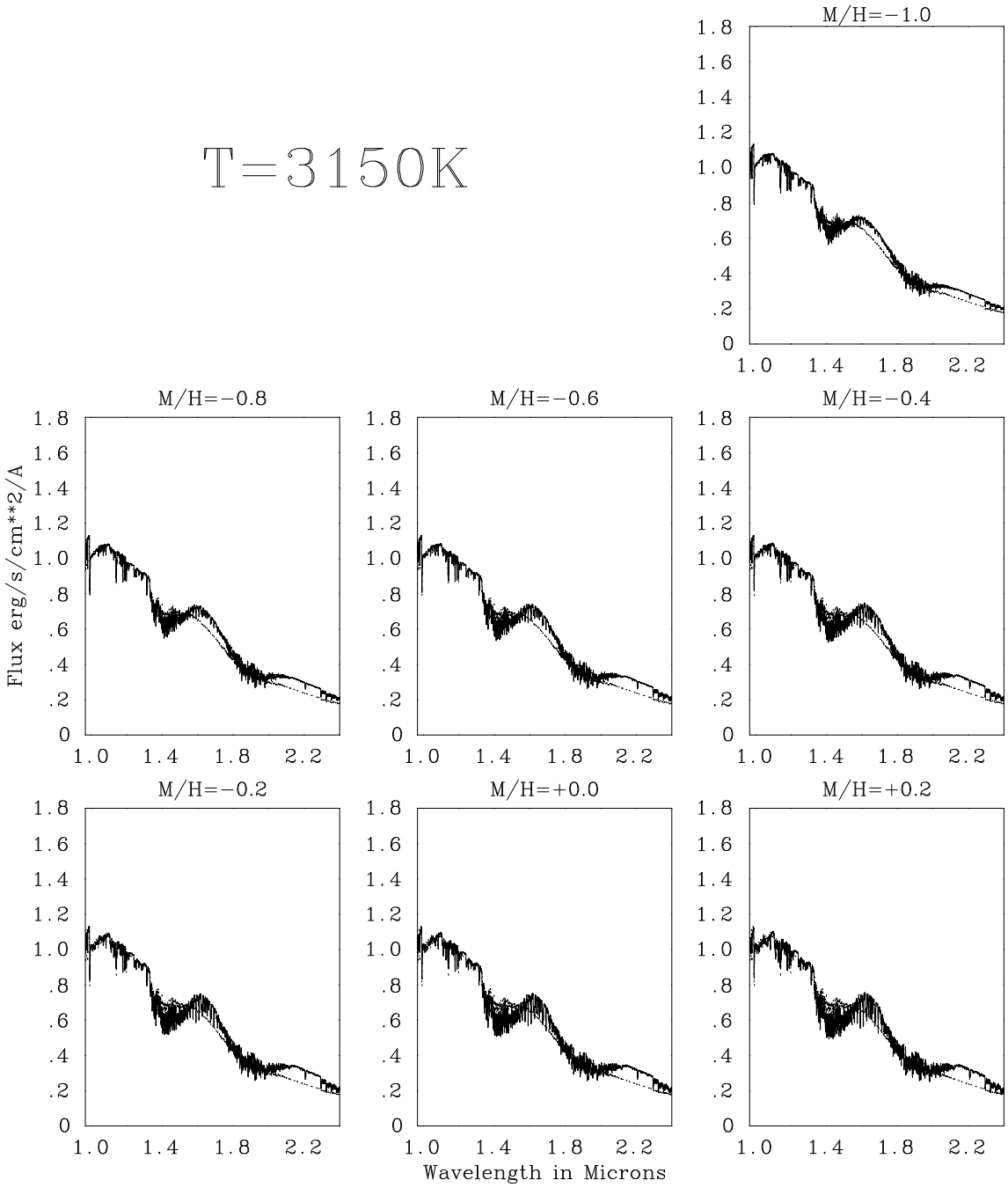

Figure 9.22: Infrared SED comparison at T_{eff}=3150 K

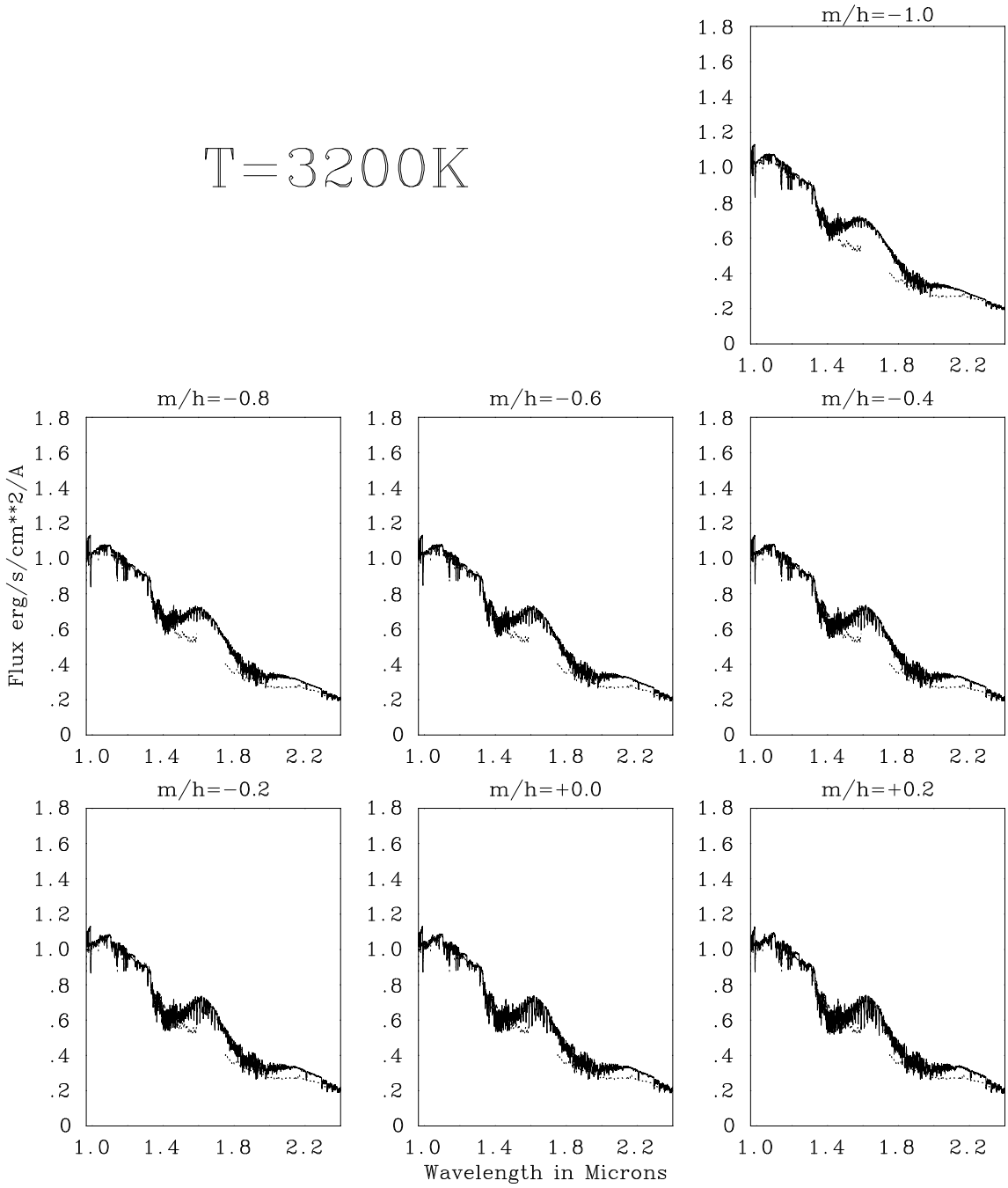

Figure 9.23: Infrared SED comparison at T_{eff}=3200 K

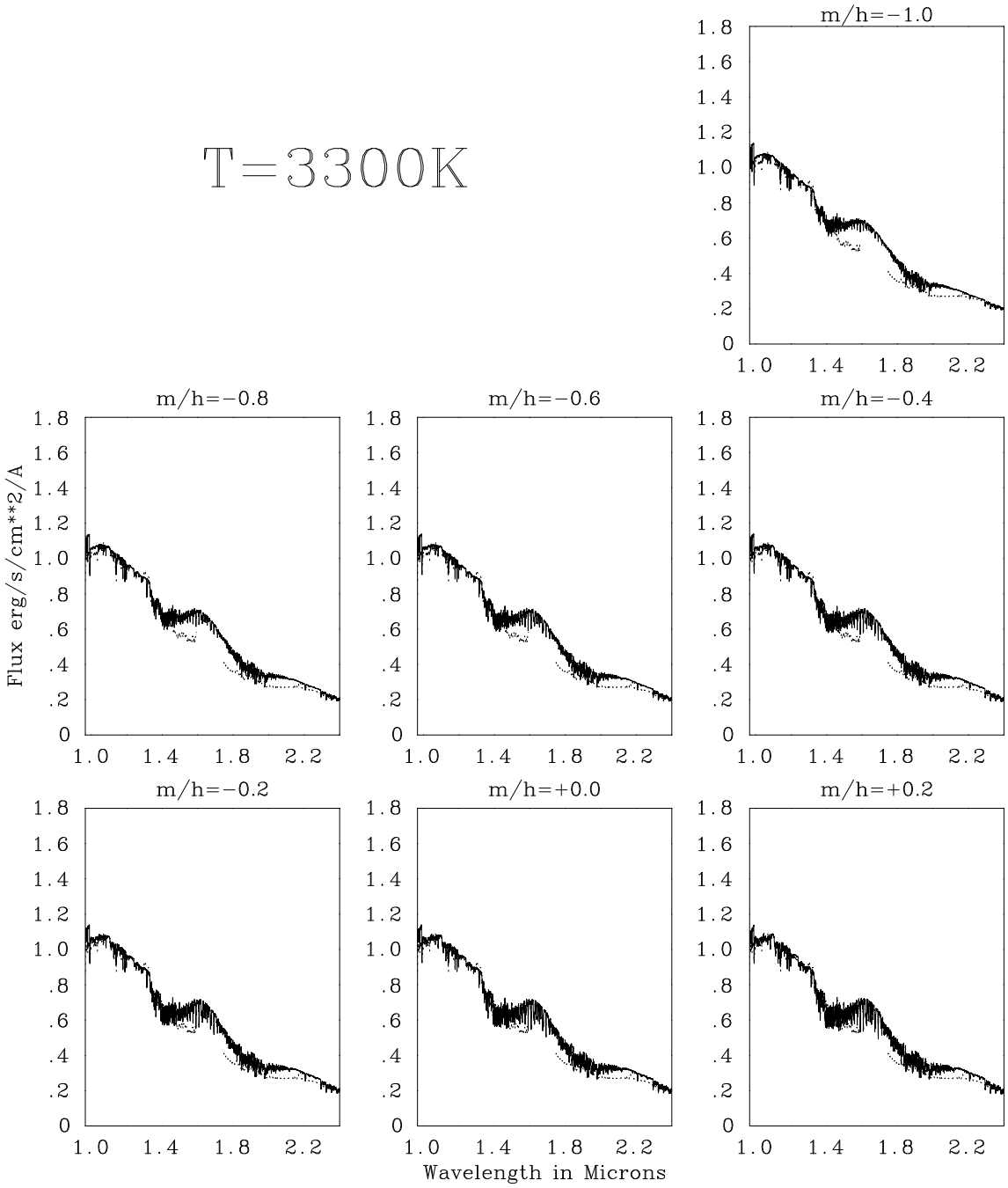

Figure 9.24: Infrared SED comparison at T_{eff}=3300 K

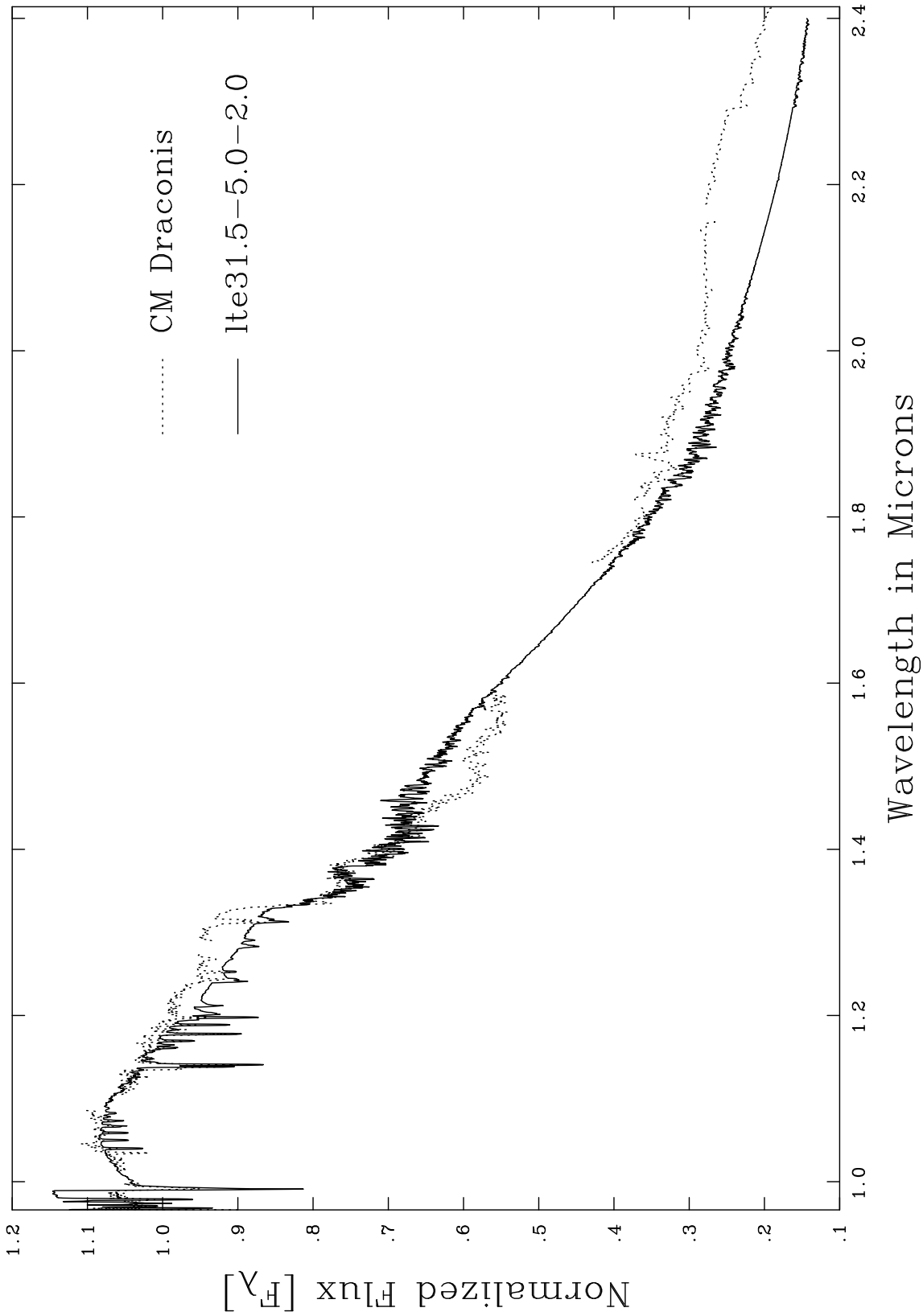

Figure 9.25: SED comparison of synthetic and observed spectrum. The models have been computed at T_{eff}=3150 K with $[M/H]$ = -2.0. This comparison shows how very low metallicity models do not fit the SED.

$T_{\rm eff}$	3000	3100	3150	3200	3300	3400	
-0.2							
-0.4					$\star$		
-0.6	$\star$	$\star$		$\star$			
-0.8			$\star$	$\star$			
-1.0						$\star$	

$[M/H]$	$+0.2$	0.0	-0.2	-0.4	-0.6	-0.8	-1.0
3000							
3100							
3150						$\star$	
3200	$\star$			$\star$	$\star$	$\star$	$\star$
3300	$\star$	$\star$	$\star$		$\star$		
3400							$\star$

Table 9.5: Upper: best metallicity match within each effective temperature as seen from a SED comparison with the infrared observed region. Lower: best effective temperature match within each metallicity as seen from a SED comparison with the infrared observed region.

agreement with CB95 in that the $T_{\rm eff}$ = 3300 K models match the observations better. However this agreement is somewhat misleading since CB95 used the "Base" grid of model atmospheres of Allard & Hauschildt (1995) which caused the interior models to yield cooler effective temperature at a given mass then the more recent NextGen models, including the ones used here.

In contrast to CB95, we do not find at lower temperatures that the high metallicities models agree better with the observations. Indeed, although there is a better match at low metallicity for models of all temperature, the 3300 K models show the least sensitivity to changes in metallicities. It is therefore more difficult to exclude high metallicities at higher temperatures.

As a consequence of the water opacity problem, no real choice of parameters could be made based only on the match of the general flux distribution. The shape of this distribution is likely to be strongly dependent on the shape of hot vibrational water bands (see Jones *et al*, 1995), a problem which might soon be resolved by a new water linelist that is currently being tested. However, the observed infrared SED indicates clearly a sub-solar mixture for the system.

9.6.2 Strong lines identification and analysis

We divide our spectral region in four subregions:

0.97–1.16 μm,

1.16–1.20 μm,

1.20–1.35 μm,

2.20–2.40 μm.

The region between 1.35 and 2.2 μm is excluded since it is dominated by the water bands and therefore not reliable for detailed comparison. We used Leggett *et al*'s (1996) list of strong atomic lines for our analysis.

Figure 9.26 confirms the result of the previous section at both $T_{\rm eff}$ = 3150 and 3300 K, in the region from 2.2 to 2.5 μm. In particular, the CO bands at $\sim$ 2.353 μm are well

matched by the model at $T_{\rm eff}$ =3300 K, [M/H]= -1.0. In fact, the CO bands at 2.29 and 2.32 μm are far too strong in all models but get nearer to the observations as the metallicity is lowered.

We then compared the four subregions for all the temperatures at the metallicities of $-1.0, -0.8, -0.6$ and -0.4. Figures 9.27 to 9.29 show this for the first three regions. such a comparison for all the temperatures.

Jones *et al* (1996) show a spectral sequence from 1.16 to 1.22 μm where strong atomic features are sensitive to different temperatures and metallicities: in particular we notice that the strong K I line at 1.177 μm decreases in strength as the temperature increases. We find the same effect in Figure 9.28 and overall we note that the observed K I line is matched better by the model at 3300K. Some detailed examples are as follows:

- In the 1.16–1.20 μm region, the K I lines at $\sim$ 1.169 and 1.177, the Si lines at $\sim$ 1.198–1.199 are all better fitted by higher temperatures models. It is interesting to note that the K I line at 1.169 μm seem to be too strong in the 3300 K model but too weak in the 3400 K one. The 1.177 μm K I line is better fitted by the 3400 K model.

- In the 1.20–1.35 μm region, the K I lines at 1.2432 and 1.2522 μm are well reproduced by the 3100 K models, while the Ca I lines at 1.3034 and 1.3086 μm are better fitted at 3200K.

Table 9.6 lists the best match in effective temperature for each strong line considered; their metallicity sensitivity is relatively small, however, for completeness, the table lists the best match in metallicity as well.

So far our analysis is based on a general flux distribution match and on the profiles of strong lines. However strong lines do not appear to be sensitive to metallicity changes; moreover, they are more subject to saturation. Furthermore many of these lines are blended so a different approach is explored below.

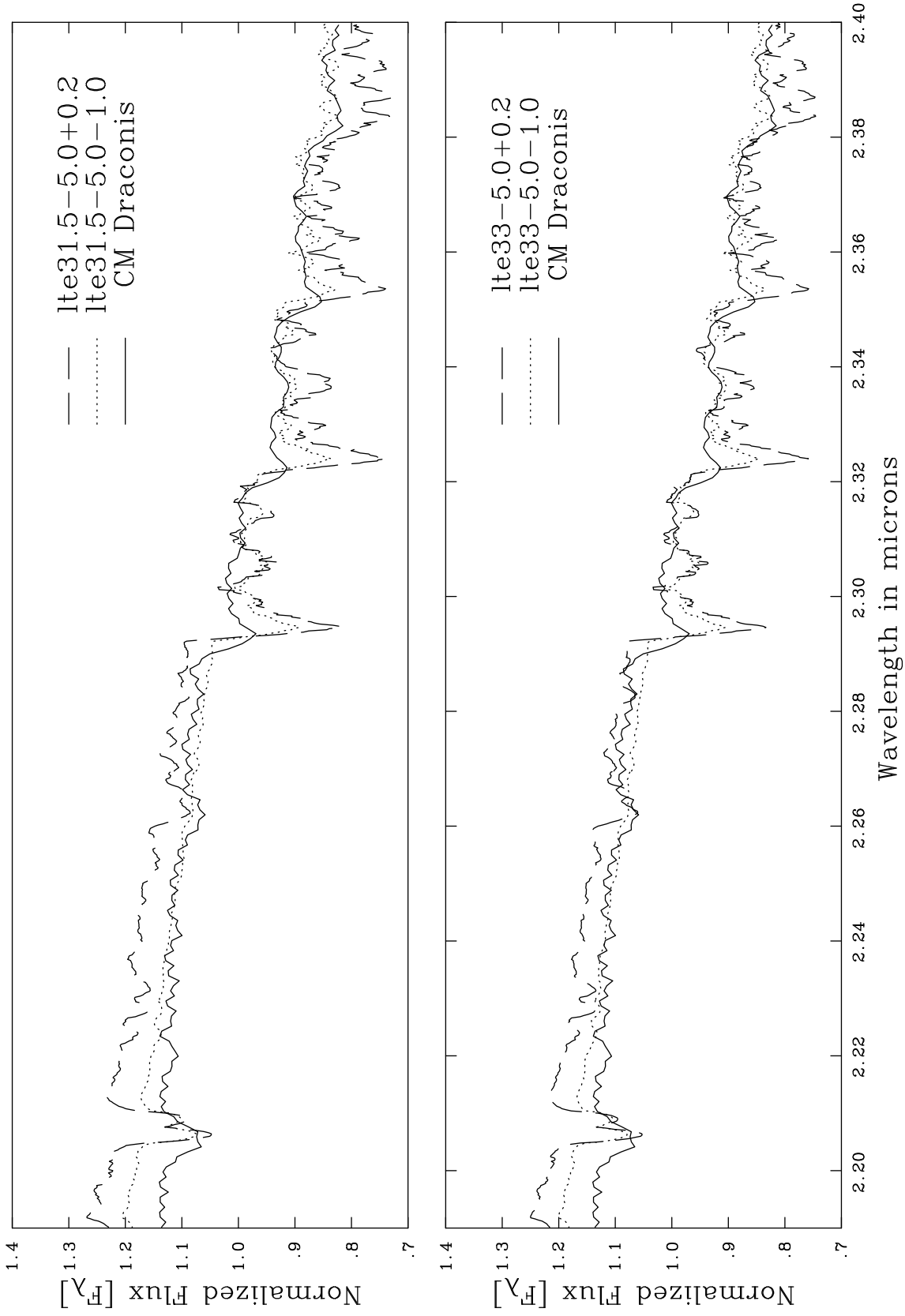

Figure 9.26: Detailed comparison of models with different metallicities. Top: [M/H]= $+0, 2, -1.0$ at T_{eff}=3150K. Bottom: [M/H]= $+0, 2, -1.0$ at T_{eff}=3300K.

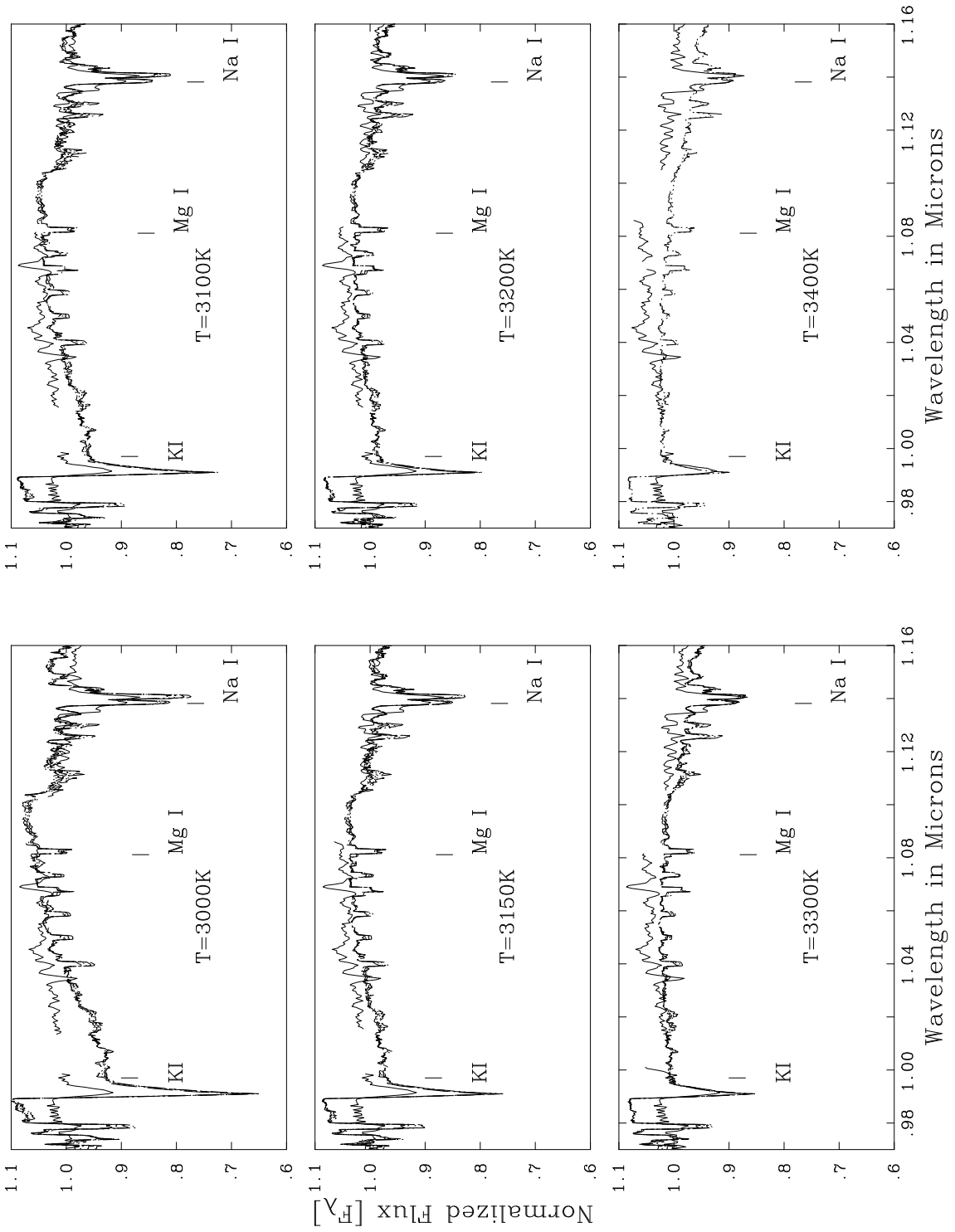

Figure 9.27: Comparisons of the region 0.95–1.16 μm. Continuous line is CM Dra; dashed, dotted, dot–dotted and double dot–dotted lines are the models at respectively [M/H]= -0.4, -0.6, -0.8, -1.0.

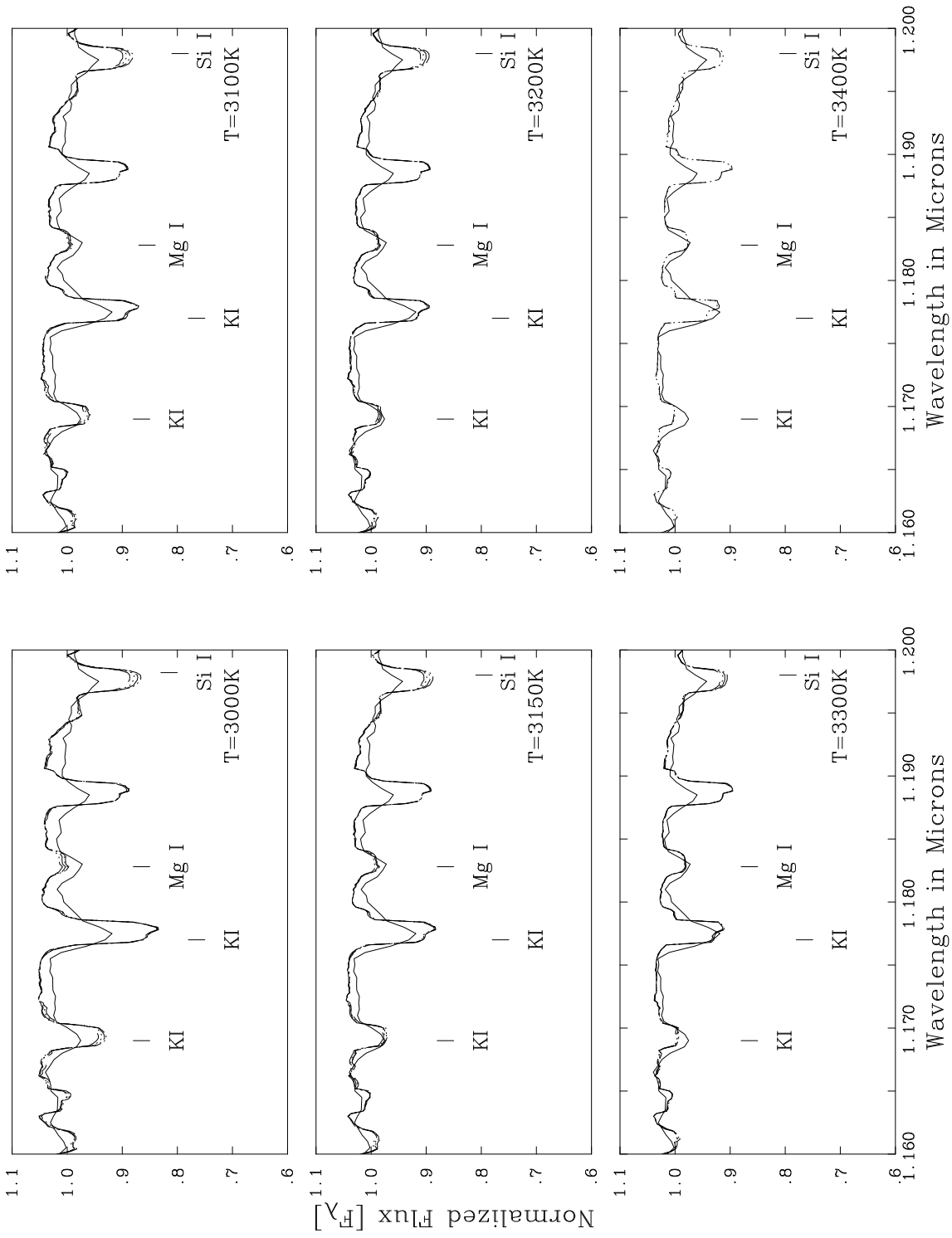

Figure 9.28: Comparisons of the region 1.16–1.2 μm. Again continuous line is CM Dra; dashed, dotted, dot–dotted and double dot–dotted lines are the models at respectively [M/H]= -0.4, -0.6, -0.8, -1.0.

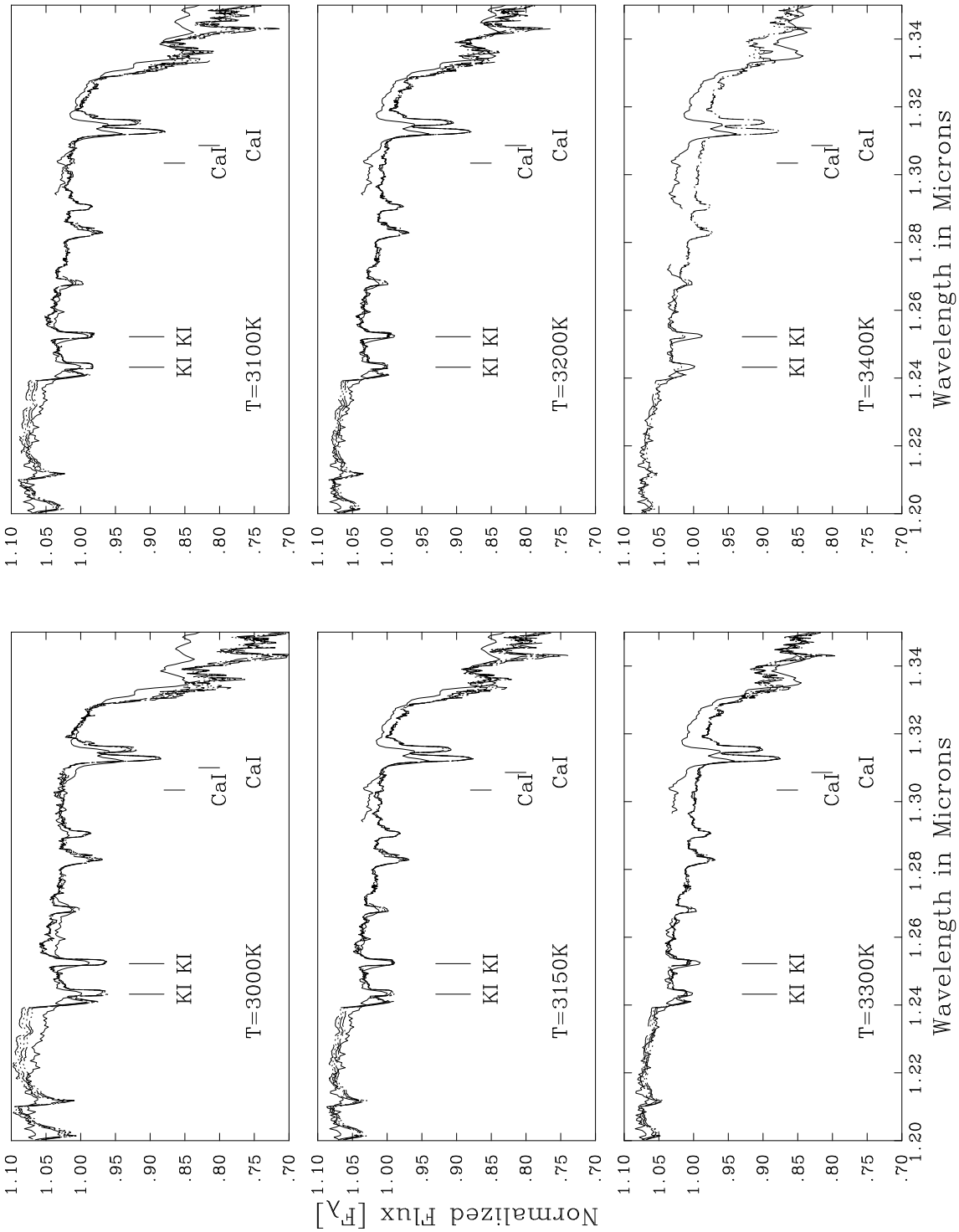

Figure 9.29: Comparisons of the region 1.2–1.34 μm. Continuous line is CM Dra; dashed, dotted, dot–dotted and double dot–dotted lines are the models at respectively [M/H]= -0.4, -0.6, -0.8, -1.0.

Table 9.6: The best model fit for each strong feature considered in the infrared region as a function of the effective temperature and of metallicity

λ	*Element*	$T_{\rm eff}$	$[M/H]$
0.9961	NaI	3200	-1.0
1.1690	KI	3400	-1.0
1.1770	KI	3300	-0.8
1.1820	MgI	3300	-0.6
1.2032	Si	3300	-1.0
1.2084	MgI	3300	-1.0
1.2104	Si	3300	-1.0
1.2432	KI	3150	-1.0
1.2522	KI	3150	-1.0
2.2056	NaI	3150	-1.0
2.2084	NaI	3150	-1.0
2.2651	CaI	3300	-1.0
2.3348	NaI	3300	-1.0
2.3379	NaI	3300	-1.0

9.6.3 Detailed spectral analysis

Our preliminary spectral analysis reduces the metallicity range to between −0.6 and −1.0, while candidate effective temperatures ranges from 3150 to 3400K. A more detailed analysis was performed by reversing the process of identification. We used the models' identification list to find metal lines sensitive to both metallicity and temperature changes. We tried to match these lines with the observations. These weak lines should be less subject to saturation effects. A problem with this procedure is that the observed spectra are at a lower resolution than the scale of line blending. This makes the above identification harder.

We divided the spectral region of 1.0 to 2.4 μm into 40 subregions. For each subregion we applied the instrumental profile to the models to match the observations. Many subregions were excluded either because the resolution was too low for identifying any features present or because of 'contamination' by water bands.

Figures 9.30 and 9.31 show some of these subregions for models with $T_{\rm eff}$ = 3150, 3200, 3300 and 3400K.

Table 9.7 lists the best effective temperature and metallicity match for each reliable atomic line. Again, as for Table 9.6 the comparison has been made by eye.

- From 1.11 to 1.14 μm the 3300 K model at metallicity −1.0 give a generally better fit, in particular to the Na I at 1.1385 μm.

- From 1.14 to 1.18 μm the $T_{\rm eff}$ = 3200, 3300 K models give the best fit although it is difficult to fix the metallicity. For example, the KI line at 1.169 μm is matched better by the −1.0 model if $T_{\rm eff}$ = 3300 K is chosen, while a metallicity of −0.6 gives a better fit to the observations at $T_{\rm eff}$ = 3200 K.

- At 1.253 μm, the K I line is better matched by the 3200K, [M/H]= −1.0 model. However, we note that at 3300 K the line is too weak and a metallicity of −0.6 gives a better fit, while at 3200K, it is too strong and at [M/H]= −1.0 generally gives a better fit. Indeed this is confirmed by the model at $T_{\rm eff}$ =3400 K where the K I line

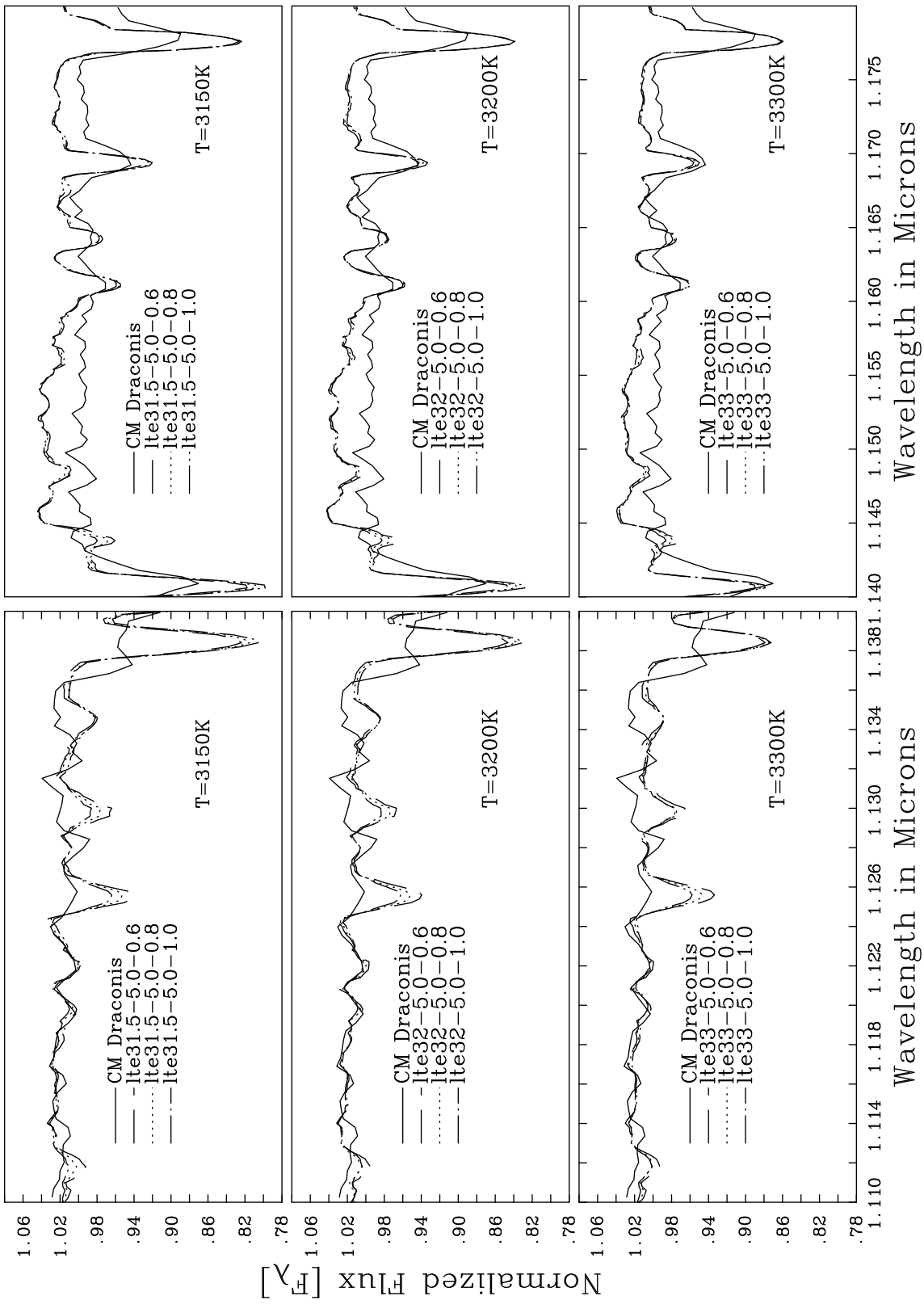

Figure 9.30: Left: Detailed comparison of the region 1.11–1.40 μm. Right: Detailed comparison of the region 1.40–1.80 μm

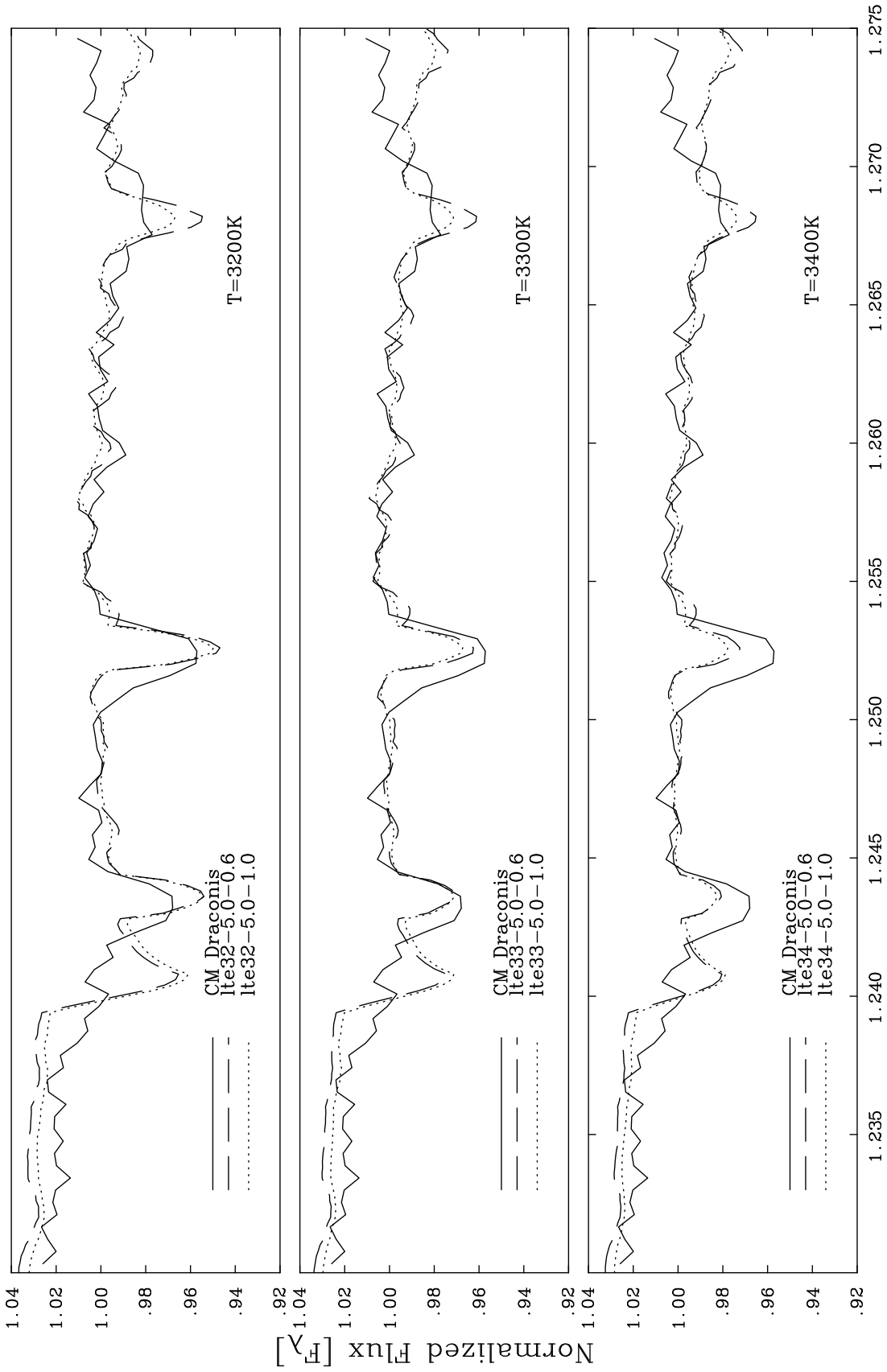

Figure 9.31: Detailed comparison of the region 1.230–1.275 μm.

is far too weak at both metallicities.

In Table 9.8, we give the best metallicity match within each effective temperature. This final analysis confirms that the high temperatures and low metallicity models give a better match to the observed spectrum of CM Dra, in particular [M/H] should be between -1.0 and -0.4. This conclusion is consistent with the results of a comparison of CM Dra to a sample of spectra stars with similar temperatures and different metallicities like Gl 213 ($T_{\rm eff}$ =3150, [M/H]= 0.0), Gl 206 ($T_{\rm eff}$ =3300, [M/H]= +0.1) (from Leggett *et al*, 1996), Gl 699 ($T_{\rm eff}$ =3100, [M/H]= -0.5) (Leggett *et al*, 1996; Jones *et al*, 1996) and Gl 299 ($T_{\rm eff}$ =3050, [M/H]= -0.5) (Leggett *et al*, 1996; Jones *et al*, 1996). However we need to note that (i) the spectra of Leggett's sample are at lower resolution than the spectrum of CM Dra; (ii) The effective temperature scale is based on an earlier 'Base' grid (Allard & Hauschildt, 1995) which is substantially different from the present one (see Allard *et al*, 1997).

Table 9.7: The best model fit for each atomic line considered as a function of the effective temperature and metallicity for the infrared region

λ (μ m)	Element	$T_{\rm eff}$	[M/H]
1.11179	Al I		-1.0
1.111973	Fe I	3200	-0.8/-1.0
1.11631	Cr I		-1.0
1.11963	Ni I	3300	-0.8
1.11984	Ni I	3300	
	Ni I	3200	-0.6
1.12214	Al I	3150	-0.8/-1.0
1.12559	Fe I		-1.0
1.12974	Fe I		-1.0
1.13819	Na I	3150	-0.6

1.13846	Na I	3300	
1.18303	Mg I	3300	-1.0
1.19156	Fe I	3300	-1.0
1.18307	Mg I	3300	-1.0
1.19541	Ti I	3300	-1.0
1.20198	Si I	3400	-0.8
1.21192	Mg I	3400	-1.0
1.24034	K I	3300	-0.6
1.24360	K I	3300	
1.25264	K I	3300	-0.6
	K I	3200	-1.0
1.25706	Ti I	3200	-0.8
1.25998	Ti I	3400	-1.0
1.26800	Na I	3400	-1.0
2.20865	Na I	3300	-1.0
2.20899	Na I	3300	-0.6
	Na I	3200	-0.8

9.7 Helium Abundance

Because of the accuracy to which masses and radii are known, it has been pointed out that CM Dra could be a test system to determine primordial helium abundances (Paczynski & Sienkiewicz, 1984). Metcalfe *et al* (1996) followed the method employed by Paczynski & Sienkiewicz for obtaining helium abundances by comparing the nuclear luminosity with the observed one. They obtained the rather high values of $Y_{\rm A} = 0.32 \pm 0.04$ and $Y_{\rm B} = 0.31 \pm 0.04$ (where Y is defined as the helium fraction with respect to the hydrogen) as against quoted primordial helium abundances, for example Olive & Steigman (1995) values of $Y_{\rm p} = 0.232 \pm 0.003$. This may be due to the neglect of systematic errors such as

Table 9.8: Best metallicity match within each effective temperature after a detail ed spectral analysis of the infrared observed region.

$T_{\rm eff}$	3000	3100	3150	3200	3300	3400
0.0						
−0.2						
−0.4	⋆	⋆				
−0.6						
−0.8						
−1.0			⋆	⋆	⋆	⋆

non-LTE effects (Sasselov & Goldwirth, 1995) in computations of the helium abundance for hot stars, though it may also arise from a lack of consideration of metallicity. Fig. 2 in Burrows *et al* (1993b) shows the effect of varying the helium abundance between 0.22 and 0.28 for solar metallicity and between 0.22 and 0.25 for zero metallicity models. For masses between 0.1 and 0.2 $M_{\odot}$, it can be seen that the luminosity of the models are much more sensitive to metallicity than to helium abundance. According to this then, a much more reliable determination of the metallicity of CM Dra ($M/M_{\odot} \sim 0.2$) could help solving the discrepancy in the value for its helium abundance.

9.8 Results of the analysis of CM Dra

Figure 9.32 summarizes Tables 9.3, 9.4, 9.5 and 9.8. It also puts our findings for the range of effective temperature. Based on a direct comparison of synthetic and observed spectra in the near infrared region and in the optical region, we have investigated the effective temperature and metallicity of the binary system CM Dra. During the course of our analysis, we found some inconsistencies.

- The comparison of the general flux distribution for both the optical and infrared

region, implied that a metallicity of −1.0 is too low for the system.

- However, a more careful spectral analysis in the infrared suggested systematically lower metallicities (as low as −1.0) and/or higher temperatures (as high as 3300K) for an optimal fit.

- A detailed analysis of the optical spectrum leads to systematically lower effective temperatures (∼ 3200K) and higher metallicity (∼ –0.6) than a similar analysis of the infrared spectra.

Some of the inconsistencies noted are probably due to the incompleteness of the line lists used for the modelling, in particular for TiO and water vapour. Also CM Dra is close to the regime where grain formation may begin to affect the photosphere and spectral distribution of late M dwarfs in a way that could explain the discrepancies that we observed in modeling CM Dra. Some condensation may cause elemental abundances of line forming elements such as Fe I, Ti I, K I, Ca I, and Na I to drop by factors of 2-10 and simulate the aspect of a hotter star in high resolution analysis of line strengths. Models incorporating the effects of some grain formation have been computed by Tsuji (1996a,b) who argued that grain formation is the event responsible for this long-standing infrared discrepancy. However his models only begin to show strong grain formation for $T_{eff} \leq 2700$ K i.e. spectral types later than about M6 (Jones & Tsuji, 1997), leaving hotter cases unexplained.

We are however led to conclude that, although the systematic differences of the optical and IR derived parameters arise partly from both the observational uncertainties and the incompleteness of the current line lists, it is unlikely that any single metallicity parameter will reproduce all the spectral features. This suggests that CM Dra could be chemically peculiar and might not be reproduced by models based on solar abundances nor solar abundances patterns.

The inclusion of more accurate molecular linelists and possibly of better atomic data, as well as better spectral coverage and resolution of the observations are necessary for a confirmation of CM Dra chemical peculiarity and a more accurate determination of the

effective temperature and metallicity of CM Dra.

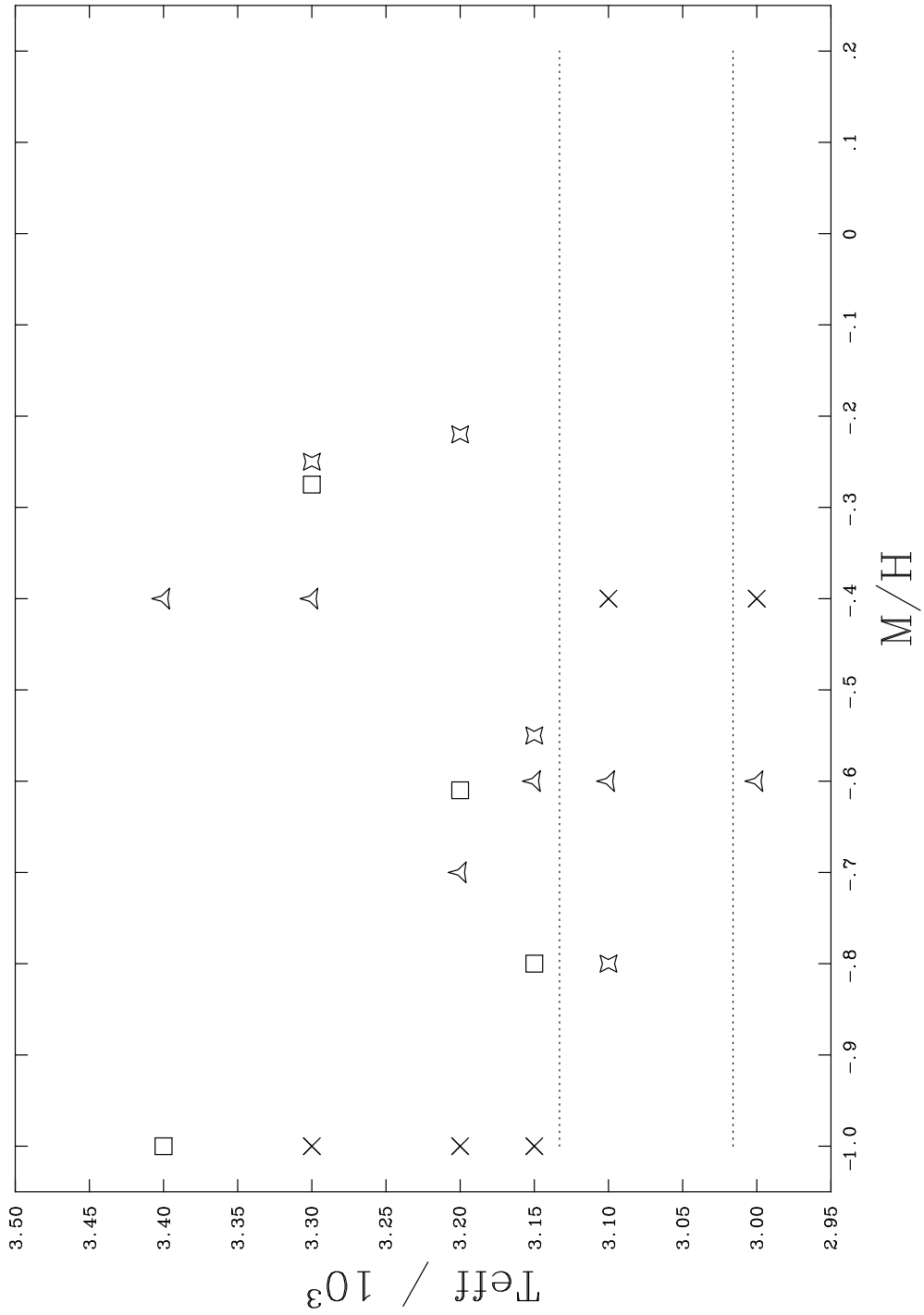

Figure 9.32: Summary of results. Square = IR results after a SED analysis (Table 9.3); Star (4 vertices) = Optical results after a SED analysis (Table 9.4); Cross = IR results after a detailed analysis (Table 9.5); Star (3 vertices) = Optical results after a detailed analysis (Table 9.8. The rectangle shows the range of Stefan-Boltzmann temperatures obtained from section 9.4.

Chapter 10

Conclusions and Future Work

This thesis is an attempt to cover partly some of the problems related to cool stellar atmospheres from a theoretical and observational point of view.

Originally, the goal of the thesis was to only compute a complete water linelist that, among other uses, would have been included into models of cool stellar atmospheres. During this project this goal became 'mangled' with others.

10.1 The Water linelists

When we started this project it was already obvious from the literature (Chapter 1 and 3) that reliable data on hot water were urgently needed. To confirm this, we ran some tests to prove the importance of reliable data on hot water, and we proved the incompleteness of molecular data included in model atmospheres. We then tried to show how our variational method could solve at least problems due to water opacity in the infrared (Chapter 2). Previous methods to compute molecular data have proven inaccurate. We have shown how *ab initio* calculations can give spectroscopic accuracy for triatomic molecules. Based on the same method described in Chapter 4, a new linelist for H_3^+ (Neale *et al*, 1996) has been made.

Water is now also known to play an important role in the interpretation of the spectra of sunspots; in the radiative cooling process of gas in circumstellar outflows, in dissocia-

tive and non-dissociative magnetohydrodynamic shocks in dense molecular clouds, in star forming regions and finally in extragalactic sources like AGN. Our first linelist, VTP1 (Chapter 5), is freely available on the Web. It has been used by groups working on water masers in star forming regions and AGN to assign strong emission lines with spectroscopic accuracy. ZVPT (Chapter 6) has been used and is still used, to assign water in sunspots. The density of water lines in sunspots requires that transitions should be predicted to better than 0.1 cm^{-1} for assignments. This proved to be possible with ZVPT once the systematicity of the errors had been worked out. These assignments finally demonstrated the utility and accuracy of linelists generated using variational nuclear motion calculations. Our final linelist, VT2 (Chapter 7) is however still incomplete. As mentioned in the conclusions of Chapter 7, we decided to stop VT2 computation for lack of computer time and the awareness of a new published water linelist (PS). I hope to have shown in Chapter 7 that the PS linelist might still be insufficient for reproducing the water opacity in cool stellar atmospheres.

However, from Chapter 7 discussion a question quickly arise: are the models not yet matching because the right composition and quantity of dust has not yet been included properly, or because water data are still insufficiently accurate? Could it be a combination of both? Whatever the right answer will be, we have proved with VTP1 and ZVPT the validity of DVR3D. We believe that by completing VT2 we can provide an answer to the above question.

10.2 Parameters for low mass stars

In Chapter 1 we stressed the importance of the low–mass stellar mass function in large scale. We also underlined how it must be derived from the stellar luminosity function because it can not be observed directly. Many different models have been trying to find an accurate luminosity-mass relationship. Unfortunately there is disagreement among them (Burrows *et al*, 1993b; D'Antona & Mazzitelli, 1994; Baraffe *et al*, 1995 and many others). In order to distinguish between these competing models, one requires precise parameters

for low-mass eclipsing binaries. They represent the only place where reliable masses, radii and temperature can be directly determined. CM Dra is currently the only known example of such a system near the bottom of the main sequence and as such represents the *only* solid reference point to which theoretical models of low-mass stars can be compared. In order to use it at its best, we need to narrow down those essential parameters such as the effective temperature and the metallicity of the system. This was the aim of Chapter 9 where we began a spectroscopic study of CM Dra both in the infrared and in the optical. The results were puzzling and at the same time revealing.

We did not manage uniquely to pick out best metallicity and temperature for CM Dra. However, a complete spectroscopic analysis both in the infrared and in the optical has never been done before. Within each of the wavelength regions we have indeed constrained the values for both the temperature and the metallicity. However, we found disagreement between the two analyses. This led us to hypothesize on the (i) accuracy of the models, (ii) accuracy of the observations, (ii) the nature of CM Dra.

The type of analysis performed is similar to previous spectral analysis techniques. Many have used strong features to place M dwarfs within a spectral sequence (Leggett 1992; Leggett *et al*, 1996; Kirkpatrick *et al*, 1993). Others use single elements, such as lithium, to decide if a substellar object is a brown dwarf or not (Rebolo *et al*, 1995 etc.). However, a large sample of strong and weak lines has never before been used to discern effective temperature to uncertainty of 50K or metallicity to uncertainty of 0.2 in the infrared *and* optical togheter. We have proved how sensitive atomic features are to changes in these two key parameters. We find no reason why the width and strength of atomic lines should be biassed. The question to ask is: is the analysis not conclusive because of the inaccuracy of the observations, or because of the incompleteness of the models, or both? Or is CM Dra a chemically peculiar system? In principle, with very high resolution and S/N observations and high quality models, this question could be answered.

The quality of the models is indeed improving rapidly. The extensive analysis per-

formed in Chapter 9 formed the basis of three observational proposals. In collaboration with Dr. P. Maxted (University of Southampton), Dr. H. R. A. Jones (Tokyo, LJMU), Dr. F. Allard (Wichita State University) and Dr. P. H. Hauschildt (University of Georgia) we have been awarded telescope time at the JKT (the 1-m Jacobus Kapteyn Telescope) to do differential photometry and obtain lightcurves for CM Dra, WHT (the 4.2-m William Herschel Telescope) to obtain very high resolution optical spectra of the region 0.4–1.0 μm and UKIRT (UK Infrared Telescope) to obtain the same but for small restricted regions in the infrared. We have indeed obtained beautiful data which are waiting to be reduced and analyzed. The resolution will be high enough to disentangle the two components. Such analysis will allow the determination of a reliable T_{eff} scale, which is still missing for M-dwarfs, and it will provide accurate mass - magnitude - T_{eff} relationships. A detailed spectral analysis of CM Dra is a first step towards new types of analyses, achievable now because of the improvements of the instruments.

Beside the accomplishments on CM Dra and related to CM Dra general conclusions can be drawn:

(i) Despite the uniqueness of CM Dra, we believe that the type of analysis performed above should be a good tool to investigate the effective temperature, metallicity and surface gravity scales. Usually most comparisons rely mainly on a Spectral Energy Distribution analysis with some help from the most reliable and already identified strong atomic lines.

Provided a certain reliability of the models (assumed anyway when performing any type of general or detailed analysis), synthetic identification of weak atomic lines can be used to find the best sensitive lines to temperatures, metallicities and surface gravities. With the ever increasing power of the current infrared and optical telescopes, high resolution data are starting becoming available making the line identification task easier.

(ii) Most of the previous studies of LMS have relied mainly on the infrared part of the spectrum. Although, it contains most of the flux, it is not unique in containing forests of interesting and sensitive atomic lines. We believe the optical spectrum can be used in the

same way as the infrared.

(iii) Finally, while in the above study, molecular opacities were a nuisance more than a help, with the coming of new and accurate molecular linelists, overall of water, molecules could seriously become a good thermometer for LMS, ultimately deciding their precise effective temperature scale.

Abe Y, Matsui T, 1988, *J. Atmos. Sci.*, **45**, 3081

Adams F C, Fatuzzo M, 1996, *Astrophysical Journal*, **464**, 256

Alexander D R, Johnson H R, 1989, *Astrophysical Journal*, **345**, 1014

Allard F, 1990, *Ph.D Thesis*, University of Heidelberg

Allard F, Hauschildt P H, Miller S, Tennyson J, 1994, *Astrophysical Journal*, **426**, 39

Allard F, 1995, *Nature*, **378**, 441

Allard F, Hauschildt P H, 1995, *Astrophysical Journal*, **445**, 433

Allard F, Lawlor T, Alexander D R, Hauschildt P H, 1995, *AAS*

Allard F, Hauschildt P H, Baraffe I, Chabrier G, 1996, *Astrophysical Journal* , **456**, 123L

Allard F, Hauschildt P H, Alexander D R, Starrfield S, 1997, *Annual Reviews of Astronomy and Astrophysics*, in press

Allen C W, 1973, *Astrophysical quantities*, London

Auman J J, 1967, *Astronomy and Astrophysics Supplement Series*, **14**, 171

Bačič Z & Light J C, 1986, *J. Chem. Phys.*, **85**, 4594

Banwell C N, McCash E M, 1972, *Fundamentals of molecular spectroscopy*, UK

Baraffe I, Chabrier G, Allard F, Hauschildt P H, 1995, *Astrophysical Journal*, **446**, L35

Barlow M J *et al*, 1996, *Astronomy and Astrophysics Letters*, **315**, 241

Basri G, Marcy G W, 1997, *Proceedings of the Brown Dwarfs and Extrasolar Planets Conference*, in press

Becklin E E, Macintosh B, Zuckerman B, 1995, *Astrophysical Journal*, **449**, 117

Berriman G, Reid N, 1987, *Monthly Notices of the RAS*, **227**, 315

Bessell M S, Brett J M, Wood P R, Scholz M, 1989, *Astronomy and Astrophysics*, **213**, 209

Bessell M S, Stringfellow G S, 1993, *Annual Reviews of Astronomy and Astrophysics*, **31**, 433

Blitz L, 1996, unpublished

Bohm-Vitense E, 1958, *Z. Astrophys.*, **46**, 108

Born M, Oppenheimer R J, 1927, *Ann. Phys.*, **84**, 457

Bowers R L, Deeming T, 1984, *Astrophysics - Stars* , **Vol. 1**, Los Alamos National Laboratory, Los Alamos

Brett J M, 1995a, *Astronomy and Astrophysics Supplement Series*, **109**, 263

Brett J M, 1995b, *Astronomy and Astrophysics*, **295**, 736

Brett J M, Plez B, 1993, *Proc. ASA*, **10**, 250

Brown J M, Hougen J T, Huber K–P, Johns J W C, Kopp I, Lefrebvre–Brion H, Merer A J, Ramsay D A, Rostos J, Zare R N, 1975, *J. Mol. Spectrosc.*, **55**, 500

Bucknell M G, Handy N C, Boys S F, 1974, *Molecular Physics*, **28**, 759

Burrows A, Hubbard W B, Lunine J I, 1993a, *Proc. 8th Cambridge Workshop*, **93**, 1

Burrows A, Hubbard W B, Saumon D, Lunine J I, 1993b, *Astrophysical Journal*, **406**, 158

Burrows A, Hubbard W B, Lunine J I, 1994, *ASP Conf. Ser.*, **64**, 528

Camy-Peyret C, Flaud M, Maillard J P, Guelachvili G, 1977, *Mol. Phys.*, **33**, 1641

Carney G D, Sprandel L L, Kern C W, 1978, *Advan. Chem. Phys.*, **37**, 305

Carter S, Handy N C, 1987, *J. Chem. Phys.*, **87**, 4294

Chabrier G, Baraffe I, 1995, *Astrophysical Journal*, **451**, 29

Chen W, Neufeld D A, 1995, *Astrophysical Journal* , **453**, 99L

Choi S E, Light J C, 1992, *J. Chem. Phys.*, **97**, 7031

Colina L, Bohlin R C, 1994, *Astrophysical Journal*, **108**, 1931

Collins J G, Faïj T D J, 1974, *Journal of Quantitative Spectroscopy and Radiative Transfer*, **14**, 1259

D'Antona F, Mazzitelli I, 1994, *Astrophysical Journal Supplement Series*, **90**, 467

D'Antona F, Mazzitelli I, 1996, *Astrophysical Journal*, **456**, 329

Dahn C C, Liebert J, Harrington R S, 1986, *Astrophysical Journal*, **91**, 621

De Marchi G, Paresce F, 1997, *Astrophysical Journal*, **476**, 19

Draine B T, Roberge W G, Dalgarno A, 1983, *Astrophysical Journal*, **264**, 485

Fernley J A, Miller S, Tennyson J, 1991, *J. Mol. Spectrosc.*, **150**, 597

Ferriso C C, Ludwig C B, Thomson A L, 1966, *Journal of Quantitative Spectroscopy and Radiative Transfer*, **6**, 241

Flaud J M, Camy-Peyret C, 1976, *Molecular Physics*, **32**, 499

Flaud J M, Camy-Peyret C, Guelachvili G, 1977, *J. Mol. Spectrosc.*, **65**, 219

Flaud J M, Camy-Peyret C, Toth R A, 1981, *Selected Constants: Water Vapour Line Parameters from Microwave to Medium Infrared*, Pergamon, Oxford

Flaud J M, Camy-Peyret C, Bykiv A, Naumenko O, Petrova T, Scherbakov A, Sinitsa L, 1997, *J. Mol. Spectrosc.*, **183**, 300

Forrest W J, Shure M, Skrutskie M F, 1988, *Astrophysical Journal* , **330**, 119L

Fowler A, 1904, *Proc. R. Soc.*, **73**, 219

Fulton N G, 1994, *Ph.D Thesis*, University of London

Gabriel W, Reinsch E-A, Rosmus P, Carter S, Handy N C, 1993, *J. Chem. Phys.*, **99**, 897

Gizis J, 1997, *Astronomical Journal*, **113**, 806

Gould A, Bahcall J N, Flynn C, 1996, *Astrophysical Journal*, **465**, 759

Hall D N B, 1970, *Observations of the infrared sunspot spectrum between 11340A and 24778A.*, **116**

Halonen L and Carrington T Jr, 1988, *J. Chem Phys.*, **88, 4171**

Hambly N C, Jameson R F, 1991, *Monthly Notices of the RAS*, **249**, 137

Hauschildt P H, 1991, *Ph.D Thesis*, University of Heidelberg

Hawkins M R S, Bessell M S, 1988, *Monthly Notices of the RAS*, **234**, 177

Henderson J R, 1990, *Ph.D thesis*, University of London

Henderson J R, Tennyson J, 1993, *Computer Physics Communications*, **75**, 365

Henry T J, McCarthy D W, 1993, *Astrophysical Journal*, **106**, 773

Herzberg G, 1945, *Molecular Spectra and Molecular Structure*, Malabar, Florida

Hoy A R, Mills I M, Strey G, 1972, *Mol. Phys.*, **24**, 1265

Horne K, 1986, *Publication of the Astronomical Society of the Pacific*, **98**, 609

Huber K P, Herzberg G, 1979, *Constants of Diatomic Molecules*, New York

Jameson R F, Skillen I, 1989, *Monthly Notices of the RAS*, **239**, 247

Jensen P, 1988, *Journal of Chemical Society-Faraday transactions II*, **84**, 1315

Jensen P, 1989, *J. Mol. Spectrosc.*, **133**, 438

Jones H R A, Longmore A J, Jameson R F, Mountain C M, 1994, *Monthly Notices of the RAS*, **267**, 413

Jones H R A, Longmore A J, Allard F, Hauschildt P H, Miller S, Tennyson J, 1995, *Monthly Notices of the RAS*, **277**, 767

Jones H R A, Longmore A J, Allard F, Hauschildt P H, 1996, *Monthly Notices of the RAS*, **280**, 77

Jones H R A, Tsuji T, 1997, *Astrophysical Journal* , **480** , 39L

Jørgensen U G, 1992, *Rev. Mex. Astron. Astrofis*, **23**, 49

Jørgensen U G, Jensen P, 1993, *J. Mol. Spectrosc.*, **161**, 219

Jørgensen U G, 1994, *Astronomy and Astrophysics*, **284**, 179

Kauppinen J, Karkkainen T, Kyro E, 1979, *J. Mol. Spectrosc.*, **71**, 14

Kippenhan R, 1962, *Proc. xxviii course*, Technical report, Internat. School 'Enrico Fermi'

Kirkpatrick J D, Kelly D M, Rieke G H, Liebert J, Allard F, Wehrse R, 1993, *Astrophysical Journal*, **402**, 643

Kirkpatrick J D, Henry T J, Simons D A, 1995, *Astronomical Journal*, **109**, 797

Kui R, 1991, *Ph.D Thesis*, National University of Australia

Lacy C H, 1977, *Astrophysical Journal*, **218**, 444

Lee S-G, 1984, *Astronomical Journal*, **89**, 720

Leggett S K, Hawkins M R S, 1988, *Monthly Notices of the RAS* , **234**, 1065

Leggett S K, 1992, *Astrophysical Journal Supplement Series*, **82**, 351

Leggett S K, Allard F, Berriman G, Dahn C C, Hauschildt P H, 1996, *Astrophysical Journal Supplement Series*, **104**, 117

Leinert C, Haas M, Allard F, Wehrse R, McCarthy D W, Jahreiss J H, Perrier C, 1990, *Astronomy and Astrophysics*, **236**, 399

Lepine J R D, Ortiz R, Epchtein N, 1995, *Astronomy and Astrophysics*, **299**, 453

Light J C, Hamilton I P, Lill J V, 1985, *J. Chem. Phys.* , **92**, 1400

Lord Rayleigh, 1937, *Theory of Sound*, **Vol. 1**, sec. 88, Macmillan, London

Ludwig C B, 1971, *Applied Optics*, **10**, 1057

Ludwig C B, Malkmus W, Reardon J E, Thomson J A L, 1973, *Handbook of Infrared radiation From Combustion Gases NASA SP-3080,*

Lunine J I, Hubbard W B, Marley M S, 1986, *Astrophysical Journal*, **310**, 238

Lynas-Gray A E, Miller S, Tennyson J, 1995, *J. Mol. Spectrosc.*, **169**, 458

Magazzu A, Martin E L, Rebolo R, 1993, *Astrophysical Journal* , **404**, 17L

Mandin J Y, Dana V, Camy-Peyret C, Flaud J M, 1992, *J. Mol. Spectrosc.*, **152**, 179

Martin E L, Zapatero Osorio M R, Rebolo R, 1996, *Proc. 9th Cambridge Workshop*, **109**, 615

Mera D, Chabrier G, Baraffe I, 1996, *Astrophysical Journal*, **459**, L87

Metcalfe T S, Mathieu R D, Latham D W, Torres G, 1996, *Astrophysical Journal*, **456**, 356

Michaud G, Charbonneau P, 1991, *Space Science Reviews*, **57**, 1

Mihalas D, Binney J, 1981, *Galactic astronomy: Structure and kinematics*, 2nd Edition, San Francisco, CA, W. H. Freeman and Co.

Miller S, Tennyson J, Jones H R A, Longmore A J, from Lecture Notes in Physics, "Molecules in the Stellar Environment", ed. U.G. Jørgensen, Springer 1994, p 296

Monet D G, Dahn C C, Vrba F J, Harris H C, Pier J R, Luginbuhl C B, Ables H D, Harold D, 1992, *Astronomical Journal*, **103**, 638

Mould J R, 1975, *Astronomy and Astrophysics*, **38**, 282

Mould J R, 1976, *Astronomy and Astrophysics*, **48**, 443

Nakajima T, Oppenheimer B R, Kulkarni S R, Golimowski D A, Matthews K, Durrance S T, 1995, *Nature*, **378**, 473

Neale L, Miller S, Tennyson J, 1996, *Astrophysical Journal*, **464**, 516

Neufeld D A, Melnick G J, 1987, *Astrophysical Journal*, **322**, 266

Neufeld D A, Maloney P R, Conger S, 1994, *Astrophysical Journal* , **436**, 127L

Neufeld D A *et al*, 1996, *Astronomy and Astrophysics Letters*, **315**, 237

Oke J B, 1990, *Astrophysical Journal*, **99**, 1621

Olive K A, Steigman G, 1995, *Astrophysical Journal Supplement Series*, **97**, 49

Oppenheimer B R, Kulkarni S R, Matthews K, Nakajima T, 1995, *Science*, **270**, 1478

Paczynski B, Sienkiewicz R, 1984, *Astrophysical Journal*, **286**, 332

Paresce F, De Marchi G, Romaniello M, 1995, *Astrophysical Journal*, **440**, 216

Partridge H, Schwenke D W, 1997, *J. Chem. Phys.*, **106**, 4618

Phillips W J, 1990, *J. Quant. Spect. Rad. Trans.*, **43**, 13

Polyansky O L, 1985, *J. Mol. Spectrosc.*, **112**, 79

Polyansky O L, Tennyson J, 1992, *J. Mol. Spectrosc.*, **154**, 246

Polyansky O L, Jensen P, Tennyson J, 1994, *J. Chem. Phys.*, **101**, 7651

Polyansky O L, Jensen P, Tennyson J, 1996a, *J. Chem. Phys.*, **105**, 6490

Polyansky O L, Busler J R, Guo B, Zhang K, Bernath P, 1996b, *J. Molec. Spectrosc.*, **176**, 305

Polyansky O L, Zobov N F, Viti S, Tennyson J, Bernath P F, Wallace L, 1997a, *Science*, **277**, 346

Polyansky O L, Zobov N F, Viti S, Tennyson J, Bernath P F, Wallace L, 1997b, *Astrophysical Journal* , in press

Polyansky O L, Zobov N F, Viti S, Tennyson J, Bernath P F, Wallace L, 1997c, *J. Molec. Spectrosc.*, in press

Polyansky O L, Tennyson J, Bernath P F, 1997d, *J. Mol. Spectrosc.*, in press

Popper D M, 1980, *Annual Review of Astronomy and Astrophysics*, **18**, 115

Puxley P J, Ramsay S K, Beard S M, 1992, *in Grosbol P., roc. 4th ESO/ST-ECF data analysis workshop*

Radau R, 1928, *Phys. Rev.*, **32**, 812

Ray B S, 1932, *Z. Physik*, **78**, 74

Ray T P, Beckwith S V W, 1994, *Star formation and techniques in infrared and mm-wave astronomy*, Lecture Notes in Physics

Rebolo R, Martin E L, Magazzu' A, 1992, *Astrophysical Journal*, **389**, 83

Rebolo R, Zapatero Osorio M R, Martin E L, 1995, *Nature*, **377**, 128

Reid I N, Hawley S L, Gizis J E, 1995, *Astronomical Journal*, **110**, 1838

Riviere PH, Langlois S, Soufiani A, Taine J, 1995, *J. Quant. Spect. Rad. Trans.*, **53**, 221

Rosen B, 1970, *Tables Internationales de Constantes Selectionnees*, **17**, New York

Rosenberg B J, Ermler W C, Shavitt I, 1976, *J. Chem. Phys.*, **65**, 4072

Rothman L S *et al*, 1987, *Applied Optics*, **26**, 4058

Rothman L S *et al*, 1992, *J. Quant. Spect. Rad. Trans.*, **48**, 469

Rothman L S, Gamache R, Schroeder J W, McCann A and Wattson R B, 1995, *SPIE Proc.*, **2471**, 105

Rothman L S, 1996, Private Communications.

Rucinski S M, 1978, *Acta Astronomica*, **28**, 167

Ruiz M T, Leggett S K, Allard F, 1997, *Proc. 10th Cambridge Workshop*, in press

Sasselov D, Goldwirth D S, 1995, *Astrophysical Journal* , **444**, 5L

Sandage A, 1986, *Annual Review of Astronomy and Astrophysics*, **24**, 421

Saumon D, Bergeron P, Lunine J I, Hubbard W B, Burrows A, 1994, *Astrophysical Journal*, **424**, 333

Schryber J H, Miller S, Tennyson J, 1995, *J. Quant. Spect. Rad. Trans.*, **53**, 373

Schwenke D W, 1992a, *Chem. Phys. Lett.*, **189**, 91

Schwenke D W, 1992b, *Comput. Phys. Commun,*, **70**, 1

Schwenke D W, 1996, *J. Phys. Chem*, **100**, 18884

Sutcliffe B T, Tennyson J, 1987, *J. Chem. Soc., Faraday Trans.*, **83**, 1663

Suzuki I, 1971, *Bull. Chem. Soc. Jap.*, **44**, 3277

Suzuki I, 1975, *Bull. Chem. Soc. Jap.*, **48** , 3565

Tennyson J, Sutcliffe B T, 1982, *J. Chem. Phys.*, **77**, 4061

Tennyson J, Sutcliffe B T, 1986, *Mol. Phys.*, **58**, 1067

Tennyson J, 1992, *J. Chem. Soc. Faraday Transactions*, **88**, 3271

Tennyson J, Sutcliffe B T, 1992, *International Journal of Quantum Chemistry* , **42**, 941

Tennyson J, Miller S, LeSueur C R, 1993, *Computer Physics Communications*, **75**, 339

Tennyson J, Henderson J R, Fulton N G, 1995, *Computer Physics Communications*, **86**, 175

Tinney C G, Mould J R, Reid I N, 1992, *Astrophysical Journal*, **396**, 1 73

Tinney C G, 1993, *Astronomical Journal*, **105**, 1169

Tinney C G, Mould J R, Reid N, 1993, *Astronomical Journal*, **105**, 1045

Tinney C G, Reid I N, Gizis J, Mould J R, 1995, *Astronomical Journal*, **110**, 3014

Toth R A, 1991, *J. Opt. Soc. Am. B*, **11**, 2236

Toth R A, 1993, *J. Opt. Soc. Am. B*, **10**, 1526

Toth R A, 1994, *Appl. Opt.*, **33**, 4851

Townes C H, Schawlow A L, 1975, *Microwave Spectroscopy*, Dover, New York

Tsuji T, 1966, *PASJ*, **18**, 127

Tsuji T, Ohnaka K, 1994, *Proceedings JD 16 IAU*, **94**, 17

Tsuji T, Ohnaka K, Aoki W, 1996a, *Astronomy and Astrophysics*, **305**, 1

Tsuji T, Ohnaka K, Aoki W, Nakajima T, 1996b, *Astronomy and Astrophysics*, **308**, 29

Veeder G J, 1974, *Astronomical Journal*, **79**, 1056

Wallace L, Livingston W, 1992, *An Atlas of a Dark Sunspot Umbral Spectrum from 1970 to 8640 cm-1*

Wallace L, Livingston W, Bernath P, 1994, *An Atlas of the sunspot spectrum from 470 to 1233 cm-1 (8.1 to 21 micrometer) and the photospheric spectrum from 460 to 630 cm-1 (16 to 22 micrometer)*

Wallace L, Bernath P, Livingston W, Hinkle K, Busler Guo B, Zhang K, 1995, *Science*, **268**, 1165

Wallace L, Livingston W, Hinkle K, Bernath P, 1996, *Astrophysical Journal Supplement Series*, **106**, 165

Watson J K G, 1977, *Vibrational Spectra and Structure*, edited by J. R. Durig (Elsevier, Amsterdam), **6**, 1

Wattson R B, Rothman L S, 1992, *J. Quant. Spectrosc. Radiat. Trans.*, **48**, 763

Wilson S E B, Decius J C, Cross D C, 1980, *Molecular Vibrations. The theory of Infrared and Raman Vibrational spectra*, Dover, New York

Yates J A, Cohen R J, Hills R E, 1995, *Monthly Notices of the RAS*, **273**, 529

Zeidler K T E-M, Koester D, 1982, *Astronomy and Astrophysics*, **113**, 173

Zelik M, Smith E v P, 1987, *Introductory Astronomy and Astrophysics*, New York

Zobov N F, Polyansky O L, LeSueur C R, Tennyson J, 1996, *Chemical Physics Letters*, **260**, 381

Zuckerman B, Becklin E E, 1987, *Astrophysical Journal Letters*, **319**, 99

van Altena W F, Lee J T-L, Hoffleit D, 1995, *Catalogue of Trigonometric parallaxes*, Yale University Observatory

Viti S, Jones H R A, Schweitzer A, Allard F, Hauschildt P H, Tennyson J, Miller S, Longmore A J, 1996, *Monthly Notices of the RAS*, in press

Viti S, Jones H R A, Tennyson J, Allard F, Hauschildt P H, 1997b, *Proceedings of the Brown Dwarfs and Extrasolar Planets Conference*, in press